Pyroclastic eruptions in mid-ocean ridge settings: insights from Axial Seamount, Juan de Fuca Ridge, and analogue experiments

Christoph Helo

Department of Earth and Planetary Sciences
McGill University
Montréal, Québec, Canada

November 2011

A thesis submitted to McGill University in partial fulfillment of the requirements of the degree of Doctor of Philosophy

"[…] We know a great deal. And we know not only many details of doubtful intellectual interest but also things which are of considerable practical significance and, what is even more important, which provide us with deep theoretical insight, and with a surprising understanding of the world."

"[…] Our ignorance is sobering and boundless. Indeed, it is precisely the staggering progress of the natural sciences (to which my first thesis alludes) which constantly opens our eyes anew to our ignorance, even in the field of the natural sciences themselves. This gives a new twist to the Socratic idea of ignorance. With each step forward, with each problem which we solve, we not only discover new and unsolved problems, but we also discover that where we believed that we were standing on firm and safe ground, all things are, in truth, insecure and in a state of flux."

Karl R. Popper

Contents

Abstract

This investigation addresses the origin and nature of explosive volcanism in deep submarine environments. Volcaniclastic deposits were sampled as sediment cores from Axial Seamount, a basaltic caldera volcano situated on the Juan de Fuca mid-ocean ridge in the northeast Pacific Ocean. These prominent volcaniclastic deposits resemble those found on other mid-ocean ridge sites. The deposits are interpreted as pyroclastic reflecting explosive eruptions. On Axial Seamount, the volcaniclastic material comprises mainly basaltic glass fragments displaying a range of morphologies, including limu o Pele and Pele's hair. In the present study, glass fragments from several core sections were examined for their morphological characteristics, as well as for major, trace and volatile element compositions. Plagioclase-hosted melt inclusions recovered from selected sections of the volcaniclastic sediments were also analysed for their major, trace and volatile element budgets.

The glass fragments show MgO of 9.4–6.5 wt. %, and $[La/Yb]_N$ generally between 0.95 and 1.1, with the exception of one sample group showing $[La/Yb]_N$ of 0.6–0.85. CO_2 concentrations in the melt inclusions were found to vary greatly due to decompression degassing, with concentrations ranging from 260 ppm to 9160 ppm. Cooling histories of glass fragments were estimated by differential scanning calorimetry (DSC), indicating extremely rapid quench rates of up to 10^6 K s^{-1} during eruptions. The physical properties of the fragments, i.e., their morphologies and cooling rates, as well as the CO_2 budget of the magmatic system, are consistent with explosive activity primarily driven by high levels of magmatic CO_2.

In order to better understand eruption behaviour and magma fragmentation in high-

pressure environments such as the deep ocean, a series of decompression experiments were performed using gum rosin-acetone mixtures as an analogue for magma-volatile systems. These experiments demonstrate that ascent rates and fragmentation behaviour of magma are influenced by various extrinsic and intrinsic parameters such as pre-eruptive bubble content and variations in conduit diameter. These factors can facilitate explosive eruptions in high-pressure environments.

Résumé

Ce travail aborde l'origine et la nature du volcanisme explosif des environnements sous-marins profonds. Des carottes de dépôts volcano-clastiques ont été échantillonnées au volcan Axial, une caldeira basaltique sous-marine située sur la ride médio-océanique Juan de Fuca dans le nord-est du Pacifique. Ces dépôts volcano-clastiques proéminents ressemblent à ceux trouvés sur d'autres sites de ride médio-océanique. Les dépôts sont interprétés comme étant d'origine pyroclastique, donc ayant été formés au cours d'éruptions explosives. Au volcan Axial, le matériel volcano-clastique est composé principalement de fragments de verre basaltique de morphologies diverses, incluant des limu o Pele et des cheveux de Pele. Au cours de cette étude, les caractéristiques morphologiques et la composition en éléments majeurs, traces et volatiles de fragments de verre provenant de plusieurs sections de carottes ont été déterminées. Des inclusions de verre contenues dans des cristaux de plagioclase ont également été analysées afin d'évaluer leur budget en éléments majeurs, traces et volatiles.

Les fragments de verre ont une teneur en MgO de 9.4–6.5 %m et des rapports $[La/Yb]_N$ généralement entre 0.95 and 1.1, à l'exception d'un groupe d'échantillons ayant

des ratios $[La/Yb]_N$ de 0.6–0.85. La teneur en CO_2 des inclusions de verre fluctue grandement dû au dégazage de décompression avec des mesures variant de 260 à 9160 ppm. L'historique de refroidissement des fragments de verre a été estimé par calorimétrie différentielle à balayage et les résultats indiquent des taux de refroidissement extrêmement rapide de plus de 10^6 K s^{-1} durant les éruptions. Les propriétés physiques des fragments, i.e. leurs morphologies et leurs taux de refroidissement, ainsi que le budget du système magmatique en CO_2 suggèrent une activité volcanique explosive essentiellement entrainée par les teneurs élevées en CO_2 magmatique.

Afin de mieux comprendre le comportement éruptif et la fragmentation du magma dans des environnements de haute pression tels les fonds marins, des expériences de décompression ont été menées en utilisant des mélanges de colophane et d'acétone en tant qu'analogue des systèmes magma-gaz. Ces expériences démontrent que les rythmes de montée du magma et sa fragmentation sont influencés par plusieurs paramètres extrinsèques et intrinsèques tels que la concentration de bulles dans le magma avant l'éruption et le diamètre du conduit magmatique. Ces facteurs peuvent faciliter le volcanisme explosif en milieu sous-marin à haute pression.

Acknowledgements

I would like to express my gratitude to all who have made this thesis possible. Thanked are all members of the administration staff at the Earth and Planetary Sciences Department for their enduring and patient support with administrative questions and IT issues. Evenly acknowledged is the technical stuff for help in sample preparation and analyses, especially Lang Shi for his exhaustless patience and advice on electron microprobe analysis.

I would like to thank the faculty staff of the Earth and Planetary Sciences Department for their advice and support throughout the years. In particular I would like to give my thanks to my thesis supervisor Prof. John Stix and advisory committee, Prof. Don Francis and Prof. Bill Minarik, for their continuous support, trust, and guidance.

The Monterey Bay Aquarium Research Institute, specifically Dr. Dave Clague, is more than gratefully recognized for the initiation of this thesis, provision of the samples, and most importantly for fruitful scientific discussions and advice. Dr. Nobumichi Shimizu, Woods Hole Oceanographic Institution, Prof. Don Dingwell and Dr. Kai-Uwe Hess, University of Munich, and Dr. Jeremy Phillip, University of Bristol, are appreciated for their interest in collaborating on parts of my project and providing lab facilities and scientific advice.

I would also like to express my appreciation for the strong support I have received through several fellowships at McGill University, including R.H. Tomlinson, GEOTOP, and J.W. McConnell Memorial Fellowships.

I am most grateful to my wife Julia for her endless support and patience throughout the years and spatial distance.

General introduction

One of the frontiers in deep-sea geology is the recognition of widespread volcaniclastic deposits at mid-ocean ridges and near-ridge seamount systems, consisting of various types of basaltic glass fragments. These have been described from several sites in the Pacific, including the Juan de Fuca Ridge, the Gorda Ridge, the Blanco transform fault, near-ridge seamounts, the East Pacific Rise and the Fiji back-arc basin (cf. Clague et al., 2009, and references within), as well as from the ultraslow spreading Gakkel ridge in the Artic Basin (Sohn et al., 2008). The production of volcaniclastic sediment therefore occurs over a wide range of water depths to > 4000 m below sea level.

Volcaniclastic deposits usually contain limu o Pele fragments comprising thin melt films commonly described as remnants of bubble walls. Originally, explosions driven by seawater-steam expansion were thought to produce such fragments from advancing sheet flows (Clague et al., 2000; Maicher and White, 2001). However, this mechanism has been questioned since the discovery of limu o Pele at depths below the critical point of water, where significant fluid expansion is inhibited. Subsequent studies have invoked a pyroclastic origin instead, i.e., fragmentation of magma initiated or primarily driven by magmatic gas (e.g., Clague et al., 2003; Davis and Clague, 2003; Sohn et al., 2008; Helo et al., 2011). Nonetheless, a hydrovolcanic origin is still preferred in a recent study by Schipper and White (2010).

Although such deposits may represent explosive, strombolian-type activity in mid-ocean ridge environments, the general eruption mechanism is poorly constrained, and little is known about the evolution of larger submarine volcanic edifices and caldera systems, or their role as highly permeable layers upon hydrothermal systems. The

recognition of these deposits as pyroclastic in origin has important consequences for the volatile budget of mid-ocean ridges, in particular carbon dioxide, as well as for the behaviour of these volatile phases during their ascent from the mantle into the shallow magma reservoir. Importantly, significant deposits of such volcaniclastic debris containing abundant limu o Pele have been found on Axial Seamount, Juan de Fuca Ridge in the northeast Pacific (Clague et al. 2009; this study).

Both the Juan de Fuca Ridge and Axial Seamount in particular are among the most intensely studied and best characterized parts of the global mid-ocean ridge system. The Juan de Fuca Ridge is a spreading centre off the coast of Oregon, about 500 km in length, separating the Juan de Fuca and the northeast Pacific plates. It is a remnant of the disintegration of the Farallon ridge as it was partly subducted beneath the North American Plate between 55 Ma and 30 Ma (Davis and Currie, 1993). As a medium-rate spreading centre, it shares many morphological and bathymetric features with fast-spreading systems, e.g., small summit graben and pronounced axial highs. Geochemical studies have revealed a great diversity of mid-ocean ridge basalt (MORB) compositions ranging from depleted to enriched (e.g., Karsten et al., 1990; Van Wagoner and Leybourne, 1991; Smith et al., 1994; Cousens et al., 1995). The central section of the Juan de Fuca Ridge is one of the few cases of a mid-ocean ridge segment interacting with a hot-spot system (Rhodes et al., 1990; Hooft and Detrick, 1995; Chadwick et al., 2005). This interaction with the Cobb hot-spot gives rise to the prominent Axial Seamount volcanic edifice; since the early 1980's, this site has become the centre of attention for studies along the Juan de Fuca Ridge. During 1981-1984 the first multibeam sonar survey was conducted with the NOAA vessel *Surveyor*, and the first active black smoker vents in

the northeast Pacific Ocean were discovered during dives with the submersible *Pisces* along the summit region (Chase et al., 1985). During the past several decades, it has continuously been the target for numerous ship surveys and submersible and remotely controlled vehicle dives, which have collected a large set of geological, geophysical and geochemical data. In addition, volcanic monitoring systems and acoustic extensometers have been installed recording temperature, ground deformation (Fox, 1993; Chadwick et al., 1999), and seismic activity (Dziak and Fox, 1999a). High-resolution multibeam mapping employing the MBARI Mapping Autonomous Underwater Vehicle (AUV) during the 2006-2007 NOAA NeMO cruises provided a new generation of detailed bathymetry maps of Axial Seamount at a resolution of 1 m (Thomas et al., 2006; Caress et al., 2007; Clague et al., 2007).

These surveys and investigations delineate a picture of an active caldera system situated over an overlapping spreading centre between the north and south rift segments and rising to about 1390 m below sea level (Embley et al., 1990; Johnson and Embley, 1990). Both rift zones are interpreted as constructional ridges mainly formed by dike injections from a central magma reservoir beneath the caldera. The summit of Axial Seamount is characterized by a distinct plateau hosting a collapse caldera, 3x8 km in size, hosting numerous fissures extending from the northeast and southwest rims into the north and south rift zones. A variety of lava flow types ranging from lineated sheet flows to jumbled and lobate flows or occasionally pillow lavas have been erupted from these fissures, and the southern caldera wall has been buried by several voluminous flows (Appelgate, 1990; Embley et al., 1990; Thomas et al., 2006; Caress et al., 2007; Clague et al., 2007). A well-developed hydrothermal system is expressed by the notable high-

temperature venting site *ASHES*, the low-temperature venting site *CASM*, and a widely distributed diffuse low-temperature field including the site *Axial Gardens* (Chase et al., 1985; Massoth et al., 1989; Baker et al., 1990; Butterfield et al., 2004).

The presence of a substantial magma reservoir was suggested by early gravity and magnetic anomaly data (Hildebrand et al., 1990; Tivey and Johnson, 1990) and was mapped in detail by seismic tomography to extend from shallow depths below the seafloor to 6 km below the seafloor (West et al., 2001; Kent et al. 2003). This reservoir is fed by a robust magma supply system associated with the Cobb hot-spot (West et al., 2003), for which mantle excess temperatures of 30–40°C have been estimated (Hooft and Detrick, 1995). This fairly constant magma flux from the source region, forming a long-lived crustal reservoir, distinguishes Axial Seamount from the other segments along the Juan de Fuca Ridge. Axial Seamount has erupted as recently as 1998, the first seafloor eruption detected remotely and monitored by in-situ instruments. For this eruption, the observed seismicity, horizontal and vertical ground deformation data revealed a clear picture of a lateral magmatic dike injection from the caldera region 50 km down the south rift zone, causing 3 m of subsidence of the caldera floor with a prominent lava flow erupted along the east rim (Chadwick et al., 1998, 1999; Dziak and Fox, 1999b; Embley et al., 1999; Fox, 1999; Fox et al., 2001; Chadwick et al. 2002; Chadwick, 2003). Subsequent reservoir inflation and uplift of the caldera floor occurred of at a rate of 13 – 22 cm yr^{-1} (Chadwick et al., 2006; Nooner and Chadwick, 2009) Most of the lavas erupted on Axial Seamount appear fairly homogeneous in terms of their degree of fractionation and mild depletion, and are slightly enriched in highly incompatible trace element including light rare earth elements compared to basalts erupted along adjacent rift

zones. Only occasionally is primitive and more depleted MORB erupted from the caldera. The Axial Seamount geochemical fingerprint is generally interpreted as a signature of interaction between ridge magmas and those of the Cobb hot-spot (Rhodes et al., 1990; Chadwick et al., 2005).

This extensive dataset makes Axial Seamount a well-characterized mid-ocean ridge segment and an ideal locality for detailed studies of mid-ocean ridge eruptions. In this study, volcaniclastic sections from Axial Seamount were investigated to examine the origin of the volcaniclastic fragments, and apply their potential in deciphering the history and evolution of the caldera system. The chemical composition of the glass fragments and plagioclase-hosted melt inclusions was used to constrain the incompatible trace element budget of the local mantle source and the evolution of the magma within the shallow magmatic reservoir. To explore the role of magmatic volatiles as a potential driving force for eruptions producing volcaniclastic particles, specific attention was paid to dissolved water and carbon dioxide concentrations in the glass fragments and melt inclusions. Investigation of the physical aspects of these eruptions, in particular fragmentation mechanisms, were carried out by examining the different types of glassy fragments using optical and scanning electron microscopy, and by estimating quench rates with differential scanning calorimetry. Analogue experiments using gum rosin-acetone mixtures were used to elucidate the behaviour of magma as it ascends, vesiculates, and fragments within the conduit under decompressions scaled to those of submarine environments. These experiments constrain the parameters that induce fragmentation under high confining pressures.

General references

Appelgate, T.B., 1990. Volcanic and structural morphology of the south flank of Axial Volcano, Juan de Fuca Ridge: results from a Sea MARC I side scan sonar survey. J. Geophys. Res. 95, 12765-12783.

Baker, E.T., McDuff, R.E., Massoth, G.J., 1990. Hydrothermal Venting from the Summit of a Ridge Axis Seamount: Axial Volcano, Juan de Fuca Ridge. J. Geophys. Res. 95, 12843-12854.

Butterfield, D.A., Roe, K.K., Lilley, M.D., Huber, J.A., Baross, J.A., Embley, R.W., Massoth, G.J., 2004. Mixing, reaction and microbial activity in the sub-seafloor revealed by temporal and spatial variation in diffuse flow vents at Axial Volcano, in: Wilcock, W.S.D., DeLong, E.F., Kelley, D.S., Baross, J.A., Cary, S.C. (Eds.), Subseafloor Biosphere at Mid-Ocean Ranges, Geophysical Monograph Series 144, pp. 269-289.

Caress, D.W., Clague, D.A., Chadwick Jr., W.W., Butterfield, D.A., Paduan, J.B., Thomas, H., Conlin, D., Thompson, D., 2007. AUV mapping of Axial Seamount, Juan de Fuca Ridge: the northern caldera floor and northeast rim. EOS Trans. AGU 88, T33B–1355.

Chadwick, J., Perfit, M., Ridley, I., Kamenov, G., Chadwick, W., Embley, R., le Roux, P., Smith, M., 2005. Magmatic effects of the Cobb hot spot on the Juan de Fuca Ridge. J. Geophys. Res. 110.

Chadwick, W.W., Jr, Embley, R.W., Merle, S., Tunnicliffe, V., Stakes, D., Maher, N., Reynolds, J., 1998. Lava Flows from the January 1998 Eruption of Axial Volcano, Juan de Fuca Ridge: Multibeam Depth Changes and Seafloor Observations from the ROPOS ROV. Eos Trans. AGU 79, (45, Fall Meet. Suppl.), Abstract V71A-02.

Chadwick, W.W., Embley, R.W., Milburn, H.B., Meinig, C., Stapp, M., 1999. Evidence for deformation associated with the 1998 eruption of Axial Volcano, Juan de Fuca Ridge, from acoustic extensometer measurements. Geophys. Res. Lett. 26, 3441-3444.

Chadwick, W.W., Jr, Embley, R.W., Merle, S.G., 2002. Emplacement processes of two 1998 lava flows with contrasting morphology, inferred from high-resolution bathymetry and bottom observations at Axial Seamount, Juan de Fuca Ridge. Eos

Trans. AGU 83, (4, Ocean Sci. Meet. Suppl.), Abstract OS41L-02.

Chadwick, W.W., Jr., 2003. Quantitative constraints on the growth of submarine lava pillars from a monitoring instrument that was caught in a lava flow. J. Geophys. Res. 108, 2534.

Chadwick, W.W., Nooner, S.L., Zumberge, M.A., Embley, R.W., Fox, C.G., 2006. Vertical deformation monitoring at Axial Seamount since its 1998 eruption using deep-sea pressure sensors. J. Volcanol. Geotherm. Res. 150, 313-327.

Chase, R.L., Delaney, J.R., Karsten, J.L., Johnson, H.P., Juniper, S.K., Lupton, J.E., Scott, S.D., Tunnicliffe, V., Hammond, S.R., McDuff, R.E., 1985. Hydrothermal vents on an axis seamount of the Juan de Fuca ridge. Nature 313, 212-214.

Clague, D.A., Davis, A.S., Bischoff, J.L., Dixon, J.E., Geyer, R., 2000. Lava bubble-wall fragments formed by submarine hydrovolcanic: explosions on Lo'ihi Seamount and Kilauea Volcano. Bull. Volcanol. 61, 437-449.

Clague, D.A., Davis, A.S., Dixon, J.E., 2003. Submarine Eruptions on the Gorda Mid-Ocean Ridge, in: White, J.D.L., Smellie, J.L., Clague, D.A. (Eds.), Explosive Subaqueous Volcanism, Geophysical Monograph 140. AGU, Washington, DC, pp. 111-125.

Clague, D.A., Caress, D.W., Chadwick Jr., W.W., Butterfield, D.A., Paduan, J.B., Thomas, H., Conlin, D., Thompson, D., 2007. AUV mapping of Axial Seamount, Juan de Fuca Ridge: the southern caldera floor and upper south rift. EOS Trans. AGU, T33B–1354.

Clague, D.A., Paduan, J.B., Davis, A.S., 2009. Widespread strombolian eruptions of mid-ocean ridge basalt. J. Volcanol. Geotherm. Res. 180, 171-188.

Cousens, B.L., Allan, J.F., Leybourne, M.I., Chase, R.L., Wagoner, N., 1995. Mixing of magmas from enriched and depleted mantle sources in the northeast Pacific: West Valley segment, Juan de Fuca Ridge. Contrib. Mineral. Petrol. 120, 337-357.

Davis, A.S., Clague, D.A., 2003. Hyaloclastite from Miocene Seamounts Offshore Central California: Compositions, Eruptions Styles, and Depositional Processes, in: White, J.D.L., Smellie, J.L., Clague, D.A. (Eds.), Explosive Subaqueous Volcanism, Geophysical Monograph 140. AGU, Washington, DC, pp. 129-141.

Davis, E.E., Currie, R.G., 1993. Geophysical observations of the northern Juan de Fuca

Ridge system - lessons in sea-floor spreading. Can. J. Earth Sci. 30, 278-300.

Dziak, R.P., Fox, C.G., 1999a. Long-term seismicity and ground deformation at Axial Volcano, Juan de Fuca Ridge. Geophys. Res. Lett. 26, 3641-3644.

Dziak, R.P., Fox, C.G., 1999b. The January 1998 earthquake swarm at axial volcano, Juan de Fuca Ridge: Hydroacoustic evidence of seafloor volcanic activity. Geophys. Res. Lett. 26, 3429-3432.

Embley, R.W., Murphy, K.M., Fox, C.G., 1990. High-resolution studies of the summit of Axial Volcano. J. Geophys. Res. 95, 12785-12812.

Embley, R.W., Chadwick, W.W., Clague, D., Stakes, D., 1999. 1998 Eruption of Axial Volcano: multibeam anomalies and sea-floor observations. Geophys. Res. Lett. 26, 3425-3428.

Fox, C.G., 1993. Five years of ground deformation monitoring on axial seamount using a bottom pressure recorder. Geophys. Res. Lett. 20, 1859-1862.

Fox, C.G., 1999. In situ ground deformation measurements from the summit of axial volcano during the 1998 volcanic episode. Geophys. Res. Lett. 26, 3437-3440.

Fox, C.G., Chadwick, W.W., Embley, R.W., 2001. Direct observation of a submarine volcanic eruption from a sea-floor instrument caught in a lava flow. Nature 412, 727-729.

Head, J.W., Wilson, L., 2003. Deep submarine pyroclastic eruptions: theory and predicted landforms and deposits. J. Volcanol. Geotherm. Res. 121, 155-193.

Helo, C., Longpré, M.-A., Shimizu, N., Clague, D.A., Stix, J., 2011. Explosive eruptions at mid-ocean ridges driven by CO_2-rich magmas. Nature Geosciences 4, 260-263.

Hildebrand, J.A., Stevenson, J.M., Hammer, P.T.C., Zumberge, M.A., Parker, R.L., Fox, C.G., Meis, P.J., 1990. A seafloor and sea surface gravity survey of Axial Volcano. J. Geophys. Res. 95, 12751-12763.

Hooft, E.E.E., Detrick, R.S., 1995. Relationship between axial morphology, crustal thickness, and mantle temperature along the Juan de Fuca and Gorda Ridges. J. Geophys. Res. 100, 22499-22508.

Jaupart, C., Vergniolle, S., 1989. The generation and collapse of a foam layer at the roof of a basaltic magma chamber. J. Fluid. Mech. 203, 347-380.

Johnson, H.P., Embley, R.W., 1990. Axial Seamount - an active ridge axis volcano on the

central Juan de Fuca Ridge. J. Geophys. Res. 95, 12689-12696.

Karsten, J.L., Delaney, J.R., Rhodes, J.M., Liias, R.A., 1990. Spatial and temporal evolution of magmatic systems beneath the Endeavour segment, Juan de Fuca Ridge: tectonic and petrologic constraints J. Geophys. Res. 95, 19235-19256.

Kent, G., Harding, A., Babcock, J., Orcutt, J., Detrick, R., Canales, J.P., van Ark, E., Carbotte, S., Diebold, J., Nedimovic, M., 2003. A New View of 3-D Magma Chamber Structure Beneath Axial Seamount and Coaxial Segment: Preliminary Results from the 2002 Multichannel Seismic Survey of the Juan de Fuca Ridge. Eos Trans. AGU 84, Abstract B12A-0755.

Maicher, D., White, J.D.L., 2001. The formation of deep-sea Limu o Pele. Bull. Volcanol. 63, 482-496.

Massoth, G.J., Butterfield, D.A., Lupton, J.E., McDuff, R.E., Lilley, M.D., Jonasson, I.R., 1989. Submarine venting of phase-separated hydrothermal fluids at Axial Volcano, Juan de Fuca Ridge. Nature 340, 702-705.

Nooner, S.L., Chadwick, W.W., Jr., 2009. Volcanic inflation measured in the caldera of Axial Seamount: Implications for magma supply and future eruptions. Geochem. Geophys. Geosyst. 10, Q02002.

Rhodes, J.M., Morgan, C., Liias, R.A., 1990. Geochemistry of Axial Seamount lavas: magmatic relationship between the Cobb hotspot and the Juan de Fuca Ridge. J. Geophys. Res. 95, 12713-12733.

Schipper, C.I., White, J.D.L., 2010. No depth limit to hydrovolcanic limu o Pele: analysis of limu from Lo'ihi Seamount, Hawai'i. Bull. Volcanol. 72, 149-164.

Smith, M.C., Perfit, M.R., Jonasson, I.R., 1994. Petrology and geochemistry of basalts from the southern Juan de Fuca Ridge: Controls on the spatial and temporal evolution of mid-ocean ridge basalt. J. Geophys. Res. 99, 4787-4812.

Sohn, R.A., Willis, C., Humphris, S., Shank, T.M., Singh, H., Edmonds, H.N., Kunz, C., Hedman, U., Helmke, E., Jakuba, M., Liljebladh, B., Linder, J., Murphy, C., Nakamura, K.-i., Sato, T., Schlindwein, V., Stranne, C., Tausenfreund, M., Upchurch, L., Winsor, P., Jakobsson, M., Soule, A., 2008. Explosive volcanism on the ultraslow-spreading Gakkel ridge, Arctic Ocean. Nature 453, 1236-1238.

Thomas, H., Caress, D., Conlin, D., Clague, D., Paduan, J., Butterfield, D., Chadwick,

W., Tucker, P., 2006. Mapping AUV Survey of Axial Seamount. EOS Trans. AGU 87, V23B-0615.

Tivey, M.A., Johnson, H.P., 1990. The magnetic structure of axial seamount, Juan de Fuca Ridge. J. Geophys. Res. 95, 12735-12750.

Van Wagoner, N.A., Leybourne, M.I., 1991. Evidence for magma mixing and a heterogeneous mantle on the West Valley segment of the Juan de Fuca Ridge. J. Geophys. Res. 96, 16295-16318.

West, M., Menke, W., Tolstoy, M., Webb, S., Sohn, R., 2001. Magma storage beneath Axial volcano on the Juan de Fuca mid-ocean ridge. Nature 413, 833-836.

West, M., Menke, W., Tolstoy, M., 2003. Focused magma supply at the intersection of the Cobb hotspot and the Juan de Fuca ridge. Geophys. Res. Lett. 30.

Chapter 1. Pyroclastic eruptions and magma dynamics at Axial Seamount, Juan de Fuca Ridge, northeast Pacific Ocean

Christoph Helo,[1] David A. Clague,[2] John Stix[1]

[1]*Department of Earth & Planetary Sciences, McGill University, 3450 University Street, Montréal H3A 2A7, Canada*

[2]*Monterey Bay Aquarium Research Institute, 7700 Sandholdt Road, Moss Landing, CA 95039, USA*

Manuscript I – to be published.

Abstract

Widespread volcaniclastic deposits occur at Axial Seamount, a caldera system on the Juan de Fuca Ridge, northeast Pacific Ocean. These unconsolidated deposits consist predominantly of glass fragments of mid-ocean ridge basalt (MORB) composition and are similar to those found on other (MOR) sites and produced during pyroclastic activity. Volcaniclastic horizons crop out only at the top of the caldera rim and are absent within the steep caldera walls, suggesting that pyroclastic activity prevailed mainly during and/or after the major caldera collapse event(s). We have investigated volcaniclastic sediment cores from the northeast and central-west caldera flanks for their particle morphology and major and trace element composition of the glass fragments. MgO in the glasses ranges from 9.4 to 6.5 wt. %, indicating a substantial variability in the degrees of fractionation. Trace element ratios are generally fairly uniform, $[La/Yb]_N$ is 0.95–1.1 and Ba/Zr is 0.2–0.3, but concentrations vary with MgO content. One set of primitive, light rare earth element (LREE) depleted samples with $[La/Yb]_N$ of 0.6–0.85 are exceptional. The REE concentration data are evaluated in terms of an open-system magma reservoir re-establishing steady-state after significant reservoir evacuation. Using know reservoir dimensions, and magma flux estimates, this model provides a time constraint for the reservoir equilibration and thus a minimum deposition age of about 4–15 ka. Exploration of mantle melting models indicates (1) a mean source composition that is enriched in highly incompatible large ion lithophile elements (LILE) to about twice that of average depleted MORB mantle (DMM), and (2) the LREE depleted compositions are well explained as higher-degree melts of the same mantle source rather than as derivatives of a

distinct depleted source.

1. Introduction

The Juan de Fuca Ridge (JdFR) and adjacent seamounts are among the well-studied parts of the global mid-ocean ridge system, and has been the focus of numerous geochemical and geophysical investigations (e.g., Eaby et al., 1984; Wilson, 1988; Davis and Currie, 1993; Sours-Page et al., 1999). As a spreading centre segment that is modified by interaction with a mantle plume, the Axial Seamount segment has been of particular interest (e.g., Massoth et al., 1989; Embley et al., 1990; Johnson and Embley, 1990; Fox et al., 2001), providing insights into plume-ridge interaction processes (Rhodes et al., 1990; Chadwick et al., 2005). Within the past 15 years technical advances in sampling, i.e., highly efficient remotely controlled vehicles (ROVs) and high-resolution bathymetric mapping, have provided remarkable details, with novel insights into the structural evolution and morphological compositions of seamount and ridge segments. Recent surveys and expeditions on Axial Seamount have documented the existence of extensive volcaniclastic deposits (Zonenshain et al., 1989; Thomas et al., 2006; Caress et al., 2007; Clague et al., 2007; Clague et al., 2009), similar to deposits previously found on other ridges, and suggested in many cases to correlate with particular stages in the evolution of seamount edifices (Clague et al., 2009).

In this study we present morphological and geochemical analyses of basaltic glass fragments from volcaniclastic deposits recovered from Axial Seamount. Based on morphological arguments, we identify the eruptions as pyroclastic resulting from magmatic foam disruption within the upper conduit. We evaluated the main

compositional spread in the geochemical data in terms of a conceptual model. Following strong caldera collapse and magma withdrawal the system re-evolves from primitive to more fractionated compositions, assuming a constant magma flux through the reservoir and continuous fractionation and mixing within the reservoir. The according timescales are characterized in terms of the magma residence time. As the magmatic evolution is reflected in the deposits this model provides constraints on the timescales of deposition. Trace element compositions of the glass fragments, combined with melt inclusion data published in an earlier study (Helo et al., 2011), are used to better constrain the melting regime and plume-induced enrichment of large ion lithophile elements (LILE) in the mantle source beneath Axial Seamount ridge segments. We further examine the origin of occasionally erupted, more primitive and depleted liquids, which provide insights into melt migration and mixing within the reservoir beneath Axial Seamount.

2. Regional geology

2.1 Juan de Fuca ridge system and Axial Seamount

As part of the northeast Pacific ridge systems, the Juan de Fuca Ridge evolved from the fragmentation of the Farallon Plate at about 55 Ma ago (Davis and Currie, 1993). Spanning almost 500 km between the Blanco and the Sovanco transform faults, the ridge is divided from north to south into the following segments: the Middle Valley, West Valley and Endeavour, the Northern Symmetrical (S6), CoAxial (S5), Axial Seamount's north and south rift zones (S3, S4), Vance (S2) and Cleft (S1) segments (Fig. 1a). With half spreading rates of the individual segments varying between 26 and 29 mm yr^{-1} (Davis

and Currie, 1993; Tivey, 1994), the Juan de Fuca Ridge is a medium-rate spreading centre, morphologically distinct from the similarly medium spreading Gorda Ridge south of the Blanco transform fault (Hooft and Detrick, 1995; Carbotte et al., 2006; Carbotte et al., 2008). Most of the segments along the Juan de Fuca Ridge are characterized by axial highs and small summit graben rather than deep rift valleys. The Middle and West Valley segments differ from the rest of Juan de Fuca Ridge trend, exhibiting rift valleys of significant depth (Van Wagoner and Leybourne, 1991; Davis and Currie, 1993).

Axial Seamount is the most prominent morphological feature along the Juan de Fuca Ridge. It is the surface expression of the interaction with the Cobb hot spot and is associated as such with the Cobb-Eickelberg seamount chain on the Pacific Plate, and Son of Brown Bear and Thompson Seamounts on the Juan de Fuca Plate (Desonie and Duncan, 1990). The superposition results in a distinctive bathymetry and morphology, characterized by a shallow volcanic edifice rising to about 1390 m below sea level and elevated up to 1000 m relative to adjacent rift zones and basins (Embley et al., 1990). The summit plateau hosts a U-shaped, 3 x 8 km caldera, similar in dimension to Kilauea caldera, Hawaii (Rowland et al., 1999), and slightly smaller than Krafla caldera in Iceland (Rymer et al., 1998). Lava flows along the upper south rift zone have progressively filled the southeast part of the caldera depression. The peculiar non-circular geometry (Fig. 1b) and its oblique orientation between the north and south rift zone seem best explained by overlapping spreading centres (Embley et al., 1990). Rift zones extend ~50 km to the north and south of the caldera. A magma reservoir is inferred from seismic tomography at depths between 2.5 and 6 km beneath the caldera (West et al., 2001). Based on recent spatial uplift pattern Chadwick et al. (2006) and Nooner and Chadwick (2009) inferred a

comparable depth for strong magma storage at ~ 3.5 km beneath the seafloor. Due to enhanced magma supply from the mantle region beneath Axial Seamount (West et al., 2003) the north and south rift zones are dominated by constructional volcanic features, rather than extensional graben, as present on other Juan de Fuca Ridge segments. Magma can be fed directly into the rift zones by lateral diking from this reservoir, as seismically monitored during the January 1998 eruption (Dziak and Fox, 1999).

2.2 Volcaniclastic deposits on Axial Seamount

Large areas of the flanks near the caldera rim are characterized by thick volcaniclastic glass deposits that buried lava flows entirely as first described by Zonenshain et al. (1989) and mapped in greater detail by Thomas et al. (2006), Caress et al. (2007), and Clague et al. (2007) using a high-resolution mapping AUV. Similar, but significantly thinner deposits occur on some lava flows inside the caldera, especially near the centre (Clague et al., 2009). For two 15-cm sediment piston cores from the west and north caldera rim, Zonenshain et al. (1989) derived basal ages of about 12,000 years by ^{14}C-dating, although their age data were not published. In contrast, very little pyroclastic material is found on the caldera floor, which has been repaved repeatedly with recent lava flows. Likewise, the 1998 eruption was dominantly effusive producing only thin sedimentary deposits. Thinner, more dispersed glass-rich deposits have also been recognized and described from numerous spreading centre sites in the Pacific, including the Juan de Fuca Ridge, the Gorda Ridge, the Blanco transform fault, near-ridge seamounts, the East Pacific Rise and the Fiji back-arc basin (cf. Clague et al., 2009, and references within), as well as from the ultraslow spreading Gakkel ridge in the Arctic Basin (Sohn et al., 2008). Thus, the production of volcaniclastic sediment along mid-

ocean ridges occurs over a wide range of water depths, from ~1400 m on the summit of Axial Seamount to about 4000 m in the rift valley of the Gakkel ridge. Many sites have abundant limu o Pele among the glass fragments. Commonly, the deepest sites have less limu o Pele and more angular glass fragments than shallower sites (Clague et al., 2009). Samples from near-ridge seamounts (e.g., President Jackson, Taney and Vance Seamounts) consist of lithified volcaniclastic rocks ranging from sandy mudstones to fine breccias; these commonly crop out to the top of nearly vertical caldera walls (Davis and Clague, 2000; Davis and Clague, 2003a; Clague et al., 2006). Most on-ridge sites comprise unconsolidated volcaniclastic deposits where glass particles are intermixed with pelagic sediment (Clague et al., 2003b; Davis and Clague, 2003b) and commonly occur on top of lava flows of similar chemistry (Clague et al., 2009). The volcaniclastic deposits on the flanks of Axial Seamount are exceptionally widespread and thick outside the caldera and include layers that consist predominantly of sand-sized and coarser glass fragments with only minor finer particles.

The physical eruption and deposition model that has emerged over the past several years suggests that pyroclastic fragments are produced by strombolian bubble burst events accompanying effusive activity (Clague et al., 2003a; Clague et al., 2003b; Davis and Clague, 2003a; Clague et al., 2009; Helo et al., 2011). Contrasting, Maicher and White (2001) and Schipper and White (2010) argue for seawater-steam driven bubbles rising through sheet lava flows advancing over wet sediment. The abundance of volcaniclastic debris produced during on eruption, i.e., the extent of strombolian activity has been found to correlate positively with effusion or conduit rise rate inferred from the morphologies of underlying lava flows. The recognition of very high pre-eruptive CO_2

concentrations in Axial Seamount magmas provides a mechanism to drive such explosive strombolian-type eruptions (Helo et al., 2011). For the volcaniclastic deposits on Gakkel ridge, Sohn et al. (2008) favored Hawaiian fire fountain activity to account for the wide clast dispersal. Using the model of Head and Wilson (2003), they calculated a CO_2 budget that significantly exceeds CO_2 concentrations measured in melt inclusions (Shaw et al., 2010). Clast dispersal modeling indicates entrainment of particles into the rising eruption plume and deep-sea currents as the dominant cause for the wide dispersal observed at Axial Seamount and partially for that at Gakkel ridge sites (Clague et al., 2009; Barreyre et al., 2011).

3. Methods

3.1 Sampling volcaniclastic units

Sequences of volcaniclastic sediment on Axial Seamount were collected as pushcores and vibracores during the ROV Tiburon dives *T1009* and *T1010* during the MBARI 2006 expedition. We sampled 20 cores along two traverses on the northeast and central-west flanks proximal to the caldera rim at a water depth of ~ 1400 m (Fig. 1b, Supplementary Table S1). Pushcores were collected in 30 cm long transparent tubes with the robotic manipulator arm of the ROV. Thicker sediment sections were sampled by a vibracorer attached to the ROV employing alumina tubes. The vibracore tubes penetrated up to 2 m into the sediment, yet sequences retained within the tubes were no more than 30 cm in length. Although we do not have a clear indication whether the sequences represent the top, middle or bottom section of the deposits, vibracores sampled adjacent to

pushcores differ in their stratigraphy suggesting that no surficial sediments were sampled by the vibracores.

3.2 Chemical analyses

Major element, S and Cl compositions were determined for limu o Pele shards and angular fragments from each volcaniclastic unit at Axial Seamount with a JEOL 8900 electron microprobe at McGill University using a beam current of 15 nA, an accelerating voltage of 15 kV and a defocused beam of 10 μm diameter. Most major elements were calibrated on VG-99 standard glass, K_2O and Cl on KN9 standard glass. VG-99, KN9, and VG-2 standards were interspersed in the course of the measurements to check for spectrometer drift and accuracy. Values reported here were internally recalibrated to VG-2 for inter-laboratory consistency. For each unit, 10 to 15 angular fragments and 10 to 15 limu o Pele shards were analyzed, typically with three spots per grain.

Trace element analyses of the volcaniclastic glasses were conducted by inductively-coupled plasma mass spectrometry at McGill University, using a New Wave UP 213 nm Laser Ablation System coupled to a Perkin Elmer Elan 6100 DRCplus. The energy density of the laser was 8 to 9.5 J/cm^2. Samples were ablated with 10 Hz on continuous line scans using a spot size of 120 μm. The dwell time was 20 s, except for Nb and U (30 s), and oxide production rates were monitored using ^{248}ThO. Data were calibrated against ^{29}Si and ^{43}Ca and processed with the program Glitter. Cs was highly heterogeneous, displaying strong peaks during line scanning. Cs values reported here are peak-filtered. The 1σ analytical errors based on counting statistics are as follows: Rb (4 %), Ba (5 %), U (6 %), Th (6 %), Sr (4 %), Nb (3), Zr (5 %), Hf (6 %), Y (13 %), La (8 %), Ce (4%), Pr (5%), Nd (6%), Sm (8 %), Eu (5 %), Gd to Dy (10 %), Ho (11 %), Er and Tm (12 %),

Yb (10 %), and Lu (13 %). Melt inclusions were analysed for trace element concentrations by secondary ion mass spectrometry; for details see the original paper (Helo et al., 2011). Reported 1σ errors based on the reproducibility of a basaltic in-run standard are 8 % or better for Sr, Nb, Zr and Y, and 11 % for Ba.

4. Results

4.1 Description of the volcaniclastic deposits

Similar to the situation on many near ridge seamounts (Davis and Clague, 2000; Davis and Clague, 2003a; Clague et al., 2006), no volcaniclastic sections were observed at deeper levels of the inner caldera walls. During the dives, the sediment on the flanks was locally found to be up to 2 m thick. The volcaniclastic sections (Fig. 3) usually consist of a grain supported fabric of black glass fragments, with some biogenic clastic component (dominantly radiolaria). The intermixed matrix consists of brown-reddish pelagic mud with abundant clays of Fe-rich smectitic composition. Layers containing a strong hydrothermal clay component of yellow-green colour are apparent in many of the pushcores (Fig. 3). The sampled horizons of the deposits range from sand to muddy (silt + clay) sand. The pelagic and hydrothermal mud size fraction (< 63 μm) generally comprises less than ~ 40 % (Supplementary Figure S1). Only two samples have a mud component of > 50 %. Particular horizons have a coarse to very coarse sand (>500 μm) component above 50 % and generally stand out as distinct layers (Fig. 3) Sporadic fragments larger than the sand fraction were only observed in very rare instances and were usually excluded from the granulometric analyses to avoid strong bias. Some of the

depletion in fine grain sizes may originate from transport of the cores in an elevator carted along by the ROV during the dive. Median grain sizes Φ_{50} range from $\Phi \sim -0.06$ to $\Phi \sim 3.6$. Individual cores can show a wide range of size distributions, containing continuum of coarse to more fine grained horizons (e.g., upper two panels in Supplementary Figure S1). The size distributions are generally unimodal to bimodal, often with very broad major peaks. Modes of the distributions are between Φ~–0.3 and Φ~3.2, with standard deviations (sorting coefficients) from 1.1 to 2.3 indicating poor sorting (Hallsworth and Knox, 1999). The distributions are usually positively skewed, tailing out in the fines (Supplementary Fig. S2). For the two finest samples the size distribution parameter could not be derived as both their median and mode lie outside the minimum sieve size used (< 63 μm). Distribution parameters were determined by decoding the data using the program DECOLOG (Borselli and Sarocchi, 2009). A detailed granulometric analysis of the entire core material to reveal potential trends with the distance from the rim was beyond the scope of this paper.

The morphology of volcaniclastic glass fragments is similar to that described and illustrated in detail by Clague et al. (2009) comprising very rapidly quenched glass with variably abundant plagioclase fragments as the only phenocryst phase. The glass fragments cover a wide range of morphologies (Fig. 4), from dominant angular shapes, through limu o Pele with transitions into tube pumice forms, to stretched ribbons, bifurcated rods and Pele's hair. Angular fragments can differ in surface textures. Many exhibit irregular textures with fractures often indicative of failure across the brittle-ductile glass transition. Occasionally fragments have surface textures influenced by a significant degree of vesicularity (Fig. 4g). Many samples have smooth and fairly even surface

texture with sharp edges (Fig. 4h). Limu o Pele also display substantial variability. Most common are simple, flat to gently curved forms, or bent and rolled-up forms, variable in thickness between ~ 5 μm to 200 μm (Fig. 4a, b). Depending on the thickness, their colour varies from highly translucent yellow-brownish, to light and dark brown/green. Less commonly, limu o Pele show a high degree of complexity with strongly folded, bifurcating fragments, or fragments transitioning into tube pumice shapes. Occasional pumiceous grains are characterized by long tube vesicles (Fig. 4i). Their very smooth outer surfaces and the almost planar fracture surface perpendicular to the vesicle elongation resemble failure structures of a melt stretched beyond its tensile strength. Pele's hair form long needles, curled knotty structures, often with notable changes in diameter from the end to the middle. Some have distinct bifurcations and remnants of adhering limu o Pele (Fig. 4c). The complex morphologies demonstrated by the volcaniclastic glass fragments, especially the transitions among limu o Pele, tube pumice forms and stretched ribbons, suggest an origin from a magmatic foam being erupted and rapidly quenched.

4.2 Major element composition

Major element compositions of 540 glass fragments from the volcaniclastic sections on the central-west and northeast flanks of Axial Seamount are shown in Table S1 of the supplementary dataset, and Figures 3 and 4. All recovered glass fragments are of tholeiitic basalt composition with SiO_2 from 48.1 to 50.4 wt. %. The volcaniclastic deposits reveal a notable range in their degree of fractionation, indicated by an MgO content from 9.3 to 6.4 wt. %. In particular, the MgO data form four clusters. The first, is the most primitive with MgO between 9.3–9.0 wt. % accounting for 5 % of all samples,

the second has MgO 8.7–8.0 wt.% accounting for 30 % of all samples, the third has MgO 7.6–7.1 wt. % accounting for 41 % of all samples and the most evolved cluster has MgO 7.0–6.4 wt. % accounting for 19 % of the samples (Fig. 5c). The remaining 5% of the samples fall in the transitions between the clusters. The transition between the last two groups is almost continuous and coincides with an inflection point of Ca/Al and CaO concentration. The occurrence of both the least and the most fractionated compositions appear more common on the central-west flank site. The range in MgO documented within the volcaniclastites is wider than seen in lavas recovered from Axial Seamount (Rhodes et al., 1990; Chadwick et al., 2005) and volcaniclastic samples from the north rim and south caldera floor (Clague et al., 2009). Most published data on lava flow glass and aphyric whole rock compositions from Axial Seamount have MgO < 8 wt. %. Whole rock compositions of visually appearing aphyric basalts with up to 11 wt. % MgO have been reported from the south rift zone (Rhodes et al., 1990). The incompatible major element TiO_2 in the volcaniclastic glass is 0.88–1.72 wt. % in good agreement with the existing datasets. Its correlation trend with MgO slightly differs from that seen in basalts from other segments of the central and southern Juan de Fuca Ridge. K_2O is on average somewhat more enriched compared to the central and southern Juan de Fuca Ridge (Eaby et al., 1984; Liias, 1986; Rhodes et al., 1990; Smith et al., 1994; Melson and O'Hearn, 2003; Chadwick et al., 2005; Clague et al., 2009).

Samples of MgO > 9 wt. % are related by fractional crystallization of olivine and plagioclase up to the inflection point, which indicates the onset of clinopyroxene fractionation. The primitive sample group appear to have experienced a slightly different liquid line of ascent and have a shorter crustal residence time. Mixing with the more

evolved resident magma could cause the intermediate MgO values (8.5–9.0 wt. %) that fall off the main fractionation trend, as supported by the trace element data (see below).

Glass fragments within individual cores and individual subsampled units can exhibit very different degrees of fractionation. The fragment-to-fragment variability in MgO expressed as 1σ standard deviation of the individual units ranges from 0.1 to 0.9 wt. %. Glass fragments from within one unit may thus differ in their MgO content by more than 2 wt. %. This implies that a single core section of about 1 cm thickness can host the chemical fingerprint of multiple eruptions. In some cores the variability was found to change over a certain depth range within the core; other cores did not reveal any systematic change over a comparable depth range (Fig. 6). Angular fragments and limu o Pele were generally found to agree well in their composition (supplementary Fig. S3).

4.3 Trace element composition

Trace element data of the basaltic glass fragments are displayed in Table 2 and Figures 6–8. As demonstrated above, the data generally represent numerous eruptions covering various stages of magmatic evolution. Trace element compositions of plagioclase-hosted melt inclusions recovered from these volcaniclastic deposits have been reported in a previous paper (Helo et al., 2011) focusing on the volatile record and are integrated into the discussion here.

Trace element compositions of the volcaniclastic deposits fall within the overall range in basalts erupted along the Juan de Fuca ridge system. Most samples are characterized by a depletion in highly incompatible elements and fairly flat rare earth element (REE) patterns (e.g., $[La/Yb]_N$ = 0.95–1.1; Fig. 8). In comparison with most

basaltic lava samples recovered from the caldera system, the volcaniclastic units appear to display a greater diversity in absolute trace element concentrations. For example, La and Yb concentrations in most volcaniclastic clasts vary from 3.1–4.8 μg/g and 2.2–3.3 μg/g, whereas the literature data for caldera lavas reported in Rhodes et al. (1990) and Chadwick et. al. (2005) cluster closely around 5 μg/g and 3.1 μg/g, respectively (Fig. 8a). Likewise, Zr concentrations in the clastic material range from 60 to 100 μg/g similar to the spread observed in the rift zone lavas, whereas most lavas have ~100 μg/g. The behaviour of Sr (Fig. 9d) deviates slightly from other trace elements with values close to 145 μg/g, almost identical to reported values from the caldera and clearly distinct from compositions erupted along other Juan de Fuca Ridge segments (Liias, 1986; Rhodes et al., 1990; Chadwick et al., 2005). LILE and other highly incompatible element ratios show little variability and concentrations are strongly correlate with each (Fig. 9a, b).

Distinct is a group of eight samples (unit *T1009-VC9 3.0*) displaying trace element signature outside the general range seen in the volcaniclastic glass (Figs. 7–9). This group falls into two subgroups: (1) LREE depleted compositions (e.g., $[La/Yb]_N \sim 0.6$ and Zr/Y = 2.3–2.0) that are primitive, with MgO > 9 wt. %, and (2) compositions intermediate between the primitive, depleted and the general range (e.g., $[La/Yb]_N \sim 0.85$, and Zr/Y = 3.0–2.6). The first subgroup has some similarity to the most depleted signatures found along the Juan de Fuca Ridge (Fig. 9c) which occur more commonly along the northern segments (Endeavour, Middle and West Valley), but a few similar samples have been described from segments south of Axial Seamount and the North and South rift zones (Rhodes et al., 1990). Compositions similar to the second subgroup have been described by Chadwick et al. (2005).

The greater compositional diversity of the melt inclusion data is partly due to the higher analytical error of the SIMS measurements, particular for Ba, but still suggests a more heterogeneous nature of the melt inclusions. A set of melt inclusions appears to be characterized by higher abundance of highly incompatible LILE concentrations (Fig. 9b), whereas moderately incompatible elements appear to be more depleted in a number of melt inclusions, e.g., Nb < 3 μg/g and Zr < 60 μg/g (Fig. 9b, c).

5. Discussion

5.1 Pyroclastic eruptions

The morphology of the volcaniclastic glass fragments is indicative of bubble burst events driven by collapsing of small scale foam structures, similar to mild strombolian bubble bursts argued for in previous studies (cf. Clague et al. 2009). The presence of fluidal forms, e.g., forms intermediate between droplets and Pele's hair, coiled Pele's hair, and complex limu o Pele and Pele's hair, argues for such a scenario. In particular the complex morphologies such as limu o Pele bifurcating or transitioning into tube pumice structures and branching Pele's hair are best explained as remnants of a magmatic foam. The tube pumice structures with their smooth outer surfaces resemble fragments produced during fibre elongation experiments, demonstrating that parts of the foam were torn apart under pure shear condition coincidently with rapid quenching. Analysis of the highly elongated vesicles observed within individual limu o Pele shards is consistent with simple shear processes (Helo, unpublished data). Due to the low viscosity of basaltic liquids, sheared vesicles rebound quickly upon stress release. Hence, fragmentation must have

been initiated within the uppermost parts of the conduit, immediately prior to contact with seawater and rapid cooling of the clasts to assure preservation of the stretched vesicle geometry.

Direct assessment of the mass of pyroclasts produced during a single eruption and associated accumulation rates of these deposits is difficult to estimate. The sediment cores are comprised of grain supported volcaniclastic material mostly > 63 μm, and none of the cores displays a distinct hiatus. Average accumulation rates are therefore likely to exceed the pelagic background sedimentation rate of > 0.1 mm/yr using the Quaternary pelagic sedimentation rate on the Gorda Ridge (Phipps, 1977). A single horizon of 1 cm thickness would thus represent less than 100 years. The strong heterogeneity in major element compositions seen in many of the cores argues for thin layers deposited from a single eruption, followed by complexities in the deposition history, such as reworking and fluctuating eruption sites with time. Some reworking of the sequences by bioturbation was occasionally evident from field observations. Extensive lateral transport is less likely due to the proximity to the caldera rim and the generally well preserved nature of the delicate fragments. Horizons that are compositionally more homogeneous suggest either a period of eruptions with a higher pyroclastic output per eruption or more frequent eruptive activity.

Most of the sampled volcaniclastic sections hence represent stages in the evolution of the magmatic reservoir feeding Axial Seamount over time. As no pyroclastic sections were observed within the caldera wall, deposits record geochemical fingerprints of the syn-collapse and post-collapse history of the caldera subsidence event(s). The high abundance of less fractionated compositions in the volcaniclastic sections compared to

the youngest eruption products, can be interpreted in terms of a recovering phase following a major disruption of the magmatic system, i.e., after a significant magma withdrawal and caldera collapse event. Based on the homogeneity of lavas recovered from Axial Seamount, the magma reservoir has been described as a well-mixed system (Perfit et al., 1988). However, the variably fractionated compositions documented within the volcaniclastic deposits are not consistent with such a scenario over long time periods. Instead they more likely document an open system in transition, during which a steady-state regime is not yet re-established. We interpret this evolution as a direct consequence of strong reservoir evacuation and caldera collapse. The thick post-caldera volcaniclastic deposits and the lack of similar pre-caldera deposits in the caldera walls suggest conditions favouring pyroclastic eruptions prevailing during this phase of the magmatic evolution. It is thus possible that the caldera collapse events may have promoted pyroclastic activity. Rapid reservoir evacuation is likely associated fast ascent rates that have been observed to correlate positively with pyroclast production (Clague et al., 2009).

The majority of the volcaniclastic samples can be related by fractionation of olivine + plagioclase and, at later stages, clinopyroxene. In addition, relatively primitive compositions with distinctive incompatible trace element ratios are occasionally erupted, revealing three important characteristic about the plumbing system: (1) the presence of a distinct, depleted regime, (2) LREE depleted samples are exclusively primitive in their major element composition, and (3) the relative short crustal residence time of these magmas, preventing extensive fractionation. The positive correlation between K_2O/TiO_2 and $[La/Yb]_N$ seen in our samples (supplementary Figure S4), allows us to approximate $[La/Yb]_N$ of all primitive samples with MgO > 9 wt. % (Fig. 5c) to around 0.6–0.8,

identifying the entire group as LREE depleted. This group therefore relates to a different melting and/or source regime. Although a more depleted mantle source could be responsible for the LREE depleted signature, an enhanced degree of melting better accounts for the low absolute abundance of trace elements (e.g., Ba, Zr, Sr, Fig. 9) as well as higher Ca/Al at a given MgO content. The shorter crustal storage times reflected by the primitive nature indicate that these magmas follow spatially distinct pathways during ascent and pooling in the crust. The particular ascent and residence history is unique to only the LREE-depleted magma batches erupted along Axial Seamount. Possible scenario linking magmatic and structural dynamics at Axial Seamount may involve occasional rapid pooling of depleted melts due to enhanced melting beneath the caldera or the rift zones, and ascent and injection into a delimited section of the magmatic pluming system from which the magma is expelled. Caldera collapse may promote this by (1) affecting melt pathways in the root zone of the magma reservoir, (2) increasing the large-scale permeability in the periphery of the system by faulting, facilitating magma migration, and (3) removal of the more evolved magma resident within the reservoir. These scenarios are explored in greater detail in the last discussion section.

5.2 Steady-state magma reservoir

Axial Seamount is underlain by a notable magma reservoir as documented by *West et al.* (2001) who have estimated the total magma volume stored in the shallow part of the reservoir to be up to 200 times the volume erupted during the 1998 eruption. This study implies that magma extraction is only partial during individual eruptions, and magma storage is a long-term feature at Axial Seamount. Earlier geochemical investigations have suggested a well-mixed reservoir to account for the restricted compositional range of

recovered lavas (Perfit et al., 1988; Rhodes et al., 1990). We have evaluated the notable spread in trace element concentrations seen in the volcaniclastic glass in terms of an open-system (re-)evolving towards steady-state. In the conceptual model, strong caldera collapse has significantly disturbed the system and evacuated the shallow reservoir. Subsequent replenishment and evolution of the magma reservoir gradually drives the system from hosting primary primitive, low trace element compositions to the well-mixed more evolved high trace element compositions. This evolution is reflected in the pyroclastic deposits, whereas the steady-state level is reflected in both the deposits and the recent lava flows.

Adopting the steady-state model of Albarède (1995), a constant flux of new magmatic liquid with a trace element concentration c^i_{in} (represented by the primitive, low trace element compositions of the pyroclastic deposits) is fed into the reservoir of an initial concentration of c^i_0,while equal amounts of magma are lost by eruption and magmatic dyking. Continuous fractional crystallization and mixing with fresh magma continuously fed into the reservoir increases incompatible element concentrations until a steady-state is reached (represented by the more evolved high trace element compositions of the deposits and the young lava flows). In our calculations, a cumulate assemblage of olivine and plagioclase and a suspended plagioclase fraction of 5 % was used; the corresponding equations are presented in Appendix A. Apart from the element residence time and proportion of cumulate versus erupted mass fractions, the model allows the calculation of the time taken to approach steady-state. Since the volcaniclastic samples with highest incompatible trace element concentrations generally agree in composition with the younger lava flows (Chadwick et al., 2005) indicating that steady-state

conditions have been approached, this provides a minimum constraint on the time frame represented by the volcaniclastic deposits. This time window is of particular interest, as it is possibly linked to the major caldera collapse event or events. The geochemical model used differs from model of O'Hara (1977) and Albarède (1985) by the use of a constant flux through the system (true steady-state), instead of a unique sequence of eruption, refilling and fractionation cycles. It offers the advantage of timescales that can be converted to absolute values rather than being expressed as number of cycles. Calculations are based on La and Yb concentrations for four reasons. (1) $[La/Yb]_N$ is fairly constant; (2) maximum La and Yb concentrations are in good agreement with concentrations in lava flows indicating that steady-state has been reached; (3) incompatible elements require longer timescales to approach steady-state concentrations, and (4) partition coefficients for the given magmatic conditions can be well constrained using current models and data sets ($D_{La}^{ol} = 3.2 \times 10^{-6}$, $D_{Yb}^{ol} = 0.014$, $D_{La}^{plg} = 0.16$, and $D_{Yb}^{plg} = 0.015$; see Appendix C).

A time averaged magma flux of 590 kg s^{-1} (corresponding to ~7 × 10^6 m^3 a^{-1}) into the reservoir was derived from the total spreading rate of 53 mm a^{-1}, a crustal thickness of ~ 10 km for the central 15 km of the spreading segment (Hooft and Detrick, 1995), and the density of the local crust (Gilbert et al., 2007). This agrees with supply rates of 7.5 × 10^6 – 14 × 10^6 m^3 a^{-1} seen in the past decade (Chadwick et al., 2006; Nooner and Chadwick, 2009). The volume of the magma present in the reservoir is seismically constrained between 5 and 21 km^3 (West et al., 2001) equal to 1.35 × 10^{13} kg and 5.67 × 10^{13} kg. From this a magma residence time within the reservoir of about 730–3050 yr and La and Yb residence times of 1020–4200 yr and 1040–4300 yr result (Eq. 2a, b). In

Figure 11 the temporal evolution of La and Yb versus the ratio of total input to reservoir mass is shown ($M_{in}/M_{reservoir}$). After a mass turnover of less than three times the reservoir mass, steady-state is reached within 5 %, i.e., trace element enrichment over the initial concentration has reached 95 % of the enrichment at steady-state. Almost six times the reservoir mass is required to achieve equilibrium within 1 %. Using the derived magma flux and the reservoir size estimate, steady-state is established within 1 % in less than 4 ka to 15 ka. This provides a minimum timeframe for deposition of the volcaniclastic deposits and an age constraint on caldera formation. Our derived minimum age range is consistent with the stable isotope age of 12 ka reported by Zonenshain et al. (1989) for two piston cores. Considering this time span of continuous magmatic evolution, Axial Seamount is capable to sustain a long-lived magma reservoir, unlike most near-ridge seamounts (Clague et al., 2000).

The cumulate fraction required to increase the concentrations to steady-state level is less than 0.4, indicating that the incoming magma flux is to a large extent balanced by mass removal through magma withdrawal from the reservoir. This value appears quite robust as an order of magnitude; a significant increase would require extremely low element concentrations of the input magma (Fig. 11b). During the 1998 eruption, 70 % – 90 % of the 0.2 km^3 of magma extracted from the reservoir beneath the caldera was injected into the rift zones (Embley et al., 1999). In the light of this event, the high ratio of extracted to accumulate mass fractions ϕ/X may indicate the importance of diking for the formation of the upper crust along the Axial segment. It also implies that events such as the 1998 eruption would have on average occurred about every 40 years. Recent inflation suggests a recurrence interval of ~20 a (Nooner and Chadwick 2009).

For comparison we have evaluated the term ϕ/X by a model of a system that is continuously differentiating, but periodically refilled and tapped (Albarede, 1985, his Eq. 4), shown in Figure 12. The parameters ϕ and X in this model are relative to the reservoir liquid mass at the beginning of each cycle. Their ratio is always constant for a given steady-state concentration, regardless of the absolute values. For Axial Seamount, ϕ/X of 2:1 results, in fair agreement with the 3:2 ratio of the first model. With the above mentioned constraints on the size of the reservoir and the 1998 eruption, less than 2 % of the reservoir mass fractionates during one cycle, and equilibrium is roughly approached after 30 to 200 cycles.

5.3 The melting regime beneath the Axial segment

The Juan de Fuca Ridge system including the Cobb-Eickelberg Seamount chain is distinguished by two general compositional trends (Fig. 9c). Basalts from the central and southern Juan de Fuca Ridge and Vance seamounts clearly follow a depleted trend, whereas the northern Juan de Fuca Ridge (Endeavour segment, Middle and West Valley segments) and the Cobb-Eickelberg chain dominate the more enriched array. These trends are testimony to large scale mixing relations and heterogeneities of the northeast Pacific upper mantle (Desonie and Duncan, 1990; Rhodes et al., 1990; Chadwick et al., 2005).

In order to better constrain the nature of the melting regime beneath Axial Seamount and adjacent rift segments, we have evaluated fractional and near-fractional (continuous/critical) melting models (Plank and Langmuir, 1992; Albarède, 1995) for different mantle compositions. As two possible end-member compositions we have used the average depleted MORB mantle (DMM) and the "enriched" depleted MORB mantle

(E-DMM), both after Workman and Hart (2005). The E-DMM constitutes a reservoir that is slightly enriched above the average DMM (cf. Workman and Hart, 2005 for details), with highly incompatible LILE about twice that of DMM. Shown in Figure 10 are trajectories for instantaneous and integrated melt compositions. Instantaneous melts become rapidly depleted beyond the mantle values with strongly fractionated element ratios resulting in ultra-depleted signatures (e.g., Sobolev and Shimizu, 1993; Shimizu, 1998), whereas integrated compositions converge towards the mantle value. Ba/Zr becomes most fractioned during the initial melting stages. The volcaniclastic glasses follow the melting trajectory defined by pooled or aggregated continuous melts of E-DMM compositions (Fig. 10). Hence, the mean source composition sampled by the melting column beneath Axial Seamount is characterized by a LILE inventory twice the DMM. The melt inclusion data suggests that this E-DMM signature is derived by mixing of melts derived from more depleted mantle subdomains, most likely DMM, with melts derived from more enriched mantle subdomains. If the source is indeed heterogeneous on a small scale, pooling of ascending melt parcels at the top of the melting column or the deeper volcanic plumbing system is efficient, producing melts that have a restricted range in Ba/Zr of about 0.2–0.3 (Fig. 10b, c). This is consistent with the E-DMM source value of 0.2 (Workman and Hart, 2005).

Differences in the degree of Ba/Zr fractionation generated by degrees of melting beyond the initial stage are indicative of chemically distinctive mantle domains, whilst variable Y/Nb or $[La/Yb]_N$ can be derived by different degrees of melting of a common source. Uniform LILE enrichment as seen in all volcaniclastic samples including the LREE depleted suite is therefore consistent with melts generated from one common

source composition. Deriving the LREE depleted signature of samples *T1009-VC9 3.0-B-2, 3, 4, and 6* from a distinct depleted source, such as the DMM, would require a stronger fractionation of Ba/Zr. By contrast, a higher mean extent of melting of the same mantle domain will produce melts less fractionated in $[La/Yb]_N$, but close in Ba/Zr to melts reflecting smaller degrees of melting (Fig. 10c). The LREE samples thus reflect a higher percentage of melting of the E-DMM source.

5.4 Extraction and migration dynamics of the depleted, primitive magmas

The LREE depleted melts are exclusively primitive and therefore have experienced both, a specific melting/melt extraction and ascent history, avoiding interaction with the main magma reservoir to retain their specific geochemical character. The primitive nature of many near-ridge seamount lavas has been used to argue for short crustal storage due to low melt supply and rapidly solidifying magma reservoirs (Fornari et al., 1988; Clague et al., 2000). However, as discussed above, a long-lived reservoir is likely to be present beneath the Axial caldera. This can be resolved if these magmas pool within subordinate, short-lived reservoirs that are fed sporadically by higher-degree melts. Communication between these reservoirs and the long-lived magmatic pluming system is manifested in hybrid compositions intermediate in MgO content and LREE depletion (Fig. 8b).

One possibility to enhance the mean extend of melting is the entrainment of mantle domains of lower solidus temperature, e.g., due to increased water contents (Asimow et al., 2004). In such a case, produced higher-degree melts would mix with the resident magma in the reservoir, rather than erupt as distinctively primitive, depleted compositions. Alternatively, periodic tapping of melts from selective parts of the upper melting regime may provide a source of liquids reflecting a greater mean extend of

melting. Two different parts of the mantle melting regime can be invoked. First, the central part of the melting regime beneath the reservoir, where pooling with lower degree melts from the corners of the melting regime, is yet incomplete. This is similar in effect to incomplete focusing within the melting regime (Plank and Langmuir, 1992). Second, if part of the upwelling plume spreads laterally along axis after ponding at the base of the lithosphere (Sleep, 1996), a part of the residual melting column undergoes lateral transport in an extensional regime. This residual melting column could occasionally experience continual melting, producing significant volumes of high-degree melts beneath the rift zones, particularly if melt extraction during the preceding horizontal upwelling episode was incomplete.

The greater abundance of primitive compositions in the volcaniclastic sections compared to the young sheet lava flows (this study, Chadwick et al., 2005) may indicate potential relations between magma migration dynamics and structural dynamics. During reservoir evacuation and roof collapse, the sub-caldera reservoir conditions change from overpressure over underpressure to pressures reflecting the lithostatic level of the subsided reservoir roof (Martí et al., 2000). Existing pathways for melt migration in the root zone of the reservoir may be disturbed after the collapse, impeding or at least affecting melt extraction pattern from the melting column beneath the caldera. At the same time, the peripheral zone of the caldera becomes extensively faulted (Walter and Troll, 2001), providing transient magma pathways and short-lived storage capacity. In consequence of this antithetical effect on melt migration, melt extraction from the mantle may be (1) more restricted to the central part of the melting regime or (2) enhanced beneath the rifts zones due to continuous melting. In both cases higher-degree melts are

tapped. In the latter case, large-scale permeability ample to migrate these magmas towards the evacuated sub-caldera reservoir region could be facilitated by reactivating radial caldera faults that are initiated during pre-collapse inflation (Troll et al., 2002). The eruption of primitive, depleted compositions thus demonstrates the spatial proximity of different melting and pooling conditions associated with individual melt migration paths and storage histories within the sub-volcanic lithosphere of the Axial Seamount and its rift zones.

6. Conclusions

Pyroclastic eruptions at Axial Seamount have produced widespread volcaniclastic deposits, most prominently during the syn-collapse and/or post-collapse history of the caldera system. Geochemical analysis of the volcaniclastic deposits at mid-ocean ridge sites provides a useful and simple tool for the investigation of magmatic and volcanic processes, as a single core or core section can represent numerous eruptive events and is comparatively simple to collect with the ROV. On Axial Seamount volcaniclastic basaltic glass fragments from the northeast and central-west flanks reveal a diversity in major element and trace element chemistry caused by various degrees of fractionation. This can be explained in terms of an open system magma reservoir re-equilibrating after a large magma evacuation event. Modelling La and Yb concentrations within a reservoir experiencing a constant input flux and continuous magma fractionation results in a timescale of several thousand years to approach steady state concentrations. This value is interpreted as a minimum timeframe for the formation of the volcaniclastic deposits and provides an age constraint on the timing of the caldera formation. The results also reveal

that large parts of the input mass are balanced by magma loss through eruption and dyking. In contrast, trace element ratios are uniform, with the exception of some rare primitive samples showing distinct LREE depletion. Ba/Zr and $[La/Yb]_N$ values, including those with $[La/Yb]_N < 1$, are consistent with pooled continuous melts derived from various degrees of melting of an E-DMM source (Workman and Hart, 2005), where the LREE depleted compositions reflect a high-extend of melting. Magma dynamics delineated here are, in parts, interpreted as consequence of substantial magma withdrawal and collapse of the Axial caldera affecting post-collapse melt migration and magma evolution within the reservoir.

Appendix A – Steady state reservoir

A model of a steady-state magma reservoir adapted from Albarède (1995), where new magmatic liquid is continuously introduced into a magmatic reservoir, while equal amounts of liquid are lost by crystallization of a mineral assemblage and eruption. A constant fraction of the mineral phases is suspended within the liquid. The suspended phase proportions may differ from the cumulate proportions. System parameters used are as follows:

M_{res}: mass of magma reservoir, M_{res} = constant (5.7×10^{13} kg)

c_0^i : initial concentration of element *i* in the reservoir

Q : flux of fresh magma feeding into the reservoir (590 kg s^{-1})

c_{in}^i : average concentration of element *i* in the fresh magma, taken as equal to c_0^i

c_{liq}^i : concentration of element *i* in the liquid in the reservoir

$1 - \phi$: cumulate fraction relative to the total of cumulate + erupted liquid, ϕ = constant

$1 - F$: fraction of suspended crystals in the liquid, F = constant (0.95)

$c_{liq}^i D_i = c_{min}^i$: concentration of element *i* in the crystal phases

D_i: bulk distribution coefficient of the cumulate assemblage

D_i^{sus} : bulk distribution coefficient of the suspended crystal phases

Balancing the budget of element *i* (i.e., the rate of concentration change) within the

reservoir with the flux Q_{in} and Q_{out} of the system yields:

$$M_{res}\frac{\mathrm{d}c^i_{res}}{\mathrm{d}t} = M_{res}\left(\frac{\mathrm{d}c^i_{liq}}{\mathrm{d}t}F + \frac{\mathrm{d}c^i_{liq}}{\mathrm{d}t}(1-F)D^{sus}_i\right) =$$

$$= Qc^i_{in} - Q\left[c^i_{liq}\left(F+(1-F)D^{sus}_i\right)\phi + c^i_{liq}(1-\phi)D_i\right]. \quad (1)$$

Defining:

$$\beta_i = F + (1-F)D^{sus}_i\,,\ \alpha_i = \phi\beta + (1-\phi)D_i\,,$$

the magma and element residence time $\tau_m = M_{res}/Q$ and $\tau_i = \tau_m\frac{\beta_i}{\alpha_i}$, (2a,b)

equation (1) is

$$\tau_m\frac{\beta_i}{\alpha_i}\frac{\mathrm{d}c^i_{liq}}{\mathrm{d}t} + c^i_{liq} = \frac{c^i_{in}}{\alpha_i}, \quad (3)$$

giving the steady state concentration c^i_{in}/α_i for $\mathrm{d}c^i_{liq}/\mathrm{d}t = 0$, and integrated

$$c^i_{liq}(t) = c^i_0\exp\left(-\frac{t}{\tau_m}\frac{\alpha_i}{\beta_i}\right) + \frac{c^i_{in}}{\alpha_i}\left[1-\exp\left(-\frac{t}{\tau_m}\frac{\alpha_i}{\beta_i}\right)\right]. \quad (4)$$

Appendix B – Partition coefficients

Trace element partition coefficients for olivine and plagioclase were calculated using the lattice strain model (e.g., Blundy and Wood, 1994, 2003) and appropriate literature data. General model parameters are displayed in Table A1. REE partitioning into the plagioclase M-site was calculated using the middle REE Nd as a proxy with a temperature (T) and anorthite component ($0<X_{an}<1$) dependence according to Bindeman

et al. (1998):

$$\ln D_{Nd} = \frac{-19.9(\pm 3.6)\, X_{\text{an}} - 9.4(\pm 2.0)}{TR\,10^{-3}}, \qquad (4)$$

where R is the gas constant in J $mol^{-1}K^{-1}$, and the proxy equation is (Blundy and Wood, 2003, their Eq. 8):

$$D_{REE} = D_{Nd} \exp\left[-910.18\, E_M^{3+} \frac{1}{T}\left[r_{0(M)}^{3+} \frac{1}{2}\left(r_{Nd}^2 - r_{REE}^2\right) - \frac{1}{3}\left(r_{Nd}^3 - r_{REE}^3\right)\right]\right], \quad (5)$$

where E_M^{3+} denotes the elastic response of the M-site for trivalent cations, and $r_{0(M)}^{3+}$ the radius of this site.

M^{VI}-site partitioning data for olivine were found by fitting data of Beattie (1994) covering a temperature range of 300 K to the Blundy and Wood (1994) model to find the strain compensated partition coefficient $D_{0(M)}^{3+}$:

$$D_{REE} = D_{0(M)}^{3+} \exp\left\{-910.18 E_M^{3+} \frac{1}{T}\left[r_{0(M)}^{3+} \frac{1}{2}\left(r_{REE} - r_{0(M)}^{3+}\right)^2 - \frac{1}{3}\left(r_{REE} - r_{0(M)}^{3+}\right)^3\right]\right\}. \quad (6)$$

No size distinction was made between M1- and M2-sites (cf. Beattie, 1994; Blundy and Wood, 2003). Regressing the $D_{0(M)}^{3+}$–temperature data did not yield a significant dependence of $D_{0(M)}^{3+}$ on temperature for the 300 K interval (Fig. A1). All D_{REE} were then calculated according Equation (6).

Table A1 Lattice strain model parameter used.

Parameter	Value	Source
r_{REE} [Å]	e.g., 1.109 (Nd), 1.16 (La), 0.985 (Yb)	Shannon (1976)
Plagioclase		
E_M^{3+}, [GPa]	$190.3X_{\text{an}} + 208.4(1 - X_{\text{an}})$	Blundy and Wood (1994)
$r_{0(M)}^{3+}$, [Å]	$1.228 - 0.057X_{\text{an}}$	Blundy and Wood (2003)
Olivine		
E_M^{3+}, [GPa]	360	Blundy and Wood (2003)
$r_{0(M)}^{3+}$, [Å]	0.710	Blundy and Wood (2003)
$D_{0(M)}^{3+}$	0.0138	Fitting Beattie (1994) data

References

Albarede, F., 1985. Regime and trace-element evolution of open magma chambers. Nature 318, 356-358. doi:10.1038/318356a0.

Albarède, F., 1995. Introduction to Geochemical Modelling. Cambridge University Press, Cambridge.

Asimow, P.D., Dixon, J.E., Langmuir, C.H., 2004. A hydrous melting and fractionation model for mid-ocean ridge basalts: Application to the Mid-Atlantic Ridge near the Azores. Geochem. Geophys. Geosyst. 5, Q01E16. doi:10.1029/2003gc000568.

Barreyre, T., Soule, S.A., Sohn, R.A., 2011. Dispersal of volcaniclasts during deep-sea eruptions: Settling velocities and entrainment in buoyant seawater plumes. J. Volcanol. Geotherm. Res. 205, 84-93. doi:10.1016/j.jvolgeores.2011.05.006.

Beattie, P., 1994. Systematics and energetics of trace-element partitioning between olivine and silicate melts: Implications for the nature of mineral/melt partitioning. Chem. Geol. 117, 57-71. doi:10.1016/0009-2541(94)90121-X.

Bindeman, I.N., Davis, A.M., Drake, M.J., 1998. Ion microprobe study of plagioclase-basalt partition experiments at natural concentration levels of trace elements. Geochim. Cosmochim. Acta 62, 1175-1193. doi:10.1016/S0016-7037(98)00047-7.

Blundy, J., Wood, B., 1994. Prediction of crystal–melt partition coefficients from elastic moduli. Nature 372, 452-454.

Blundy, J., Wood, B., 2003. Mineral-melt partitioning of Uranium, Thorium and their daughters, in: Bourdon, B., Henderson, G., Lundstrom, C.C., Turner, S. (Eds.), Uranium series geochemistry, Reviews in Mineralogy and Geochemistry 52. The mineralogical Society of America, Washington, DC, pp. 59-123.

Borselli, L., Sarocchi, D., 2009. Deconvolution of mixtures of lognormal components inside particle size distributions, http://www.decolog.org, retrieved March 2011.

Carbotte, S.M., Detrick, R.S., Harding, A., Canales, J.P., Babcock, J., Kent, G., Van Ark, E., Nedimovic, M., Diebold, J., 2006. Rift topography linked to magmatism at the intermediate spreading Juan de Fuca Ridge. Geology 34, 209-212. doi:10.1130/g21969.1.

Carbotte, S.M., Nedimovi, R., M., Canales, J.P., Kent, G.M., Harding, A.J., Marjanovi, Milena, 2008. Variable crustal structure along the Juan de Fuca Ridge: Influence of

on-axis hot spots and absolute plate motions. Geochem. Geophys. Geosyst. 9, Q08001. doi:10.1029/2007gc001922.

Caress, D.W., Clague, D.A., Chadwick Jr., W.W., Butterfield, D.A., Paduan, J.B., Thomas, H., Conlin, D., Thompson, D., 2007. AUV mapping of Axial Seamount, Juan de Fuca Ridge: the northern caldera floor and northeast rim. EOS Trans. AGU 88, T33B–1355.

Chadwick, J., Perfit, M., Ridley, I., Kamenov, G., Chadwick, W., Embley, R., le Roux, P., Smith, M., 2005. Magmatic effects of the Cobb hot spot on the Juan de Fuca Ridge. J. Geophys. Res. 110. doi:10.1029/2003JB002767.

Chadwick, W.W., Nooner, S.L., Zumberge, M.A., Embley, R.W., Fox, C.G., 2006. Vertical deformation monitoring at Axial Seamount since its 1998 eruption using deep-sea pressure sensors. J. Volcanol. Geotherm. Res. 150, 313-327. doi:10.1016/j.jvolgeores.2005.07.006.

Clague, D.A., Reynolds, J.R., Davis, A.S., 2000. Near-ridge seamount chains in the northeastern Pacific Ocean. J. Geophys. Res. 105, 16541–16561. doi:10.1029/2000JB900082.

Clague, D.A., Batiza, R., Head, J.W.I., Davis, A.S., 2003a. Pyroclastic and Hydroclastic Deposits on Loihi Seamount, Hawaii, in: White, J.D.L., Smellie, J.L., Clague, D.A. (Eds.), Explosive Subaqueous Volcanism, Geophysical Monograph 140. AGU, Washington, DC, pp. 73-95.

Clague, D.A., Davis, A.S., Dixon, J.E., 2003b. Submarine Eruptions on the Gorda Mid-Ocean Ridge, in: White, J.D.L., Smellie, J.L., Clague, D.A. (Eds.), Explosive Subaqueous Volcanism, Geophysical Monograph 140. AGU, Washington, DC, pp. 111-125.

Clague, D.A., Paduan, J., Cousens, B., Cornejo, L., Perfit, M., Wendt, R., Helo, C., 2006. Caldera formation on the Vance Seamounts. Eos Trans. AGU 87(52), V43A-1781.

Clague, D.A., Caress, D.W., Chadwick Jr., W.W., Butter fi eld, D.A., Paduan, J.B., Thomas, H., Conlin, D., Thompson, D., 2007. AUV mapping of Axial Seamount, Juan de Fuca Ridge: the southern caldera floor and upper south rift. EOS Trans. AGU 88, T33B–1354.

Clague, D.A., Paduan, J.B., Davis, A.S., 2009. Widespread strombolian eruptions of mid-

ocean ridge basalt. J. Volcanol. Geotherm. Res. 180, 171-188. doi:10.1016/j.jvolgeores.2008.08.007.

Cousens, B.L., Allan, J.F., Leybourne, M.I., Chase, R.L., Wagoner, N., 1995. Mixing of magmas from enriched and depleted mantle sources in the northeast Pacific: West Valley segment, Juan de Fuca Ridge. Contrib. Mineral. Petrol. 120, 337-357. doi:10.1007/bf00306512.

Davis, A.S., Clague, D.A., 2000. President Jackson Seamounts, northern Gorda Ridge: tectonomagmatic relationship between on- and off-axis volcanism. J. Geophys. Res. 105, 27939-27956. doi:10.1029/2000jb900291.

Davis, A.S., Clague, D.A., 2003a. Hyaloclastite from Miocene Seamounts Offshore Central California: Compositions, Eruptions Styles, and Depositional Processes, in: White, J.D.L., Smellie, J.L., Clague, D.A. (Eds.), Explosive Subaqueous Volcanism, Geophysical Monograph 140. AGU, Washington, DC, pp. 129-141.

Davis, A.S., Clague, D.A., 2003b. Got glass? Glass from sediment and foraminifera tests contribute clues to volcanic history. Geology 31, 103-106.

Davis, E.E., Currie, R.G., 1993. Geophysical observations of the northern Juan de Fuca Ridge system - lessons in sea-floor spreading. Can. J. Earth Sci. 30, 278-300.

Desonie, D.L., Duncan, R.A., 1990. The Cobb-Eickelberg Seamount chain: hotspot volcanism with mid-ocean ridge basalt affinity. J. Geophys. Res. 95, 12697-12711. doi:10.1029/JB095iB08p12697.

Dixon, J.E., Clague, D.A., Eissen, J.-P., 1986. Gabbroic xenoliths and host ferrobasalt from the southern Juan de Fuca Ridge. J. Geophys. Res. 91, 3795-3820. doi:10.1029/JB091iB03p03795.

Dziak, R.P., Fox, C.G., 1999. The January 1998 earthquake swarm at axial volcano, Juan de Fuca Ridge: Hydroacoustic evidence of seafloor volcanic activity. Geophys. Res. Lett. 26, 3429-3432.

Eaby, J., Clague, D.A., Delaney, J.R., 1984. Sr isotopic variations along the Juan de Fuca Ridge. J. Geophys. Res. 89, 7883-7890.

Embley, R.W., Murphy, K.M., Fox, C.G., 1990. High-resolution studies of the summit of Axial Volcano. J. Geophys. Res. 95, 12785-12812.

Embley, R.W., Chadwick, W.W., Clague, D., Stakes, D., 1999. 1998 Eruption of Axial

Volcano: multibeam anomalies and sea-floor observations. Geophys. Res. Lett. 26, 3425-3428.

Fornari, D.J., Perfit, M.R., Allan, J.F., Batiza, R., Haymon, R., Barone, A., Ryan, W.B.F., Smith, T., Simkin, T., Luckman, M.A., 1988. Geochemical and structural studies of the Lamont seamounts: seamounts as indicators of mantle processes. Earth Planet. Sci. Lett. 89, 63-67, 70-83. doi:10.1016/0012-821X(88)90033-7.

Fox, C.G., Chadwick, W.W., Embley, R.W., 2001. Direct observation of a submarine volcanic eruption from a sea-floor instrument caught in a lava flow. Nature 412, 727-729.

Gilbert, L.A., McDuff, R.E., Johnson, P.H., 2007. Porosity of the upper edifice of Axial Seamount. Geology 35, 49-52.

Hallsworth, C.R., Knox, R.W.O.B., 1999. Volume 3, Classification of sediments and sedimentary rocks, British Geological Survey Research Report, RR 99-03, BGS Rock Classification Scheme. British Geological Survey.

Head, J.W., Wilson, L., 2003. Deep submarine pyroclastic eruptions: theory and predicted landforms and deposits. J. Volcanol. Geotherm. Res. 121, 155-193.

Helo, C., Longpré, M.-A., Shimizu, N., Clague, D.A., Stix, J., 2011. Explosive eruptions at mid-ocean ridges driven by CO_2-rich magmas. Nature Geosciences 4, 260-263. doi:10.1038/ngeo1104.

Hofmann, A.W., 1988. Chemical differentiation of the earth - the relationship between mantle, continental crust, and oceanic crust. Earth Planet. Sci. Lett. 90, 297-314.

Hooft, E.E.E., Detrick, R.S., 1995. Relationship between axial morphology, crustal thickness, and mantle temperature along the Juan de Fuca and Gorda Ridges. J. Geophys. Res. 100, 22499-22508.

Johnson, H.P., Embley, R.W., 1990. Axial Seamount - an active ridge axis Volcano on the central Juan de Fuca Ridge. J. Geophys. Res. 95, 12689-12696.

Karsten, J.L., 1988. Spatial and temporal variations in the petrology, morphology and tectonics of a migrating spreading center: the Endeavor Segment, Juan de Fuca Ridge. PhD thesis, University Washington.

Karsten, J.L., Delaney, J.R., Rhodes, J.M., Liias, R.A., 1990. Spatial and temporal evolution of magmatic systems beneath the Endeavour segment, Juan de Fuca

Ridge: tectonic and petrologic constraints J. Geophys. Res. 95, 19235-19256. doi:10.1029/JB095iB12p19235.

Kelemen, P.B., Yogodzinski, G.M., Scholl, D.W., 2003. Along-strike variation in lavas of the Aleutian island arc: implications for the genesis of high Mg# andesite and the continental crust, in: Eiler, J. (Ed.), Inside the Subduction Factory, Geophysical Monograph 138. AGU, Washington, DC, pp. 222-276.

Langmuir, C.H., Vocke Jr, R.D., Hanson, G.N., Hart, S.R., 1978. A general mixing equation with applications to Icelandic basalts. Earth Planet. Sci. Lett. 37, 380-392.

Liias, R.A., 1986. Geochemistry and petrogenesis of basalts erupted along the Juan de Fuca Ridge. PhD thesis, University of Massachusetts Amherst.

Maicher, D., White, J.D.L., 2001. The formation of deep-sea Limu o Pele. Bull. Volcanol. 63, 482-496.

Martí, J., Folch, A., Neri, A., Macedonio, G., 2000. Pressure evolution during explosive caldera-forming eruptions. Earth Planet. Sci. Lett. 175, 275-287. doi:10.1016/S0012-821X(99)00296-4.

Massoth, G.J., Butterfield, D.A., Lupton, J.E., McDuff, R.E., Lilley, M.D., Jonasson, I.R., 1989. Submarine venting of phase-separated hydrothermal fluids at Axial Volcano, Juan de Fuca Ridge. Nature 340, 702-705. doi:10.1038/340702a0.

McDonough, W.F., Sun, S.S., 1995. The composition of the earth. Chem. Geol. 120, 223-253.

Melson, W.G., O'Hearn, T., 2003. Smithsonian glass file.

Nooner, S.L., Chadwick, W.W., Jr., 2009. Volcanic inflation measured in the caldera of Axial Seamount: Implications for magma supply and future eruptions. Geochem. Geophys. Geosyst. 10, Q02002. doi:10.1029/2008gc002315.

O'Hara, M.J., 1977. Geochemical evolution during fractional crystallisation of a periodically refilled magma chamber. Nature 266, 503-507. doi:10.1038/266503a0.

Perfit, M.R., Heatherington, A.L., Hughes, S., Jonasson, I.R., Franklin, J.M., 1988. Geochemistry of basalts from Axial Volcano; an example of a well-mixed Axial magma chamber. EOS 69, 1467.

Phipps, J.B., 1977. Late Quaternary variations in the silt mineralogy of deep sea cores from the Gorda Ridge, Northeast Pacific. The Journal of Geology 85, 619-624.

Plank, T., Langmuir, C.H., 1992. Effects of the melting regime on the composition of the oceanic crust. J. Geophys. Res. 97, 19749-19770. doi:10.1029/92jb01769.

Rhodes, J.M., Morgan, C., Liias, R.A., 1990. Geochemistry of Axial Seamount lavas: magmatic relationship between the Cobb hotspot and the Juan de Fuca Ridge. J. Geophys. Res. 95, 12713-12733. doi:10.1029/JB095iB08p12713.

Rowland, S.K., MacKay, M.E., Garbeil, H., Mouginis-Mark, P.J., 1999. Topographic analyses of Kilauea Volcano, Hawai'i, from interferometric airborne radar. Bull. Volcanol. 61, 1-14.

Rymer, H., Cassidy, J., Locke, C.A., Sigmundsson, F., 1998. Post-eruptive gravity changes from 1990 to 1996 at Krafla volcano, Iceland. J. Volcanol. Geotherm. Res. 87, 141-149.

Salters, V.J.M., Stracke, A., 2004. Composition of the depleted mantle. Geochem. Geophys. Geosyst. 5, 27. doi:10.1029/2003gc000597.

Schipper, C.I., White, J.D.L., 2010. No depth limit to hydrovolcanic limu o Pele: analysis of limu from Lo'ihi Seamount, Hawai'i. Bull. Volcanol. 72, 149-164. doi:10.1007/s00445-009-0315-5.

Shannon, R., 1976. Revised effective ionic radii and systematic studies of interatomic distances in halides and chalcogenides. Acta Crystallographica Section A 32, 751-767. doi:doi:10.1107/S0567739476001551.

Shaw, A.M., Behn, M.D., Humphris, S.E., Sohn, R.A., Gregg, P.M., 2010. Deep pooling of low degree melts and volatile fluxes at the 85 degrees E segment of the Gakkel Ridge: Evidence from olivine-hosted melt inclusions and glasses. Earth Planet. Sci. Lett. 289, 311-322. doi:10.1016/j.epsl.2009.11.018.

Shimizu, N., 1998. The geochemistry of olivine-hosted melt inclusions in a FAMOUS basalt ALV519-4-1. Phys. Earth Planet. Int. 107, 183-201.

Sleep, N.H., 1996. Lateral flow of hot plume material ponded at sublithospheric depths. J. Geophys. Res. 101, 28065-28083. doi:10.1029/96jb02463.

Smith, M.C., Perfit, M.R., Jonasson, I.R., 1994. Petrology and geochemistry of basalts from the southern Juan de Fuca Ridge: Controls on the spatial and temporal evolution of mid-ocean ridge basalt. J. Geophys. Res. 99, 4787-4812. doi:10.1029/93jb02158.

Sobolev, A.V., Shimizu, N., 1993. Ultra-depleted primary melt included in an olivine from the Mid-Atlantic Ridge. Nature 363, 151-154. doi:10.1038/363151a0.

Sohn, R.A., Willis, C., Humphris, S., Shank, T.M., Singh, H., Edmonds, H.N., Kunz, C., Hedman, U., Helmke, E., Jakuba, M., Liljebladh, B., Linder, J., Murphy, C., Nakamura, K.-i., Sato, T., Schlindwein, V., Stranne, C., Tausenfreund, M., Upchurch, L., Winsor, P., Jakobsson, M., Soule, A., 2008. Explosive volcanism on the ultraslow-spreading Gakkel ridge, Arctic Ocean. Nature 453, 1236-1238. doi:10.1038/nature07075.

Sours-Page, R., Johnson, K.T.M., Nielsen, R.L., Karsten, J.L., 1999. Local and regional variation of MORB parent magmas: evidence from melt inclusions from the Endeavour Segment of the Juan de Fuca Ridge. Contrib. Mineral. Petrol. 134, 342-363.

Stakes, D.S., Franklin, J.M., 1994. Petrology of igneous rocks at Middle Valley, Juan de Fuca Ridge. Proceedings of the Ocean Drilling Program, Scientific Results 139, 79-102. doi:10.2973/odp.proc.sr.139.1994.

Thomas, H., Caress, D., Conlin, D., Clague, D., Paduan, J., Butterfield, D., Chadwick, W., Tucker, P., 2006. Mapping AUV survey of Axial Seamount. EOS Trans. AGU 87, V23B-0615.

Tivey, M.A., 1994. Fine-scale magnetic anomaly field over the southern Juan de Fuca Ridge: Axial magnetization low and implications for crustal structure. J. Geophys. Res. 99, 4833-4855. doi:10.1029/93jb02110.

Troll, V.R., Walter, T.R., Schmincke, H.U., 2002. Cyclic caldera collapse: Piston or piecemeal subsidence? Field and experimental evidence. Geology 30, 135-138. doi:10.1130/0091-7613(2002)030<0135:cccpop>2.0.co;2.

Van Wagoner, N.A., Leybourne, M.I., 1991. Evidence for Magma Mixing and a Heterogeneous Mantle on the West Valley Segment of the Juan de Fuca Ridge. J. Geophys. Res. 96, 16295-16318. doi:10.1029/91jb00592.

Walter, T., Troll, V., 2001. Formation of caldera periphery faults: an experimental study. Bull. Volcanol. 63, 191-203. doi:10.1007/s004450100135.

West, M., Menke, W., Tolstoy, M., Webb, S., Sohn, R., 2001. Magma storage beneath Axial volcano on the Juan de Fuca mid-ocean ridge. Nature 413, 833-836.

West, M., Menke, W., Tolstoy, M., 2003. Focused magma supply at the intersection of the Cobb hotspot and the Juan de Fuca ridge. Geophys. Res. Lett. 30. doi:10.1029/2003GL017104.

Wilson, D.S., 1988. Tectonic history of the Juan de Fuca Ridge over the Last 40 Million years. J. Geophys. Res. 93, 11863-11876. doi:10.1029/JB093iB10p11863.

Workman, R.K., Hart, S.R., 2005. Major and trace element composition of the depleted MORB mantle (DMM). Earth Planet. Sci. Lett. 231, 53-72. doi:10.1016/j.epsl.2004.12.005.

Zonenshain, L.P., Kuzmin, M.I., Bogdanov, Y.A., Lisitsin, A.P., Podrazhansky, A.M., 1989. Geology of Axial Seamount, Juan de Fuca Spreading Center, Northeastern Pacific, in: Sinton, J.M. (Ed.), Evolution of Mid-ocean Ridges, Geophysical Monograph/IUGG Series 57. AGU, Washington, D.C., pp. 53-64.

Acknowledgments

We thank the Captain and crew of the RV Western Flyer and the pilots of the ROV Tiburon for their support and expertise during the 2006 MBARI Vance Expedition. The expedition and D.A.C. were supported through a grant to MBARI from the David and Lucile Packard Foundation. J.S. was supported by grants from the Natural Sciences and Engineering Research Council of Canada. C.H. was supported by R. H. Tomlinson, GEOTOP and J. W. McConnell Memorial Fellowships at McGill University.

Table

Table 1 Trace element composition of volcaniclastic glasses from Axial Seamount.

Sample [a]	T1009-VC1 14.0-						T1009-VC1 20.8-						
	GIM1-D36	GIM1-D37	GIM2-D32	GIM2-D34	GIM1-L39	GIM1-L40	GIM1-D13	GIM1-D14	GIM1-D15	GIM2-D16	GIM2-D17	GIM2-L19	GIM1-L19
	(GlassIn M1_36d)	(GlassIn M1_37d)	(GlassIn M2_32d)	(GlassIn M2_34d)	(GlassIn M1_39L)	(GlassIn M1_40L)	(GlassIn M1_13d)	(GlassIn M1_14d)	(GlassIn M1_15d)	(GlassIn M2_16d)	(GlassIn M2_17d)	(GlassIn M1_19L)	(GlassIn M2_19L)
Ni (µg/g)	39	40	40	39	46	46	52	51	52	56	52	89	
Cs [b]	0.08	0.04	0.02	0.03	0.08	0.05	0.11	0.04	0.64	0.02	0.02	0.04	
Rb	2.0	2.0	1.9	1.9	2.1	2.0	1.7	1.7	1.8	1.9	1.8	1.5	
Ba	24.9	24.9	24.3	25.1	23.6	24.4	22.2	23.4	22.1	24.4	24.3	19.4	25.3
U	0.11	0.11	0.09	0.10	0.11	0.11	0.08	0.09	0.09	0.09	0.09	0.08	
Th	0.29	0.27	0.31	0.32	0.24	0.24	0.26	0.25	0.24	0.31	0.28	0.22	
Sr	144	145	144	146	139	146	147	146	144	150	149	141	
Nb	4.5	4.4	4.4	4.5	4.3	4.1	4.0	4.0	4.1	4.3	4.2	3.3	
Zr	91	85	99	109	78	80	93	88	87	92	94	80	
Hf	2.4	2.2	2.7	2.9	2.0	2.0	2.5	2.4	2.2	2.5	2.5	2.2	
Y	27.4	25.6	29.6	32.6	30.6	29.8	26.9	28.5	26.0	27.9	29.9	23.5	29.0
La	4.4	4.1	4.5	4.8	4.5	4.4	4.0	4.1	4.0	4.3	4.5	3.3	4.5
Ce	13.4	13.2	13.2	13.5	12.9	12.7	11.0	11.2	10.9	12.1	11.7	9.4	12.6
Pr	2.1	2.1	2.1	2.2	2.0	2.0	1.8	1.9	1.8	1.9	2.0	1.5	2.0
Nd	10.0	9.8	9.9	10.6	10.2	10.1	9.0	9.5	8.8	9.3	9.8	7.8	9.9
Sm	3.5	3.1	3.5	3.7	3.5	3.6	3.0	3.1	3.0	3.1	3.2	2.7	3.3
Eu	1.2	1.1	1.1	1.2	1.1	1.1	1.0	1.1	1.1	1.1	1.1	1.0	1.1
Gd	3.6	3.5	3.5	4.2	3.9	4.0	3.6	3.5	3.7	3.8	3.9	3.1	3.8
Tb	0.8	0.7	0.8	0.9	0.9	0.8	0.8	0.8	0.7	0.8	0.8	0.6	0.8
Dy	4.7	4.2	5.0	5.3	5.0	4.8	4.5	4.6	4.3	4.6	5.2	3.7	4.9
Ho	1.0	1.0	1.1	1.2	1.1	1.1	1.0	1.1	1.0	1.1	1.1	0.9	1.1
Er	3.2	2.8	3.3	3.6	3.4	3.4	3.0	3.4	3.0	3.2	3.4	2.6	3.4
Tm	0.4	0.4	0.5	0.6	0.5	0.5	0.4	0.5	0.4	0.4	0.5	0.4	0.5
Yb	3.0	2.7	3.0	3.3	3.1	3.0	2.7	2.8	2.7	2.7	2.9	2.4	2.8
Lu	0.4	0.4	0.4	0.5	0.5	0.5	0.4	0.4	0.4	0.4	0.4	0.4	0.5

Sample [a]	T1009-VC9 3.0-								T1010-VC11 28.0-				
	D1	D2	D3	D4	D5	D6	D7	D8	GIM1-D1	GIM1-D2	GIM1-D3	GIM2-D22	GIM2-D24
									(GlassIn M1_1d)	(GlassIn M1_2d)	(GlassIn M1_3d)	(GlassIn M2_22d)	(GlassIn M2_24d)
Ni (µg/g)	65	144	135	139	68	141	67	69	55	53	58		
Cs [b]	0.01	n.a.	0.01	0.02	0.01	0.01	0.01	0.02	0.03	0.08	0.12		
Rb	1.4	0.8	0.8	0.7	1.3	0.8	1.4	1.4	1.8	1.9	1.9		
Ba	19.8	11	11	10.9	19.9	10.9	20.2	19.1	24.5	23.8	23.1	25.3	23.9
U	0.08	0.05	0.04	0.04	0.08	0.04	0.08	0.08	0.10	0.10	0.11		
Th	0.22	0.12	0.14	0.11	0.23	0.12	0.25	0.23	0.24	0.29	0.26		
Sr	137	105	107	103	138	104	137	141	149	149	144		
Nb	3.3	1.9	2.0	1.9	3.4	1.8	3.4	3.3	4.1	4.4	4.1		
Zr	83	46	49	44	79	43	84	71	75	90	78		
Hf	2.3	1.4	1.4	1.4	2.2	1.3	2.5	1.9	2.0	2.3	2.0		
Y	29.0	21.2	21.7	21.0	26.5	21.4	29.4	27.6	23.4	23.5	21.5	28.5	29.9
La	3.7	1.9	2.1	1.9	3.4	1.9	3.7	3.7	3.9	3.9	3.7	4.5	4.5
Ce	n.a.	5.6	5.8	5.7	10.0	5.4	10.4	10.5	11.9	11.5	11.3	12.6	12.0
Pr	1.7	0.9	0.9	0.9	1.7	1.0	1.7	1.8	1.9	1.9	1.8	1.9	1.9
Nd	8.7	5.1	5.4	5.3	8.3	5.2	8.7	8.4	8.7	8.9	8.8	9.9	9.9
Sm	2.9	2.1	2.0	2.2	3.1	2.1	3.1	3.2	2.9	2.9	2.7	3.3	3.5
Eu	1.1	0.7	0.8	0.8	1.1	0.7	1.1	1.1	1.0	1.1	1.0	1.1	1.1
Gd	3.7	2.9	2.6	2.3	3.1	2.6	3.8	3.4	3.0	3.2	3.0	3.5	3.7
Tb	0.8	0.6	0.5	0.6	0.7	0.6	0.8	0.7	0.6	0.7	0.6	0.7	0.8
Dy	4.7	3.5	3.5	3.4	4.4	3.4	4.8	4.6	3.8	3.9	3.7	4.8	5.0
Ho	1.1	0.8	0.8	0.8	1.0	0.8	1.1	1.0	0.9	0.9	0.8	1.1	1.1
Er	3.3	2.4	2.3	2.2	3.0	2.5	3.4	3.2	2.6	2.6	2.4	3.2	3.4
Tm	0.5	0.3	0.4	0.4	0.4	0.4	0.4	0.5	0.4	0.4	0.3	0.5	0.5
Yb	2.7	2.0	2.3	2.0	2.8	2.0	3.0	2.8	2.4	2.5	2.4	2.8	3.0
Lu	0.5	0.3	0.3	0.3	0.4	0.3	0.4	0.4	0.3	0.4	0.3	0.4	0.5

All samples analyzed by laser ablation inductively coupled mass spectroscopy; n.a. not analyzed.
[a] Sample identification used in Helo et al. (2011) given in parentheses. [b] Peak-filtered average (see methods).

Table 1 continued.

Sample[a]	T1010-VC11 28.0-		T1010-VC15 12.6-							
	GIM2-L21	GIM2-L25	GIM2-D1	GIM2-D2	GIM2-D3	GIM2-D4	GIM2-D11	GIM2-L6	GIM2-L8	GIM2-L9
	(GlassInM2_21L)	(GlassInM2_25L)	(GlassInM2_1d)	(GlassInM2_2d)	(GlassInM2_3d)	(GlassInM2_4d)	(GlassInM2_11d)	(GlassInM2_6L)	(GlassInM2_8L)	(GlassInM2_9L)
Ni (µg/g)	52	51	101	100	89	95	101	92	95	94
Cs[b]	0.02	0.02	0.02	0.02	0.02	0.02	0.05	0.03	0.03	0.02
Rb	1.8	1.9	1.6	1.6	1.7	1.6	1.7	1.4	1.6	1.6
Ba	24.3	24.7	20.6	20.7	21.6	21	21.5	17.5	20.9	
U	0.09	0.09	0.08	0.08	0.08	0.08	0.09	0.07	0.08	0.08
Th	0.30	0.31	0.21	0.23	0.23	0.23	n.a.	0.21	0.22	0.21
Sr	147	153	145	147	155	146	145	140	146	143
Nb	4.2	4.5	3.6	3.7	3.6	3.6	3.7	3.2	3.6	3.6
Zr	93	94	65	69	78	72	68	65	69	67
Hf	2.5	2.5	1.7	1.8	2.2	2.0	1.9	1.8	1.9	1.8
Y	24.8	28.4	23.7	21.0	23.5	23.8	25.2	21.2	22.9	
La	4.2	4.4	3.5	3.3	3.7	3.6	3.6	3.1	3.5	
Ce	12.0	12.0	10.1	10.4	10.9	10.1	10.3	8.4	10.3	
Pr	1.9	2.0	1.7	1.6	1.8	1.6	1.7	1.4	1.6	
Nd	9.2	9.9	8.2	7.8	8.4	8.1	8.3	7.0	8.0	
Sm	3.1	3.4	2.9	2.7	2.9	2.8	2.9	2.5	2.8	
Eu	1.1	1.1	1.0	0.9	1.0	1.0	1.0	0.9	1.0	
Gd	3.1	3.9	3.1	2.9	3.0	3.1	3.3	2.8	3.1	
Tb	0.7	0.8	0.7	0.6	0.7	0.6	0.7	0.6	0.6	
Dy	4.3	4.8	4.2	3.4	3.9	4.1	4.2	3.5	4.0	
Ho	0.9	1.1	0.9	0.8	0.9	0.9	0.9	0.8	0.8	
Er	2.8	3.3	2.7	2.3	2.8	2.7	2.8	2.5	2.6	
Tm	0.4	0.5	0.4	0.3	0.4	0.4	0.4	0.3	0.4	
Yb	2.6	3.0	2.4	2.2	2.5	2.4	2.4	2.2	2.3	
Lu	0.4	0.4	0.4	0.3	0.4	0.4	0.4	0.3	0.3	

Sample[a]	T1010-VC16 18.5						
	GIM1-D24	GIM1-D25	GIM1-D27	GIM2-D27	-GIM2-D29	GIM1-L31	GIM2-DL30
	(GlassInM1_24d)	(GlassInM1_25d)	(GlassInM1_27d)	(GlassInM2_27d)	(GlassInM2_29d)	(GlassInM1_31L)	(GlassInM2_30L)
Ni (µg/g)	49	50	49	50	58	50	40
Cs[b]	0.03	0.01	0.03	0.02	0.01	0.02	0.02
Rb	1.7	1.8	1.7	1.8	1.8	1.7	1.9
Ba	22.7	22.1	22.6	24	24.2	22.6	24.5
U	0.09	0.10	0.09	0.09	0.10	0.09	0.10
Th	0.27	0.26	0.28	0.27	0.29	0.24	0.33
Sr	142	143	143	149	146	143	146
Nb	3.8	3.9	3.9	4.2	4.4	3.9	4.5
Zr	84	82	89	91	90	76	112
Hf	2.2	2.2	2.4	2.4	2.5	1.9	3.1
Y	25.9	27.1	28.2	29.1	31.4	25.8	34.3
La	4.0	4.0	4.0	4.3	4.3	3.9	4.8
Ce	10.8	11.1	11.3	11.9	11.8	11.1	13.5
Pr	1.7	1.8	1.8	1.9	2.0	1.8	2.2
Nd	8.4	9.2	9.1	9.5	9.8	8.7	11.1
Sm	3.0	3.1	3.0	3.2	3.4	3.0	3.7
Eu	1.0	1.0	1.0	1.1	1.2	1.0	1.2
Gd	3.6	3.7	3.8	3.7	4.0	3.2	4.5
Tb	0.7	0.8	0.8	0.8	0.9	0.7	0.9
Dy	4.3	4.6	4.7	4.8	5.2	4.3	5.5
Ho	1.0	1.0	1.1	1.1	1.2	1.0	1.3
Er	2.8	3.1	3.2	3.4	3.6	2.8	3.8
Tm	0.4	0.5	0.5	0.5	0.5	0.4	0.6
Yb	2.5	2.7	2.8	3.0	3.0	2.6	3.2
Lu	0.4	0.4	0.4	0.5	0.5	0.4	0.5

Figure legends

Figure 1 **(a)** Schematic overview of the Juan de Fuca de Fuca ridge system. Individual spreading segments S1 to S7 and the northernmost Endeavour (EndS), Middle Valley (MV) and West Valley (WV) segments are indicated. **(b)** Bathymetric map of Axial Seamount's summit region displaying the U-shaped collapse caldera. Sample sites, as well as the photographed locations presented in Figure 2 are shown. The map is after MBARI EM300 data at 20 m resolution.

Figure 2 **(a), (b)** Unconsolidated deposits of black volcaniclastic glass fragments at the top of the caldera rim on Axial Seamount, photographed during **(a)** dive *D70* at the northeast rim and **(b)** dive *D75* at the central west rim. Sampling of volcaniclastic sequences by **(c)** the vibracorer attached to the ROV *Tiburon*, and **(d)** a pushcore retrieved using the ROV manipulator arm. Photographed locations are indicated in Figure 1b.

Figure 3 Two exemplifying volcaniclastic sediment cores. Boxes indicate sub-sampled horizons. See Supplementary Figure S1 for grains size distribution of the individual horizons.

Figure 4 Morphological variety of glass fragments recovered from the volcaniclastic sediment cores. **(a)** Photomicrograph, and **(b)** scanning electron microscope (SEM) images of mostly flat to slightly curved limu o Pele fragments. **(c)** Various forms of Pele's hair fragments. **(d)**, **(e)** Photomicrographs**, (f)** and SEM images of more complex limu o Pele shapes. Most limu o Pele occur as shown in **(a)**, **(b)** and **(d)**. Angular particles show surface textures from **(g)** irregular, rough and fractured to **(h)** fairly smooth and even, still sharp at the edges. **(i)** Occasionally, fragments have variable amounts of tubular vesicles, resembling tube pumices.

Figure 5 Major element composition of volcaniclastic glass deposits from Axial Seamount. **(a)** Early stages of magma evolution are characterized by olivine and plagioclase fractionation indicated by increasing Ca/Al with decreasing Mg, reaching an inflection point where the liquid becomes depleted in Ca due to clinopyroxene fractionation. The most primitive, Mg-rich samples fall off the main trend indicating an independent fractionation history. Black and grey lines enclose most of the literature data for Axial Seamount and rift zone lavas, respectively. **(b)** The trend of TiO_2 with MgO for the volcaniclastic sections agrees well with literature data for the caldera and the rift zones, and is distinct from the overall Juan de Fuca Ridge trend. **(c)** The incompatible element ratio K_2O/TiO_2 is fairly constant, except for the most primitive samples showing lower ratios. **(a)–(c)** See text for literature references. **(d)** Sulphur correlates with TiO_2 showing no decrease due to degassing.

Figure 6 Variation in MgO content within the volcaniclastic sediment cores from Axial Seamount. Depth is relative to the top of the sediment core section. The top of cores *T1009-PC5* and *T1010-PC2* coincides with the surface of the deposits at the sample sites.

Figure 7 Normalized trace element concentrations of glass fragments from selected volcaniclastic sediment sequences on Axial Seamount. **(a)** Fragments with intermediate to low MgO values exhibit generally flat to slightly depleted REE patterns (shaded area). The primitive samples of layer *T1009-VC9 3.0* are distinctly depleted in LREE. **(b)** Highly incompatible trace elements are generally depleted, with the primitive samples characterized by a stronger depletion. This suggests the occasional generation of discrete magma batches of distinct composition beneath Axial Seamount. Normalization values are from McDonough and Sun (1995), order of trace element incompatibility from Hofmann (1988).

Figure 8 Light rare earth element depletion/enrichment in volcaniclastic glasses from Axial Seamount. **(a)** Most sample exhibit chondrite normalized $[La/Yb]_N$ ~1, typical for basalts erupted at the Axial caldera. A subset of samples from *T1009-VC9 3*.0 indicates the sporadic injection of distinctly depleted magmas into the Axial pluming system. Axial caldera and rift zones data: Rhodes et al. (1990) and Chadwick et al. (2005); southern Juan de Fuca Ridge data: Liias (1986) and Smith et al. (1994). **(b)** The depleted magmas are of more primitive nature. Mixing of these magmas with more evolved melts is evident by hybrid compositions. Dashed line: binary mixing after Langmuir et al. (1978).

Figure 9 Trace element concentrations and ratios of volcaniclastic glass and melt inclusions from Axial Seamount. **(a), (b)** Large ion lithophile element ratios are fairly uniform in the volcaniclastic samples including the LREE-depleted samples from sequence *T1009-VC9 3.0*. **(b)** Highly incompatible elements strongly correlate in the volcaniclastic glass, compared to the more scattered melt inclusion and southern Juan de Fuca Ridge basalt data. **(c)** Zr, and Y data of the Juan de Fuca Ridge system can be characterized by an enriched (upper line) and a depleted (lower line) mixing trend. Axial Seamount basalts and volcaniclastic deposits plot between these trends. FC is fractional crystallization of ol+plg **(d)** Sr compositions of most volcaniclastites fall between the depleted and enriched compositional trends characterizing the Juan de Fuca Ridge system. **(c)**, **(d)** The depleted sample set of *T1009-VC9 3.0* is shown in yellow. Melt inclusion, Axial caldera and rift zone data: see text; southern Juan de Fuca Ridge and Vance Seamounts data: Dixon et al. (1986) and as in Figure 8; northern Juan de Fuca Ridge data: Karsten (1988), Karsten et al. (1990), Van Wagoner and Leybourne (1991), Stakes and Franklin (1994), Cousens et al. (1995); Cobb-Eickelberg data: Desonie and Duncan (1990).

Figure 10 Melting models for the mantle beneath Axial Seamount for **(a)** Zr/Nb, **(b)** Y/Nb, and **(c)** $[La/Yb]_N$ versus Ba/Zr. **(a, b)** Shown are trajectories for pooled continuous melts (CoMPo, red line), aggregated fractional melts (FMAg, green line) and continuous melting (CoM, black line) for an average depleted MORB mantle (DMM) and an enriched DMM source (dashed lines and solid lines, respectively). Aggregated continuous melting (not shown) produces trajectories similar to CoMPo. A mantle volume porosity of 0.01 was assumed. The volcaniclastic samples fall on a single curve coincident with the E-DMM melting trajectory. Sediment layer *T1009-VC9 3.0* samples are shown in yellow. **(c)** The distinct depletion in LREE, but similar Ba/Zr seen in a subset set of samples is consistent with a higher percentage of melting of a common mantle domain. Melting of a more depleted mantle would affect Ba/Zr, as indicated by the DMM melting trajectory. **(a–c)** Mantle compositions and mineral modes of Workman and Hart (2005) were used: ol (0.57), opx (0.28), cpx (0.13) and sp (0.02). Distribution coefficients are after Salters and Stracke (2004), except for sp (Kelemen et al., 2003). Dots on the trajectories denote increments of melt fractions of **(a)**, (**b)** 5 % and **(c**) 2.5 %. In the case of pooled melts these described mean melt fractions. Samples of sequence *T1009-VC9 3.0* are in yellow. Southern Juan de Fuca Ridge data*:* Smith et al. (1994); melt inclusion, northern Juan de Fuca Ridge, and Cobb-Eickelberg data: as in Figure 9.

Figure 11 Steady-state evolution model for the Axial Seamount magma reservoir (after Albarède, 1995). **(a)** Assuming a constant magma flux into the reservoir, rare earth element concentrations are progressively enriched to the steady-state concentration by fractional crystallization. The timescale is represented as the total mass input M_{in} over time relative to the constant reservoir mass $M_{reservoir}$. Steady-state is reached within 1 % , (c_i/c_0 is 99 % if at steady state c_i/c_0 = 100 %) after a turn over mass less than six times the reservoir mass. Three intermediate states of enrichment are indicated, τ_i denotes the respective element residence time. Initial and final element concentrations are minimum

and maximum values from the dataset. **(b)** Dependence of the modeled erupted fraction (relative to the cumulate fraction) on the constant input concentration.

Figure 12 Model of Axial Seamount magma reservoir as a system experiencing periodic replenishment and eruption and continual fractional crystallization (after Albarede, 1985). Shown are steady-state concentration versus the fraction X crystallizing during each cycle for different erupting fractions ϕ, indicated at the top for La; the same ϕ values apply to Yb. X, ϕ relative to liquid mass when replenishment resumes. Pure fractional crystallization (i.e., complete reservoir evacuation during each cycle) indicated as red lines. Initial and final concentrations as in Figure 11. The steady-state level indicates $\phi/X \sim 2$. Possible combinations of X and ϕ for the 1998 eruptive event are shown.

Append. Figure A1 Rare earth element portioning into olivine. Regression of the strain-compensated partition coefficients $D_{0(M)}^{3+}$ derived from the lattice strain fit (Blundy and Wood, 2003) using partition coefficient D_M^{3+} data from *Beattie* (1994) yields no significant temperature dependence over a 300 K interval (dashed line). Error bars are smaller than symbol size. The data point in parentheses was excluded from regression. *Inlay*: lattice strain fits of trivalent cations portioning onto the M^{VI}-site. Ionic radii from Shannon (1976).

Figures

Figure 1

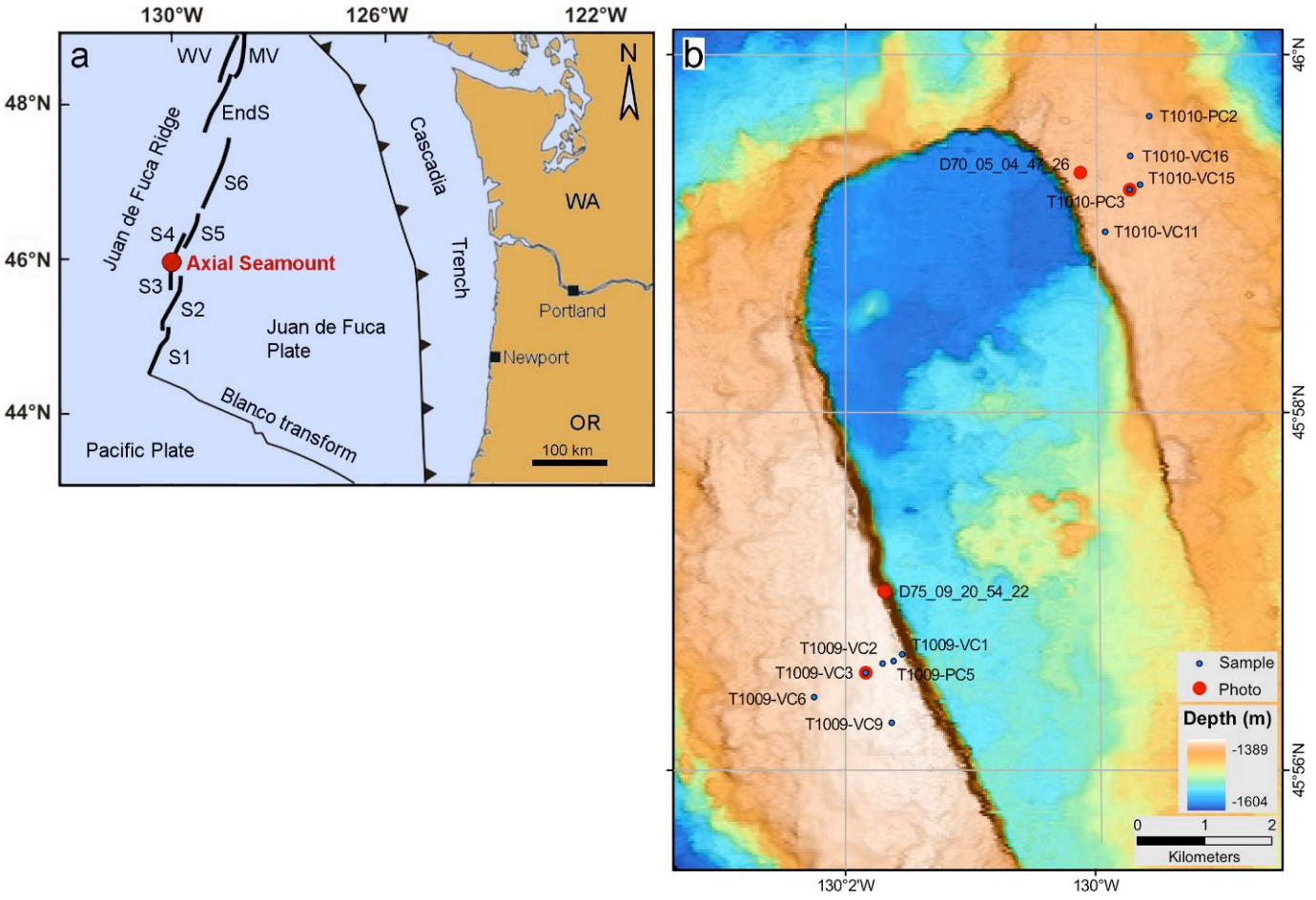

Figure 2

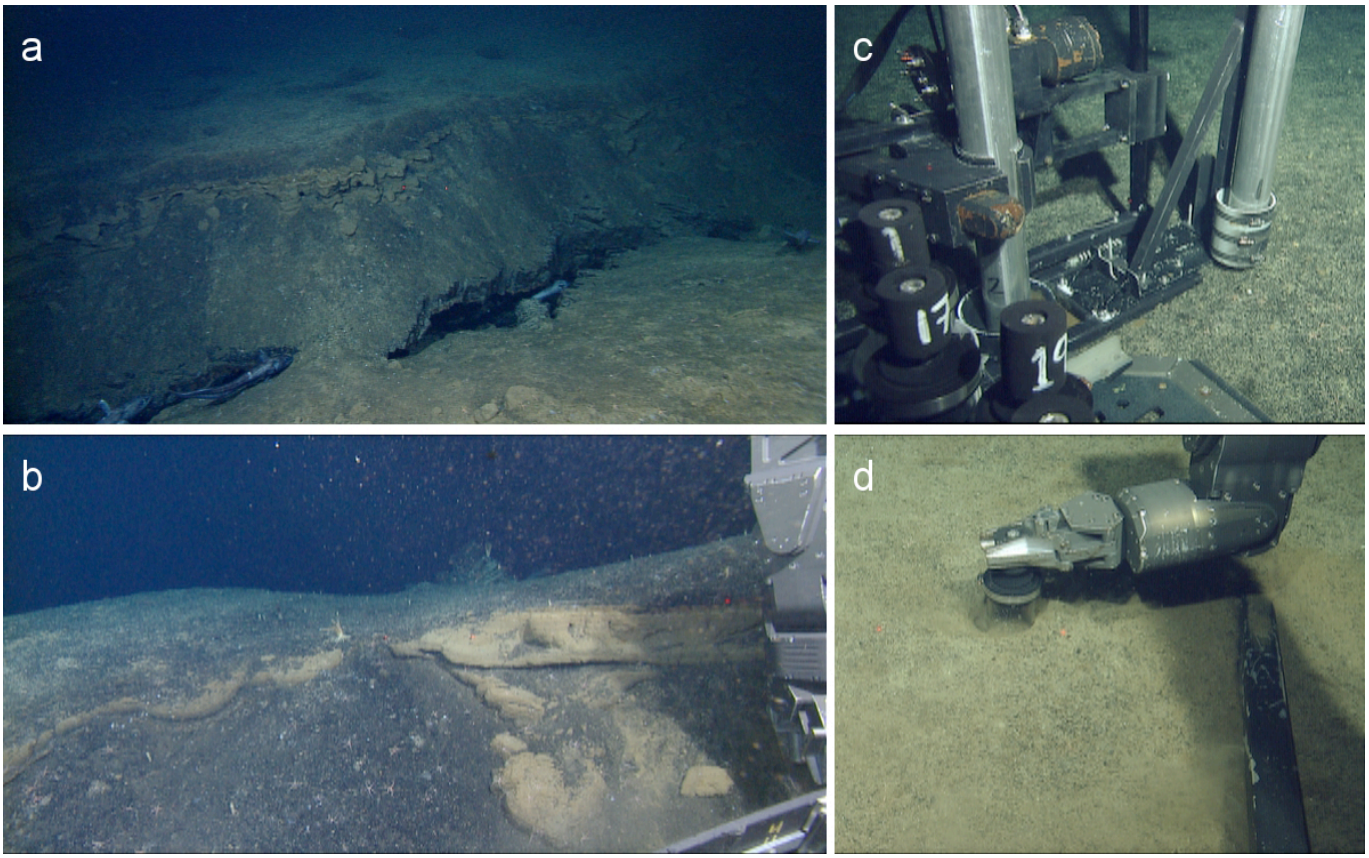

Figure 3

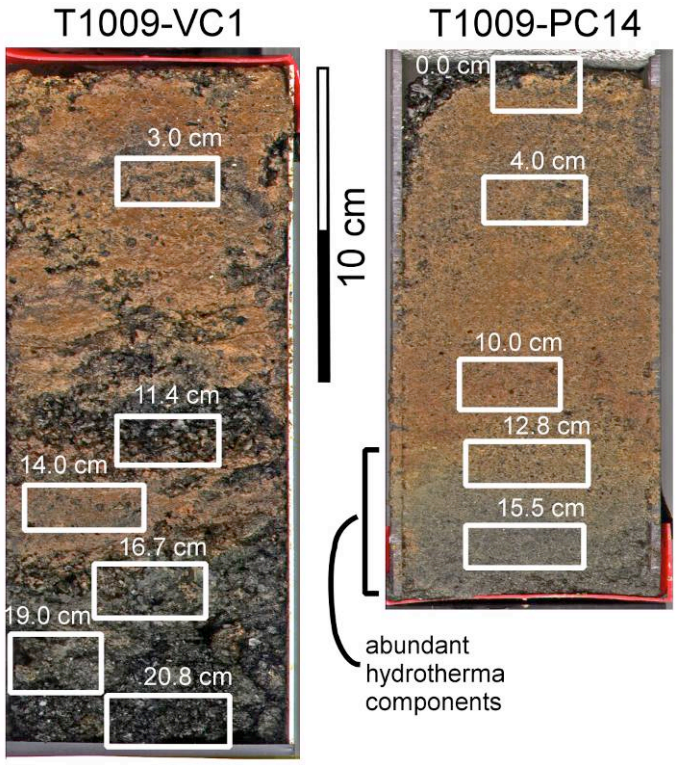
T1009-VC1
T1009-PC14
3.0 cm
11.4 cm
14.0 cm
16.7 cm
19.0 cm
20.8 cm
10 cm
0.0 cm
4.0 cm
10.0 cm
12.8 cm
15.5 cm
abundant
hydrotherma
components

Figure 4

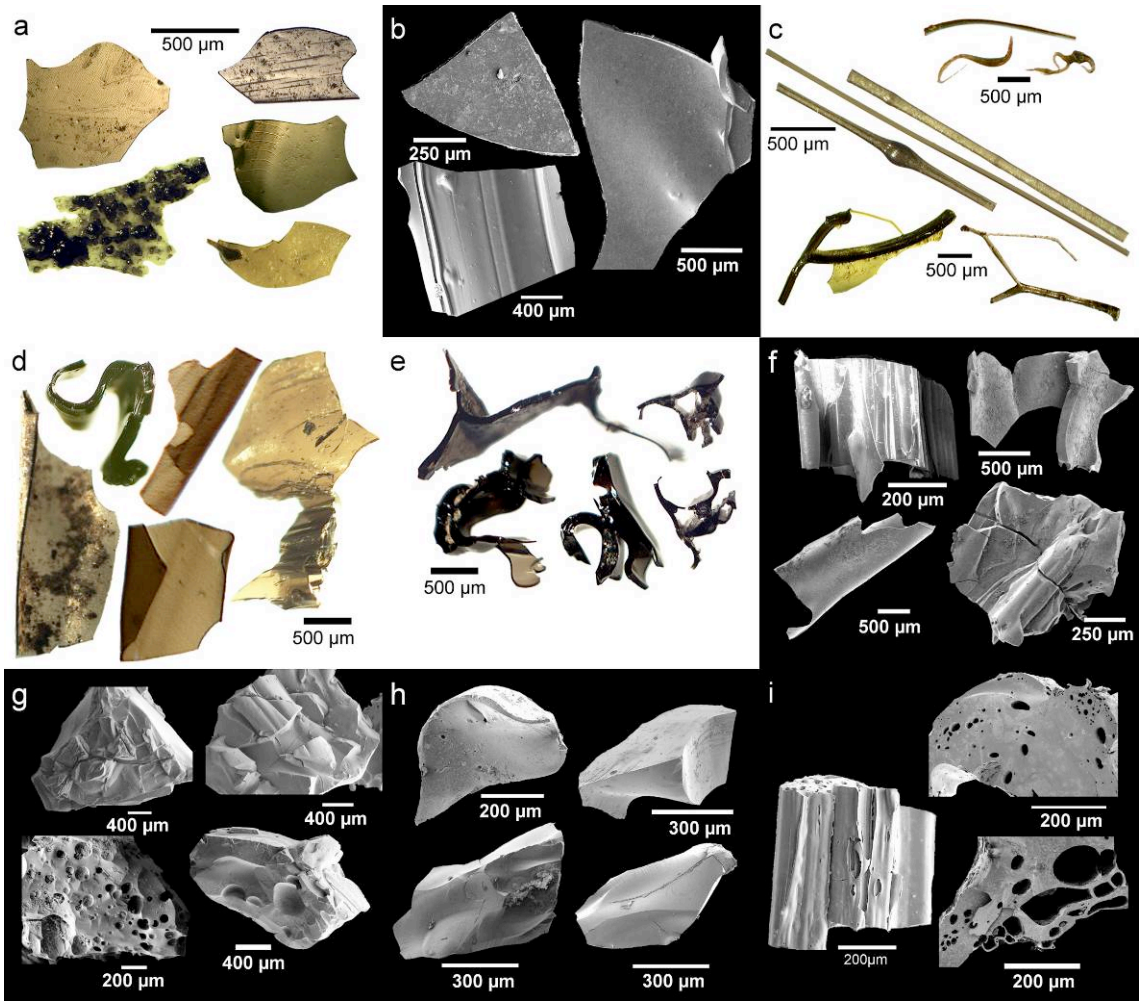
a
500 µm
b
250 µm
500 µm
400 µm
c
500 µm
500 µm
500 µm
d
500 µm
e
500 µm
f
500 µm
200 µm
500 µm
250 µm
g
400 µm
400 µm
200 µm
400 µm
h
200 µm
300 µm
300 µm
300 µm
i
200 µm
200µm
200 µm

Figure 5

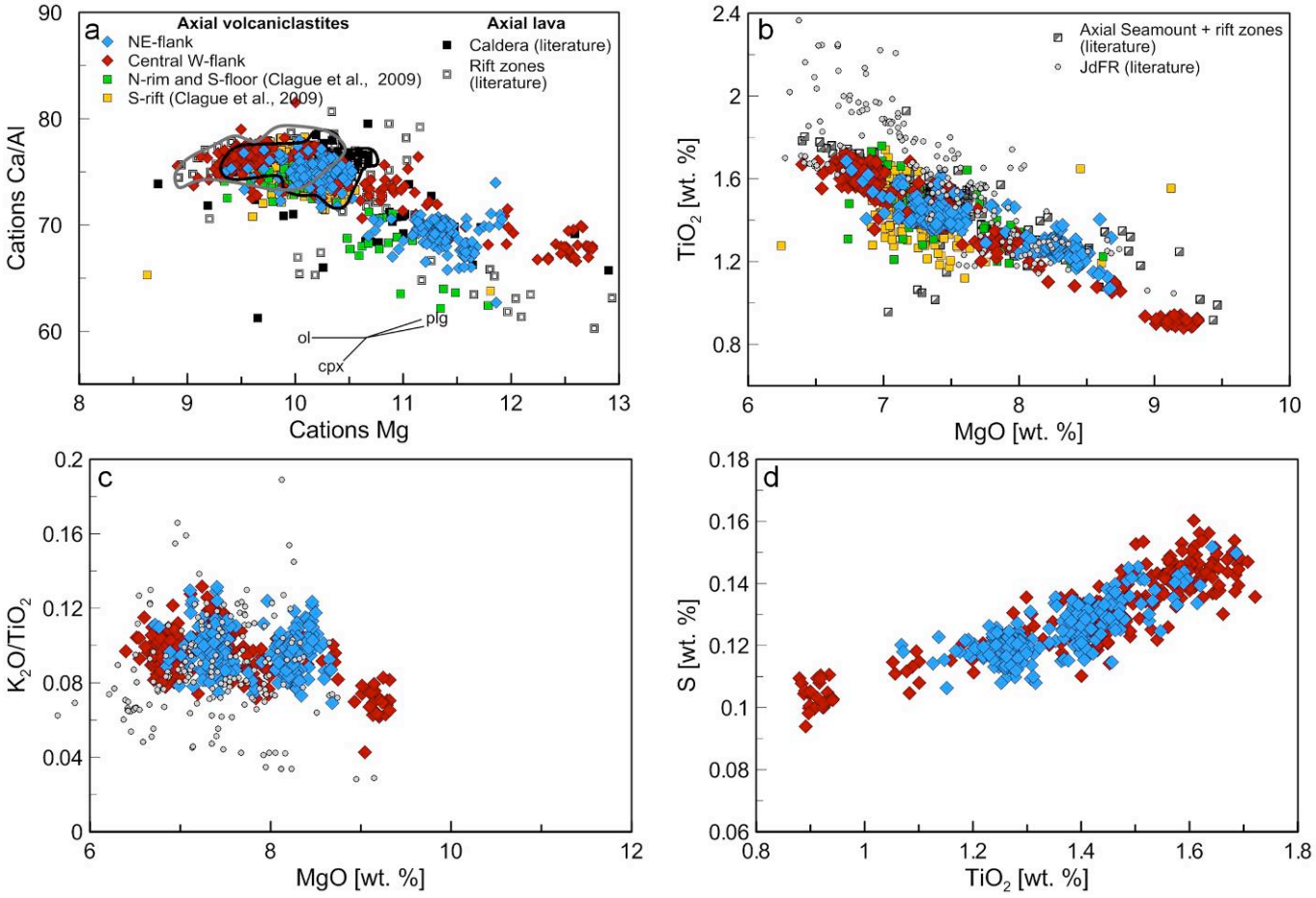
a
Axial volcaniclastites
NE-flank
Central W-flank
N-rim and S-floor (Clague et al., 2009)
S-rift (Clague et al., 2009)
Axial lava
Caldera (literature)
Rift zones (literature)
ol
plg
cpx
Cations Ca/Al
Cations Mg
b
Axial Seamount + rift zones (literature)
JdFR (literature)
TiO2 [wt. %]
MgO [wt. %]
c
K2O/TiO2
MgO [wt. %]
d
S [wt. %]
TiO2 [wt. %]

Figure 6

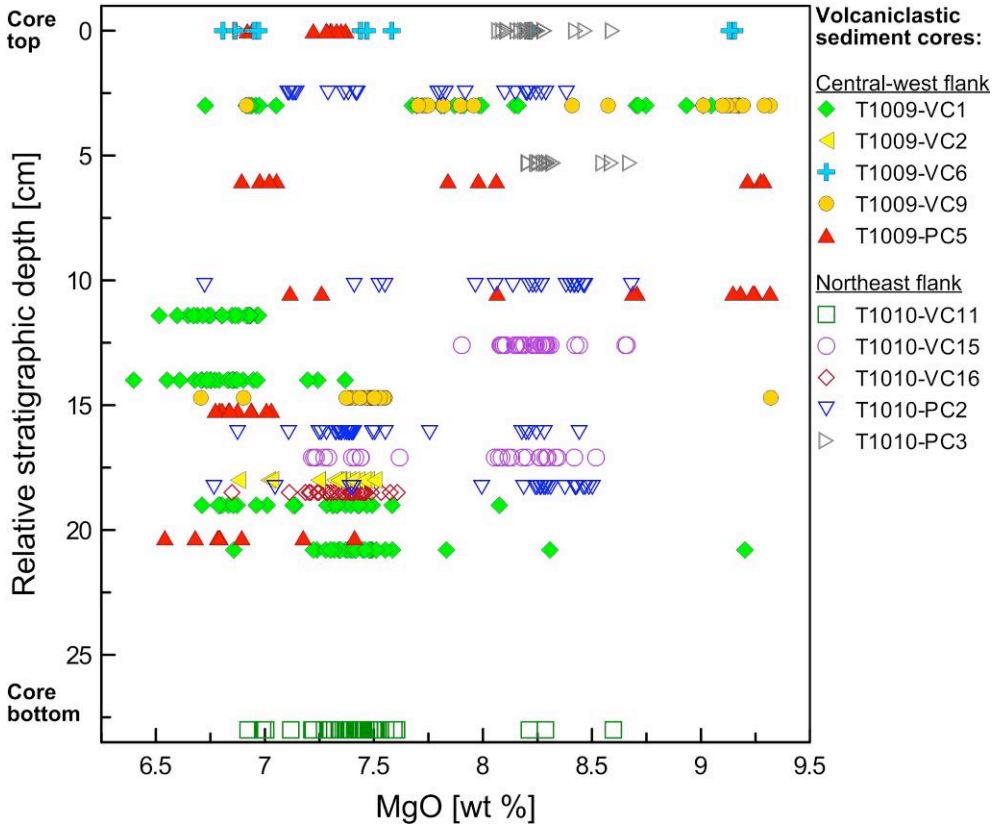
Core top
0
5
10
15
20
25
Core bottom
Relative stratigraphic depth [cm]
6.5
7
7.5
8
8.5
9
9.5
MgO [wt %]
Volcaniclastic sediment cores:
Central-west flank
T1009-VC1
T1009-VC2
T1009-VC6
T1009-VC9
T1009-PC5
Northeast flank
T1010-VC11
T1010-VC15
T1010-VC16
T1010-PC2
T1010-PC3

Figure 7

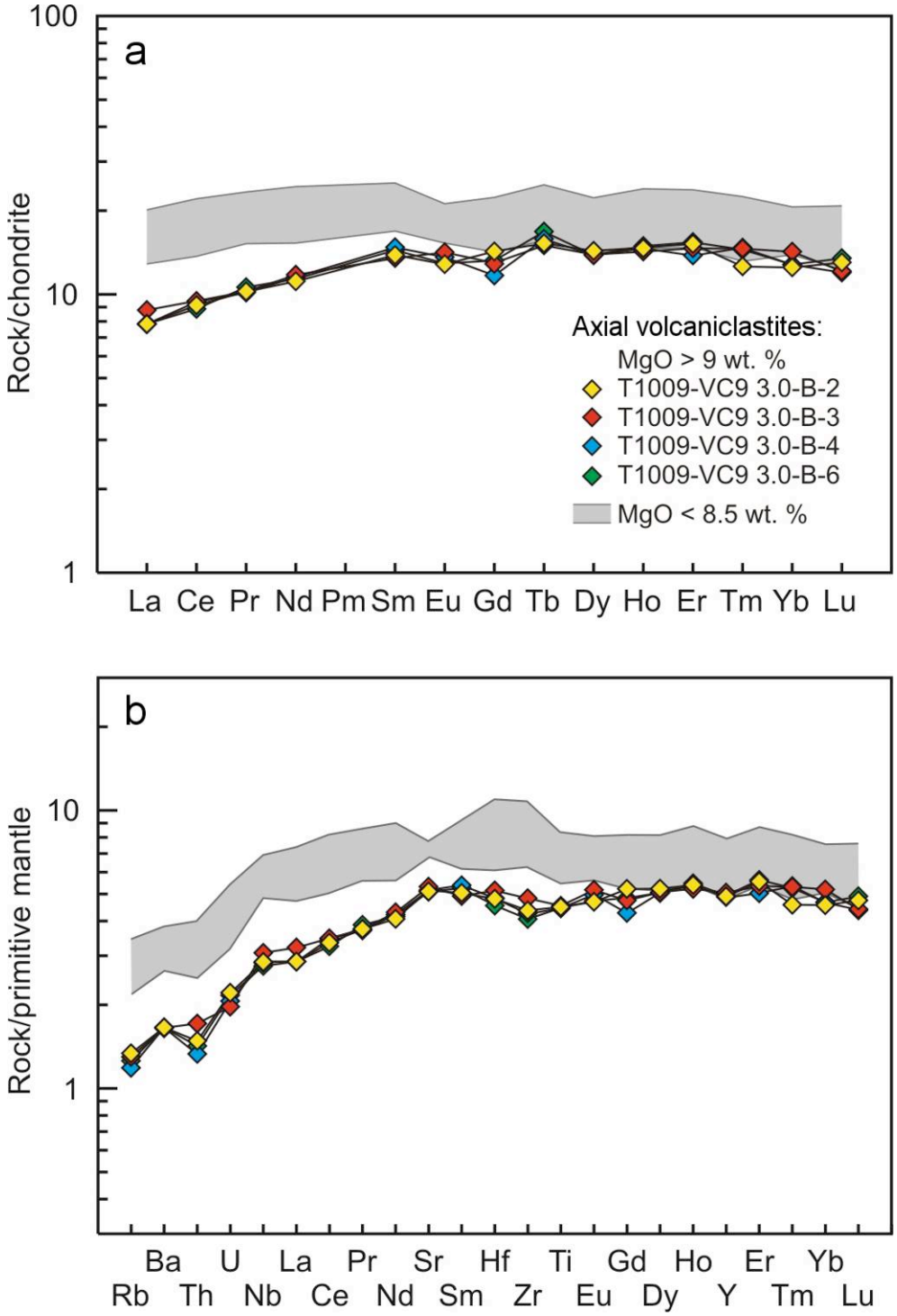
a
100
10
1
Rock/chondrite
La Ce Pr Nd Pm Sm Eu Gd Tb Dy Ho Er Tm Yb Lu
Axial volcaniclastites:
MgO > 9 wt. %
T1009-VC9 3.0-B-2
T1009-VC9 3.0-B-3
T1009-VC9 3.0-B-4
T1009-VC9 3.0-B-6
MgO < 8.5 wt. %
b
10
1
Rock/primitive mantle
Ba U La Pr Sr Hf Ti Gd Ho Er Yb
Rb Th Nb Ce Nd Sm Zr Eu Dy Y Tm Lu

Figure 8

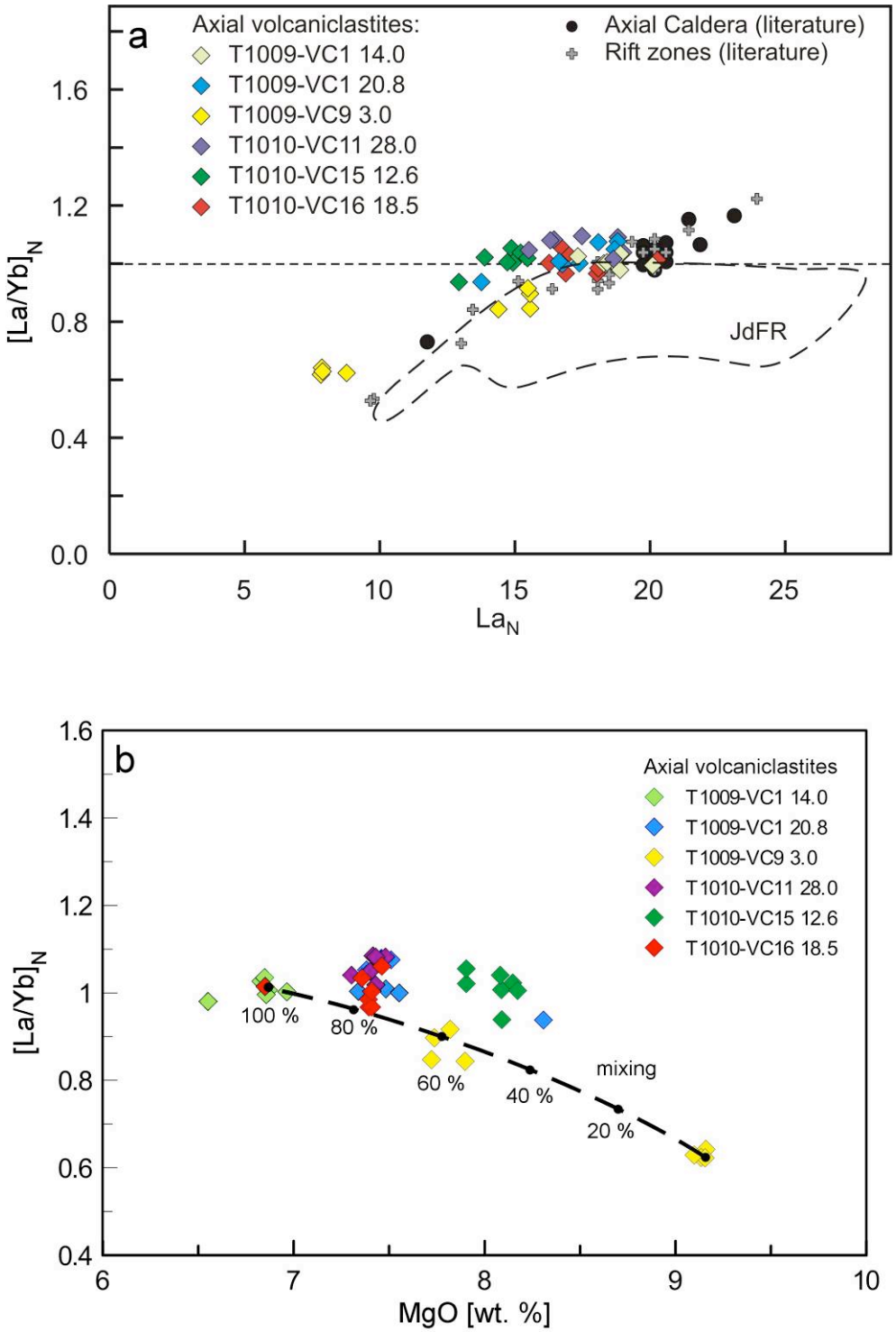
a
Axial volcaniclastites:
T1009-VC1 14.0
T1009-VC1 20.8
T1009-VC9 3.0
T1010-VC11 28.0
T1010-VC15 12.6
T1010-VC16 18.5
Axial Caldera (literature)
Rift zones (literature)
JdFR
[La/Yb]N
LaN
b
Axial volcaniclastites
T1009-VC1 14.0
T1009-VC1 20.8
T1009-VC9 3.0
T1010-VC11 28.0
T1010-VC15 12.6
T1010-VC16 18.5
100 %
80 %
60 %
40 %
20 %
mixing
[La/Yb]N
MgO [wt. %]

Figure 9

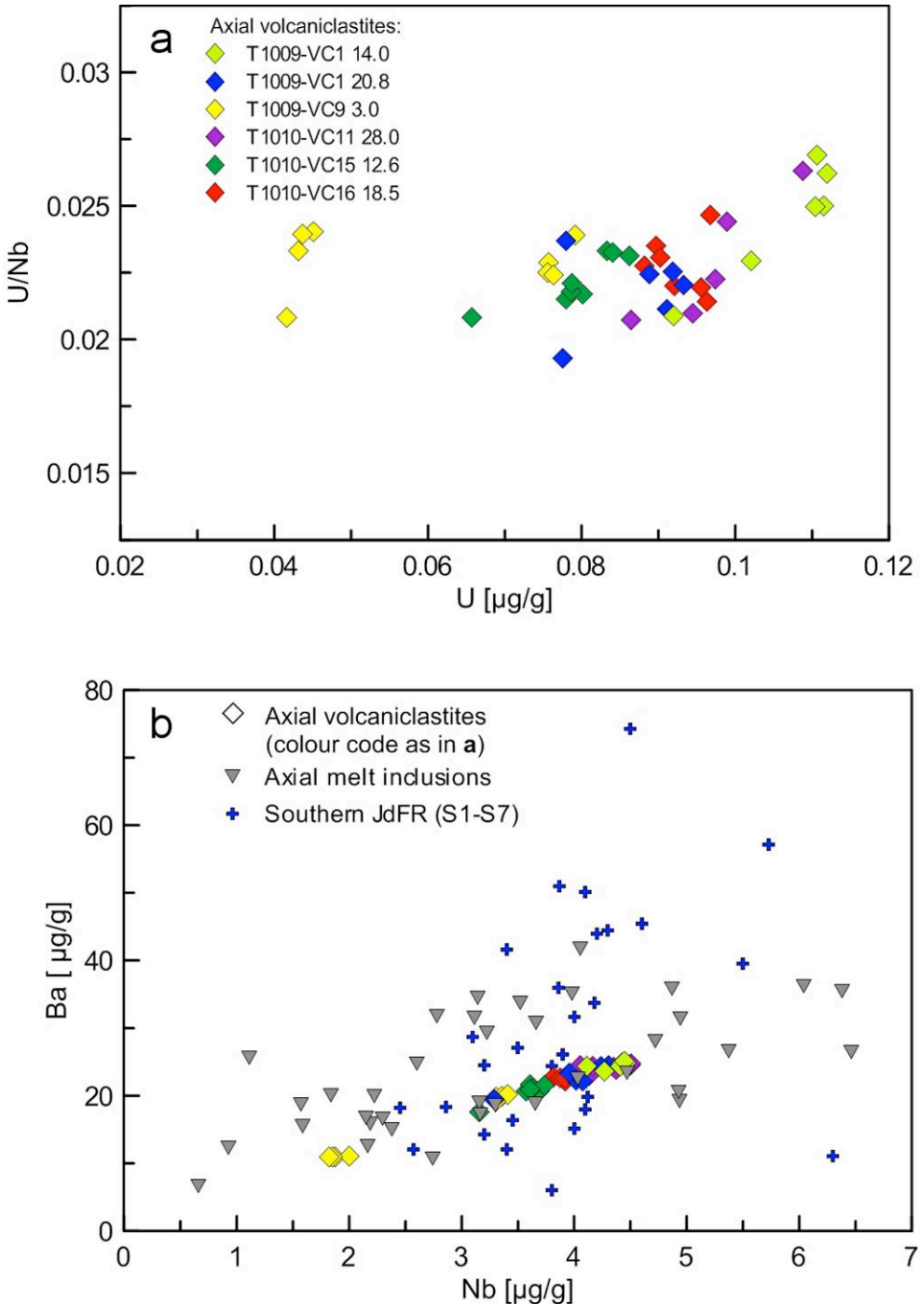
a
Axial volcaniclastites:
T1009-VC1 14.0
T1009-VC1 20.8
T1009-VC9 3.0
T1010-VC11 28.0
T1010-VC15 12.6
T1010-VC16 18.5
U/Nb
0.03
0.025
0.02
0.015
0.02
0.04
0.06
0.08
0.1
0.12
U [µg/g]
b
Axial volcaniclastites
(colour code as in a)
Axial melt inclusions
Southern JdFR (S1-S7)
Ba [µg/g]
80
60
40
20
0
0
1
2
3
4
5
6
7
Nb [µg/g]

Figure 9 continued

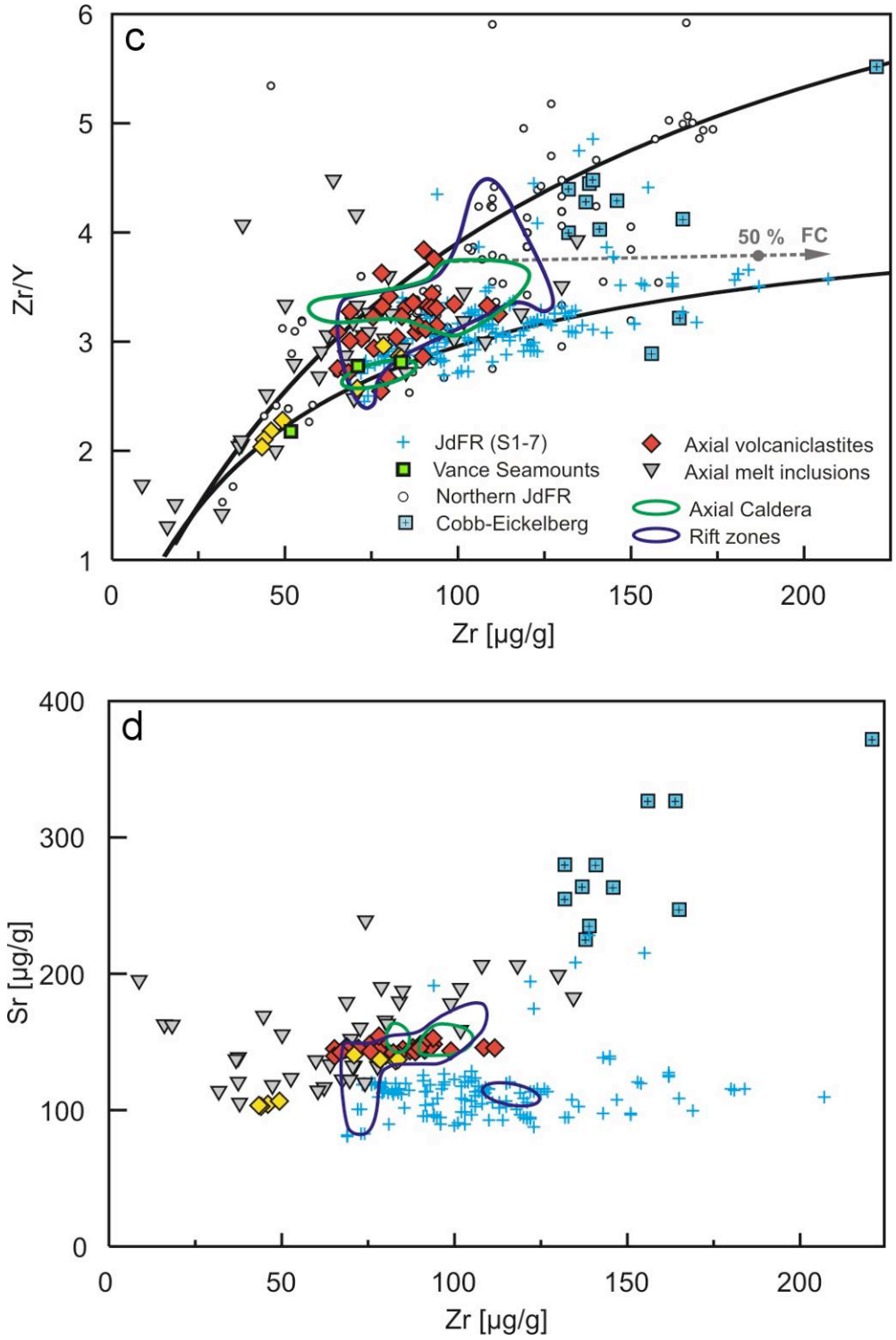

Figure 10

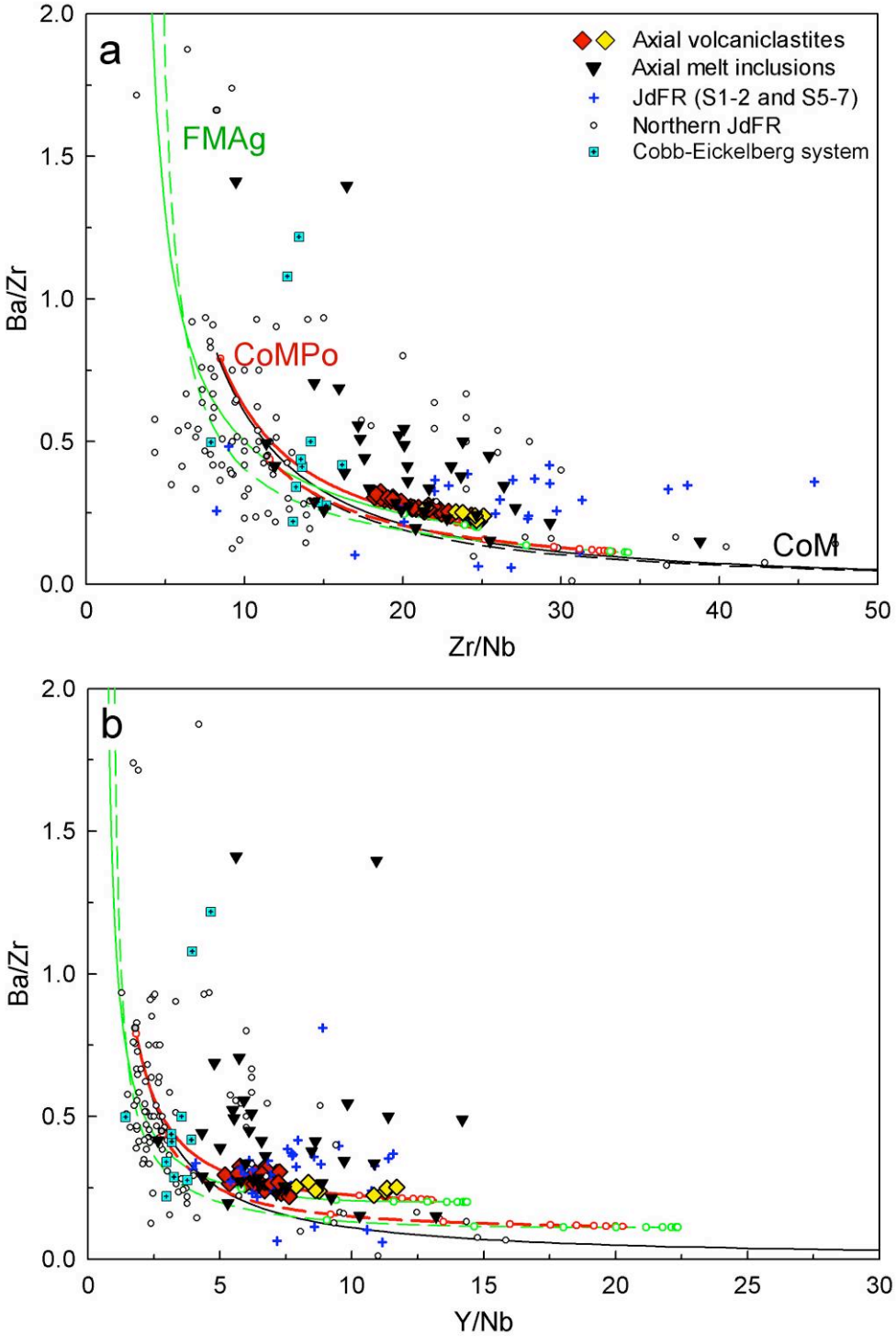
a
Axial volcaniclastites
Axial melt inclusions
JdFR (S1-2 and S5-7)
Northern JdFR
Cobb-Eickelberg system
FMAg
CoMPo
CoM
Ba/Zr
Zr/Nb
b
Ba/Zr
Y/Nb

Figure 10 continued

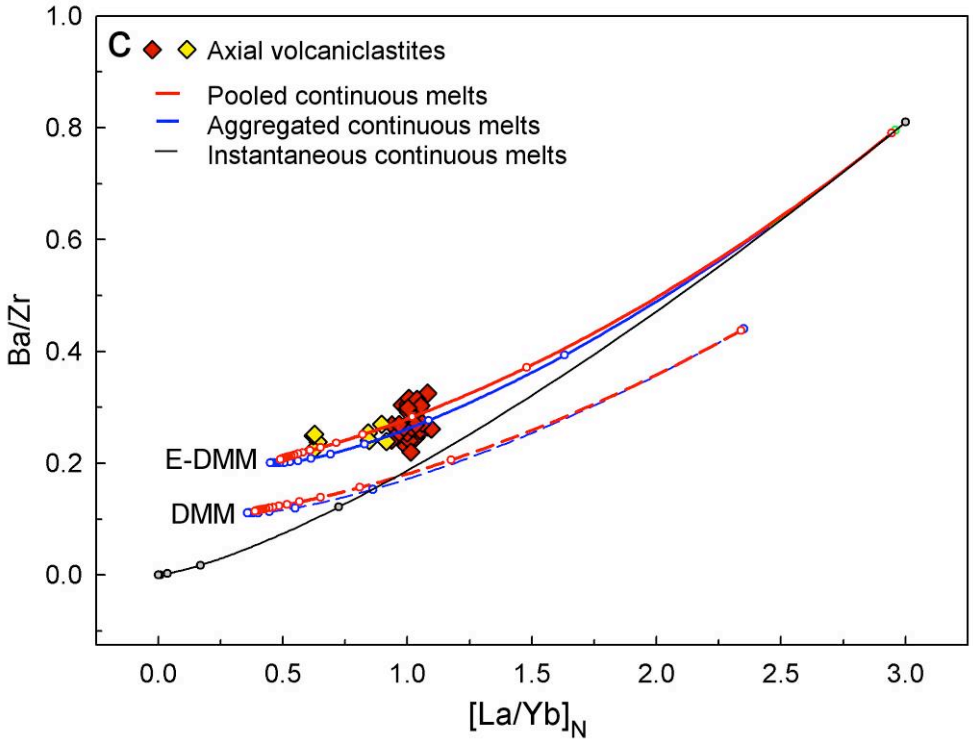

Figure 11

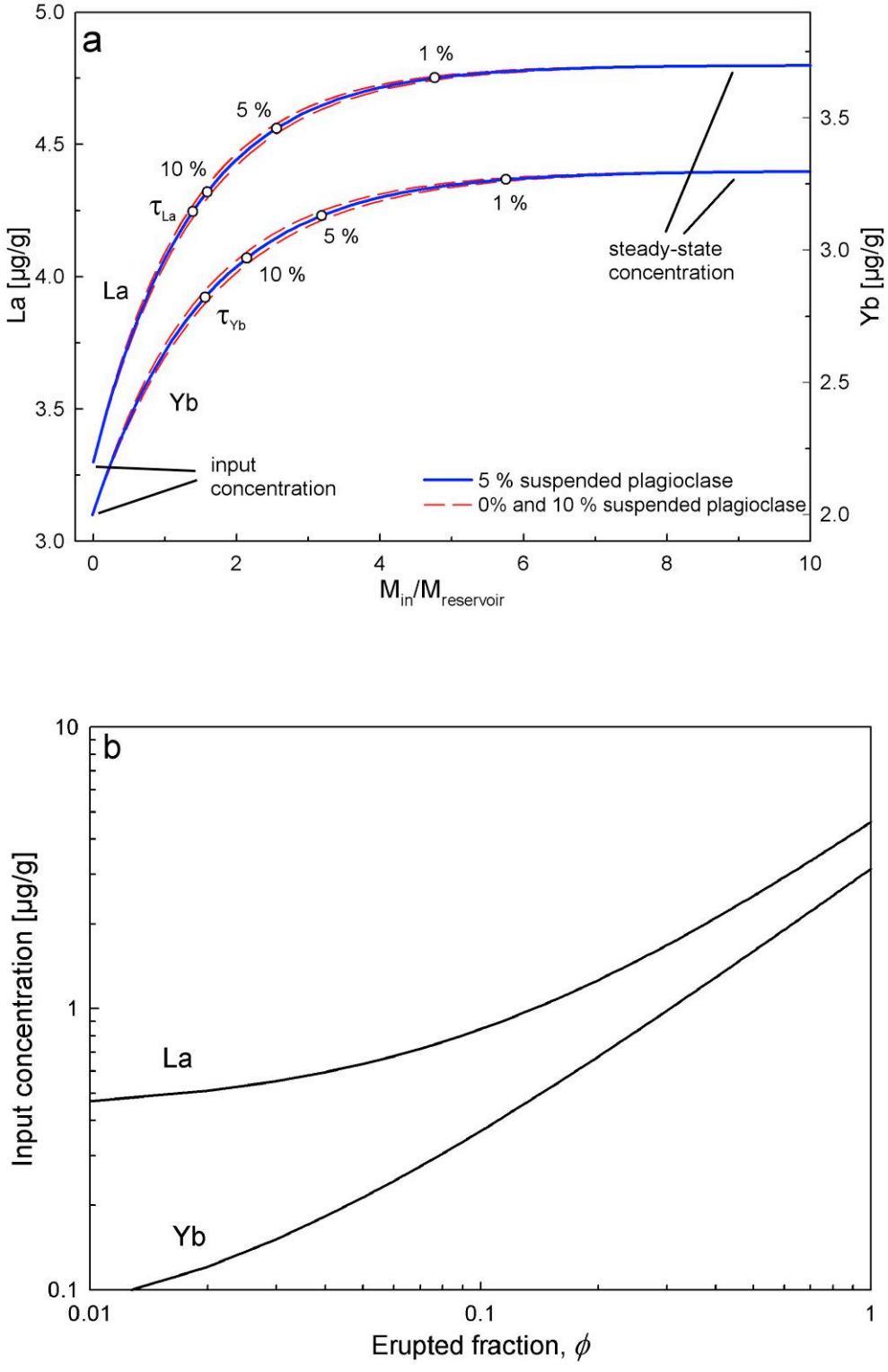
a
La [µg/g]
Yb [µg/g]
$M_{in}/M_{reservoir}$
1 %
5 %
10 %
τ_{La}
τ_{Yb}
La
Yb
steady-state concentration
input concentration
5 % suspended plagioclase
0% and 10 % suspended plagioclase
b
Input concentration [µg/g]
Erupted fraction, ϕ
La
Yb

Figure 12

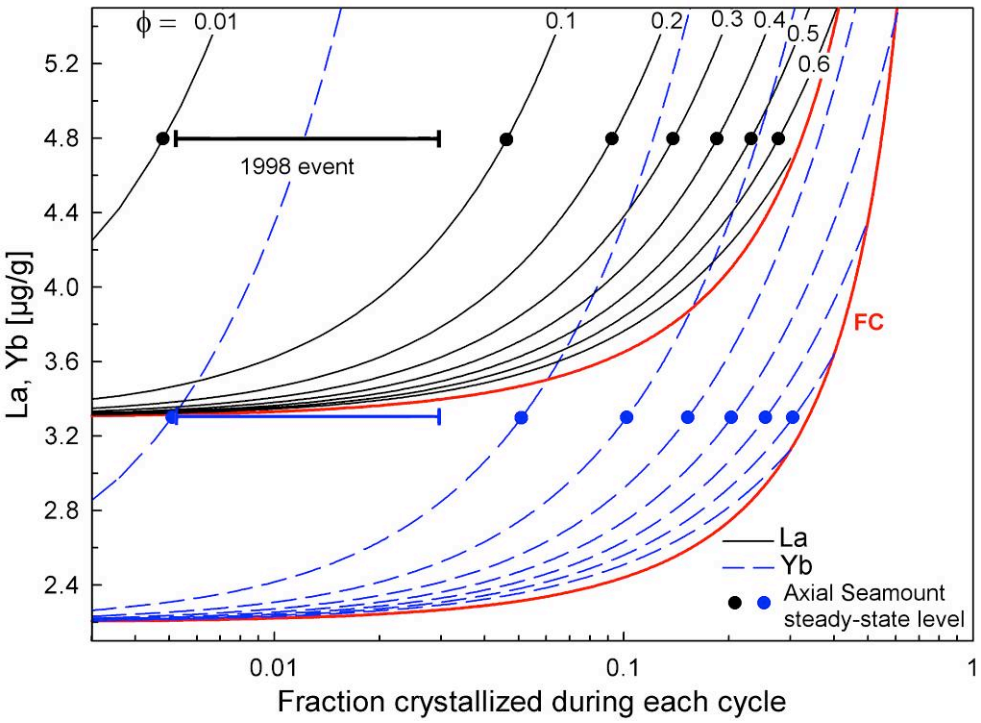
ϕ = 0.01
0.1
0.2
0.3
0.4
0.5
0.6
1998 event
FC
La
Yb
Axial Seamount
steady-state level
La, Yb [µg/g]
5.2
4.8
4.4
4.0
3.6
3.2
2.8
2.4
0.01
0.1
1
Fraction crystallized during each cycle

Appendix Figure A1

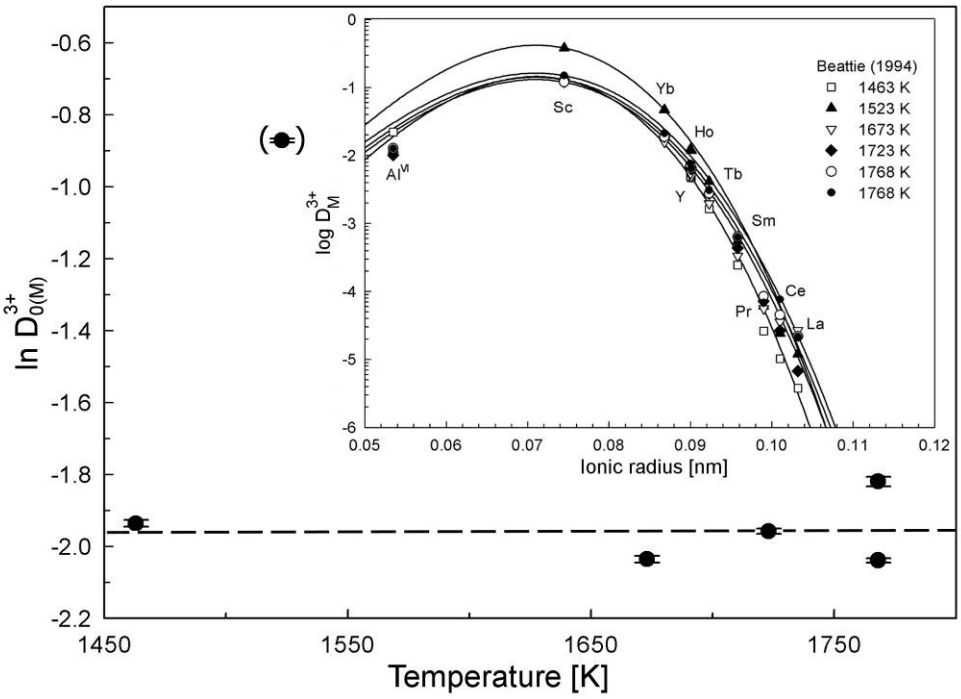

Supplementary data and information

Supplementary Table S1 Major element composition of volcaniclastic sequences on Axial Seamount.

Sample[a]	T1009-VC1 3.0-																	
	D1	D2	D3	D4	D5	D6	D7	D8	D9	D1b	D2b	D3b	D4b	D5b	D6b	D7b	D8b	D9b
SiO_2 (wt%)	48.61	49.20	49.41	49.76	49.42	49.00	49.19	49.26	48.75	49.56	49.48	48.86	49.39	49.63	48.54	49.78	48.79	48.50
TiO_2	0.93	1.29	1.51	1.59	1.58	1.30	1.57	1.29	1.09	1.53	1.16	1.06	1.18	1.28	0.89	1.57	1.09	0.92
Al_2O_3	17.08	15.45	14.41	14.64	14.43	15.34	14.32	15.32	16.35	14.50	15.83	16.50	15.87	15.32	17.13	14.36	16.42	17.23
FeO^t	8.97	10.53	11.57	11.60	11.39	10.47	11.41	10.52	9.60	11.66	10.03	9.65	9.96	10.70	8.91	11.52	9.66	8.91
MnO	0.12	0.11	0.17	0.15	0.20	0.11	0.17	0.13	0.10	0.24	0.22	0.19	0.20	0.21	0.16	0.17	0.13	0.16
MgO	8.89	7.63	6.86	6.95	6.86	7.73	6.62	7.86	8.65	7.04	8.16	8.76	8.18	7.95	8.97	6.95	8.71	9.18
CaO	12.54	12.29	12.19	11.96	12.02	12.19	12.07	12.31	12.26	12.16	12.51	12.56	12.60	12.52	12.60	12.22	12.59	12.69
Na_2O	2.11	2.54	2.68	2.70	2.71	2.50	2.62	2.45	2.25	2.71	2.50	2.26	2.46	2.48	2.13	2.68	2.27	2.21
K_2O	0.065	0.138	0.135	0.160	0.163	0.126	0.169	0.121	0.100	0.151	0.103	0.087	0.114	0.113	0.066	0.150	0.104	0.066
P_2O_5	0.091	0.092	0.141	0.166	0.112	0.100	0.103	0.085	0.081	0.110	0.086	0.074	0.095	0.096	0.062	0.120	0.070	0.053
Cl	0.034	0.025	0.029	0.034	0.033	0.005	0.043	0.008	0.007	0.025	0.008	0.006	0.009	0.015	0.023	0.025	0.008	0.006
S	0.110	0.122	0.145	0.146	0.143	0.125	0.139	0.124	0.114	0.142	0.115	0.111	0.121	0.122	0.099	0.146	0.113	0.100
Total	99.55	99.42	99.23	99.86	99.07	99.00	98.42	99.49	99.35	99.82	100.21	100.11	100.18	100.44	99.58	99.70	99.96	100.03

Sample	T1009-VC1 3.0-								
	D10b	L1	L2	L3	L4	L5	L6	L7	L8
SiO_2 (wt%)	49.04	49.58	48.80	49.06	48.89	49.00	49.68	49.44	49.01
TiO_2	1.27	1.54	0.92	1.45	1.33	1.33	1.31	1.34	1.28
Al_2O_3	15.50	14.26	16.67	15.76	15.27	15.48	15.04	14.96	14.84
FeO^t	10.50	11.65	8.91	10.31	10.23	10.20	10.77	10.86	10.56
MnO	0.19	0.18	0.18	0.19	0.23	0.16	0.19	0.23	0.18
MgO	7.78	6.89	8.98	7.68	7.91	6.81	7.86	7.79	7.91
CaO	12.47	11.97	12.50	12.25	12.37	12.34	12.17	12.08	12.29
Na_2O	2.51	2.72	2.06	2.65	2.53	2.57	2.54	2.55	2.49
K_2O	0.108	0.158	0.039	0.144	0.098	0.123	0.104	0.120	0.107
P_2O_5	0.092	0.128	0.088	0.084	0.097	0.096	0.112	0.094	0.091
Cl	0.019	0.029	*0.010*	0.031	0.015	0.042	0.018	0.016	0.014
S	0.130	0.142	0.104	0.114	0.119	0.133	0.130	0.127	0.134
Total	99.62	99.25	99.27	99.71	99.07	98.29	99.91	99.61	98.91

	T1009-VC1 11.4-							
	D1	D2	D3	D4	D5	D6	D7	D8
SiO_2 (wt%)	49.19	49.18	49.49	49.77	49.36	49.76	49.71	49.19
TiO_2	1.63	1.62	1.63	1.68	1.67	1.59	1.59	1.62
Al_2O_3	14.36	14.29	14.43	14.50	14.35	14.52	14.30	14.32
FeO^t	11.54	11.57	12.09	11.76	11.71	11.59	11.76	12.11
MnO	0.16	0.16	0.19	0.19	0.17	0.18	0.17	0.19
MgO	6.88	6.85	6.90	6.49	6.57	6.90	6.77	6.94
CaO	12.02	12.12	12.01	11.76	11.88	11.93	11.95	12.07
Na_2O	2.63	2.65	2.60	2.91	2.69	2.70	2.72	2.70
K_2O	0.164	0.15	0.137	0.175	0.160	0.151	0.152	0.181
P_2O_5	0.118	0.12	0.133	0.127	0.126	0.114	0.124	0.095
Cl	0.020	0.034	0.030	0.046	0.037	0.022	0.030	0.037
S	0.146	0.14	0.143	0.153	0.141	0.144	0.147	0.141
Total	98.87	98.89	99.78	99.55	98.86	99.59	99.43	99.60

All elements analyzed by electron microprobe; FeO^t is all Fe as FeO; n.a.: not analyzed.

[a] Sample numbers refer to Tiburon dive (T), sample type: vibracore (VC) or pushcore (PC), relative stratigraphic depth, and fragment type: dense (D) or limu o Pele (L).

Supplementary Table S1 continued.

Sample	T1009-VC1 11.4-															T1009-VC1 19.0	
	D9	D10	D11	D12	D13	L1	L2	L3	L4	L5	L6	L7	L8	L9	L10	D1	D2
SiO_2 (wt%)	49.15	49.96	49.77	49.50	49.63	49.40	49.93	49.74	49.78	49.85	49.65	49.30	49.37	49.75	49.24	49.40	49.54
TiO_2	1.61	1.64	1.59	1.61	1.60	1.61	1.56	1.63	1.64	1.60	1.65	1.53	1.71	1.69	1.66	1.41	1.60
Al_2O_3	14.35	14.43	14.33	14.37	14.28	14.06	14.24	14.10	14.07	14.00	14.08	14.34	14.21	14.21	14.03	15.22	14.51
FeO^t	11.70	11.81	11.73	11.60	11.61	11.87	11.99	11.91	11.86	11.83	12.12	11.57	12.20	12.03	11.91	11.16	11.76
MnO	0.19	0.23	0.19	0.22	0.20	0.23	0.21	0.19	0.26	0.18	0.19	0.24	0.22	0.30	0.20	0.18	0.20
MgO	6.87	6.73	6.89	6.88	6.82	6.79	6.66	6.71	6.63	6.77	6.56	6.78	6.68	6.80	6.57	7.13	6.80
CaO	12.08	11.84	11.99	11.96	11.89	11.84	11.66	11.89	11.89	11.94	11.82	11.88	11.85	11.80	11.54	12.23	11.93
Na_2O	2.69	2.76	2.75	2.71	2.71	2.83	2.84	2.75	2.84	2.85	2.85	2.75	2.77	2.87	2.80	2.77	2.63
K_2O	0.130	0.138	0.156	0.156	0.131	0.151	0.171	0.153	0.147	0.146	0.189	0.148	0.163	0.160	0.166	0.147	0.173
P_2O_5	0.108	0.117	0.128	0.114	0.123	0.134	0.102	0.153	0.133	0.133	0.114	0.114	0.151	0.118	0.125	0.121	0.145
Cl	0.040	0.030	0.029	0.029	0.028	0.028	0.026	0.024	0.026	0.04	0.066	0.024	0.044	0.028	0.049	0.035	0.035
S	0.142	0.144	0.139	0.143	0.148	0.141	0.148	0.136	0.136	0.160	0.137	0.136	0.135	0.146	0.148	0.131	0.138
Total	99.07	99.82	99.68	99.29	99.18	99.08	99.53	99.39	99.42	99.48	99.42	98.81	99.52	99.91	98.43	99.94	99.46

Sample	T1009-VC1 19.0																	
	D3	D4	D5	D6	D7	D8	D9	D1b	D2b	D3b	D4b	D5b	D6b	D7b	D8b	D9b	D10b	L1
SiO_2 (wt%)	49.11	48.85	48.94	49.02	49.78	48.94	49.31	49.16	49.71	49.17	49.31	49.12	49.34	49.28	49.25	48.98	49.47	49.65
TiO_2	1.41	1.43	1.60	1.39	1.64	1.53	1.40	1.41	1.56	1.61	1.61	1.20	1.46	1.41	1.43	1.46	1.41	1.68
Al_2O_3	15.01	15.03	14.58	15.17	14.25	15.06	15.07	15.29	14.42	14.43	14.45	15.97	14.96	15.13	14.77	14.84	14.96	13.99
FeO^t	10.46	10.83	11.01	10.88	11.61	10.89	10.68	10.94	11.85	11.71	11.87	9.91	10.69	10.92	10.93	10.92	10.80	11.91
MnO	0.13	0.15	0.17	0.10	0.20	0.17	0.13	0.21	0.16	0.22	0.21	0.18	0.20	0.20	0.22	0.20	0.17	0.21
MgO	7.23	7.24	6.90	6.87	6.75	7.37	7.30	7.11	6.78	6.83	6.77	8.05	7.45	7.57	7.26	7.33	7.41	6.66
CaO	12.28	12.36	12.15	12.15	11.92	12.23	12.19	12.40	12.00	12.11	12.04	12.47	12.33	12.35	12.45	12.38	12.47	11.86
Na_2O	2.62	2.63	2.64	2.63	2.78	2.63	2.60	2.69	2.84	2.80	2.83	2.50	2.60	2.62	2.68	2.61	2.62	2.80
K_2O	0.142	0.159	0.132	0.147	0.132	0.167	0.143	0.142	0.149	0.144	0.146	0.106	0.167	0.137	0.143	0.167	0.148	0.154
P_2O_5	0.108	0.109	0.099	0.123	0.127	0.125	0.114	0.101	0.116	0.119	0.104	0.092	0.103	0.112	0.103	0.127	0.126	0.126
Cl	0.014	0.02	0.015	0.043	0.006	0.024	0.021	0.023	0.023	0.023	0.025	0.010	0.018	0.016	0.013	0.008	0.013	0.019
S	0.122	0.127	0.141	0.125	0.144	0.121	0.128	0.129	0.147	0.145	0.140	0.115	0.127	0.130	0.132	0.133	0.130	0.147
Total	98.63	98.94	98.38	98.65	99.33	99.25	99.09	99.62	99.76	99.32	99.50	99.73	99.44	99.87	99.39	99.15	99.73	99.22

Supplementary Table S1 continued.

Sample	T1009-VC1 19.0							T1009-VC2-18.0-									
	L2	L3	L4	L5	L6	L7	L8	D1	D2	D3	D4	D5	D6	D7	D8	D9	D10
SiO_2 (wt%)	49.62	49.28	49.16	48.89	49.57	48.90	49.03	50.44	50.45	50.33	50.32	50.36	50.31	50.53	50.53	50.40	50.33
TiO_2	1.53	1.46	1.63	1.43	1.63	1.47	1.38	1.54	1.46	1.39	1.45	1.50	1.45	1.51	1.59	1.42	1.49
Al_2O_3	14.37	14.59	13.88	14.66	14.04	14.70	14.95	14.72	14.92	15.03	14.86	14.86	14.94	14.39	14.32	14.89	14.77
FeO^t	11.56	10.67	11.75	10.88	11.96	10.79	10.91	10.64	10.77	10.79	10.60	10.72	10.80	11.58	11.74	10.63	10.79
MnO	0.28	0.15	0.24	0.21	0.27	0.18	0.20	0.210	0.240	0.218	0.235	0.206	0.243	0.224	0.264	0.252	0.151
MgO	7.12	7.16	6.68	7.22	6.81	7.36	7.36	7.28	7.44	7.52	7.44	7.35	7.40	7.06	6.92	7.43	7.48
CaO	12.36	11.90	11.81	12.14	11.74	12.27	12.27	12.39	12.40	12.37	12.22	12.31	12.37	12.19	11.95	12.32	12.36
Na_2O	2.70	2.64	2.77	2.65	2.81	2.45	2.62	2.76	2.65	2.61	2.64	2.63	2.67	2.77	2.79	2.67	2.64
K_2O	0.133	0.154	0.148	0.150	0.155	0.136	0.162	0.173	0.154	0.151	0.154	0.148	0.156	0.144	0.172	0.146	0.156
P_2O_5	0.114	0.090	0.139	0.106	0.145	0.098	0.090	0.119	0.113	0.115	0.107	0.123	0.110	0.120	0.121	0.110	0.109
Cl	0.015	0.026	0.018	0.028	0.022	0.017	0.015	0.023	0.013	0.012	0.018	0.014	0.018	0.023	0.027	0.013	0.015
S	0.125	0.134	0.128	0.126	0.141	0.121	0.132	0.134	0.129	0.123	0.121	0.125	0.125	0.137	0.136	0.127	0.128
Total	99.93	98.24	98.36	98.48	99.29	98.48	99.12	100.43	100.74	100.65	100.17	100.35	100.59	100.69	100.57	100.42	100.42

Sample	T1009-VC2-18.0-					T1009-VC6 upm									
	D11	D12	D13	D14	D15	D1	D2	D3	D4	D5	D6	D7	D8	D9	D10
SiO_2 (wt%)	50.17	50.43	50.38	50.23	50.56	50.41	50.53	50.22	50.54	50.61	49.58	50.63	50.10	50.43	49.56
TiO_2	1.44	1.52	1.47	1.41	1.45	1.60	1.42	1.37	1.56	1.62	0.93	1.52	1.11	1.29	0.91
Al_2O_3	14.89	14.40	14.95	14.94	14.91	14.34	15.00	14.99	14.47	14.43	17.01	14.45	16.15	15.32	17.02
FeO^t	10.55	11.49	10.82	10.61	10.75	11.71	10.66	10.73	11.62	11.81	8.82	11.47	9.72	10.39	8.98
MnO	0.199	0.209	0.210	0.197	0.216	0.208	0.196	0.216	0.213	0.214	0.174	0.200	0.173	0.180	0.165
MgO	7.34	7.06	7.36	7.54	7.39	6.84	7.49	7.50	7.00	6.93	9.22	7.01	8.30	7.64	9.22
CaO	12.34	12.10	12.30	12.51	12.38	12.10	12.32	12.35	12.16	12.04	12.58	12.10	12.78	12.54	12.72
Na_2O	2.64	2.74	2.66	2.63	2.60	2.82	2.67	2.65	2.70	2.87	2.17	2.75	2.38	2.67	2.20
K_2O	0.143	0.156	0.145	0.151	0.148	0.154	0.152	0.151	0.143	0.164	0.067	0.141	0.104	0.104	0.057
P_2O_5	0.110	0.118	0.108	0.107	0.116	0.124	0.109	0.106	0.122	0.119	0.064	0.122	0.089	0.081	0.064
Cl	0.026	0.026	0.021	0.026	0.013	0.024	0.011	0.016	0.026	0.023	0.009	0.026	0.013	0.018	0.005
S	0.122	0.135	0.130	0.118	0.125	0.146	0.132	0.118	0.137	0.139	0.101	0.135	0.109	0.120	0.105
Total	99.97	100.39	100.55	100.48	100.66	100.48	100.70	100.42	100.68	100.96	100.72	100.55	101.03	100.80	101.00

Supplementary Table S1 continued.

Sample	T1009-VC9 3.0-																	
	D1	D2	D3	D4	D5	D6	D7	D8	D9	D10	L1	L2	L3	L4	L5	L6	L7	L8
SiO_2 (wt%)	50.22	49.58	49.59	49.59	50.16	49.63	50.23	50.10	50.25	49.66	49.07	50.02	49.50	49.67	49.42	49.91	50.17	50.69
TiO_2	1.29	0.91	0.92	0.90	1.31	0.90	1.21	1.26	1.30	0.94	0.93	1.26	0.95	1.08	0.93	1.09	1.31	1.54
Al_2O_3	15.56	17.03	16.96	17.03	15.45	16.98	15.47	15.50	15.37	16.88	16.96	15.52	17.06	16.48	17.04	16.41	15.40	14.53
FeO^t	10.22	8.81	9.08	8.82	10.29	8.83	10.41	10.32	10.50	9.05	9.07	10.20	8.94	9.62	8.95	9.72	10.32	11.56
MnO	0.221	0.139	0.169	0.153	0.175	0.169	0.214	0.200	0.193	0.152	0.163	0.180	0.198	0.172	0.142	0.209	0.183	0.250
MgO	7.87	9.23	9.23	9.23	7.95	9.17	7.77	7.77	7.78	9.21	9.40	8.00	9.28	8.63	9.06	8.50	7.80	6.98
CaO	12.45	12.63	12.64	12.67	12.47	12.69	12.49	12.41	12.41	12.61	12.49	12.51	12.56	12.36	12.51	12.60	12.58	12.20
Na_2O	2.51	2.19	2.20	2.17	2.48	2.19	2.52	2.54	2.53	2.20	2.517	2.521	2.175	2.302	2.222	2.300	2.574	2.738
K_2O	0.104	0.058	0.063	0.068	0.128	0.067	0.107	0.119	0.112	0.071	0.08	0.11	0.06	0.10	0.07	0.10	0.11	0.15
P_2O_5	0.084	0.058	0.063	0.057	0.099	0.066	0.091	0.089	0.089	0.064	0.070	0.089	0.072	0.085	0.054	0.072	0.085	0.115
Cl	0.012	0.023	0.005	0.006	0.013	0.008	0.022	0.016	0.014	0.004	0.052	0.015	0.005	0.008	0.012	0.009	0.014	0.025
S	0.122	0.101	0.101	0.105	0.122	0.095	0.112	0.119	0.121	0.103	0.102	0.117	0.104	0.112	0.101	0.106	0.123	0.135
Total	100.66	100.76	101.02	100.78	100.63	100.80	100.64	100.44	100.66	100.95	100.91	100.54	100.90	100.61	100.51	101.02	100.66	100.94

Sample	T1009-VC9 3.0-			T1009-VC9 14.7-														
	L9	L10	L11	D1	D2	D3	D4	D5	D6	D7	D8	D9	D10	D11	D12	D13	D14	
SiO_2 (wt%)	49.47	50.43	49.62	49.27	49.28	49.40	49.33	49.15	49.07	49.26	49.15	48.24	48.91	48.92	49.08	48.92	48.91	
TiO_2	0.90	1.29	0.92	1.39	1.41	1.42	1.42	1.39	1.37	1.59	1.39	0.91	1.38	1.40	1.39	1.38	1.43	
Al_2O_3	16.83	15.47	16.93	14.98	14.94	14.81	14.81	14.94	14.93	14.29	14.91	16.86	14.89	14.79	14.81	14.88	14.81	
FeO^t	8.84	10.48	8.99	10.90	10.81	10.78	10.96	10.98	10.86	11.86	10.73	8.92	10.73	10.93	10.85	10.90	10.89	
MnO	0.173	0.200	0.154	0.226	0.199	0.199	0.168	0.194	0.207	0.206	0.202	0.175	0.211	0.212	0.211	0.179	0.179	
MgO	9.34	7.79	9.17	7.53	7.46	7.40	7.36	7.52	7.49	6.64	7.46	9.26	7.40	7.48	7.43	7.46	7.34	
CaO	12.55	12.57	12.53	12.48	12.36	12.41	12.42	12.41	12.33	11.95	12.33	12.60	12.35	12.36	12.32	12.32	12.50	
Na_2O	2.185	2.572	2.228	2.64	2.63	2.63	2.67	2.66	2.60	2.79	2.60	2.15	2.58	2.61	2.67	2.61	2.59	
K_2O	0.06	0.10	0.06	0.144	0.143	0.153	0.147	0.146	0.148	0.150	0.146	0.064	0.148	0.135	0.146	0.139	0.148	
P_2O_5	0.060	0.092	0.061	0.116	0.113	0.098	0.104	0.118	0.124	0.118	0.101	0.064	0.109	0.102	0.106	0.111	0.108	
Cl	0.018	0.013	0.006	0.017	0.018	0.014	0.021	0.018	0.015	0.023	0.017	0.005	0.016	0.014	0.031	0.015	0.013	
S	0.099	0.125	0.104	0.134	0.126	0.132	0.130	0.130	0.130	0.145	0.132	0.109	0.130	0.130	0.130	0.132	0.131	
Total	100.53	101.14	100.77	99.83	99.50	99.44	99.54	99.66	99.27	99.02	99.16	99.35	98.86	99.07	99.17	99.05	99.05	

Supplementary Table S1 continued.

Sample	T1009-VC9 14.7-															
	D15	L1	L2	L3	L4	L5	L6	L7	L8	L9	L10	L11	L12	L13	L14	L15
SiO_2 (wt%)	48.93	50.41	50.34	50.09	50.31	50.33	50.21	50.39	50.17	50.38	50.22	50.13	50.44	50.43	50.33	50.31
TiO_2	1.42	1.44	1.41	1.40	1.37	1.39	1.39	1.45	1.39	1.44	1.45	1.47	1.57	1.46	1.43	1.42
Al_2O_3	14.84	15.04	14.86	14.94	15.02	15.10	15.07	15.09	15.08	15.07	15.05	15.24	14.49	15.03	14.88	15.04
FeO^t	10.70	10.64	10.62	10.71	10.72	10.81	10.76	10.78	10.58	10.75	10.81	10.78	11.28	10.79	10.82	10.79
MnO	0.175	0.207	0.191	0.198	0.210	0.189	0.201	0.209	0.220	0.181	0.187	0.192	0.161	0.220	0.190	0.196
MgO	7.39	7.41	7.39	7.50	7.47	7.56	7.51	7.54	7.49	7.55	7.48	7.55	6.91	7.43	7.48	7.56
CaO	12.32	12.30	12.32	12.33	12.34	12.36	12.31	12.39	12.37	12.26	12.33	12.27	12.04	12.34	12.40	12.40
Na_2O	2.62	2.67	2.65	2.65	2.64	2.65	2.66	2.68	2.66	2.63	2.66	2.64	2.77	2.64	2.71	2.66
K_2O	0.152	0.147	0.160	0.137	0.134	0.135	0.136	0.152	0.151	0.152	0.129	0.135	0.146	0.163	0.153	0.152
P_2O_5	0.108	0.111	0.111	0.120	0.104	0.111	0.108	0.110	0.105	0.114	0.112	0.118	0.115	0.110	0.116	0.116
Cl	0.016	0.022	0.021	0.021	0.024	0.017	0.017	0.016	0.015	0.016	0.019	0.014	0.022	0.018	0.025	0.016
S	0.133	0.120	0.125	0.110	0.121	0.123	0.124	0.123	0.125	0.121	0.124	0.127	0.136	0.122	0.124	0.121
Total	98.81	100.52	100.19	100.20	100.44	100.78	100.50	100.94	100.35	100.66	100.58	100.67	100.08	100.74	100.66	100.76

Sample	T1009-PC5 0.0-										T1009-PC5 6.0-						
	D1	D2	D3	D4	D5	D6	D7	D8	D9	D10	D1	D2	D3	D4	D5	D6	D7
SiO_2 (wt%)	49.84	50.04	49.86	49.78	49.91	49.73	49.79	49.69	49.84	49.91	49.61	50.48	50.19	50.30	50.03	50.14	50.23
TiO_2	1.53	1.43	1.41	1.47	1.54	1.47	1.49	1.48	1.47	1.49	1.33	1.25	1.59	1.50	1.25	1.54	1.48
Al_2O_3	14.58	14.64	14.57	14.58	14.33	14.55	14.45	14.53	14.62	14.54	15.75	15.05	14.19	14.27	15.68	14.33	14.34
FeO^t	10.70	10.73	10.67	10.90	11.37	10.80	11.28	10.74	10.73	10.75	10.17	10.25	11.70	11.63	9.91	11.50	11.60
MnO	0.19	0.23	0.19	0.21	0.24	0.19	0.21	0.24	0.17	0.22	0.18	0.19	0.17	0.24	0.17	0.20	0.25
MgO	7.19	7.27	7.26	7.29	6.89	7.34	6.91	7.31	7.30	7.27	8.01	7.88	6.90	6.99	8.11	7.06	7.05
CaO	12.33	12.31	12.40	12.43	12.07	12.37	12.34	12.37	12.36	12.43	12.36	12.52	12.12	12.14	12.60	12.19	12.25
Na_2O	2.73	2.69	2.69	2.72	2.74	2.65	2.73	2.70	2.68	2.73	2.61	2.59	2.77	2.68	2.51	2.74	2.74
K_2O	0.17	0.16	0.18	0.18	0.19	0.17	0.16	0.18	0.18	0.16	0.102	0.090	0.152	0.150	0.110	0.142	0.141
P_2O_5	0.11	0.10	0.10	0.11	0.12	0.13	0.10	0.11	0.10	0.13	0.095	0.082	0.115	0.113	0.102	0.121	0.108
Cl	0.02	0.02	0.02	0.02	0.03	0.02	0.03	0.03	0.02	0.02	0.011	0.006	0.029	0.024	0.013	0.025	0.024
S	0.143	0.139	0.134	0.141	0.142	0.134	0.133	0.135	0.139	0.143	0.122	0.126	0.145	0.144	0.122	0.140	0.145
Total	99.53	99.76	99.49	99.83	99.58	99.56	99.65	99.52	99.61	99.79	100.34	100.51	100.07	100.18	100.59	100.15	100.35

Supplementary Table S1 continued.

Sample	T1009-PC5 6.0-			T1009-PC5 10.5-										T1009-PC5 15.2-		
	D8	D9	D10	D1	D2	D3	D4	D5	D6	D7	D8	D9	D10	D1	D2	D3
SiO_2 (wt%)	49.03	48.96	49.18	49.48	49.78	49.80	48.95	48.93	48.60	49.04	48.84	48.83	49.69	49.79	49.81	49.80
TiO_2	0.88	0.89	0.90	1.10	1.29	1.58	0.92	0.92	0.90	0.92	0.94	1.05	1.57	1.55	1.58	1.56
Al_2O_3	16.92	16.84	16.94	16.05	14.93	14.55	16.72	16.60	16.63	16.57	16.71	16.16	14.41	14.36	14.24	14.28
FeO^t	9.00	9.00	8.98	9.68	10.76	11.15	9.02	8.94	9.04	9.12	9.15	9.49	11.14	11.39	11.60	11.73
MnO	0.14	0.14	0.14	0.20	0.21	0.20	0.17	0.16	0.19	0.15	0.17	0.15	0.22	0.22	0.25	0.21
MgO	9.24	9.29	9.34	8.75	8.11	7.26	9.32	9.16	9.22	9.26	9.16	8.64	7.08	6.91	6.76	6.80
CaO	12.68	12.61	12.67	12.62	12.55	12.29	12.47	12.70	12.76	12.75	12.77	12.59	12.14	12.19	12.11	11.97
Na_2O	2.16	2.18	2.15	2.31	2.54	2.69	2.18	2.15	2.15	2.21	2.19	2.26	2.71	2.71	2.81	2.79
K_2O	0.063	0.056	0.061	0.100	0.134	0.174	0.060	0.058	0.074	0.064	0.075	0.105	0.200	0.14	0.14	0.14
P_2O_5	0.051	0.058	0.069	0.059	0.094	0.109	0.058	0.052	0.067	0.056	0.051	0.077	0.123	0.13	0.11	0.12
Cl	0.004	0.005	0.004	0.010	0.015	0.036	0.007	0.014	0.006	0.020	0.005	0.008	0.026	0.03	0.03	0.03
S	0.110	0.108	0.106	0.119	0.125	0.138	0.110	0.101	0.105	0.110	0.103	0.114	0.136	0.136	0.152	0.139
Total	100.29	100.13	100.53	100.48	100.53	99.97	99.98	99.78	99.74	100.27	100.16	99.46	99.44	99.54	99.60	99.57

Sample	T1009-PC5 15.2-							T1009-PC5 20.3							
	D4	D5	D6	D7	D8	D9	D10	L1	L2	L3	L4	L5	L6	L7	L8
SiO_2 (wt%)	49.93	49.76	49.78	48.95	49.73	49.98	49.96	49.70	49.18	49.52	49.68	49.50	49.41	49.55	49.33
TiO_2	1.55	1.59	1.49	1.56	1.58	1.56	1.51	1.56	1.50	1.59	1.57	1.55	1.59	1.43	1.57
Al_2O_3	14.28	14.34	14.30	14.18	14.27	14.30	14.28	14.37	15.22	14.50	14.36	14.60	14.39	14.86	14.44
FeO^t	11.72	11.84	11.44	11.77	11.72	11.54	11.47	11.61	11.04	11.70	11.71	11.99	11.72	11.10	11.68
MnO	0.25	0.22	0.22	0.20	0.24	0.24	0.22	0.23	0.19	0.23	0.20	0.18	0.21	0.20	0.19
MgO	6.86	6.79	7.00	6.85	6.73	6.82	6.99	6.76	7.39	6.64	6.75	6.51	6.86	7.17	6.74
CaO	12.02	12.03	12.22	12.02	11.92	12.09	12.23	11.97	12.14	11.94	12.08	11.95	12.12	12.47	11.99
Na_2O	2.80	2.78	2.67	2.84	2.78	2.76	2.68	2.83	2.71	2.88	2.77	2.84	2.81	2.75	2.82
K_2O	0.14	0.16	0.14	0.14	0.17	0.14	0.14	0.151	0.160	0.168	0.164	0.161	0.163	0.140	0.147
P_2O_5	0.11	0.12	0.12	0.11	0.11	0.11	0.12	0.117	0.111	0.124	0.115	0.122	0.119	0.104	0.114
Cl	0.03	0.02	0.03	0.03	0.03	0.03	0.03	0.019	0.018	0.016	0.019	0.027	0.021	0.018	0.024
S	0.143	0.146	0.152	0.142	0.150	0.143	0.153	0.143	0.128	0.138	0.143	0.141	0.143	0.129	0.144
Total	99.84	99.79	99.56	98.79	99.43	99.72	99.79	99.48	99.78	99.46	99.57	99.58	99.57	99.91	99.18

Supplementary Table S1 continued.

Sample	T1010-VC15 17.1-																	
	D1	D2	D3	D4	D5	D6	D7	D8	D9	D10	D11	D12	D13	D14	D15	L1	L2	L3
SiO_2 (wt%)	49.62	49.23	49.33	49.29	49.89	50.07	49.12	49.93	48.86	48.76	49.72	49.18	48.77	49.06	49.27	49.63	50.18	49.47
TiO_2	1.41	1.30	1.26	1.27	1.51	1.47	1.26	1.44	1.31	1.29	1.41	1.45	1.26	1.25	1.25	1.28	1.56	1.25
Al_2O_3	14.77	15.97	15.84	15.98	14.43	14.37	15.89	14.86	15.94	15.91	14.91	15.09	16.03	16.06	15.95	16.16	15.19	16.00
FeO^t	10.72	9.97	9.98	9.92	11.25	11.09	9.99	10.88	10.25	10.15	10.81	10.76	9.91	9.87	9.95	9.78	10.66	9.91
MnO	0.20	0.19	0.22	0.19	0.25	0.21	0.21	0.23	0.19	0.22	0.24	0.18	0.18	0.17	0.19	0.187	0.213	0.162
MgO	7.41	8.30	8.20	8.35	7.24	7.21	8.16	7.30	8.44	8.32	7.40	7.57	8.22	8.28	8.27	8.12	7.44	8.56
CaO	12.37	12.21	12.22	12.18	12.37	12.24	12.15	12.38	12.37	12.25	12.22	12.04	12.14	12.10	12.17	12.37	12.07	12.23
Na_2O	2.63	2.59	2.60	2.59	2.68	2.70	2.63	2.71	2.56	2.57	2.68	2.68	2.60	2.66	2.63	2.58	2.80	2.59
K_2O	0.130	0.116	0.117	0.093	0.156	0.152	0.101	0.126	0.107	0.112	0.129	0.160	0.109	0.108	0.122	0.134	0.201	0.132
P_2O_5	0.139	0.105	0.105	0.110	0.135	0.109	0.104	0.129	0.103	0.100	0.114	0.115	0.100	0.108	0.106	0.097	0.115	0.087
Cl	0.018	0.009	0.014	0.009	0.028	0.010	0.018	0.029	0.009	0.014	0.017	0.016	0.013	0.015	0.008	0.009	0.014	0.012
S	0.131	0.120	0.120	0.113	0.142	0.135	0.116	0.127	0.110	0.115	0.122	0.137	0.120	0.117	0.123	0.110	0.125	0.114
Total	99.54	100.11	100.02	100.10	100.09	99.77	99.75	100.15	100.24	99.81	99.76	99.38	99.45	99.81	100.04	100.47	100.58	100.50

Sample	T1010-VC15 17.1-								T1010-PC2 2.5-								
	L4	L5	L6	L7	L8	L9	L10	L11	D1	D2	D3	D4	D5	D6	D7	D8	D9
SiO_2 (wt%)	49.24	49.67	50.13	50.13	49.50	49.36	49.96	49.51	50.14	49.82	49.39	49.57	49.07	49.00	49.14	48.88	48.85
TiO_2	1.23	1.27	1.41	1.40	1.25	1.25	1.39	1.26	1.27	1.48	1.29	1.39	1.47	1.44	1.26	1.24	1.29
Al_2O_3	16.63	16.12	15.00	15.00	16.12	16.07	15.06	16.14	16.52	15.96	16.32	15.11	15.83	15.61	16.03	16.44	15.95
FeO^t	9.76	9.79	10.68	10.72	10.00	9.79	10.73	10.00	9.95	10.06	10.00	10.82	10.41	10.22	9.94	9.81	9.94
MnO	0.184	0.171	0.202	0.193	0.155	0.192	0.181	0.179	0.19	0.23	0.19	0.21	0.20	0.19	0.17	0.19	0.19
MgO	8.34	8.15	7.45	7.28	8.10	8.13	7.22	8.09	8.26	7.96	8.25	7.40	7.82	7.79	8.18	8.38	8.21
CaO	12.28	12.32	12.29	12.42	12.30	12.26	12.40	12.26	12.09	11.77	12.21	12.28	12.10	12.07	12.19	12.23	12.20
Na_2O	2.46	2.61	2.64	2.63	2.59	2.62	2.66	2.61	2.62	2.82	2.57	2.62	2.94	2.86	2.52	2.45	2.57
K_2O	0.139	0.127	0.138	0.131	0.124	0.118	0.144	0.125	0.121	0.165	0.119	0.143	0.109	0.111	0.119	0.142	0.135
P_2O_5	0.095	0.102	0.107	0.097	0.099	0.099	0.107	0.096	0.094	0.129	0.096	0.102	0.107	0.103	0.102	0.100	0.089
Cl	0.010	0.008	0.012	0.020	0.009	0.018	0.020	0.009	0.009	0.014	0.011	0.018	0.016	0.014	0.015	0.010	0.011
S	0.120	0.110	0.125	0.118	0.115	0.108	0.123	0.113	0.122	0.126	0.121	0.133	0.132	0.128	0.122	0.123	0.114
Total	100.49	100.44	100.20	100.15	100.36	100.02	100.00	100.39	101.40	100.54	100.55	99.80	100.21	99.53	99.79	100.00	99.56

Supplementary Table S1 continued.

Sample	T1010-PC2 2.5																	
	D10	D11	D12	D13	D14	L1	L2	L3	L4	L5	L6	L7	L8	L9	L10	L11	L12	L13
SiO_2 (wt%)	49.77	49.78	49.26	49.20	49.04	48.80	48.81	49.02	49.43	49.38	48.81	49.51	49.12	48.70	49.63	49.30	48.87	48.81
TiO_2	1.58	1.59	1.28	1.26	1.28	1.26	1.27	1.61	1.39	1.39	1.47	1.58	1.38	1.25	1.56	1.57	1.27	1.51
Al_2O_3	14.47	14.45	16.01	16.00	15.93	15.99	16.10	15.21	14.92	15.04	15.65	14.52	14.85	15.98	14.39	15.29	16.07	15.31
FeO^t	11.30	11.16	9.93	9.91	10.03	9.97	10.02	10.65	10.74	10.88	10.39	11.25	10.89	10.02	11.06	10.72	10.01	10.57
MnO	0.23	0.22	0.18	0.16	0.19	0.20	0.18	0.17	0.19	0.23	0.20	0.23	0.19	0.17	0.19	0.21	0.18	0.21
MgO	7.11	7.12	8.10	8.21	8.21	8.27	8.19	7.39	7.34	7.26	7.77	7.09	7.30	8.24	7.06	7.13	8.18	7.36
CaO	12.12	12.15	12.33	12.27	12.34	12.36	12.31	12.14	12.35	12.40	12.14	12.18	12.37	12.39	12.14	12.14	12.24	12.06
Na_2O	2.76	2.78	2.53	2.52	2.54	2.51	2.58	3.03	2.62	2.59	2.92	2.81	2.62	2.56	2.75	3.05	2.58	2.86
K_2O	0.192	0.197	0.127	0.126	0.119	0.124	0.126	0.120	0.153	0.149	0.119	0.186	0.146	0.128	0.202	0.122	0.130	0.163
P_2O_5	0.126	0.122	0.091	0.102	0.093	0.104	0.094	0.115	0.108	0.110	0.102	0.136	0.111	0.099	0.131	0.118	0.090	0.125
Cl	0.042	0.044	0.015	0.011	0.011	0.009	0.010	0.017	0.027	0.023	0.015	0.046	0.027	0.010	0.047	0.036	0.017	0.032
S	0.142	0.141	0.120	0.115	0.118	0.121	0.119	0.133	0.127	0.132	0.130	0.140	0.129	0.119	0.139	0.135	0.119	0.127
Total	99.84	99.75	99.96	99.89	99.90	99.71	99.82	99.61	99.40	99.59	99.71	99.69	99.13	99.67	99.31	99.83	99.76	99.14

Sample		T1010-PC2 10.2-															
	L14	D1	D2	D3	D4	D5	D6	D7	D8	D9	D10	D11	D12	D13	D14	L1	L2
SiO_2 (wt%)	49.07	48.47	48.51	48.77	48.40	48.86	48.81	48.15	48.64	49.80	48.11	48.47	48.81	48.40	48.33	48.94	49.08
TiO_2	1.41	1.20	1.30	1.32	1.19	1.25	1.45	1.24	1.23	1.69	1.32	1.24	1.27	1.23	1.21	1.29	1.28
Al_2O_3	15.01	16.77	16.37	16.18	16.72	16.33	15.93	16.66	16.63	14.41	17.51	16.84	16.43	16.88	16.62	16.29	16.28
FeO^t	10.83	9.95	10.05	10.19	9.81	9.83	10.08	9.87	9.71	11.95	9.09	9.97	9.89	9.79	9.81	10.06	10.05
MnO	0.19	0.19	0.19	0.18	0.21	0.22	0.21	0.15	0.19	0.21	0.20	0.19	0.20	0.18	0.16	0.20	0.18
MgO	7.31	8.41	8.26	8.05	8.47	8.23	7.93	8.42	8.43	6.72	8.68	8.40	8.14	8.42	8.43	8.30	8.25
CaO	12.43	12.38	12.28	12.28	12.41	12.16	11.87	12.11	12.27	11.88	12.08	12.22	12.36	12.27	12.27	12.35	12.40
Na_2O	2.65	2.39	2.60	2.63	2.46	2.58	2.78	2.47	2.45	2.80	2.72	2.48	2.58	2.47	2.44	2.56	2.58
K_2O	0.150	0.137	0.126	0.115	0.145	0.118	0.180	0.131	0.138	0.187	0.091	0.128	0.120	0.130	0.137	0.111	0.106
P_2O_5	0.106	0.091	0.093	0.105	0.101	0.093	0.115	0.102	0.094	0.131	0.096	0.104	0.107	0.100	0.093	0.108	0.110
Cl	0.027	0.010	0.011	0.023	0.010	0.009	0.013	0.012	0.009	0.019	0.008	0.010	0.010	0.010	0.009	0.015	0.013
S	0.124	0.116	0.119	0.119	0.117	0.123	0.124	0.125	0.118	0.150	0.108	0.120	0.118	0.126	0.118	0.122	0.118
Total	99.32	100.10	99.92	99.96	100.04	99.79	99.49	99.44	99.92	99.94	100.00	100.16	100.05	100.02	99.62	100.36	100.46

Supplementary Table S1 continued.

Sample	T1010-PC2 10.2-									T1010-PC2 16.1-							
	L3	L4	L5	L6	L7	L8	L9	L10	L11	D1	D2	D3	D4	D5	D6	D7	D8
SiO_2 (wt%)	48.43	48.92	49.29	48.47	49.23	49.39	49.41	48.70	48.66	48.85	49.16	49.15	49.22	48.73	49.48	49.00	49.32
TiO_2	1.21	1.26	1.36	1.27	1.52	1.56	1.53	1.27	1.20	1.37	1.43	1.38	1.51	1.24	1.36	1.43	1.44
Al_2O_3	16.67	16.40	15.13	16.62	15.32	15.33	15.38	16.21	16.78	15.15	15.08	15.00	14.85	16.28	15.27	15.19	15.12
FeO^t	9.97	9.98	10.95	9.80	10.47	10.70	10.76	9.98	9.88	10.89	10.78	10.94	11.06	9.89	11.00	10.84	10.73
MnO	0.18	0.19	0.21	0.17	0.19	0.22	0.17	0.19	0.18	0.20	0.21	0.18	0.22	0.16	0.20	0.17	0.19
MgO	8.46	8.29	7.40	8.39	7.53	7.56	7.53	8.22	8.45	7.50	7.36	7.30	7.22	8.28	7.40	7.48	7.29
CaO	12.53	12.38	12.50	12.38	12.29	12.21	12.14	12.43	12.49	12.39	12.46	12.49	12.41	12.40	12.53	12.55	12.44
Na_2O	2.46	2.53	2.65	2.45	2.69	2.73	2.77	2.61	2.45	2.64	2.62	2.62	2.69	2.61	2.60	2.60	2.59
K_2O	0.120	0.107	0.119	0.126	0.168	0.160	0.174	0.106	0.123	0.117	0.129	0.138	0.123	0.116	0.130	0.136	0.115
P_2O_5	0.117	0.102	0.114	0.114	0.144	0.140	0.133	0.105	0.099	0.117	0.117	0.130	0.123	0.102	0.123	0.122	0.131
Cl	0.011	0.010	0.023	0.011	0.012	0.012	0.013	0.014	0.011	0.015	0.020	0.020	0.024	0.012	0.015	0.014	0.020
S	0.121	0.118	0.128	0.116	0.130	0.133	0.135	0.118	0.122	0.124	0.130	0.131	0.141	0.122	0.133	0.123	0.128
Total	100.28	100.29	99.88	99.92	99.70	100.13	100.14	99.95	100.44	99.36	99.49	99.49	99.58	99.94	100.24	99.66	99.52

Sample	T1010-PC2 16.1-																
	D9	D10	D11	D12	D13	D14	D15	L1	L2	L3	L4	L5	L6	L7	L8	L9	L10	L11
SiO_2 (wt%)	49.78	48.91	49.27	48.88	48.75	49.03	49.14	49.57	49.61	49.06	49.27	49.38	48.43	48.97	48.84	49.45	49.08	48.99
TiO_2	1.45	1.49	1.40	1.38	1.23	1.39	1.39	1.39	1.40	1.40	1.45	1.41	1.18	1.26	1.29	1.38	1.29	1.26
Al_2O_3	15.05	15.03	15.25	15.20	16.25	15.17	15.08	15.15	15.18	15.04	15.17	15.28	16.70	16.27	16.40	15.27	16.24	16.28
FeO^t	10.86	11.21	10.97	10.91	10.07	10.87	10.93	10.93	10.90	11.06	10.79	10.90	9.87	10.05	9.89	10.92	10.13	9.94
MnO	0.20	0.23	0.22	0.20	0.16	0.25	0.20	0.24	0.21	0.20	0.19	0.23	0.20	0.18	0.17	0.19	0.19	0.19
MgO	7.35	7.24	7.41	7.46	8.25	7.35	7.38	7.33	7.37	7.34	7.25	7.41	8.44	8.23	7.73	7.38	8.23	8.19
CaO	12.36	12.43	12.51	12.31	12.37	12.51	12.55	12.46	12.55	12.54	12.43	12.44	12.39	12.40	12.44	12.52	12.33	12.35
Na_2O	2.67	2.68	2.64	2.75	2.57	2.62	2.63	2.65	2.59	2.69	2.64	2.63	2.47	2.58	2.61	2.63	2.56	2.53
K_2O	0.138	0.149	0.130	0.119	0.108	0.126	0.128	0.121	0.121	0.131	0.130	0.133	0.115	0.111	0.110	0.131	0.108	0.109
P_2O_5	0.126	0.141	0.105	0.127	0.101	0.121	0.116	0.123	0.117	0.111	0.115	0.115	0.103	0.115	0.104	0.126	0.106	0.114
Cl	0.022	0.037	0.017	0.111	0.015	0.019	0.018	0.020	0.022	0.156	0.024	0.020	0.012	0.012	0.017	0.022	0.010	0.013
S	0.133	0.141	0.131	0.132	0.120	0.132	0.130	0.135	0.133	0.126	0.128	0.132	0.118	0.113	0.120	0.128	0.123	0.122
Total	100.14	99.69	100.07	99.59	100.00	99.59	99.70	100.11	100.20	99.86	99.59	100.09	100.01	100.29	99.71	100.14	100.40	100.09

Supplementary Table S1 continued.

Sample	T1010-PC2 16.1-				T1010-PC2 18.3-												
	L12	L13	L14	L15	D1	D2	D3	D4	D5	D6	D7	D8	D9	D10	D11	D12	L1
SiO_2 (wt%)	49.53	49.26	49.41	49.20	48.27	48.75	48.69	49.00	48.46	49.38	48.85	48.16	48.79	49.19	48.91	48.98	48.81
TiO_2	1.41	1.36	1.41	1.37	1.23	1.24	1.23	1.26	1.28	1.51	1.26	1.26	1.16	1.22	1.26	1.22	1.29
Al_2O_3	15.41	15.14	15.37	15.17	16.58	16.67	16.61	16.20	16.11	14.94	16.16	16.61	16.26	16.19	16.20	16.23	16.30
FeO^t	10.97	10.77	10.92	10.80	9.81	10.00	9.90	10.02	10.01	10.98	9.96	9.90	9.71	10.00	9.94	9.96	9.88
MnO	0.20	0.21	0.22	0.21	0.18	0.17	0.16	0.15	0.20	0.20	0.21	0.18	0.16	0.16	0.18	0.21	0.22
MgO	6.87	7.35	7.10	7.36	8.48	8.50	8.49	8.19	8.28	7.03	8.28	8.39	8.40	8.29	8.29	8.39	8.25
CaO	12.43	12.46	12.37	12.46	12.39	12.28	12.35	12.31	12.29	12.50	12.22	12.25	12.49	12.32	12.41	12.26	12.20
Na_2O	2.71	2.66	2.68	2.62	2.42	2.48	2.45	2.58	2.57	2.76	2.59	2.47	2.37	2.59	2.55	2.57	2.54
K_2O	0.130	0.138	0.124	0.115	0.144	0.154	0.135	0.128	0.140	0.150	0.127	0.131	0.113	0.145	0.120	0.123	0.141
P_2O_5	0.129	0.131	0.122	0.124	0.084	0.093	0.092	0.086	0.101	0.121	0.089	0.096	0.084	0.091	0.094	0.097	0.096
Cl	0.033	0.076	0.029	0.022	0.010	0.010	0.010	0.009	0.011	0.018	0.009	0.011	0.019	0.012	0.011	0.010	0.009
S	0.129	0.124	0.128	0.129	0.119	0.120	0.120	0.122	0.117	0.133	0.119	0.118	0.118	0.116	0.124	0.117	0.121
Total	99.94	99.69	99.88	99.58	99.71	100.48	100.24	100.06	99.57	99.72	99.88	99.58	99.68	100.33	100.08	100.16	99.86

Sample	T1010-PC2 18.3-									T1010-PC3 0.0-							
	L2	L3	L4	L5	L6	L7	L8	L9	L10	D1	D2	D3	D4	D5	D6	D7	D8
SiO_2 (wt%)	48.39	48.84	49.18	49.54	48.69	49.60	49.08	48.49	49.26	48.40	48.17	47.97	48.27	48.17	48.26	48.36	48.40
TiO_2	1.28	1.26	1.24	1.38	1.21	1.64	1.28	1.18	1.56	1.25	1.28	1.21	1.27	1.25	1.26	1.27	1.26
Al_2O_3	16.17	16.43	16.38	15.14	16.67	14.39	16.19	16.56	14.91	16.03	15.99	16.37	16.05	15.94	15.90	15.92	16.04
FeO^t	9.92	9.84	9.88	10.88	9.84	11.89	10.08	9.81	10.65	9.95	9.87	9.82	9.85	9.94	10.01	9.81	10.13
MnO	0.20	0.19	0.19	0.20	0.21	0.22	0.21	0.22	0.18	0.157	0.189	0.164	0.176	0.204	0.193	0.180	0.192
MgO	8.19	8.31	8.01	7.38	8.50	6.74	8.26	8.41	7.34	8.17	8.02	8.34	7.99	8.14	8.15	8.08	8.15
CaO	12.24	12.29	12.35	12.31	12.35	11.92	12.22	12.29	12.02	12.20	12.49	12.31	12.44	12.28	12.29	12.28	12.19
Na_2O	2.55	2.60	2.59	2.64	2.42	2.79	2.58	2.47	2.75	2.52	2.53	2.46	2.58	2.54	2.53	2.58	2.58
K_2O	0.126	0.132	0.117	0.154	0.119	0.180	0.134	0.131	0.205	0.122	0.129	0.119	0.118	0.125	0.120	0.126	0.115
P_2O_5	0.090	0.100	0.092	0.100	0.075	0.125	0.092	0.099	0.131	0.089	0.100	0.103	0.101	0.092	0.093	0.087	0.094
Cl	0.012	0.014	0.023	0.023	0.008	0.020	0.011	0.009	0.013	0.010	0.014	0.010	0.017	0.010	0.011	0.010	0.012
S	0.121	0.121	0.116	0.128	0.119	0.151	0.119	0.121	0.132	0.121	0.118	0.118	0.121	0.115	0.117	0.126	0.122
Total	99.28	100.14	100.16	99.89	100.21	99.68	100.25	99.81	99.16	99.02	98.90	98.99	98.98	98.80	98.92	98.83	99.28

Supplementary Table S1 continued.

Sample	T1010-PC3 0.0-															PC3 5.3-	
	D9	D10	D11	D12	D13	D14	D15	L1	L2	L3	L4	L5	L6	L7	L8	D1	D2
SiO_2 (wt%)	48.18	48.24	47.74	47.55	48.14	48.15	48.06	49.61	49.72	50.19	49.57	49.53	49.62	49.50	49.60	48.19	48.07
TiO_2	1.23	1.28	1.22	1.13	1.29	1.25	1.25	1.29	1.27	1.62	1.29	1.32	1.29	1.28	1.29	1.27	1.14
Al_2O_3	16.00	15.90	16.29	16.09	15.80	16.09	15.89	16.17	16.15	14.43	16.16	16.20	16.23	16.17	16.14	15.97	16.29
FeO^t	9.99	9.86	9.84	9.81	10.23	10.01	9.96	9.90	9.93	11.38	9.96	9.76	9.92	9.94	9.79	9.84	9.78
MnO	0.167	0.160	0.173	0.181	0.200	0.177	0.214	0.165	0.191	0.182	0.160	0.169	0.170	0.155	0.180	0.154	0.189
MgO	8.01	8.09	8.36	8.46	8.00	8.17	8.17	8.27	8.35	6.88	8.28	8.30	8.29	8.19	8.24	8.22	8.48
CaO	12.30	12.34	12.26	12.58	12.22	12.34	12.18	12.23	12.17	11.96	12.24	12.33	12.26	12.13	12.23	12.31	12.52
Na_2O	2.55	2.56	2.46	2.36	2.62	2.54	2.58	2.58	2.62	2.84	2.60	2.62	2.63	2.60	2.61	2.52	2.38
K_2O	0.131	0.134	0.125	0.093	0.117	0.124	0.118	0.121	0.121	0.156	0.122	0.119	0.132	0.125	0.123	0.120	0.113
P_2O_5	0.095	0.100	0.098	0.079	0.090	0.092	0.097	0.101	0.098	0.140	0.096	0.095	0.092	0.101	0.100	0.085	0.087
Cl	0.015	0.011	0.010	0.012	0.022	0.011	0.012	0.011	0.013	0.027	0.012	0.015	0.011	0.059	0.010	0.010	0.009
S	0.119	0.116	0.122	0.105	0.129	0.122	0.121	0.116	0.114	0.139	0.117	0.111	0.113	0.114	0.112	0.120	0.114
Total	98.78	98.80	98.68	98.46	98.87	99.07	98.65	100.57	100.74	99.94	100.62	100.58	100.76	100.36	100.41	98.81	99.17

Sample	PC3 5.3-												
	D3	D4	D5	D6	D7	D8	D9	D10	D11	D12	D13	D14	D15
SiO_2 (wt%)	48.17	48.23	48.12	48.16	48.11	48.04	48.17	47.53	48.18	48.26	48.15	48.04	48.11
TiO_2	1.25	1.25	1.22	1.06	1.23	1.12	1.26	1.36	1.25	1.25	1.25	1.26	1.27
Al_2O_3	15.96	16.01	15.96	16.19	16.02	16.22	15.91	16.59	15.91	16.01	15.93	16.03	15.91
FeO^t	9.99	10.00	10.02	9.57	10.00	9.62	9.82	9.77	10.01	10.00	10.03	9.99	10.03
MnO	0.172	0.166	0.187	0.160	0.173	0.180	0.170	0.158	0.176	0.210	0.158	0.154	0.195
MgO	8.16	8.22	8.20	8.58	8.19	8.49	8.19	8.21	8.12	8.13	8.16	8.16	8.15
CaO	12.28	12.33	12.29	12.57	12.37	12.45	12.22	12.01	12.34	12.18	12.23	12.33	12.23
Na_2O	2.55	2.59	2.56	2.30	2.51	2.35	2.53	2.73	2.55	2.59	2.54	2.59	2.57
K_2O	0.117	0.120	0.117	0.092	0.126	0.114	0.121	0.110	0.126	0.120	0.124	0.127	0.125
P_2O_5	0.097	0.100	0.092	0.078	0.076	0.078	0.092	0.107	0.094	0.092	0.095	0.099	0.090
Cl	0.011	0.009	0.011	0.010	0.011	0.011	0.010	0.017	0.012	0.008	0.008	0.010	0.008
S	0.117	0.122	0.116	0.117	0.123	0.121	0.119	0.114	0.118	0.123	0.115	0.120	0.119
Total	98.87	99.14	98.89	98.88	98.95	98.80	98.61	98.70	98.89	98.99	98.78	98.89	98.81

Supplementary Figure legends

Suppl. Figure S1 Cumulative grain size distributions of the volcaniclastic sediments. The units taken from the three sediment cores shown in the figure exemplify the general range of grain size distribution found in the deposits. For each unit, the depth relative to the recovered top of the corresponding core is given. Size fraction of $\Phi \geq 4$ are comprised of pyroclastic fragments with some biogenic clasts intermixed in the sections *Φ= 3-4*.

Suppl. Figure S2 Grain size distribution of selected volcaniclastic samples. Log-normal distributions (solid lines) were fit to the sample data points (solid symbols) using the programme DECOLOG (Borselli and Sarocchi, 2009). Data points for the size fraction Φ=5 (63 μm) include all fractions smaller than 63 μm. Calculated standard deviation and skewness of fine grained samples will be slightly biased, due to this overweightening.

Suppl. Figure S3 Compositional variability of each volcaniclastic sequence expressed as the standard deviation (1σ) of the MgO content. Individual sequences can show notable grain-to-grain variation. Angular fragments and limu o Pele fragments generally agree in composition.

Suppl. Figure S4 Correlation between the chondrite normalized rare earth element ratio $[La/Yb]_N$ and the incompatible major element ratio K_2O/TiO_2.

Supplementary Figures

Supplementary Figure S1

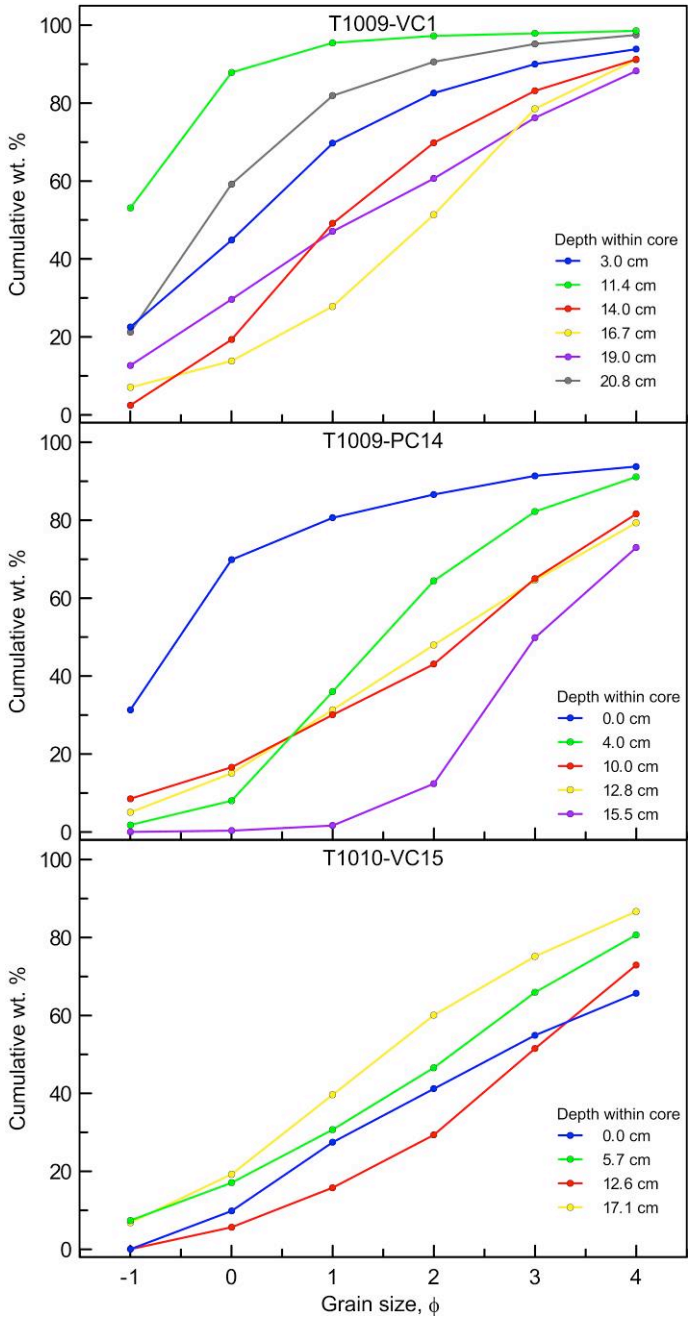

Supplementary Figure S2

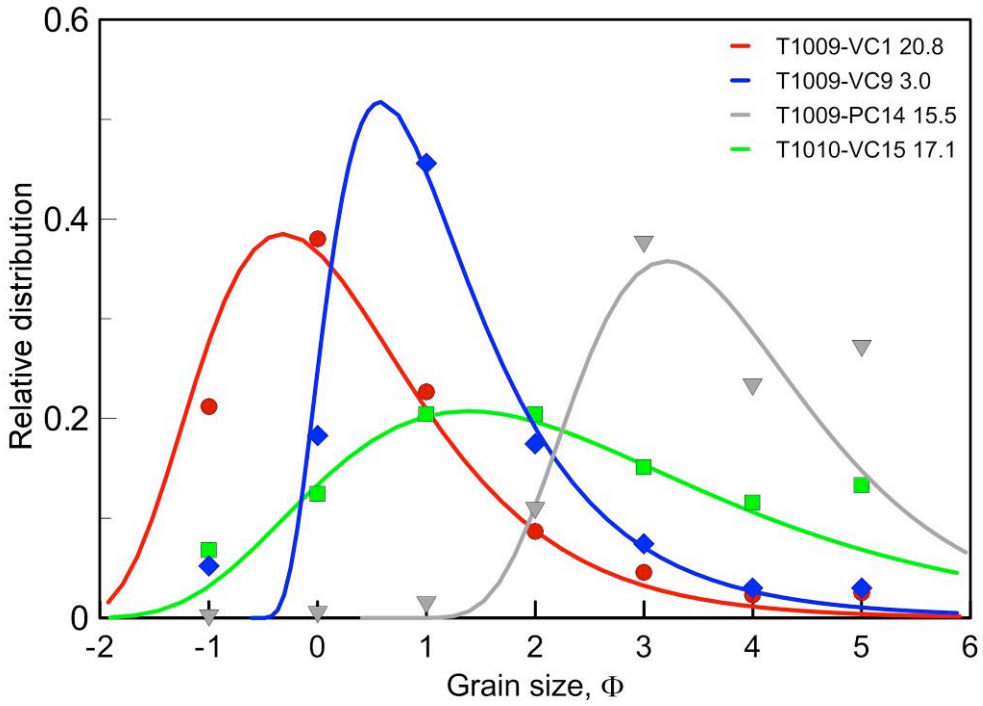

Supplementary Figure S3

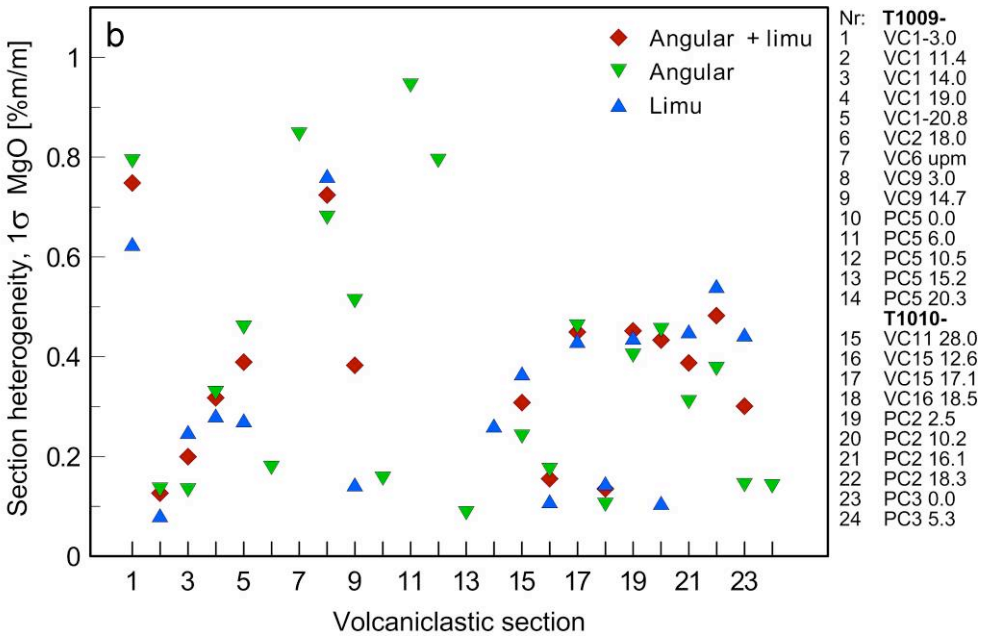

Supplementary Figure S4

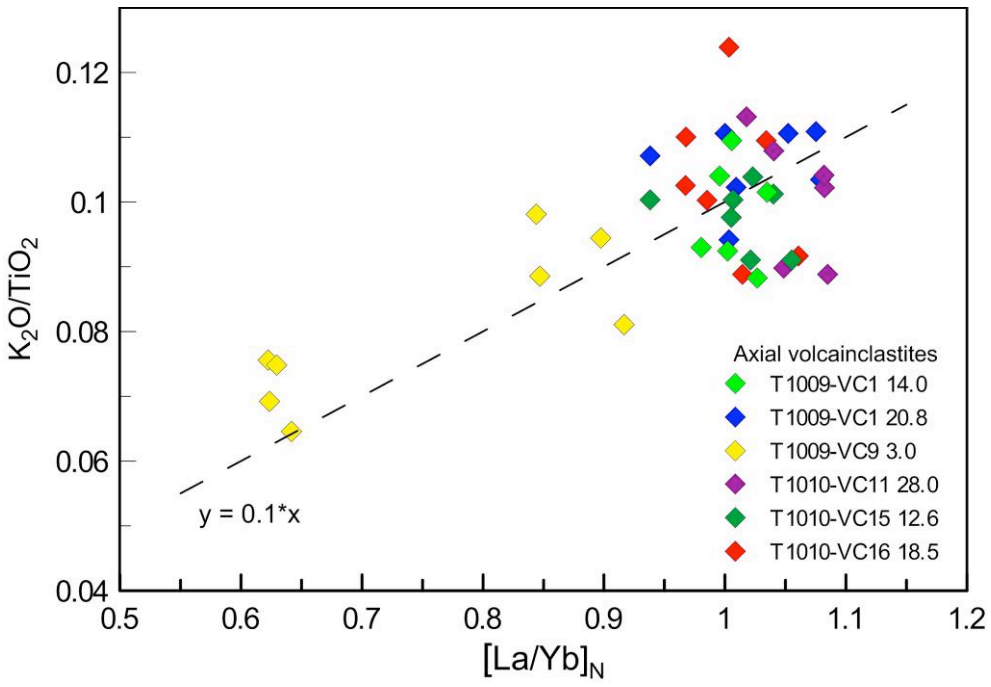

Bridge between Chapter 1 and Chapter 2:

In the preceding chapter, chemical analyses of volcaniclastic sections from Axial Seamount were used to draw a more comprehensive picture of the post-caldera history of the magmatic plumbing system and the chemical constitution of the mantle source beneath the Axial Seamount ridge segment. The sampled volcaniclastic deposits record a transitional phase of the system as indicated by the trace element signatures and the wide range of fractionation stages observed. The trace element signatures of the glass fragments and melt inclusions were used to show that individual melt parcels ascending within the melting region are heterogeneous, yet pooling at the top of the melting column is fairly efficient.

One of the most puzzling questions is the origin of these volcaniclastic deposits. As illustrated in the first chapter, the morphological and textural characteristics of the fragments strongly allude to a pyroclastic origin. This requires a substantial volatile budget and most likely the accumulation of a free gas phase within the reservoir. In order to explore this conjecture further, we have investigated the dissolved volatile concentrations in the melt inclusions, representing the pre-eruptive state, and in the glass fragments, representing the syn-/post-eruptive state, to arrive at a clearer picture of the volatile budget and the evolution of free gas phases within the magma reservoir and during eruptions.

Chapter 2. Explosive eruptions at mid-ocean ridges driven by CO_2-rich magmas

Christoph Helo[1], Marc-Antoine Longpré[1], Nobumichi Shimizu[2], David A. Clague[3], John Stix[1]

[1]*Department of Earth & Planetary Sciences, McGill University, 3450 University Street, Montreal H3A 2A7, Canada*

[2]*Woods Hole Oceanographic Institution, 266 Woods Hole Road, Woods Hole, MA 02543, USA*

[3]*Monterey Bay Aquarium Research Institute, 7700 Sandholdt Road, Moss Landing, CA 95039, USA*

Manuscript II – published as:

Helo, C., Longpré, M.-A., Shimizu, N., Clague, D.A., Stix, J., 2011. Explosive eruptions at mid-ocean ridges driven by CO_2-rich magmas. *Nature Geosciences* **4**, 260-263. doi:10.1038/ngeo1104. http://www.nature.com/ngeo/journal/v4/n4/full/ngeo1104.html

Abstract

The abundance of volatile compounds, and particularly CO_2, in the upper oceanic mantle affects the style of volcanic eruptions. At mid-ocean ridges, eruptions are generally dominated by the gentle effusion of basaltic lavas with a low volatile content. But, explosive volcanism has been documented at some ocean spreading centres[1-3], indicative of abundant volatile compounds. Estimates of the initial CO_2 concentration of primary magmas can be used to constrain the CO_2 content of the upper oceanic mantle, but these estimates vary greatly[4,5]. Here we present ion microprobe measurements of the CO_2 content of basaltic melt trapped in plagioclase crystals. The crystals are derived from volcanic ash deposits erupted explosively at Axial Seamount, Juan de Fuca Ridge, in the northeast Pacific Ocean. We report unusually high CO_2 concentrations of up to 9,160 ppm, which indicate that the upper oceanic mantle is more enriched in carbon than previously thought. And we furthermore suggest that CO_2 fluxes along mid-ocean ridges[4,5] vary significantly. Our results demonstrate that elevated fluxes of CO_2 from the upper oceanic mantle can drive explosive eruptions at mid-ocean ridges.

1. Introduction

Mid-ocean ridges (MOR) are the most active and voluminous volcanic systems on Earth, forming nearly 60 % of the Earth's crust. Owing to its large volume, MOR volcanism is a key contributor to the total CO_2 flux from the mantle to the Earth's surface. Recent work has documented the widespread existence of volcaniclastic ash deposits comprising basaltic glass fragments at MOR sites[1-3]. Although widely interpreted as primary products of submarine explosive eruptions[1,2,6], some researchers argue for

lava-seawater interaction[7,8]. Due to its low solubility, CO_2 is the only magmatic volatile phase undergoing significant exsolution as basaltic magma ascends to the seafloor[9], hence the only volatile which can drive explosive eruptions at these depths. Pyroclastic activity in MOR environments therefore is controlled by the primary CO_2 content of basaltic liquids, and consequently by the carbon budget of the mantle source. Initial CO_2 contents of variously enriched basalts from the Mid-Atlantic Ridge, including so-called "popping rock", are inferred to be between 660 and 57,600 ppm, based on their vesicularity and extent of carbon isotope fractionation[5,10]. However, such elevated CO_2 levels have never been measured directly. By contrast, dissolved CO_2 concentrations in vapour-undersaturated melt inclusions from an East Pacific Rise MOR basalt (MORB) suite, which are thought to represent the initial MORB volatile contents, show very low CO_2 contents of 44-244 ppm (ref. 4). This large discrepancy poses a significant problem to our understanding of CO_2 abundances in the MORB mantle and derived magmas.

2. Results

We analysed the dissolved volatile concentration of 47 melt inclusions entrapped in plagioclase (An_{81-91}) prior to eruption as well as host glass shards sampled from five pyroclastic ash sequences on Axial Seamount (Supplementary Tables S1, S2), to assess the pre-eruptive volatile inventory of the local MORB. The Axial caldera system is part of the intermediate-rate spreading Juan de Fuca Ridge (JdFR) between 45° 50' N and 46° N. A present-day magma reservoir is present at 2.5-6 km beneath the volcanic edifice[11]. Widespread ash deposits up to 2 m thick on the volcano's flanks include angular glass fragments, thin platy glass shards interpreted as bubble walls and termed limu o Pele

(Supplementary Fig. S1), and plagioclase phenocrysts. This volcanic ash is evidence for explosive activity accompanying effusive lava flows.

The melt inclusions are generally more primitive (7.85 to 10.85 wt % MgO) and more variable in their trace element composition than the host glass (Supplementary Fig. S2a, Supplementary Tables S1, S3). Incompatible trace element compositions (Supplementary Fig. S2b) fall within the overall range of JdFR basalts[12] indicating some variations in the mantle source chemistry. The melt inclusions exhibit an extremely large range of CO_2 concentrations, from 262 ppm up to 9,159 ppm (Fig. 1), with ~30 % of the inclusions >1,000 ppm ("high-CO_2" inclusions). Corresponding saturation pressures range from ~ 60 MPa to 1.2 GPa (using ref. 13). These are the highest CO_2 concentrations ever measured in a MORB, and are consistent with previous predictions of initial, undegassed volatile contents of MORB liquids[5,10,14,15]. Variations of other volatile elements are much more restricted. H_2O concentrations are 0.12-0.38 wt %, S 825-1379 ppm , Cl 14 – 144 ppm, and F 74-222 ppm. For comparison, melt inclusions from similar volcaniclastic deposits at the Gakkel Ridge record lower CO_2 concentrations between 170-1600 ppm[16].

3. Discussion

Decompression degassing of CO_2-rich, H_2O-poor magma results in exsolution of CO_2 with restricted H_2O partitioning into the vapour phase[9]. Within CO_2-H_2O space, the melt inclusions define a vertical trend (Fig. 1), indicating volatile saturation and decompression degassing of CO_2-rich vapour from mantle to crustal depths (40 km to 2 km, calculated from the range of CO_2-H_2O saturation pressures, and a crustal density of

2,360 kg m^{-3}, ref. 17). H_2O variability exceeds that expected from purely degassing trends. The excellent positive correlation between H_2O and F in the melt inclusions (Fig. 2a) indicates their similar geochemical behaviour and a constant H_2O/F of the local mantle source of 14.3±0.1. Hence, the H_2O variability reflects some heterogeneity of the mantle source.

The ratio also allows us to assess post-eruptive alteration in MORBs, as hydration by seawater will cause the ratio to vary as a function of H_2O. Moreover, Cl/H_2O in the melt inclusions varies only as a function of Cl (Fig. 2b). Cl is accordingly assimilated within the magma reservoir, while H_2O is not. Figure 2 reveals that the host glasses show both hydration and Cl assimilation. Hence Cl/H_2O and H_2O/F combined can be used to assess both the degree of pre-eruptive Cl assimilation and post-eruptive seawater-alteration in MORBs.

During melting, volatiles such as CO_2 behave highly incompatibly and partition strongly into the melt phase, similar to elements such as Nb (ref. 4). The melt inclusion with the highest CO_2 concentration (9,159 ppm) is volatile-oversaturated at any pressure below 1.2 GPa (calculated using ref. 13). Subsequent evolution of primitive CO_2-rich melts, as they ascend from the upper mantle to the shallow magma reservoir, can be evaluated in terms of three conceptual CO_2 degassing scenarios. First, degassing during ascent in the mantle without crystallisation would not entrap high-CO_2 melts and can be ruled out. Second, the melt inclusions show no correlation between the degree of fractionation in terms of their Ca-number or Mg-number and CO_2 content (Supplementary Fig. S3), which would be expected for continuous coeval degassing and crystallisation of plagioclase or olivine during magma ascent in the mantle. We therefore

propose a third scenario where melt entrapment occurs over shallower mantle to crustal depths, in agreement with the calcic composition of the plagioclase crystals (Supplementary Table S4),which is commonly associated with crystallisation at lower pressures[18,19]. Following the model in ref. 19, melt is entrapped as magma rises through a calcic plagioclase-rich zone within the magma plumbing system. This implies that significant volatile exsolution is delayed during the ascent of melt batches from the deeper mantle, introducing strong degrees of supersaturation. The CO_2 bubble nucleation rate depends on the extent of supersaturation, with the degree of supersaturation necessary for bubble nucleation increasing at lower pressures as magma rises[20]. As the supersaturated magma arrives and stagnates at constant pressures within the magma reservoir system at ~6 km depth, it will then experience strong CO_2 exsolution. In a similar fashion, strong degrees of supersaturation are achieved during the ascent of magma from the reservoir to the seafloor, as clearly demonstrated by our CO_2 data from the host glasses (Fig. 1b) and previous studies[5,9].

Our documentation of high CO_2 levels in primitive MORB liquid has far-reaching implications. The data provide insights into the physical evolution of the magma as it passes through the mantle into the shallow reservoir and is then erupted. At saturation pressures of ~60 MPa corresponding to a crustal depth of 2 km (using ref. 17), at least 8800 ppm CO_2 have been exsolved from a magma initially containing 9,160 ppm CO_2, translating to a vesicularity of ~10 % of free vapour. At the ocean floor this increases to ~32-34 % vesicularity. Under these conditions, expanding bubbles rising within the conduit can coalesce and drive strombolian explosions. For conditions similar to Axial Seamount, ref. 21 models a maximum magma rise velocity of 0.5-2.0 m s^{-1} and a vent

width of 0.3-0.6 m for bubble coalescence to be achieved. Alternatively, bubbles could accumulate against the reservoir roof of the magma reservoir as a foam layer[22]. When a critical thickness of foam is reached, an eruption is triggered by foam collapse at the top of the reservoir, and gas slugs rise through the conduit causing bubble bursts. We compute a minimum gas flux of ~10^{-1} kg s^{-1} for the foam to reach the critical height using a gas fraction in the foam of 0.76 and a bubble radius of 0.3 mm (see supplementary information for calculations). The two models are not mutually exclusive. If an eruption is triggered before the critical foam thickness is reached, the accumulated foam will enhance bubble coalescence within the conduit, resulting in strombolian activity according to the first model. In both scenarios, erupting gas pockets are separated by low vesicularity melt, as syn-eruptive degassing adds less than 4 % to the total vesicularity. Our key conclusion is that the very high CO_2 in the mantle and derived magmas gives rise to large amounts of CO_2-rich gas bubbles at shallow crustal levels, which in turn drive explosive submarine eruptions.

Adopting a CO_2/Nb of ~4,000 from the least degassed melt inclusion, a similar geochemical behaviour of both elements during melting[4] and a Nb abundance of the mean upper depleted mantle of 0.3 ppm (ref. 23), we calculate a minimum CO_2 content of 1200 ppm for the mantle source beneath Axial Seamount (corresponding to 330 ppm of elemental carbon). For the 100 km spreading segment supplied by Axial Seamount we find a carbon mantle flux of 23×10^8 mol yr^{-1}, using a magma production rate constrained by the thickness of the local crust[24] of 6-8 km and a spreading rate of 6 mm yr^{-1}. Likewise, using a global oceanic crust production rate of 20±3 km^3 yr^{-1} (ref. 25) and a mean N-MORB Nb content of 3.5±1.9 ppm (ref. 23), we estimate a carbon mantle flux of

$19 \pm 10 \times 10^{12}$ mol yr^{-1} at mid-ocean ridges. This flux agrees with previous high estimates of 15×10^{12} mol yr^{-1} (ref. 10) and exceeds the lower range of estimates by nearly an order of magnitude[5,16].

CO_2 and Nb data from a number of studies from the last ten years[4,5,26,27] suggest variable CO_2/Nb in parts of the upper mantle rather than a constant value (Fig. 3). If both elements behave identically during mantle processes[4], their ratio should remain constant and independent from the elemental concentrations. However, CO_2 and Nb contents from various locations reveal a strong tendency towards lower CO_2/Nb as CO_2 decreases (Fig. 3). Hence, the CO_2 variability is much greater than Nb, suggesting either degassing of volatile-saturated magma, or a heterogeneous carbon distribution in the mantle that is decoupled from non-volatile incompatible elements such as Nb. While the CO_2-H_2O data from Axial suggest strong decompression degassing, results for Siqueiros[4] and the North Atlantic ridge[5] (14 °N and 34 °N) are thought to represent undegassed CO_2 contents. Only data for the North Atlantic ridge at 14 °N show constant CO_2/Nb. All other localities appear to be affected by CO_2 degassing, heterogeneous mantle carbon distributions, or both.

4. Conclusions

Our data provide evidence of extremely high dissolved CO_2 concentrations in primitive, volatile saturated MORB magmas at depths of 35-40 km. The high CO_2 content of mantle-derived MORB magmas at Axial Seamount establishes a direct link with explosive eruptions and widespread pyroclastic deposits at MOR spreading centres. We propose that CO_2 is decoupled from other incompatible elements in parts of the upper

mantle, and CO_2 fluxes can vary significantly along mid-ocean ridges.

Appendix – methods

Volatile (H_2O, CO_2, S, F, and Cl) analysis was carried out at Woods Hole Oceanographic Institution (WHOI) utilising high mass resolution secondary ion mass spectrometry (CAMECA IMS 1280). Selection of melt inclusions was done carefully through observations under transmitted and reflected light avoiding cracks or shrinkage bubbles within inclusions. Plagioclase grains with exposed inclusions were mounted into indium metal, and a 0.3 μm alumina oxide suspension was used for final polish. Prior to gold-coating, the mounts were dried in a vacuum oven at 110° C and 10^{-3} torr for ~12 h and were stored under vacuum at 10^{-7} torr for ~24 h. They were further allowed to outgas in the machine airlock at 3×10^{-9} torr. Sample chamber pressures during analysis were $<5 \times 10^{-9}$ torr. The principal analytical procedure followed the method as described in ref. 28. The detected secondary ions (^{12}C, $^{16}O^{1}H$, ^{19}F, ^{30}Si, ^{32}S, and ^{35}Cl) were produced by a primary $^{133}Cs^{+}$ beam of 1.2-1.5 nA current and 15 μm diameter. An electron beam was employed to compensate for positive charging of the sample surface. The primary beam was rastered over a 30 × 30 μm area, and a mechanical aperture was placed at the secondary ion image plane, such that the central 15 × 15um area was analyzed after 3 min of pre-sputtering. Counting times of 10 s were used for ^{12}C and $^{16}O^{1}H$, and 5 s for ^{19}F, ^{30}Si (reference mass), ^{32}S and ^{35}Cl. Data were acquired over 10 blocks. Magnet positions were calibrated for every spot and mass resolving power was set to > 6,700 to resolve interferences of ^{17}O from $^{16}O^{1}H$ and $^{29}Si^{1}H$ from ^{30}Si. Nine standard glasses, of basaltic and basaltic andesite compositions, were used to establish calibration curves for $^{12}C/^{30}Si$,

$^{16}O^{1}H/^{30}Si$, $^{19}F/^{30}Si$, $^{32}S/^{30}Si$, and $^{35}Cl/^{30}Si$ versus the respective volatile component. CO_2 content of all standard glasses was determined by Fourier transform infrared (FTIR) spectroscopy after the method of ref. 29. The standard error on the slope of the calibration curves is 2.4 % for CO_2 and 4.8 % or better for H_2O, F, S, and Cl. The 1σ stability of the $^{12}C/^{30}Si$ signal during analyses was better than 10 %, except for sample PlgM1_3-1 (12.2 %) and PlgM2_7-1 (14.1 %). The 1σ reproducibility of the in-run standard glass P1326-2, a JdFR basalt, was 5.3 % or better for CO_2, F, S and Cl, and 7.8 % for H_2O. Details on standards and quality of analyses are given in Supplementary Tables S5 and S6, and Supplementary Figs S4–S6. Special care was taken to verify high CO_2 contents in melt inclusions: first, nine high-CO_2 melt inclusions were re-analyzed after removing gold with 0.3 μm Al_2O_3 suspension. Potential surface contamination was reduced by sputter-cleaning melt inclusions with a stronger ion beam (5 nA) for 5 minutes, instead of a regular cleaning procedure with a 1.5-nA beam. Duplicate analyses confirmed the high CO_2 concentrations initially obtained. The data reported here are the duplicate values. Second, secondary ion images of ^{12}C were observed for each melt inclusion, and a homogeneous distribution of ^{12}C was confirmed for melt inclusions. No enrichment of CO_2 in cracks or edges of melt inclusions was observed. Third, ^{12}C intensity during analysis did not display any sign of surface contamination (Supplementary Fig. S5). Fourth, the CO_2 concentration in host plagioclase adjacent to melt inclusions was much less than 30 ppm. This is considered to represent the CO_2 background.

Subsequent to the volatile analysis, trace element compositions were determined for the melt inclusions using a CAMECA IMS 3f secondary ion mass spectrometer at WHOI[30]. Calibration was carried out using the KL2-G glass standard. Trace element

concentrations of the in-run standard P1326-2 were reproducible at a $1\sigma < 8$ %, except for Ba (11 %) (Supplementary Table S6). Major element compositions for the melt inclusions and the host glasses were analysed by electron microprobe (JEOL 8900) at McGill University, using a beam current of 1.5 nA, 15 kV, and defocused beam of 5 μm diameter for the melt inclusions and 10 μm for the host glasses.

References

1. Clague, D. A., Davis, A. S. & Dixon, J. E. in *Explosive Subaqueous Volcanism* (eds White, J. D. L., Smellie, J. L. & Clague, D. A.) (American Geophysical Union, Washington, DC, 2003).

2. Clague, D. A., Paduan, J. B. & Davis, A. S. Widespread strombolian eruptions of mid-ocean ridge basalt. *J. Volcanol. Geotherm. Res.* **180**, 171-188 (2009).

3. Sohn, R. A. *et al.* Explosive volcanism on the ultraslow-spreading Gakkel ridge, Arctic Ocean. *Nature* **453**, 1236-1238 (2008).

4. Saal, A. E., Hauri, E. H., Langmuir, C. H. & Perfit, M. R. Vapour undersaturation in primitive mid-ocean-ridge basalt and the volatile content of Earth's upper mantle. *Nature* **419**, 451-455 (2002).

5. Cartigny, P., Pineau, F., Aubaud, C. & Javoy, M. Towards a consistent mantle carbon flux estimate: Insights from volatile systematics (H_2O/Ce, δD, CO_2/Nb) in the North Atlantic mantle (14 degrees N and 34 degrees N). *Earth Planet. Sci. Lett.* **265**, 672-685 (2008).

6. Davis, A. S. & Clague, D. A. in *Explosive Subaqueous Volcanism* (eds White, J. D. L., Smellie, J. L. & Clague, D. A.) (American Geophysical Union, Washington, DC, 2003).

7. Clague, D. A., Davis, A. S., Bischoff, J. L., Dixon, J. E. & Geyer, R. Lava bubble-wall fragments formed by submarine hydrovolcanic: explosions on Lo'ihi Seamount and Kilauea Volcano. *Bull. Volcanol.* **61**, 437-449 (2000).

8. Maicher, D. & White, J. D. L. The formation of deep-sea Limu o Pele. *Bull. Volcanol.* **63**, 482-496 (2001).

9. Dixon, J. E. & Stolper, E. M. An experimental study of water and carbon dioxide solubilities in mid-ocean ridge basaltic liquids. 2. Applications to degassing. *J. Petrol.* **36**, 1633-1646 (1995).

10. Javoy, M. & Pineau, F. The volatiles record of a "popping rock" from the Mid-Atlantic Ridge at 14 ° N: chemical and isotopic composition of gas trapped in the vesicles. *Earth Planet. Sci. Lett.* **107**, 598-611 (1991).

11. West, M., Menke, W., Tolstoy, M., Webb, S. & Sohn, R. Magma storage beneath Axial volcano on the Juan de Fuca mid-ocean ridge. *Nature* **413**, 833-836 (2001).

12. PetDB. Petrological Database of the Ocean Floor, http://www.petdb.org.

13. Newman, S. & Lowenstern, J. B. VOLATILECALC: a silicate melt-H_2O-CO_2 solution model written in Visual Basic for excel. *Comput. Geosci.* **28**, 597-604 (2002).

14. Gerlach, T. M. Comment on "Mid-ocean ridge popping rocks: implications for degassing at ridge crests" by P. Sarda and D. Graham. *Earth Planet. Sci. Lett.* **105**, 566-567 (1991).

15. Hekinian, R. *et al.* Deep sea explosive activity on the Mid-Atlantic Ridge near 34 degrees 50 ' N: Magma composition, vesicularity and volatile content. *J. Volcanol. Geotherm. Res.* **98**, 49-77 (2000).

16. Shaw, A. M., Behn, M. D., Humphris, S. E., Sohn, R. A. & Gregg, P. M. Deep pooling of low degree melts and volatile fluxes at the 85 degrees E segment of the Gakkel Ridge: Evidence from olivine-hosted melt inclusions and glasses. *Earth Planet. Sci. Lett.* **289**, 311-322 (2010).

17. Gilbert, L. A., McDuff, R. E. & Johnson, H. P. Porosity of the upper edifice of Axial Seamount. *Geology* **35**, 49-52 (2007).

18. Grove, L. T., Kinzler, R. J. & Bryan, W. B. in *Mantle Flow and Melt Generation at Mid-Ocean Ridges* (eds Morgan, J. P., Blackman, D. K. & Sinton, J. M.) (American Geophysical Union, Washington, DC, 1992).

19. Nielsen, R. L. *et al.* Melt inclusions in high-An plagioclase from the Gorda Ridge: an example of the local diversity of MORB parent magmas *Contrib. Mineral. Petrol.* **122**, 34-50 (1995).

20. Bottinga, Y. & Javoy, M. Midocean ridge basalt degassing - bubble nucleation. *J. Geophys. Res.* **95**, 5125-5131 (1990).

21. Head, J. W. & Wilson, L. Deep submarine pyroclastic eruptions: theory and predicted landforms and deposits. *J. Volcanol. Geotherm. Res.* **121**, 155-193 (2003).

22. Jaupart, C. & Vergniolle, S. The generation and collapse of foam layer at the roof of a basaltic magma chamber. *J. Fluid. Mech.* **203**, 347-380 (1989).

23. Hofmann, A. W. Chemical differentiation of the earth - the relationship between mantle, continental crust, and oceanic crust. *Earth Planet. Sci. Lett.* **90**, 297-314 (1988).

24. West, M., Menke, W. & Tolstoy, M. Focused magma supply at the intersection of the Cobb hotspot and the Juan de Fuca ridge. *Geophys. Res. Lett.* **30,** 1724, 4pp., doi:10.1029/2003GL017104 (2003).

25. Cogné, J. P. & Humler, E. Trends and rhythms in global seafloor generation rate. *Geochem. Geophys. Geosyst.* **7**, 17 (2006).

26. Shimizu, K. *et al.* CO_2-rich komatiitic melt inclusions in Cr-spinels within beach sand from Gorgona Island, Colombia. *Earth Planet. Sci. Lett.* **288**, 33-43 (2009).

27. Dixon, J. E. & Clague, D. A. Volatiles in basaltic glasses from Loihi seamount, Hawaii: Evidence for a relatively dry plume component. *J. Petrol.* **42**, 627-654 (2001).

28. Hauri, E. *et al.* SIMS analysis of volatiles in silicate glasses 1. Calibration, matrix effects and comparisons with FTIR. *Chem. Geol.* **183**, 99-114 (2002).

29. Fine, G. & Stolper, E. Dissolved carbon dioxide in basaltic glasses: concentrations and speciation. *Earth Planet. Sci. Lett*. **76**, 263-278 (1986).

30. Shimizu, N. & Hart, S. R. Applications of the ion-micro-probe to geochemistry and cosmochemistry. *Annu. Rev. Earth Planet. Sci.* **10**, 483-526 (1982).

Acknowledgments

The authors thank the Captain and crew of the R/V Western Flyer and the pilots of the ROV Tiburon for their support and expertise during the 2006 MBARI Vance Expedition. The expedition and DAC were supported through a grant to MBARI from the David and Lucile Packard Foundation. C.H. was supported by R.H. Tomlinson, GEOTOP and J.W. McConnell Memorial Fellowships at McGill University. J.S. was supported by grants from the Natural Sciences and Engineering Research Council of Canada. We thank Dr. Bruce Watson from the Rensselaer Polytechnic Institute for synthesising the high-CO_2 glass standard NS-1, and Dr. Charles Mandeville from the American Museum of Natural History for the FTIR determination of CO_2 content of this standard.

Figure legends

Figure 1 Dissolved CO_2 and H_2O contents in melt inclusions and host glasses, measured by SIMS. Isobars calculated using ref. 13. 1σ error bars are shown for representative values. **a**, Melt inclusions exhibit an extremely wide range in CO_2 contents. The vertical trend indicates decompression degassing from a volatile-saturated melt. **b**, Zoom of the region below 1,000 ppm CO_2. The host glasses are volatile-oversaturated for an eruption pressure of 14 MPa (grey isobar). Host glasses are equilibrated at crustal depths between 0.3 and 2 km. The continuity in CO_2 concentrations from melt inclusions to host glasses indicates limited syn-eruptive degassing.

Figure 2 H_2O, F, and Cl contents of the melt inclusions and host glasses. **a**, The excellent correlation between H_2O and F in the melt inclusions indicates similar geochemical behaviour and suggests H_2O/F in the mantle of 14.3±0.2 (2σ). The host glasses display increasing H_2O at roughly constant F, indicating hydration and alteration of the erupted basalt. **b**, Cl/H_2O in the melt inclusions is controlled solely by the amount of Cl assimilated within the magma reservoir. By contrast post-eruptive alteration of the host glasses increases both Cl and H_2O, causing Cl/H_2O to remain roughly constant. 1σ error bars are shown.

Figure 3 Bilogarithmic plot of CO_2/Nb versus CO_2. The wide range of observed CO_2/Nb is striking, generally decreasing with lower CO_2. This trend can be explained by either degassing of CO_2 from volatile-saturated magmas, or in cases where degassing can be ruled out, by CO_2 distribution in the mantle which is decoupled from Nb. Decoupling of these two elements would result in a range of initial CO_2/Nb. *Axial*: degassed, measured dissolved volatile content in melt inclusions; *Siqueiros* [4]: undegassed, measured dissolved volatile content in melt inclusions; *North Atlantic ridge* [5] *14° N* and *34° N* and *Loihi* [27]: reconstructed undegassed volatile contents.

Figures

Figure 1

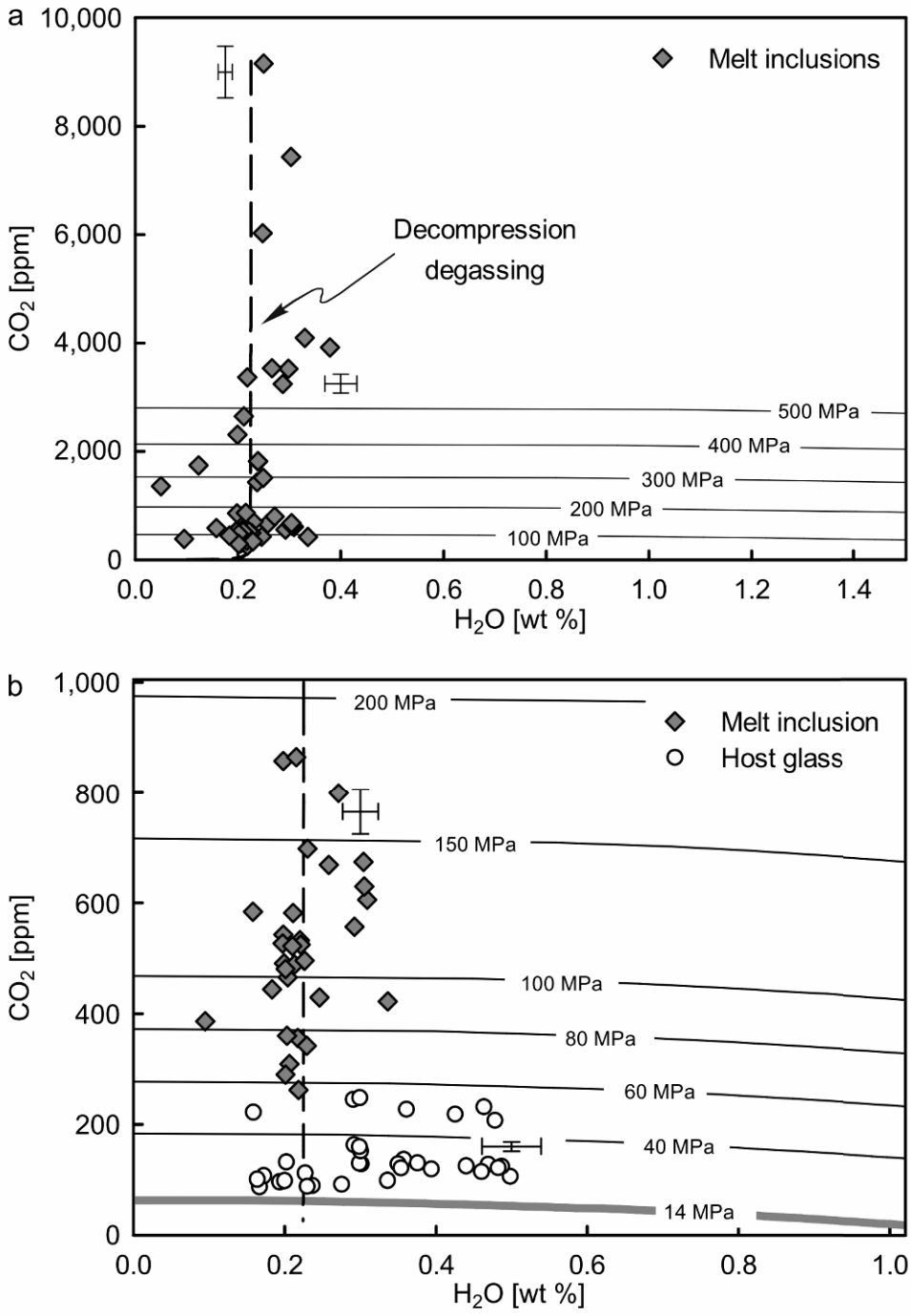

Figure 2

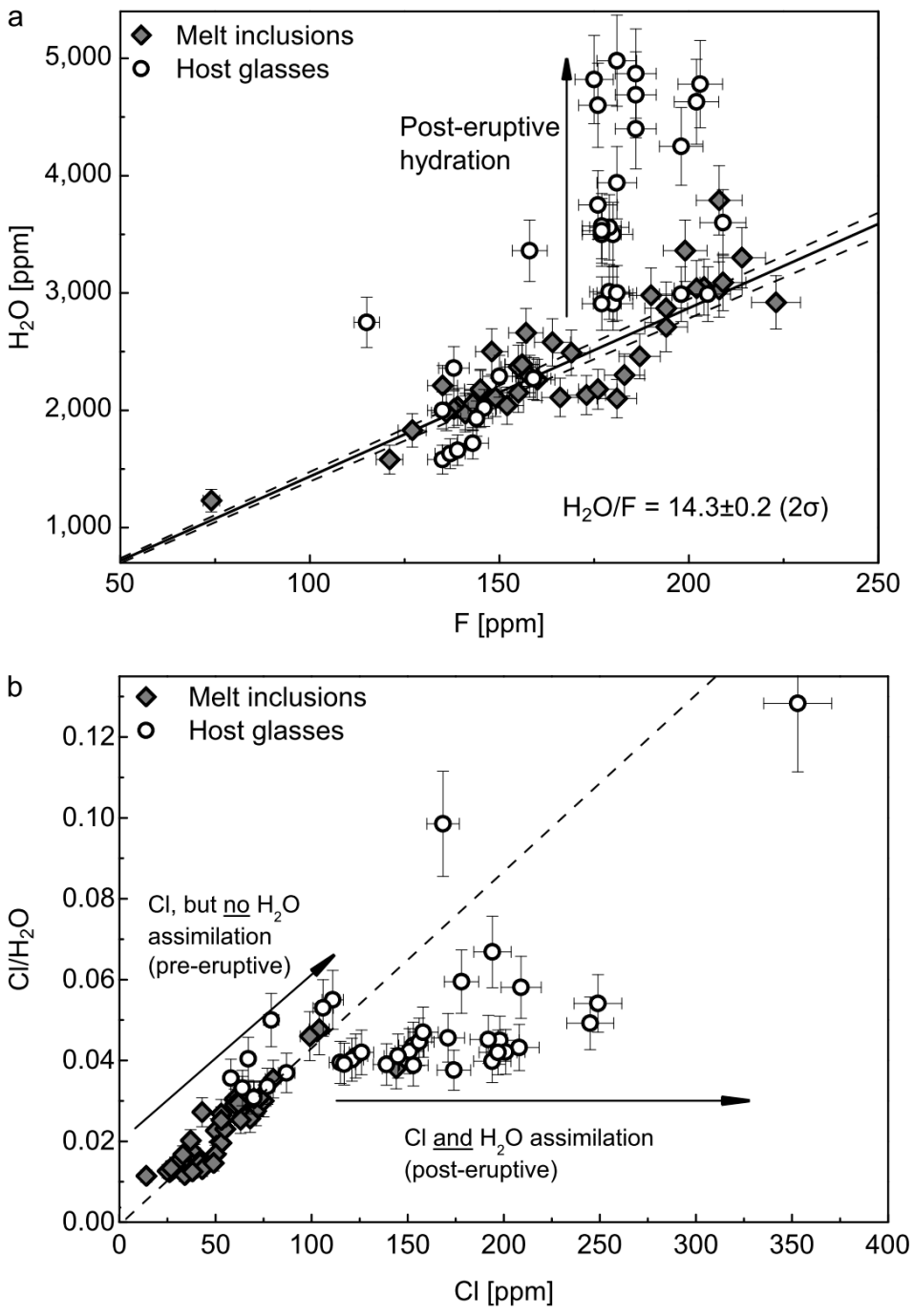
a
Melt inclusions
Host glasses
Post-eruptive
hydration
H2O/F = 14.3±0.2 (2σ)
H2O [ppm]
F [ppm]
b
Melt inclusions
Host glasses
Cl, but no H2O
assimilation
(pre-eruptive)
Cl and H2O assimilation
(post-eruptive)
Cl/H2O
Cl [ppm]

Figure 3

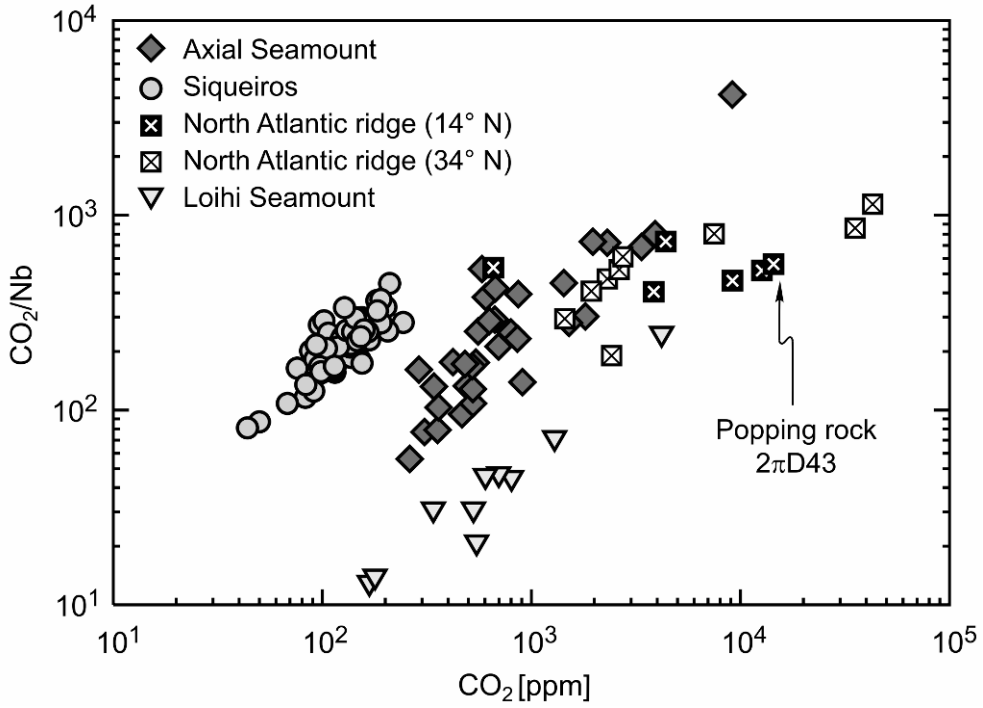
Axial Seamount
Siqueiros
North Atlantic ridge (14° N)
North Atlantic ridge (34° N)
Loihi Seamount
Popping rock
2πD43
CO2/Nb
CO2 [ppm]
10^4
10^3
10^2
10^1
10^1
10^2
10^3
10^4
10^5

Supplementary data and information

for:

Explosive eruptions at mid-ocean ridges driven by CO_2-rich magmas (Manuscript II)

Christoph Helo[1], Marc-Antoine Longpré[1], Nobumichi Shimizu[2], David A. Clague[3], John Stix[1]

Calculation of the minimum volatile flux for foam collapse

According to the model of ref. 22, a minimum CO_2 flux to achieve foam collapse can be calculated after:

$$Q_{\min} = \frac{\pi \varepsilon^2 \rho g}{3\mu(1-\varepsilon)^{-\frac{5}{2}}} \left(\frac{4\sigma}{\varepsilon \rho g d} \right)^4$$

$Q_{\min}$: minimum flux, kg s^{-1}
ε : gas fraction, 0.76
ρ : density, 2700 kg m^{-3}
g : gravitational acceleration, 9.81 m s^{-2}
μ : viscosity, 10 Pa s
σ : surface tension, 0.35 N m^{-1} (ref. 31)
d : bubble diameter, 3×10^{-4} m (ref. 20)

Supplementary references

31. Walker, D. & Mullins, O. Surface tension of natural silicate melts from 1,200°–1,500° C and implications for melt structure. Contrib. Mineral. Petrol. 76, 455-462 (1981).

32. Melson, W. Personal communication (1989).

33. Embley, R.W., Jonasson, I.R., Perfit, M.R., Franklin, J.M., Tivey , M.A., Malahoff, A., Smith, M.F., & Francis, T.J.G. Submersible investigation of an extinct hydrothermal system on the Galapagos Ridge: sulfide mounds, stockwork zone, and differentiated lavas, Can. Mineral. 26, 517-539 (1988).

34. Langmuir, C.H., Bender, J.F., Bence, A.E. & Hanson, G.N. Petrogenesis of basalts from the FAMOUS area: Mid-Atlantic Ridge. EPSL 36, 133-156 (1977).

35. Hauri, E.H. et al. Matrix effects in hydrogen isotope analysis of silicate glasses by SIMS. Chem. Geol. 235, 352-365 (2006).

36. Plank, T. Personal communication (2007).

37. Webster, J. Personal communication (1992).

38. Jochum, K.P. et al. MPI-DING reference glasses for in situ microanalysis: New reference values for element concentrations and isotope ratios. Geochem. Geophys. Geosyst. 7, 44 (2006).

39. Mandeville, C. & Watson, B. Personal communication (2010).

40. Stix, J., Gauthier, G. & Ludden, J.N. A critical look at quantitative laser-ablation ICP-MS analysis of natural and synthetic glasses. Can. Mineral. 33, 435-444 (1995).

41. Mandeville, C. W. et al. Determination of molar absorptivities for infrared absorption bands of H2O in andesitic glasses. Amer. Mineral. 87, 813-821 (2002).

42. Dixon, J. E., Stolper, E. M. & Holloway, J. R. An experimental study of water and carbon dioxide solubilities in mid ocean ridge basaltic liquids. 1. Calibration and solubility models. J. Petrol. 36, 1607-1631 (1995).

Supplementary Tables

Supplementary Table S1 Major, trace and volatile element data for melt inclusions from Axial Seamount, Juan de Fuca Ridge.

Sample	PlgInM1_1-1	PlgInM1_2-1	PlgInM1_2-2	PlgInM1_3-1	PlgInM1_3-2	PlgInM1_3-new	PlgInM1_4-1	PlgInM1_5-1	PlgInM1_8-1	PlgInM1_9-1	PlgInM1_9-2	PlgInM1_10-1	PlgInM1_12-1	PlgInM1_14-1	PlgInM1_14-2	PlgInM1_15-1	PlgInM1_16-1	PlgInM1_18-1
(wt %)																		
SiO_2		49.31	49.38	48.33	49.25	48.67	48.64	49.61	49.37	50.23	49.96	49.69	50.01	48.42	48.60		49.21	49.39
TiO_2		1.34	1.42	1.25	1.24	1.23	1.38	0.616	0.72	0.412	0.427	0.93	0.767	1.20	1.16		1.27	0.631
Al_2O_3		15.43	15.19	15.68	15.89	15.66	14.46	15.11	15.72	15.79	15.84	15.14	16.06	15.70	15.61		16.24	14.86
FeO*		10.63	10.56	9.69	9.31	9.40	11.81	11.18	10.43	9.94	10.30	10.89	9.12	10.24	9.99		9.96	10.55
MnO		0.23	0.164	0.16	0.15	0.115	0.171	0.205	0.18	0.206	0.135	0.18	0.235	0.137	0.15		0.114	0.153
MgO		9.55	9.63	8.91	9.06	8.60	9.12	7.05	9.69	10.10	10.26	9.18	10.35	8.11	8.11		9.05	9.74
CaO		12.09	12.00	12.09	12.20	12.35	12.17	12.19	12.07	11.62	11.96	12.33	11.71	11.80	11.83		12.16	11.86
Na_2O		2.54	2.57	2.52	2.57	2.60	2.63	2.59	2.52	2.50	2.51	2.60	2.55	2.66	2.64		2.56	2.23
K_2O		0.12	0.102	0.10	0.12	0.136	0.109	0.170	0.09	0.134	0.136	0.10	0.120	0.140	0.14		0.134	0.093
P_2O_5		0.11	0.129	0.13	0.13	0.117	0.098	0.000	0.07	0.024	0.025	0.07	0.038	0.139	0.11		0.115	0.065
S		0.11	0.114	0.12	0.12	0.119	0.154	0.135	0.12	0.109	0.109	0.11	0.126	0.117	0.11		0.117	0.113
Total		101.46	101.26	98.98	100.07	98.99	100.73	98.85	100.99	101.07	101.67	101.24	101.07	98.64	98.46		100.92	99.68
(ppm)																		
Ti	6935	7898	7813	7703	7581		7812	1285	4402	2542	2674	5385	4168	9770	6604		7284	6798
Cr	309	347	345	331	335		369	76	339	294	297	416	325	278	200		341	283
Sr	117	161	120	133	133		123	196	170	163	163	153	139	207	240		164	180
Y	20	24	23	21	24		24	5	18	12	12	28	18	36	24		25	25
Zr	62	73	74	71	78		68	9	45	16	18	70	37	108	74		81	69
Nb	2.3	3.7	4.9	4.9	3.2		3.2	0.9	3.1		1.1	2.7	3.3	6.0	3.7		4.9	4.0
Ba	17	19	19	20	19		17	12	32	26	26	11	19	36	31		31	35
CO_2 (ppm)	669	491	466	3366	2307		799	584	543	489	582	429	698	1814	858	1360	527	309
H_2O (wt %)	0.258	0.199	0.204	0.218	0.199		0.271	0.158	0.198	0.213	0.211	0.246	0.230	0.239	0.198	0.050	0.197	0.206
F (ppm)	164	143	152	145	141		194	121	143	173	166	187	183	156	136	10	141	143
S (ppm)	1113	1039	1158	1103	1023		1379	604	1186	963	925	1011	1114	1072	921	4	1152	950
Cl (ppm)	71	25	29	67	60		53	43	33	27	26	39	39	55	53	4	60	60
CO_2/Nb [a)]	291	133	95	687	721		250	649	175		529	159	212	302	232		108	77

Major elements were analysed by electron microprobe. Trace and volatile elements were analysed by secondary ion mass spectrometry. FeO* is all Fe as FeO.

a) Values do not represent the initial ratio, as it is affected by degassing of CO_2.

Supplementary Table S1 (continued).

Sample	PlgInM1_21-1b sims	PlgInM1 22-1	PlgInM1_ 25-1	PlgInM1_ 25-new1	PlgInM1_ 29-1	PlgInM1_ 29-2	PlgInM1_ 31-1	PlgInM1_ 33-1	PlgInM1_ 35-1	PlgInM1_ 35-2	PlgInM2_ 1-1	PlgInM2_ 1-2	PlgInM2_ 1-3	PlgInM2_ 4-1	PlgInM2_ 5-1	PlgInM2_ 7-1	PlgInM2_ 10-1	PlgInM2_ 10-2
(wt %)																		
SiO_2	48.42		48.48	48.74	49.71	48.64	48.20	50.27	49.73		49.31	49.12	50.15		49.62	48.95	48.84	48.53
TiO_2	0.90		0.947	1.35	1.07	1.07	0.89	1.39	0.969		0.419	0.572	0.931		0.94	0.61	0.754	0.573
Al_2O_3	15.68		14.84	16.03	16.27	16.84	16.45	15.59	15.83		14.71	14.61	14.73		13.45	14.65	14.75	14.23
FeO*	9.58		9.75	10.26	10.30	9.72	9.42	10.33	9.63		10.53	10.83	11.36		11.84	11.13	11.53	11.84
MnO	0.17		0.163	0.238	0.124	0.18	0.16	0.226	0.135		0.198	0.187	0.201		0.173	0.12	0.175	0.200
MgO	9.05		9.41	8.85	8.83	7.85	10.95	8.71	8.64		9.67	9.81	8.49		7.89	8.85	8.79	9.33
CaO	12.07		12.17	12.32	12.35	12.65	12.08	11.99	11.95		11.64	11.85	12.14		11.94	12.21	12.09	11.75
Na_2O	2.60		2.23	2.62	2.70	2.36	2.45	2.67	2.63		2.34	2.32	2.58		2.76	2.39	2.39	2.41
K_2O	0.14		0.122	0.115	0.110	0.09	0.14	0.127	0.157		0.080	0.110	0.107		0.164	0.10	0.086	0.134
P_2O_5	0.06		0.060	0.152	0.081	0.07	0.11	0.135	0.081		0.023	0.024	0.088		0.091	0.05	0.052	0.021
S	0.11		0.119	0.132	0.112	0.11	0.11	0.129	0.102		0.115	0.124	0.132		0.137	0.13	0.135	0.136
Total	98.78		98.27	100.82	101.65	99.58	100.95	101.58	99.85		99.02	99.55	100.90		99.01	99.20	99.59	99.14
(ppm)																		
Ti	8587	5852	5612		8736	6594	6770	5251	6737	5992	4340				5705	8390	3719	4852
Cr	250	325	363		342	379	383	271	293	340	378				383	372		
Sr	159	180	119		183	188	190	134	191	166	106				123	179	121	124
Y	30	29	24		34	31	32	14	26	22	9				22	33	18	19
Zr	102	84	47		134	85	102	64	79	80	38				70	99	37	53
Nb	4.7	2.2	2.2		6.5	3.2	4.5	5.4	4.0	4.1	2.2				2.4	4.9	1.6	2.2
Ba	28	13	16		26	29	23	27	22	42	17				15	36	19	20
CO_2 (ppm)	262	865	9159	533	496	1432	356	1514	386	525	557	4094	7436	3525	422	3917	606	630
H_2O (wt %)	0.218	0.215	0.250	0.22	0.226	0.237	0.217	0.249	0.095	0.221	0.292	0.330	0.303	0.298	0.336	0.379	0.309	0.305
F (ppm)	176	155	148		160	155	145	169	56	135	223	214	208	190	199	208	209	204
S (ppm)	1171	925	1012		1242	1105	1170	930	481	1001	1054	1069	1116	1234	1228	1212	1246	1293
Cl (ppm)	104	99	75		80	73	32	63	23	50	34	43	38	50	49	144	44	44
CO_2/Nb [a)]	56	393	4163		76	448	79	280	97	128	253				176	799	379	286

Supplementary Table S1 (continued).

Sample	PlgInM2_ 10-4	PlgInM2_ 10-5	PlgInM2_ 13-1	PlgInM2_ 14-1	PlgInM2_ 15-1	PlgInM2_ 16-1	PlgInM2_ 16-2	PlgInM2_ 16-3	PlgInM2_ 17-1	PlgInM2_ 17-2	PlgInM2_ 17-3	PlgInM2_ 17-4	PlgInM2_ 17-nobu	PlgInM2_ 18-1
(wt %)														
SiO_2	48.35	50.28	50.32	49.58		50.36	49.92	49.88	50.88	49.94	49.09	50.40	48.74	
TiO_2	0.741	0.836	0.976	1.06		0.724	0.61	0.86	0.761	0.967	0.900	0.75	1.18	
Al_2O_3	14.58	15.91	15.75	15.35		15.28	14.85	16.14	16.12	16.14	15.87	16.07	16.53	
FeO*	11.00	9.77	8.53	9.20		9.16	9.94	8.99	8.79	9.19	9.28	9.17	9.88	
MnO	0.171	0.142	0.151	0.160		0.227	0.18	0.201	0.167	0.202	0.151	0.14	0.18	
MgO	9.08	8.24	9.18	9.46		9.38	9.98	9.00	8.85	8.91	8.80	8.87	7.77	
CaO	12.00	12.00	11.931	11.89		12.10	11.63	12.31	12.28	11.75	11.88	12.02	12.50	
Na_2O	2.31	2.80	2.73	2.61		2.65	2.68	2.64	2.77	2.75	2.60	2.66	2.41	
K_2O	0.108	0.147	0.115	0.076		0.078	0.10	0.114	0.107	0.152	0.107	0.12	0.10	
P_2O_5	0.037	0.110	0.086	0.116		0.084	0.05	0.066	0.051	0.066	0.070	0.05	0.12	
S	0.146	0.108	0.084	0.099		0.087	0.09	0.111	0.093	0.094	0.098	0.09	0.12	
Total	98.52	100.35	99.85	100.05		100.13	100.01	100.30	100.86	100.15	98.84	100.33	99.53	
(ppm)														
Ti	4195				4283	6025	5380		5817	4381				9302
Cr	415				405	317	337		337	295				485
Sr	114				156	115	133		137	138				207
Y	22				15	21	17		22	18				36
Zr	32				50	60	71		60	37				118
Nb	1.6				3.1	3.5	2.8		2.6	1.8				
Ba	16				34	34	32		25	20				27
CO_2 (ppm)	674	3243	2649	1818	522	360	481	1741	342	290	3531		6027	444
H_2O (wt %)	0.304	0.287	0.211	0.239	0.210	0.203	0.201	0.123	0.229	0.201	0.266		0.248	0.183
F (ppm)	202	194	149	156	181	139	138	74	158	145	157			127
S (ppm)	1340	1309	979	1071	918	825	759	347	1089	786	909			1089
Cl (ppm)	42	42	62	55	53	27	27	14	70	64	68			37
CO_2/Nb [a)]	421				168	103	172		132	161				

Supplementary Table S2 Volatile element data for glassy ash fragments from Axial Seamount, Juan de Fuca Ridge.

Stratigraphic unit	Sample	CO_2 (ppm)	H_2O (wt %)	F (ppm)	S (ppm)	Cl (ppm)
T1009-VC1 14.0	GlassInM1_36d	227	0.36	209	1405	209
	GlassInM1_37d	207	0.478	203	1369	201
	GlassInM1_38d	128	0.469	186	1247	197
	GlassInM2_32d	90	0.236	138	1156	87
	GlassInM2_34d	112	0.227	159	1108	70
	GlassInM2_35L	87	0.166	139	1147	67
	GlassInM2_36L	107	0.172	143	1156	169
T1009-VC1 20.8	GlassInM1_13d	128	0.35	180	1211	153
	GlassInM1_14d	134	0.356	179	1227	139
	GlassInM1_15d	136	0.357	177	1202	151
	GlassInM1_19L	88	0.229	150	1110	77
	GassInM1_20L	115	0.46	176	1196	249
	GlassInM2_16d	222	0.158	135	1077	79
	GlassInM2_17d	132	0.202	146	1109	111
	GlassInM1_18L	129	0.35	177	1220	156
T1010-VC11 28.0	GlassInM1_7L	130	0.299	180	1246	123
	GlassInM1_1d	129	0.301	179	1236	121
	GlassInM1_2d	245	0.291	180	1237	194
	GlassInM1_3d	125	0.44	186	1248	198
	GlassInM1_8L	152	0.3	181	1264	126
	GlassInM1_9L	163	0.291	177	1254	115
T1010-VC15 12.6	GlassInM2_1d	92	0.275	115	1066	353
	GlassInM2_2d	98	0.336	158	1128	158
	GlassInM2_3d	96	0.193	144	1133	64
	GlassInM2_4d	218	0.425	198	1390	192
	GlassInM2_11d	160	0.299	198	1379	117
	GlassInM2_6L	248	0.299	205	1406	178
	GlassInM2_7L	101	0.163	137	1091	58
	GlassInM2_8L	98	0.2	135	1077	106
	GlassInM2_10L	232	0.463	202	1380	174
T1010-VC16 18.5	GlassInM1_24d	121	0.353	177	1232	145
	GlassInM1_25d	130	0.375	176	1240	171
	GlassInM1_27d	106	0.498	181	1224	245
	GlassInM1_29L	120	0.394	181	1267	153
	GlassInM1_31L	124	0.487	186	1262	194

Volatile elements were analysed by secondary ion mass spectrometry.

Supplementary Table S3 Major element data for host glass shards from Axial Seamount, Juan de Fuca Ridge.

Stratigraphic unit	T1009-VC1 14.0																	
(wt %)																		
SiO_2	48.67	48.60	48.66	48.83	48.31	48.54	48.96	49.03	49.14	49.17	48.81	49.11	49.28	49.04	49.44	49.43	49.18	49.54
TiO_2	1.578	1.581	1.387	1.593	1.532	1.378	1.647	1.574	1.570	1.631	1.622	1.583	1.551	1.527	1.537	1.575	1.503	1.507
Al_2O_3	13.98	13.96	14.69	14.03	14.03	14.63	14.15	14.03	14.15	14.01	13.89	14.13	13.91	13.76	13.72	13.73	13.87	13.81
FeO*	11.46	11.28	10.64	11.41	11.23	10.49	11.85	12.12	12.09	12.21	11.84	11.55	11.50	11.84	11.38	11.21	11.63	11.64
MnO	0.25	0.19	0.21	0.19	0.23	0.14	0.21	0.24	0.23	0.21	0.20	0.19	0.21	0.17	0.14	0.20	0.19	0.24
MgO	7.06	7.00	7.45	6.71	7.12	7.55	7.12	7.14	7.02	7.14	7.11	7.13	6.95	7.00	6.86	6.98	6.94	6.99
CaO	11.79	11.97	12.05	11.64	11.86	11.91	11.96	11.90	11.83	11.83	11.92	11.99	12.16	11.94	12.03	11.97	12.12	12.13
Na_2O	2.75	2.71	2.66	2.80	2.71	2.59	2.74	2.76	2.80	2.69	2.69	2.70	2.71	2.69	2.71	2.79	2.69	2.72
K_2O	0.17	0.14	0.15	0.15	0.14	0.14	0.16	0.16	0.14	0.16	0.16	0.129	0.168	0.150	0.149	0.145	0.147	0.155
P_2O_5	0.14	0.13	0.11	0.14	0.15	0.14	0.15	0.15	0.15	0.15	0.15	0.148	0.129	0.131	0.135	0.145	0.145	0.125
Cl												0.007	0.014	0.019	0.019	0.031	0.025	0.040
S	0.150	0.139	0.116	0.134	0.143	0.128	0.143	0.144	0.139	0.154	0.150	0.144	0.149	0.152	0.148	0.138	0.151	0.146
Total	98.00	97.69	98.13	97.61	97.45	97.64	99.10	99.24	99.25	99.36	98.53	98.81	98.73	98.42	98.28	98.33	98.59	99.01

Stratigraphic unit	T1009-VC1 14.0									T1009-VC1 20.8							
(wt %)																	
SiO_2	49.34	49.49	48.63	49.16	48.28	48.78	49.01	48.85	48.34	48.58	48.68	48.71	48.59	47.88	48.41	50.00	49.93
TiO_2	1.553	1.600	1.621	1.611	1.627	1.568	1.623	1.586	1.618	1.40	1.34	1.36	1.43	1.23	1.36	1.44	1.39
Al_2O_3	13.64	13.73	13.93	14.13	13.41	13.88	13.95	13.95	13.67	14.58	14.68	14.66	14.46	15.72	14.68	15.00	14.93
FeO*	11.38	11.56	11.66	11.42	11.39	11.69	11.54	11.32	11.34	10.71	10.60	10.44	10.78	9.67	10.50	11.03	10.96
MnO	0.15	0.23	0.22	0.26	0.16	0.19	0.26	0.24	0.20	0.17	0.19	0.16	0.19	0.13	0.22	0.20	0.16
MgO	7.00	6.98	7.04	6.96	7.52	7.22	6.72	7.03	7.23	7.69	7.55	7.75	7.47	8.51	7.48	7.97	7.80
CaO	12.00	12.12	11.99	11.85	12.35	12.09	11.90	11.99	11.99	11.85	12.04	11.79	11.92	11.71	11.77	12.38	12.34
Na_2O	2.60	2.70	2.81	2.84	2.79	2.85	2.97	2.84	2.79	2.58	2.55	2.59	2.63	2.51	2.62	2.71	2.76
K_2O	0.117	0.157	0.146	0.161	0.121	0.151	0.158	0.130	0.136	0.14	0.13	0.15	0.14	0.13	0.15	0.15	0.15
P_2O_5	0.109	0.133	0.137	0.131	0.156	0.118	0.141	0.149	0.138	0.13	0.14	0.12	0.13	0.10	0.12	0.12	0.14
Cl	0.023	0.025	0.029	0.026	0.021	0.021	0.024	0.025	0.024								
S	0.146	0.146	0.146	0.138	0.135	0.139	0.142	0.154	0.147	0.129	0.134	0.135	0.128	0.115	0.119	0.133	0.135
Total	98.05	98.86	98.35	98.68	97.95	98.70	98.43	98.27	97.63	97.97	98.02	97.86	97.89	97.72	97.41	101.13	100.71

Major elements were analysed by electron microprobe. FeO* is all Fe as FeO. Values for each glass shard are averaged over usually three spots.

Supplementary Table S3 (continued).

Stratigraphic unit	T1009-VC1 20.8																	
(wt %)																		
SiO_2	49.98	50.03	48.67	48.91	49.03	48.88	47.99	49.24	49.25	49.31	49.37	48.89	49.18	49.28	48.58	48.78	49.13	48.77
TiO_2	1.48	1.46	1.335	1.331	1.457	1.463	0.855	1.302	1.439	1.368	1.367	1.400	1.448	1.392	1.436	1.484	1.400	1.190
Al_2O_3	14.65	14.91	14.23	14.47	14.31	14.33	16.32	14.27	13.73	14.46	14.57	14.79	14.70	14.74	14.46	14.61	14.66	14.96
FeO*	11.13	11.03	10.55	10.65	10.59	10.44	8.82	10.63	11.48	10.65	10.77	10.60	10.51	10.55	10.67	10.79	10.67	10.29
MnO	0.19	0.22	0.22	0.16	0.11	0.18	0.19	0.19	0.24	0.23	0.23	0.19	0.19	0.20	0.24	0.14	0.18	0.24
MgO	7.89	7.73	7.67	7.82	7.71	7.55	9.46	7.47	7.06	7.58	7.77	7.82	7.63	7.87	7.72	7.87	7.92	8.27
CaO	12.32	12.32	12.35	12.35	12.42	12.26	12.59	12.58	12.17	12.19	12.36	12.36	12.31	12.45	12.33	12.37	12.27	12.55
Na_2O	2.73	2.77	2.56	2.60	2.55	2.55	2.07	2.66	2.69	2.56	2.51	2.68	2.68	2.67	2.65	2.63	2.65	2.48
K_2O	0.15	0.14	0.151	0.137	0.156	0.170	0.051	0.166	0.138	0.150	0.147	0.142	0.154	0.146	0.148	0.132	0.164	0.092
P_2O_5	0.12	0.13	0.131	0.128	0.109	0.103	0.055	0.112	0.126	0.119	0.153	0.135	0.131	0.123	0.131	0.146	0.131	0.138
Cl			0.017	0.022	0.018	0.011	0.005	0.014	0.030	0.023	0.009	0.019	0.027	0.013	0.026	0.009	0.022	0.013
S	0.132	0.134	0.128	0.128	0.125	0.131	0.107	0.131	0.136	0.125	0.130	0.129	0.128	0.125	0.128	0.135	0.118	0.120
Total	100.77	100.88	98.02	98.70	98.58	98.07	98.50	98.76	98.47	98.75	99.38	99.16	99.08	99.54	98.50	99.09	99.29	99.10

Stratigraphic unit	T1009-VC1 20.8				T1010-VC11 28.0												
(wt %)																	
SiO_2	48.06	48.44	48.97	49.27	48.61	48.90	48.84	48.47	48.36	48.32	48.78	49.85	49.74	49.90	49.93	49.88	48.84
TiO_2	1.433	1.394	1.375	1.406	1.43	1.47	1.44	1.34	1.39	1.34	1.39	1.52	1.48	1.42	1.47	1.42	1.534
Al_2O_3	14.36	14.63	14.62	14.63	14.68	14.53	14.65	14.70	14.58	14.58	14.64	14.79	14.96	14.98	14.78	14.91	14.49
FeO*	10.60	10.31	10.74	11.18	10.75	10.73	10.72	10.50	10.44	10.66	10.71	11.16	11.04	11.01	11.28	10.91	10.71
MnO	0.26	0.19	0.20	0.19	0.17	0.18	0.20	0.21	0.18	0.17	0.15	0.23	0.19	0.18	0.22	0.18	0.17
MgO	7.72	7.77	7.94	7.77	7.73	7.66	7.65	7.70	7.78	7.69	7.73	7.87	7.72	7.74	7.87	7.94	7.36
CaO	12.31	12.42	12.18	12.24	12.16	12.05	12.14	11.93	11.96	11.87	11.99	12.37	12.24	12.54	12.30	12.47	12.50
Na_2O	2.67	2.68	2.65	2.72	2.61	2.58	2.60	2.63	2.60	2.64	2.56	2.74	2.73	2.73	2.69	2.72	2.64
K_2O	0.148	0.128	0.114	0.148	0.146	0.130	0.129	0.130	0.126	0.151	0.151	0.150	0.142	0.145	0.157	0.131	0.161
P_2O_5	0.099	0.152	0.138	0.156	0.13	0.11	0.12	0.13	0.15	0.12	0.13	0.13	0.11	0.14	0.11	0.12	0.143
Cl	0.015	0.014	0.075	0.016													0.035
S	0.137	0.126	0.123	0.120	0.135	0.141	0.115	0.114	0.124	0.115	0.117	0.129	0.127	0.131	0.131	0.133	0.145
Total	97.79	98.26	99.11	99.83	98.56	98.47	98.60	97.85	97.69	97.65	98.35	100.93	100.47	100.90	100.94	100.81	98.72

Supplementary Table S3 (continued).

Stratigraphic unit	T1010-VC11 28.0																	
(wt %)																		
SiO_2	48.76	48.83	48.43	48.25	48.37	48.28	48.70	48.39	48.36	48.79	49.40	49.18	48.89	49.09	48.96	48.36	49.07	49.00
TiO_2	1.461	1.475	1.409	1.412	1.437	1.404	1.544	1.421	1.436	1.318	1.444	1.569	1.434	1.480	1.496	1.290	1.466	1.467
Al_2O_3	14.64	14.66	14.72	14.73	14.77	14.84	14.13	14.73	14.61	15.66	14.46	14.20	14.62	14.45	14.27	15.55	14.71	14.57
FeO*	10.54	10.55	10.37	10.50	10.59	10.37	11.42	10.49	10.58	9.77	10.45	11.28	10.42	10.65	10.94	9.74	10.69	10.55
MnO	0.17	0.16	0.16	0.18	0.17	0.20	0.23	0.20	0.17	0.18	0.17	0.22	0.21	0.19	0.17	0.17	0.16	0.18
MgO	7.63	7.56	7.50	7.64	7.55	7.53	7.13	7.73	7.59	8.42	7.58	7.07	7.60	7.61	7.26	8.45	7.16	7.72
CaO	12.61	12.84	12.65	12.65	12.65	12.62	12.43	12.54	12.75	12.18	12.34	12.07	12.46	12.54	12.40	12.36	12.64	12.47
Na_2O	2.56	2.60	2.60	2.63	2.62	2.62	2.69	2.58	2.59	2.57	2.63	2.82	2.59	2.64	2.77	2.53	2.67	2.63
K_2O	0.150	0.135	0.151	0.138	0.135	0.142	0.132	0.138	0.148	0.123	0.160	0.162	0.140	0.150	0.152	0.113	0.152	0.142
P_2O_5	0.128	0.106	0.128	0.123	0.142	0.127	0.124	0.129	0.150	0.113	0.140	0.139	0.117	0.119	0.137	0.102	0.110	0.113
Cl	0.014	0.012	0.023	0.019	0.019	0.018	0.026	0.022	0.016	0.010	0.020	0.019	0.015	0.013	0.009	0.010	0.034	0.017
S	0.133	0.130	0.133	0.128	0.131	0.128	0.141	0.127	0.130	0.122	0.135	0.138	0.126	0.139	0.135	0.121	0.132	0.126
Total	98.80	99.06	98.26	98.41	98.59	98.28	98.69	98.49	98.54	99.25	98.92	98.86	98.64	99.07	98.70	98.79	98.98	98.98

Stratigraphic unit	T1010-VC11 28.0								T1010-VC15 12.6								
(wt %)																	
SiO_2	48.68	48.63	48.51	48.57	48.83	48.85	49.06	48.89	48.61	48.69	48.50	48.62	48.61	48.52	48.49	48.59	48.61
TiO_2	1.491	1.436	1.422	1.426	1.408	1.427	1.468	1.409	1.28	1.27	1.35	1.29	1.28	1.09	1.30	1.25	1.282
Al_2O_3	14.42	14.26	14.52	14.45	14.51	14.49	14.49	14.42	15.81	15.88	15.77	15.86	15.77	16.05	15.87	15.82	15.74
FeO*	10.40	10.69	10.39	10.45	10.43	10.55	10.48	10.48	9.85	9.93	10.12	9.73	9.97	9.56	9.96	10.06	9.98
MnO	0.20	0.18	0.16	0.18	0.17	0.17	0.20	0.19	0.14	0.15	0.18	0.16	0.18	0.13	0.17	0.16	0.19
MgO	7.49	8.79	7.30	7.47	7.45	7.49	7.41	7.64	8.42	8.52	8.26	8.52	8.44	9.38	8.25	8.44	8.47
CaO	12.49	12.04	12.48	12.50	12.43	12.54	12.52	12.41	12.18	12.28	12.39	12.23	12.37	12.12	12.31	12.21	12.26
Na_2O	2.65	2.61	2.65	2.64	2.56	2.61	2.63	2.60	2.52	2.55	2.60	2.50	2.47	2.34	2.54	2.54	2.50
K_2O	0.138	0.135	0.135	0.138	0.142	0.160	0.131	0.152	0.122	0.125	0.117	0.119	0.123	0.106	0.124	0.107	0.122
P_2O_5	0.116	0.106	0.116	0.127	0.146	0.126	0.120	0.123	0.098	0.103	0.111	0.104	0.118	0.090	0.114	0.106	0.098
Cl	0.019	0.024	0.038	0.023	0.024	0.034	0.031	0.023									
S	0.130	0.125	0.125	0.129	0.128	0.126	0.130	0.124	0.117	0.122	0.124	0.117	0.118	0.111	0.112	0.119	0.119
Total	98.21	99.03	97.84	98.10	98.23	98.55	98.66	98.46	99.13	99.61	99.52	99.25	99.44	99.49	99.24	99.41	99.35

Supplementary Table S3 (continued).

Stratigraphic unit	T1010-VC15 12.6																	
(wt %)																		
SiO_2	48.16	48.41	48.23	48.46	48.20	48.26	48.00	48.41	48.43	48.15	48.31	47.97	48.01	48.30	47.80	47.92	48.38	48.50
TiO_2	1.312	1.156	1.320	1.337	1.089	1.297	1.304	1.292	1.341	1.272	1.333	1.375	1.265	1.269	1.292	1.305	1.291	1.309
Al_2O_3	15.58	15.90	15.64	15.65	15.80	15.53	15.89	15.39	15.63	15.55	15.50	15.46	15.52	15.61	15.99	15.55	15.50	15.60
FeO*	9.71	9.53	9.69	9.65	9.33	9.67	9.56	9.69	9.68	9.75	9.62	9.81	9.62	9.71	9.56	9.63	9.68	9.79
MnO	0.17	0.16	0.22	0.14	0.18	0.17	0.18	0.15	0.18	0.18	0.16	0.17	0.19	0.18	0.19	0.18	0.18	0.21
MgO	8.32	8.89	8.47	8.41	8.84	8.25	8.59	8.38	8.37	8.43	8.39	8.45	8.42	8.43	8.60	8.42	8.44	8.45
CaO	12.48	12.72	12.49	12.28	12.81	12.49	12.35	12.44	12.40	12.48	12.39	12.37	12.38	12.55	12.39	12.37	12.39	12.42
Na_2O	2.59	2.37	2.57	2.61	2.27	2.58	2.45	2.55	2.58	2.55	2.58	2.52	2.56	2.51	2.42	2.59	2.58	2.60
K_2O	0.119	0.117	0.113	0.128	0.103	0.121	0.126	0.115	0.117	0.134	0.129	0.124	0.131	0.120	0.134	0.132	0.118	0.125
P_2O_5	0.111	0.105	0.105	0.126	0.082	0.117	0.108	0.107	0.106	0.098	0.120	0.109	0.117	0.120	0.104	0.120	0.111	0.098
Cl	0.010	0.010	0.011	0.010	0.009	0.022	0.013	0.007	0.007	0.009	0.009	0.008	0.008	0.010	0.011	0.010	0.011	0.010
S	0.117	0.115	0.120	0.122	0.120	0.114	0.115	0.117	0.118	0.113	0.114	0.121	0.122	0.120	0.113	0.124	0.120	0.121
Total	98.68	99.48	98.97	98.91	98.82	98.62	98.68	98.64	98.95	98.70	98.65	98.48	98.34	98.91	98.59	98.35	98.79	99.22

Stratigraphic unit	T1010-VC15 12.6								T1010-VC16 18.5								
(wt %)																	
SiO_2	48.15	48.15	48.05	47.89	48.19	48.11	48.34	48.43	48.44	48.58	48.73	48.48	48.46	48.46	49.75	49.66	49.98
TiO_2	1.396	1.265	1.294	1.319	1.285	1.308	1.286	1.309	1.41	1.32	1.35	1.39	1.33	1.37	1.42	1.45	1.50
Al_2O_3	15.47	15.52	15.51	15.63	15.61	15.49	15.45	15.57	14.63	14.58	14.66	14.61	14.60	14.48	14.78	14.88	14.64
FeO*	9.82	9.84	9.77	9.69	9.78	9.55	9.57	9.78	10.55	10.30	10.59	10.52	10.38	10.37	11.08	10.96	11.12
MnO	0.13	0.19	0.19	0.18	0.19	0.18	0.17	0.17	0.19	0.16	0.20	0.18	0.21	0.19	0.19	0.20	0.19
MgO	8.45	8.45	8.23	8.42	8.32	8.21	8.41	8.48	7.63	7.51	7.58	7.62	7.56	7.57	7.79	7.80	7.84
CaO	12.46	12.42	12.46	12.26	12.41	12.54	12.30	12.34	11.65	11.76	11.61	11.77	11.71	11.75	12.24	12.42	12.39
Na_2O	2.58	2.53	2.58	2.56	2.60	2.58	2.60	2.53	2.57	2.66	2.64	2.60	2.59	2.60	2.72	2.70	2.76
K_2O	0.117	0.119	0.124	0.111	0.120	0.114	0.114	0.118	0.13	0.14	0.15	0.15	0.16	0.15	0.14	0.14	0.15
P_2O_5	0.091	0.113	0.108	0.118	0.105	0.119	0.111	0.109	0.13	0.13	0.15	0.13	0.13	0.12	0.14	0.11	0.13
Cl	0.013	0.011	0.015	0.013	0.030	0.016	0.012	0.013									
S	0.116	0.125	0.117	0.118	0.115	0.118	0.113	0.117	0.125	0.134	0.129	0.116	0.124	0.119	0.131	0.129	0.137
Total	98.79	98.73	98.44	98.29	98.74	98.32	98.49	98.97	97.44	97.27	97.79	97.57	97.25	97.17	100.39	100.44	100.83

Supplementary Table S3 (continued).

Stratigraphic unit	T1010-VC16 18.5																	
(wt %)																		
SiO_2	50.02	49.76	48.74	48.95	49.21	49.38	49.37	49.11	48.95	49.30	49.29	49.31	48.68	48.97	48.98	48.80	49.25	49.79
TiO_2	1.63	1.49	1.404	1.485	1.523	1.453	1.441	1.430	1.431	1.444	1.514	1.491	1.411	1.442	1.376	1.438	1.419	1.41
Al_2O_3	14.11	14.82	14.47	14.60	14.24	14.58	14.25	14.60	14.39	14.62	14.10	14.15	14.56	14.47	14.52	14.48	14.53	14.88
FeO*	12.18	11.18	10.44	10.46	10.84	10.43	10.63	10.44	10.56	10.53	10.71	10.65	10.63	10.56	10.61	10.51	10.53	10.37
MnO	0.25	0.21	0.19	0.20	0.19	0.20	0.22	0.14	0.19	0.21	0.17	0.17	0.21	0.22	0.16	0.17	0.19	0.195
MgO	7.25	7.79	7.57	7.37	7.50	7.73	7.56	7.57	7.59	7.56	7.38	7.45	7.30	7.60	7.72	7.58	7.79	7.48
CaO	12.05	12.33	12.39	12.32	12.33	12.58	12.56	12.32	12.54	12.38	12.30	12.44	12.47	12.39	12.28	12.38	12.45	12.38
Na_2O	2.93	2.76	2.64	2.66	2.70	2.59	2.61	2.59	2.55	2.64	2.71	2.64	2.66	2.61	2.66	2.64	2.56	2.64
K_2O	0.14	0.13	0.156	0.140	0.161	0.164	0.154	0.127	0.151	0.151	0.158	0.157	0.151	0.147	0.128	0.126	0.134	0.14
P_2O_5	0.14	0.14	0.147	0.113	0.148	0.141	0.140	0.123	0.115	0.131	0.137	0.137	0.119	0.115	0.115	0.126	0.145	0.131
Cl			0.018	0.027	0.027	0.011	0.008	0.022	0.032	0.023	0.019	0.011	0.024	0.019	0.020	0.020	0.009	0.019
S	0.144	0.133	0.126	0.127	0.136	0.136	0.131	0.132	0.115	0.129	0.145	0.140	0.129	0.126	0.134	0.126	0.133	0.124
Total	100.65	100.74	98.28	98.45	98.99	99.39	99.06	98.60	98.61	99.11	98.62	98.74	98.34	98.67	98.69	98.39	99.13	99.54

Stratigraphic unit	T1010-VC16 18.5										
(wt %)											
SiO_2	50.04	49.97	49.94	50.04	50.12	49.99	49.91	49.98	50.21	50.03	50.20
TiO_2	1.41	1.38	1.41	1.40	1.41	1.41	1.41	1.42	1.42	1.44	1.39
Al_2O_3	14.92	14.88	14.88	14.91	14.83	14.97	14.88	14.93	14.93	14.89	14.97
FeO*	10.59	10.60	10.49	10.60	10.68	10.49	10.52	10.58	10.71	10.56	10.54
MnO	0.171	0.160	0.197	0.209	0.203	0.208	0.185	0.214	0.180	0.205	0.184
MgO	7.60	7.67	7.55	7.61	7.61	7.50	7.81	7.64	7.71	7.41	7.74
CaO	12.49	12.40	12.40	12.40	12.31	12.28	12.44	12.43	12.44	12.37	12.46
Na_2O	2.66	2.64	2.68	2.67	2.69	2.70	2.59	2.67	2.64	2.72	2.66
K_2O	0.14	0.14	0.16	0.15	0.15	0.15	0.13	0.15	0.14	0.15	0.15
P_2O_5	0.119	0.126	0.119	0.120	0.144	0.124	0.114	0.116	0.126	0.136	0.120
Cl	0.019	0.016	0.022	0.019	0.024	0.029	0.013	0.017	0.018	0.033	0.017
S	0.124	0.122	0.121	0.120	0.120	0.121	0.124	0.119	0.123	0.122	0.126
Total	100.27	100.10	99.97	100.22	100.28	99.96	100.13	100.25	100.64	100.06	100.55

Supplementary Table S4 Major element composition of plagioclase phenocrysts, Axial Seamount, Juan de Fuca Ridge.

	PlgInM1_2	PlgInM1_3	PlgInM1_5	PlgInM1_10	PlgInM1_12	PlgInM1_14	PlgInM1_15	PlgInM1_16	PlgInM1_22	PlgInM1_25	PlgInM1_25	PlgInM1_29	PlgInM1_31 (Olivine)	PlgInM1_33
(wt %)														
SiO_2	46.76	47.30	47.43	46.46	46.56	47.52	47.84	46.46	46.46	46.60	46.60	46.50	40.65	46.17
TiO_2	0.02	0.03	0.03	0.03	0.01	0.03	0.01	0.03	0.02	0.03	0.03	0.03	0.01	0.03
Al_2O_3	33.32	32.86	32.72	33.16	33.67	32.69	32.35	33.45	33.63	33.80	33.80	33.41	0.06	33.33
FeO*	0.31	0.37	0.44	0.33	0.35	0.38	0.34	0.34	0.37	0.30	0.30	0.35	12.62	0.29
MgO	0.17	0.20	0.15	0.17	0.22	0.20	0.23	0.17	0.12	0.15	0.15	0.19	46.89	0.18
CaO	17.43	17.16	16.97	17.67	17.70	16.82	16.69	17.57	17.65	17.73	17.73	17.50	0.30	17.70
Na_2O	1.44	1.66	1.81	1.38	1.29	1.87	1.97	1.39	1.34	1.31	1.31	1.41	0.00	1.27
K_2O	0.00	0.01	0.01	0.00	0.01	0.01	0.01	0.01	0.01	0.02	0.02	0.01	0.00	0.01
SrO	0.02	0.01	0.03	0.01	0.00	0.01	0.00	0.02	0.01	0.00	0.00	0.01	0.00	0.00
BaO	0.01	0.02	0.03	0.00	0.00	0.00	0.00	0.02	0.01	0.00	0.00	0.02	0.01	0.01
Total	99.49	99.63	99.62	99.20	99.80	99.52	99.44	99.47	99.62	99.94	99.94	99.43	100.54	98.99

FeO* is all Fe as FeO. Values average over 3-5 spots, except PlgInM1_16 & _22, averaged over 15 & 18 spots, respectively.

Supplementary Table S5 Standard glass data used.

	All107-D20	ALV 1649-3	ALV 1654-3	ALV 519-4-1	EN113 46D	FRND 6001	GL07 D51-3	GL07 D52-5	JDH 17H	KL2-G	NS-1	P1326-2 (in-run)
(wt %)												
SiO_2	49.82	51.25	56.6	49.1	49.5	54.78	49.46	48.59	48.59	50.1	49.4	50.0
TiO_2	0.63	2.69	2.33	0.78	1.07	0.48	2.45	2.67	1.85	2.6	1.54	1.53
Al_2O_3	17.38	11.9	11.3	16.6	15.78	15.61	14.9	15.94	13.42	13.1	14.78	14.48
FeO*	7.53	15.3	14.9	8.04	9.16	8.38	10.92	10.76	12.73	10.7	9.25	10.82
MnO	n.d.	0.24	0.25	0.14	0.15	0.16	0.15	0.15	n.d.	0.17	0.19	0.16
MgO	9.94	4.71	2.49	9.51	8.29	6.42	6.79	6.3	7.05	7.26	8.95	7.3
CaO	13.06	9.23	7.16	12.47	13.18	10.93	10.59	10.14	10.81	10.8	10.69	12.18
Na_2O	1.65	2.65	3.2	2.08	2.52	1.5	2.82	3.34	2.68	2.27	2.95	2.76
K_2O	0.02	0.20	0.36	0.08	0.05	0.55	0.26	0.39	0.17	0.48	0.21	0.17
P_2O_5	0.11	0.44	0.63	n.d.	0.21	0.11	0.24	0.31	0.16	0.25	0.1	0.12
Total	100.14	98.61	99.22	98.86	99.91	98.92	98.58	98.59	97.46	97.73	98.06	99.52
CO_2 (ppm)		161		165	237		125	88			3154	
H_2O (wt %)	0.05	0.61	1.0	0.17	0.112		0.443	1.0	2.49		0.37	
F (ppm)		445	997	90	124		299	431				
S (ppm)		1640	1562	950	877	38	1126	1183				
Cl (ppm)		1433	2914	45	45	927	182	322				
(ppm)												
Ti										15587		
Cr										310		313
Sr										364		153
Y										26.8		33
Zr										159		94
Nb										15.8		4.4
Ba										123		38
Reference	32	33	33	34	35	36	35	35	37	38	39	40

FeO* is all Fe as FeO.

Supplementary Table S6 Reproducibility of the in-run standard glass P1326-2.

	Conc. (ppm)	1σ (ppm)	1σ (%)	n	Mean cps
^{30}Si				13	$(2.65\pm0.5)\times10^5$
CO_2	327	17	5.3	13	
H_2O	0.265	0.021	7.8	14	
F	191	5.6	2.9	14	
S	1277	49	3.8	14	
Cl	160	8.7	5.4	14	
^{28}Si				12	$(2.01\pm0.41)\times10^5$
Ti	9247	542	5.8%	12	
Sr	173	12	6.8%	12	
Y	33	2.3	7.0%	12	
Zr	111	7.8	7.0%	12	
Nb	5.5	0.5	8.1%	11	
Ba	32	3.5	10.8%	12	

Conc.: concentration; cps: counts per second

Supplementary Figure legends

Supplementary Figure S1 The two most common types of glass fragments from pyroclastic ash deposits on Axial Seamount. a, Photomicrographs of limu o Pele (thin melt films/bubble walls). b, Scanning electron microscope images of limu o Pele. These fragments occur in a wide range of morphologies, from fairly flat to strongly bended and folded. c, Scanning electron microscope images of angular, dense ash particles. The occurrence of both types of fragments is consistent with a strombolian type of activity, which is characterised by the eruption of gas slugs, produced by bubble coalescence and separated by low-vesicularity interstitial melt.

Supplementary Figure S2 Chemical composition of the melt inclusions and host glasses in comparison to other Juan de Fuca ridge (JdFR) basalts. a, Major element compositions and b, trace element signature of the Axial Seamount melt inclusions and host glasses are in good agreement with the compositional spectrum of the adjacent JdFR segments. Trace element data for host glasses unpublished, JdFR basalts from ref. 12. 1σ error bars are shown for representative values.

Supplementary Figure S3 Semi logarithmic plot of CO2/Nb versus Mg-number for melt inclusions. The ratio is very sensitive to degassing but insensitive to crystal fractionation. The melt inclusions reveal no correlation between degree of fractionation (Mg-number) and degassing.

Supplementary Figure S4 Calibration curves for volatile elements. Known standard element concentrations versus measured isotope ratios (counts per second/counts per second). Data are linearly regressed through the origin. The correlation parameter (a), its standard error (StdErr) and coefficient of determination (R^2) are given in each panel. Counts per second of ^{30}Si were between 2-4×10^5. **a**-**e** Curves used for the analyses. **f**, CO_2 standard data including a basaltic high-CO_2 standard glass (NS-1) verifying the linearity of the calibration over a wide range of CO_2 concentrations.

Supplementary Figure S5 $^{12}C/^{30}Si$ (counts per second/counts per second) during analyses. Shown are measurements of nine melt inclusions and one plagioclase (background). Respective CO_2 concentrations, stability of the signal in 1σ, and sample names are shown.

Supplementary Figure S6 FTIR spectra of the high-CO_2 standard (NS-1). Dissolved CO_2, present as CO_3^{2-} species, was determined by the peak height of the 1430 cm^{-1} absorbance band after subtraction of a thickness normalized spectra from a H_2O-CO_2 free basaltic glass. The inlay depicts a raw spectra of the entire band region scanned (400 cm^{-1} to 8000 cm^{-1}). Total H_2O concentration was determined from the peak height of the broad absorbance peak at 3550±20 cm^{-1} utilizing a straight line fit to the background[41]. Molar absorptivities ε_{1430} and ε_{3550} after ref. 42. Data from ref. 39.

.

Supplementary Figures

Supplementary Figure S1

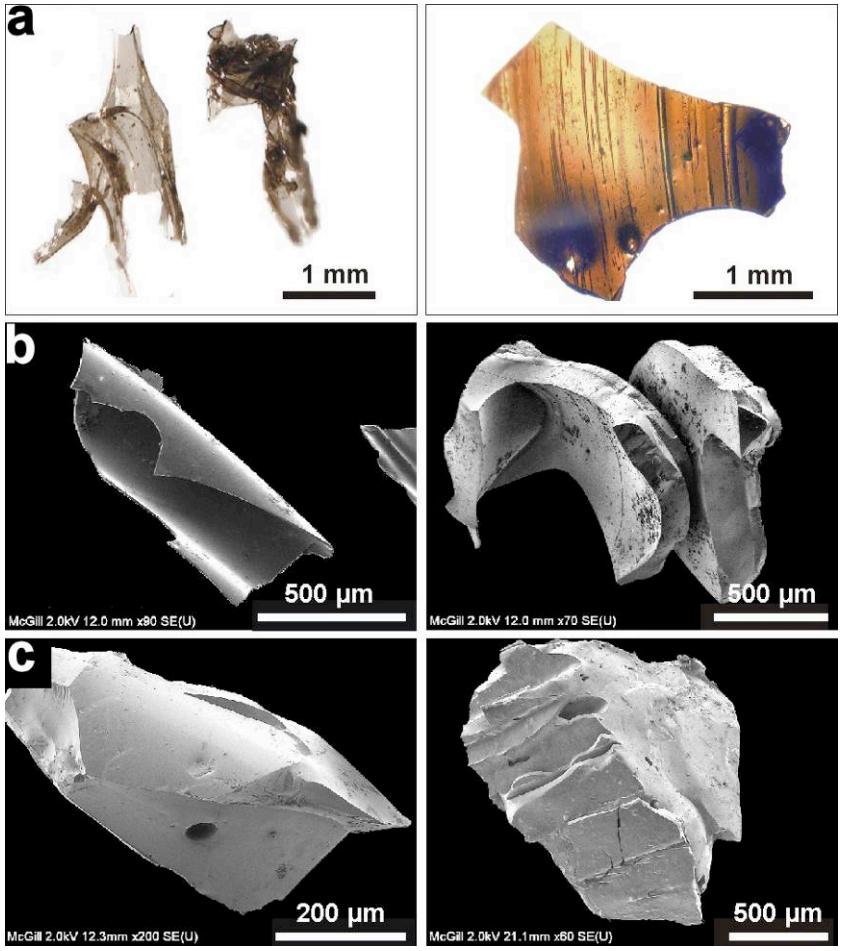

Supplementary Figure S2

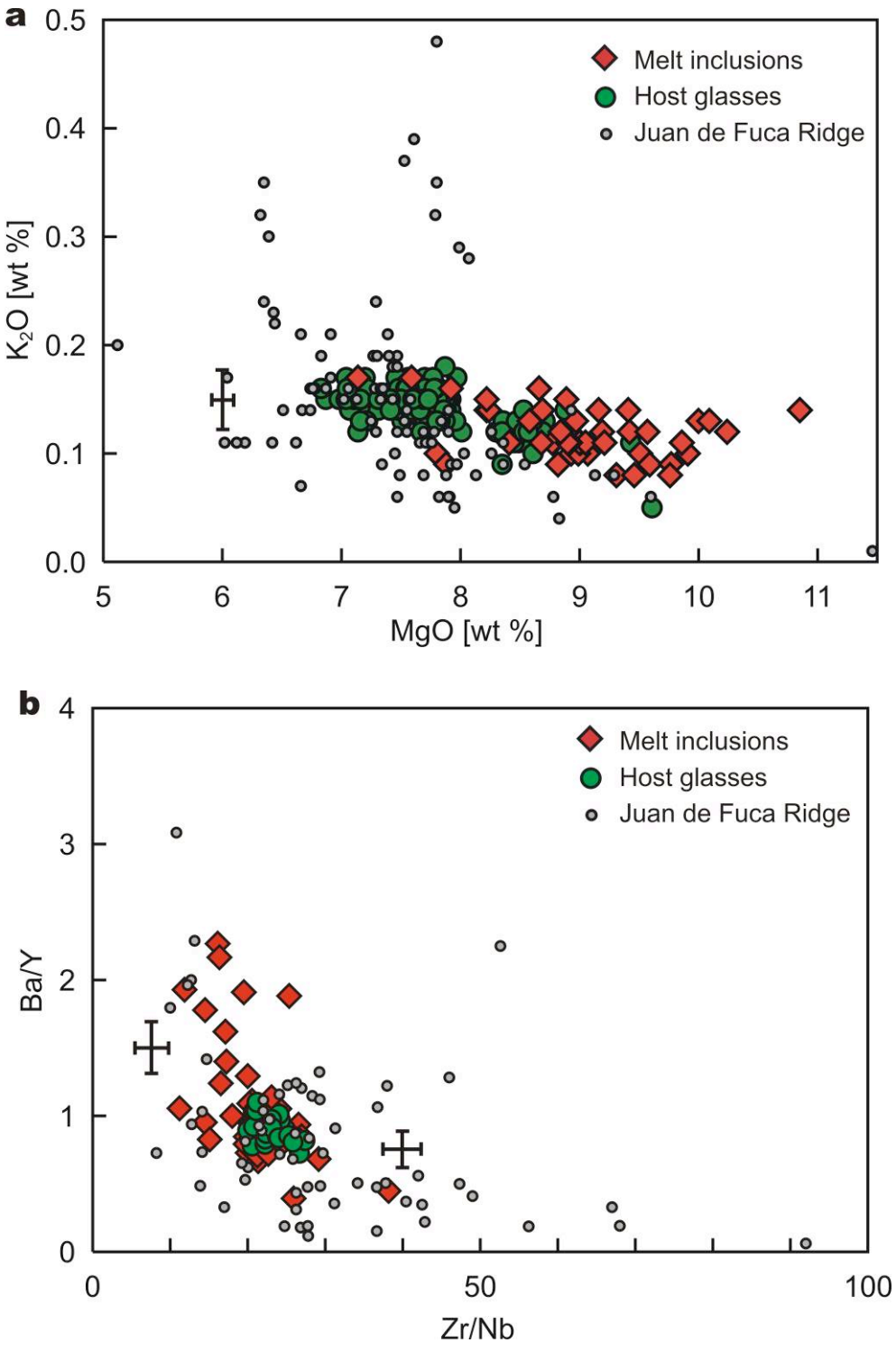

Supplementary Figure S3

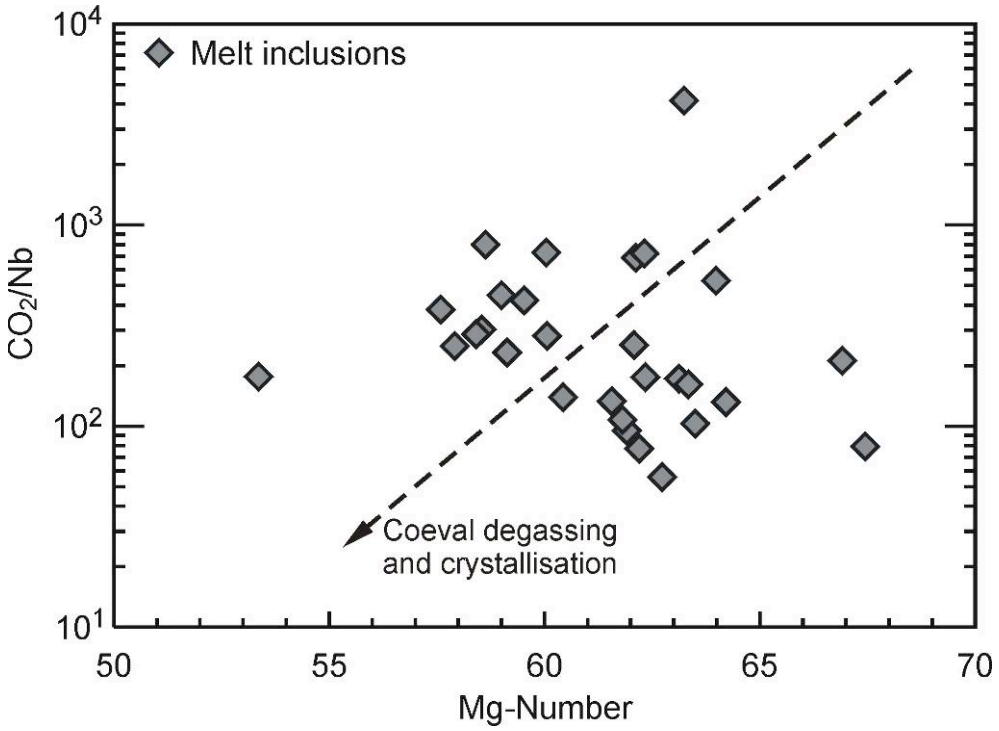

Supplementary Figure S4

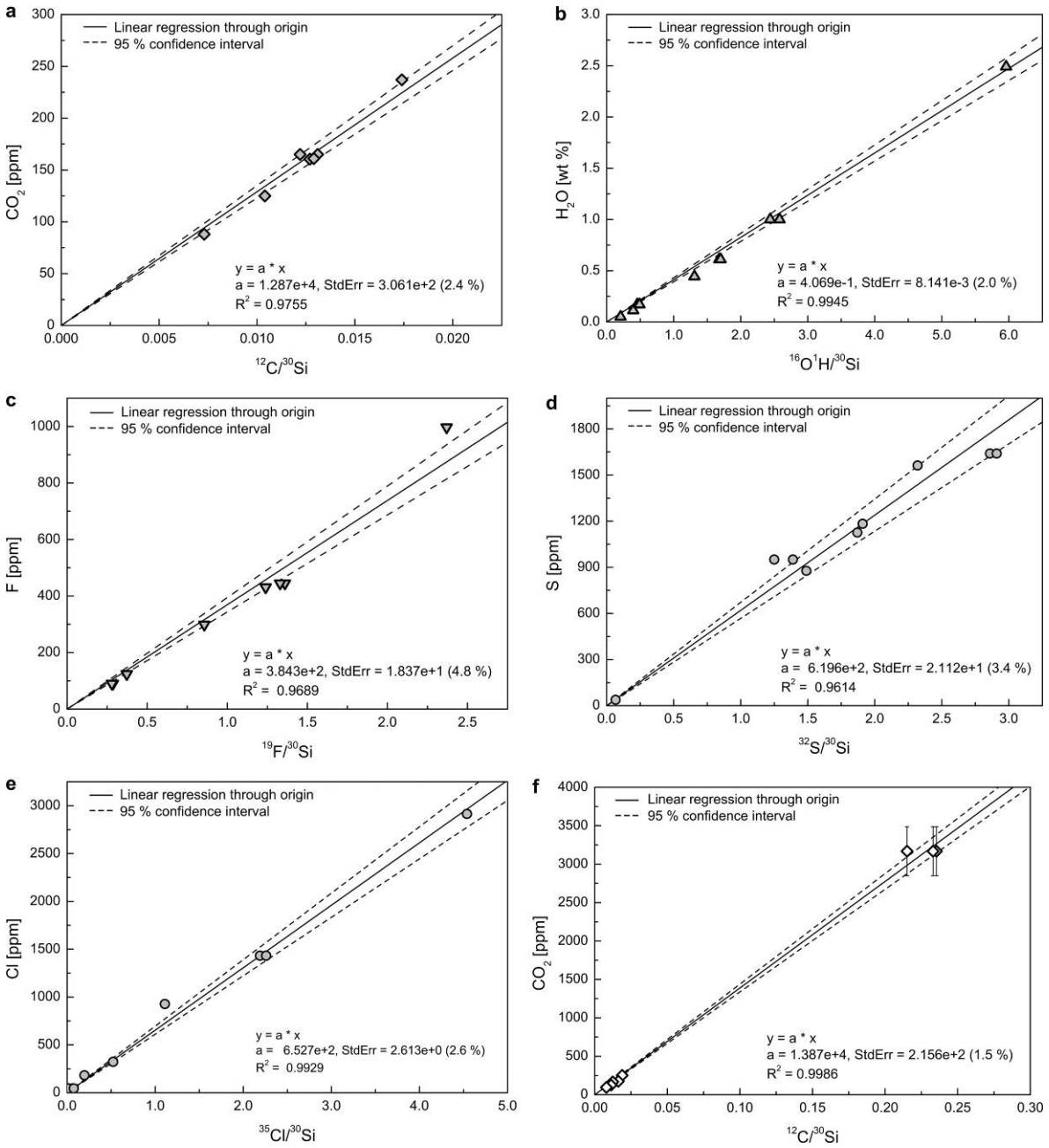

Supplementary Figure S5

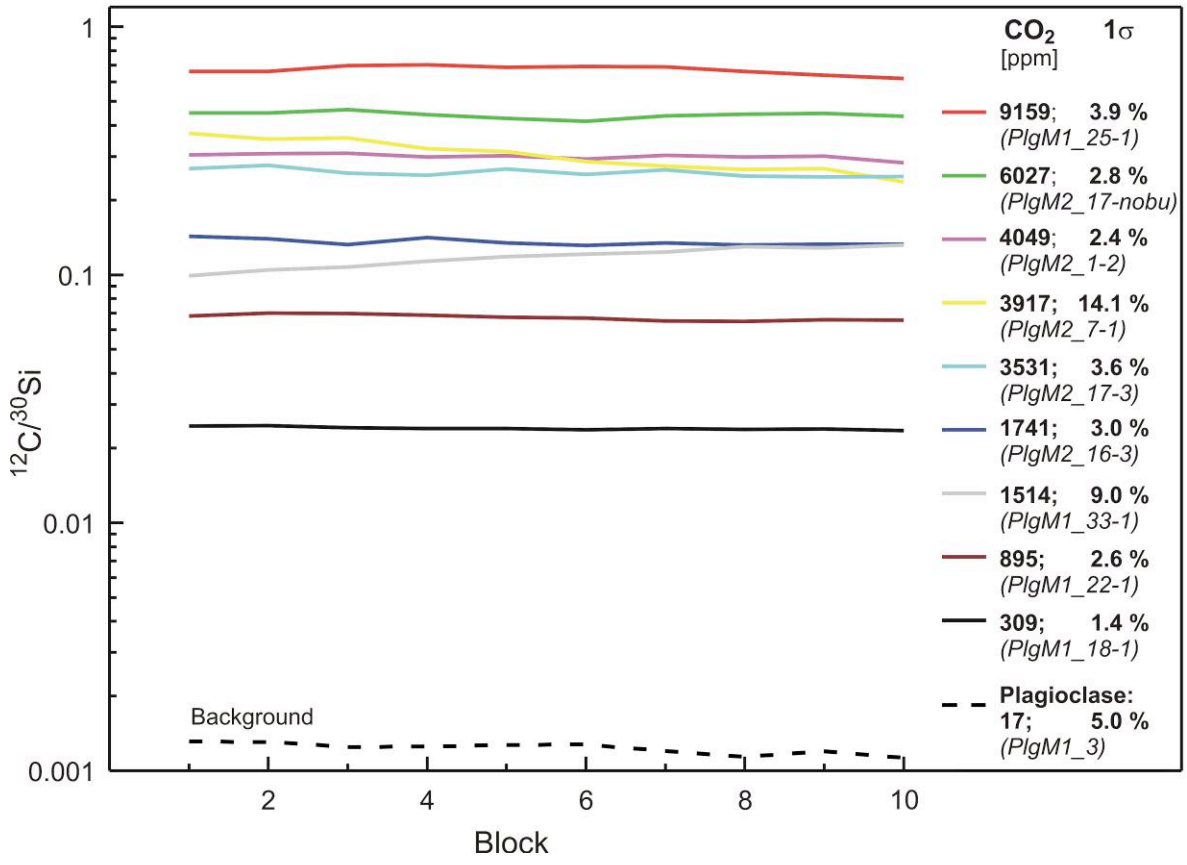

Supplementary Figure S6

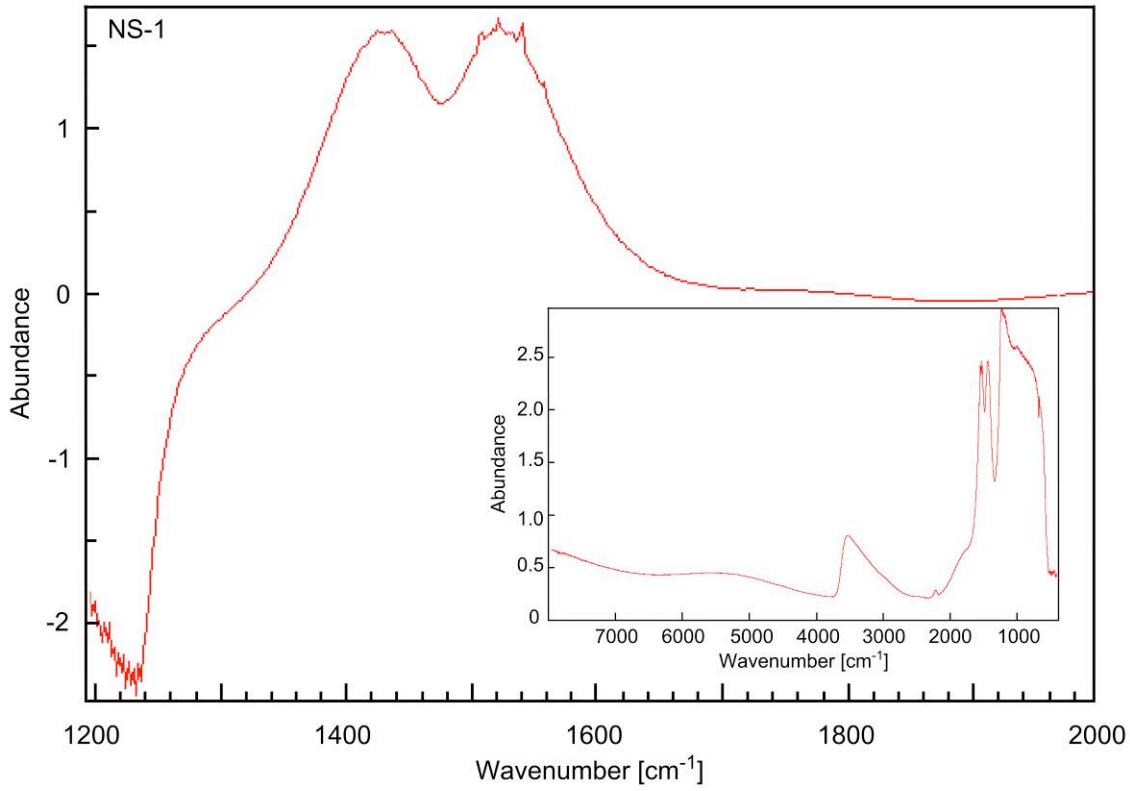

Bridge between Chapter 2 and Chapter 3:

In the previous two chapters, explosive strombolian–type activity driven by CO_2 bubbles was identified as the most plausible eruption mechanism forming the widespread volcaniclastic deposits on Axial Seamount. In comparison to such eruptions in subaerial environments, the overall fragment size is reduced, the fragments are entirely glassy, and evidence is present for both ductile and brittle fragmentation. Although eruptions in submarine and subaerial environments are governed by the same principles and processes, rapid heat transfer in submarine environments plays an important role in the fragmentation process and the overall behaviour of explosive eruptions in the deep sea. To investigate the interplay between fragmentation and quenching, the two main types of volcaniclastic glass fragments observed were analyzed by differential scanning calorimetry to model the natural cooling history of these materials.

Chapter 3. Rapidly quenched basaltic glasses from Axial Seamount: implications for submarine eruptions

Christoph Helo[1], David A. Clague[2], Donald B. Dingwell[3], John Stix[1]

[1]*Department of Earth and Planetary Sciences, McGill University, Montreal H3A 2A7, Canada*

[2] *Monterey Bay Aquarium Research Institute, 7700 Sandholdt Road, Moss Landing, CA 95039, USA*

[3]*Department of Earth and Environmental Sciences, University of Munich, Theresienstr. 41/III, Munich, Germany*

Manuscript III – to be published.

Abstract

We present a calorimetric analysis of pyroclastic glasses and glassy sheet lava flow crusts collected on Axial Seamount, Juan de Fuca Ridge, NE Pacific Ocean, at a water depth of about 1400 m. The pyroclastic glasses, (subdivided into thin limu o Pele fragments and angular, blocky clasts), were retrieved from various stratigraphic horizons in ash deposits on the upper flanks of the volcanic edifice. Each analyzed pyroclastic sample consists of a single type of fragment from one individual horizon. The heat capacity (c_p) was measured via differential scanning calorimetry (DSC) and analysed using relaxation geospeedometry to obtain the natural cooling rate across the glass transition. The limu o Pele samples (1 mm grain size fraction) and angular fragments (0.5 mm grain size fraction) exhibit cooling rates of $10^{4.3}$ to $10^{6.0}$ K s^{-1} and $10^{3.9}$ to $10^{5.1}$ K s^{-1}, respectively. The range of cooling rates determined for different pyroclastic deposits may relate to the size or intensity of the individual eruptions. The outer glassy crusts of the sheet lava flows were naturally quenched at rates between 63 K s^{-1} and 10^3 K s^{-1}. By comparing our results with published data on the very slow quenching of flow crusts, we suggest that (1) fragmentation and cooling appear to be coupled dynamically and (2) ductile deformation upon the onset of cooling is restricted due to the rapid increase in viscosity. Lastly, we explore potential consequences of ductile deformation in the vicinity of the glass transition for the development of certain flow morphologies such as inflated tube flows assuming high-temperature annealing as the origin of low apparent cooling rates in lava flow crusts.

1. Introduction

Valuable information can be learned from systems that are far from equilibrium. One example is volcanic glass that provides information on the kinetics of the cooling process. Compared to their equilibrium crystalline state, the structure and properties of glasses, such as enthalpy, are kinetically determined, exhibiting a cooling path dependence and therefore containing a thermal history (Dingwell and Webb, 1989, 1990).

Cooling strongly affects viscosity which is a key parameter controlling volcanic eruptions. Viscosity in turn may influence diffusivities (Dingwell, 1990), degassing (Navon et al., 1998), crystallization (Muncill and Lasaga, 1988), and fragmentation (Papale, 1999). Eruption style, whether explosive or effusive, depends strongly on these parameters. This holds true for silicic as well as basaltic systems, regardless of whether they are subaerial or submarine. Cooling also affects post-eruptive behaviour. The rate of heat dissipation influences the dynamics of eruption plumes, such as the extent and mode of clast dispersal. In deep-sea environments, very high rates of heat loss are expected as heat transfer occurs dominantly in the direct lava-water contact regime under non-stable film boiling conditions (Zimanowski and Büttner, 2003). Yet, apparent cooling rates from three previous studies vary greatly between 10^{6} to 10^{-2} K s^{-1} (Wilding et al., 2000; Potuzak et al., 2008; Nichols et al., 2009). While in an extreme case quench rates may approach the very short timescales of vapour expansion and fragmentation, they may likewise play a role in slower processes such as viscous shear deformation. To distinguish between these possibilities, information regarding the specific timescales is required. In order to gain a better understanding of such temperature–time evolution, significant

progress has been made towards quantifying quenching timescales.

One approach is to characterize the kinetics of the cooling process as the melt passes through the glass transition. This information, which is intrinsic to the glass structure, can be revealed via relaxation enthalpy geospeedometry using a differential scanning calorimeter (DSC) (e.g., Wilding et al. 1995, 1996). Within the past 15 years this has proven a powerful tool when applied to the emplacement of silicic lava (Gottsmann et al. 2001, 2002). Here we present calorimetric analysis of a suite of basaltic pyroclastic glasses and glassy sheet lava crusts from Axial Seamount on the Juan de Fuca spreading centre. We quantify the thermal histories of the samples in terms of the temperature at which the samples entered the glassy state, the associated stored internal excess energies, and their respective cooling rates using enthalpy relaxation-based geospeedometry. We demonstrate how the extraordinary rates of heat loss achieved during submarine pyroclastic eruptions assist the fragmentation process, and strongly impede viscous deformation as it becomes coupled to the cooling process. We further discuss the impact of such rapid heat transfer from the pyroclastic glasses to seawater upon the eruption plume and thus clast dispersal. Lastly, we discuss the potential ramifications of high temperature annealing for the rheology and formation of certain lava flow morphologies, under the assumptions that high-temperature annealing is responsible for the slow apparent cooling rates of lava flow crusts.

2. Background

2.1. Axial Seamount

Axial Seamount is the surface expression of an enhanced melting regime beneath a central segment of the Juan de Fuca Ridge (JdFR), an intermediate spreading-rate ridge with a total full-spreading rate of 6 cm yr^{-1} (Wilson, 1993; Fig. 1). The volcano is associated with the Cobb-Eickelberg seamount chain on the Pacific Plate (Johnson and Embley, 1990; Rhodes et al., 1990). Erupted lavas on Axial Seamount reflect mixing of a normal MORB source with a chemically distinct plume source (Chadwick et al., 2005). The prominent Axial volcanic edifice rises to about 1400 m below sea level, and is elevated up to 1000 m relative to the adjacent rift zones and basins. The summit is characterized by a U-shaped, 3 x 8 km diameter caldera, deepening towards the north end (Embley et al., 1990; Johnson and Embley, 1990). Its dimensions are similar to Kilauea caldera, Hawaii, and slightly smaller than Krafla caldera in Iceland (Rowland et al., 1999; Rymer et al., 1998). Adjacent to the main volcanic centre, rift zones extend ~50 km to the north and south. Due to enhanced magma supply from Axial Seamount, these rift zones form distinctive ridges dominated by constructional volcanic features, rather than the extensional faults typical for other segments of the JdFR. A magmatic reservoir is inferred at depths between 2.5 and 6 km beneath the volcano from seismic tomography (West et al., 2001). Nooner and Chadwick model an inflation source at a depth of ~ 3.5 km below the caldera. Pillow lava and sheet lava flows comprise the main constituents building the edifice (Appelgate and Embley, 1992). Wide areas along the rim and the flanks, and to a small degree the caldera floor, are covered by deposits of pyroclastic debris, that is thought to reflect pyroclastic activity (Clague et al., 2003b; Davis and

Clague, 2003; Clague et al., 2009).

2.2. Pyroclastic deposits and lava flows on Axial Seamount

We collected hyaloclastite glasses and glassy sheet lava samples during the MBARI 2006 Vance (dives *T1009* and *T1010*) and 2009 Pacific Northwest Expeditions (dive *D70*) using MBARI's remotely operated vehicles (ROV) *Tiburon* and *Doc Ricketts*. Pyroclastics were sampled along two traverses on the western and eastern flanks of Axial Seamount close to the rim employing pushcores and vibracores. The sheet lava flow samples were collected from the northeast rim of the caldera (Fig. 1B; see Clague et al., 2009 for details on sampling methods). All samples originate from a similar water depth (~1400 m below sea level). Pyroclastic units mainly comprise unconsolidated fine-grained (< 4 mm) glassy ash fragments, hydrothermal clays and broken plagioclase phenocrysts. The most abundant fragment types are angular glass fragments and limu o Pele glass shards (Fig. 2). Limu o Pele are ~10–150 μm-thick melt films, flat or slightly curved, sometimes strongly folded and bent, and interpreted as bubble walls (Clague et al., 2009). Intermixed with these are glass particles of various shapes, including Pele's hair, folded ribbons, and occasional scoriaceous and "tube-scoria" fragments. Fragment size distributions show appreciable variation within individual cores, but also core to core variations. Systematic trends with distance to the rim were not observed within the sampled. Maximum sample locality-rim distance was ~ 2 km. The chemical variability within individual cores suggests that less than 1 cm of material is deposited from single eruptive events. For thicker deposits at Loihi Seamount, Hawaii, Clague (2009) calculated accumulation rates of about 0.4 cm yr^{-1} between ~5800 yr BP and 3300 yr BP, and ~0.04 cm yr^{-1} for the last 3300 yr.

The physical model that has emerged over the past several years (Clague et al., 2003a; 2003b; Davis and Clague, 2003; Clague et al., 2009; Helo et al., 2008, 2011) suggests that pyroclastic fragments are produced by strombolian bubble burst events accompanying effusive activity. The extent of the strombolian activity and the abundance of pyroclastic debris appear to be positively correlated with effusion rates (Clague et al., 2009). In the course of an eruption, the particles are entrained into a rising eruption plume and widely dispersed (Clague et al., 2009). Other workers propose that such volcaniclastic fragments originate from interaction of sheet lava and seawater, i.e., bursting of steam-driven bubbles rising through a sheet lava flow (Maicher and White, 2001; Schipper and White, 2010). However, the occurrence of such deposits at depths below the critical point of water, as well as the discovery of high pre-eruptive CO_2 concentrations which drive explosive eruptions (Helo et al. 2011), support a pyroclastic origin.

Effusive activity on Axial Seamount has produced a wide range of lava flow types and morphologies (Embley et al., 1990). Common end-members are pillow lava flows, massive pillow mounds, and continuous sheet lava flows. Intermediate varieties include lobate lava flows, ropy lava with occasional lava whorls, or hummocky lava often confining flat sheet lava flows. Pillars and collapsed lava pits reveal the occurrence of drained lava lakes (e.g., Hammond, 1990; Zonenshain et al., 1989; Chadwick, 2003). Tumuli (Appelgate and Embley, 1992) or inflated lava flows (Fox et al., 2001; Paduan et al., 2009) have also been described on the floor of summit caldera. These various morphological lava types can be formed during the same volcanic episode. Different flow morphologies relate to variations in eruption rate, slope, and viscosity (Griffiths and Fink,

1992a, b).

2.3 The glassy state

The glassy state results from the increase in viscosity η and structural relaxation time τ as a liquid is cooled (Maxwell, 1967). Viscosity and relaxation time are linked by Maxwell's law:

$$\tau = \frac{\eta}{G_\infty}, \tag{1}$$

where G_∞ is the shear modulus at infinite frequency ($\log_{10} G_\infty$ (Pa) = 10 ± 0.5; Dingwell and Webb, 1989). The structural relaxation time is governed by the self-diffusivity of Si and O. If the relaxation time exceeds the structural relaxation rate, for example due to decreasing temperature, then the melt no longer responds as a liquid. Instead, solid-like behaviour is observed, and the system may be described as an amorphous solid, i.e., a glass. The glass transition is therefore a kinetic phenomenon, and its location in temperature-time space is unique (Dingwell, 1995; Dingwell and Webb, 1989; Webb and Dingwell, 1995). As the liquid is cooled and enters the glass transition interval, the structure becomes "frozen-in" with a configuration corresponding to the temperature at which the liquid crossed the glass transition, which in turn is rate dependent.

One approach to quantify this frozen-in structure by simplistic means is the concept of the limiting fictive temperature T_f'. It is defined as the temperature below which structural changes no longer occur (for the given timescale), and as such is a characteristic temperature located at the low temperature end of the transition interval. Determination of the limiting fictive temperature of a naturally cooled glass is the key

concept behind geospeedometry based on enthalpy relaxation, as it depends only on the cooling rate. Enthalpy is accessed via its derivative, the heat capacity c_p, using differential scanning calorimetry (Wilding et al., 1996; Wilding et al., 1995).

3. Analytical Procedure

3.1 Sample preparation

Ash particles from six individual pyroclastic units were analyzed. From each sample about 50 grains corresponding to ~20 mg of angular fragments and limu o Pele shards were carefully hand-picked and analyzed. The grain size fraction of the two particle types (~1 mm for limu o Pele shards and ~0.5 mm for angular fragments) was chosen such that they would yield comparable mean grain masses with similar amounts of total thermal energy released during the natural quench. The thickness of limu o Pele fragments was between 60 to 160 μm. From unit *T1009-VC1 20.8* we additionally analyzed the size fractions of 2 mm (limu o Pele) and 1 mm (angular fragments). Grains with visible phenocrysts or vesicles were avoided. The outermost 1-1.5 mm of the glassy sheet lava crusts were also analyzed. Prior to calorimetric analysis, the samples were ultrasonically cleaned, rinsed in distilled water, dried in an oven at 105 °C, and stored in a desiccator at room temperature.

3.2 Calorimetry

Heat capacities c_p were obtained using a differential scanning calorimeter (Netzsch® DSC 404C Pegasus). Baseline and sapphire standard measurements preceded

sample analysis and followed the same cooling/heating procedure. The standard mass used was comparable to the sample mass (21.42 mg and 42.66 mg for the pyroclastic glasses and sheet lava flow samples, respectively). The glasses were placed in a platinum crucible covered with a lid and flushed with argon during the entire period of the measurement. After an isothermal hold at 313 K, the naturally quenched glass samples were heated at a rate of 20 K min^{-1} across the glass transition into the supercooled liquid field to ensure complete structural relaxation, then cooled back to 313 K at a rate of 25 K min^{-1}. A series of heating and cooling treatments followed with heating rates of 25, 20, 15 and 10 K min^{-1}, matching the prior controlled cooling rate. Heating scans were aborted shortly after the sample had reached the supercooled liquid field to minimize chemical modification of the melt. The c_p data were then calculated using the sample mass, heat flow of the sample, the baseline and the sapphire standard (Archer, 1993) and standard mass. From the calorimetric data, the apparent cooling rate was modelled following the procedures outlined in Appendix A.

3.3 Sample stability during calorimetric analysis

Calorimetric analysis of basaltic glasses can be problematic in terms of the sample stability during measurement. When glasses are reheated under atmospheric pressures during measurement, they may undergo degassing, crystallization, unmixing, or oxidation. A successful measurement requires that the glassy part of each successive c_p curve matches that of the preceding run, thereby restricting degradation of the sample. Minor oxidation of the outer glass surface was observed, and in a few cases the onset of degassing was detected after the calorimetric peak in the c_p curve. However, significant volatile loss was not evident. Small amounts of exsolving H_2O would visibly foam dense

glass, but such behaviour was not observed. Reproducibility of the properties of the glassy state was good. As noted below, the chemical composition of the samples *D70-1SLR-1* and *D70-2SLR* were found to be identical within 1σ before and after calorimetric analysis for almost all major elements (Table 1).

3.4 Glass chemistry

Major elements, S and Cl compositions were determined for limu o Pele shards and angular fragments from each pyroclastic unit with a JEOL 8900 electron microprobe at McGill University using a beam current of 15 nA, an accelerating voltage of 15 kV and a defocused beam of 10 μm diameter. VG-99, VG-2 and KN9 standards were interspersed in the course of the measurements to check for spectrometer drift and accuracy. For each unit, 10 to 25 limu o Pele and angular fragments were analyzed with usually three spots per grain. Sheet lava glasses were averaged for 12 spots per sample.

Volatile element concentrations (H_2O, CO_2, Cl, F, and S) of the pyroclastic samples were determined with an IMS 1280 secondary ion mass spectrometer at the Woods Hole Oceanographic Institution. The samples were embedded in indium metal to ensure low backgrounds, polished, gold coated and dried prior to analysis in a vacuum oven at 110° C and 10^{-3} torr for ~ 12 h.

4. Results

4.1 Excess enthalpies and quench rates

Parameters derived from the calorimetric analyses are summarized in Table 2. All

investigated samples are characterized by a significant release of exothermic energy during the first experimental heating treatment, indicating hyperquenched configurational states (Fig. 3 and 5). The pyroclastic glasses exhibit a range in total stored excess energies ΔH_{tot} from 42 $\times 10^3$ to 30$\times 10^3$ J g^{-1} for limu o Pele fragments and 41$\times 10^3$ to 23$\times 10^3$ J kg^{-1} for angular fragments. The coarser fraction of unit *T1009-VC1 20.8* yielded stored excess energies of 27$\times 10^3$ J kg^{-1} and 37$\times 10^3$ J kg^{-1} for the limu o Pele and angular fragments, respectively. Excess energies stored in the glassy sheet lava samples are between 22$\times 10^3$ J g^{-1} and 11$\times 10^3$ J g^{-1}, generally lower than for the limu o Pele and angular fragments (Fig. 5). The process of exothermic enthalpy release starts at temperatures about 500 K (550-600 K for the sheet lavas). A striking asymmetry is observed in the distribution of released excess energy with temperature, which is more pronounced in the pyroclastic samples (Fig. 6). In detail, the distribution is often characterized by a "shoulder" or subordinate domain occurring between 600 and 700 K (~ 0.7.0.8 × T/T_g*; Fig. 6), and as such could indicate the superposition of a small second relaxation domain upon the broad main relaxation.

Limiting fictive temperatures of the limu o Pele samples are as high as 1103 K, and as low as 999 K. Angular fragments vary between 1060 K and 988 K, whereas the sheet lava flow samples entered the glassy state at temperatures between 998 K and 954 K. Limu o Pele shards and angular fragments thus experienced apparent linear cooling rates of $10^{6.3}$ to $10^{4.3}$ K s^{-1}, and $10^{5.6}$ to $10^{3.9}$ K s^{-1}, respectively. These values agree with data for similar pyroclastic fragments recovered from Loihi Seamount, including the fastest naturally quenched glasses analyzed to date (Potuzak et al., 2008). By contrast, quench rates of the outermost skin of the investigated sheet lava flows are much lower, between

$10^{3.0}$ K s^{-1} and $10^{1.8}$ K s^{-1}. These rates exceed those determined for glassy pillow lava rims and pyroclastic clasts from the Hawaii Scientific Drilling project, yielding rates of 0.1 to 72 K s^{-1} (Nichols et al., 2009), lava flow glasses and pyroclastic clasts from Seamount Six quenched at less than 0.003 to 0.4 K s^{-1} (Wilding et al., 2000).

4.2 Superimposed relaxation domains

The Axial Seamount pyroclastic deposits are the first natural glasses described to display a bimodal energy release with temperature (Fig. 6). A composite relaxation behaviour, or more specifically the existence of the small superimposed shoulder in the enthalpy relaxation curve of the glasses, has been attributed to either stored energies introduced by viscous flow, or alternately to the β-relaxation phenomenon. In contrast to the main α-relaxation, β-relaxation occurs at lower temperatures for a given time scale, or faster timescales for a given temperature, and exhibit lower activation energies (Dingwell, 1995). Martin et al. (2005) showed that mechanically induced stress can be stored when glass fibres are subjected to isothermal tensile stress within the glass transition interval. Applied stress correlated with the stored excess energies up to a certain maximum of stored energy. Work by Hornbøll et al. (2006) reached similar conclusions. In both studies, the stored viscous deformation energy introduced a relatively small exotherm at temperatures below the glass transition peak when reheated in the calorimeter. Interpretation of these experiments can however be somewhat problematic. As Hornbøll et al. (2006) indicate, it is unclear at what point the mechanical effect is introduced, i.e., during the isotherm under constant strain rates, or during the segment where the liquid is finally cooled below the glass transition.

Alternatively, subordinate relaxation domains seen in the excess energy distribution and the associated asymmetry with temperature, have been attributed to β-relaxation processes. Hornbøll and Yue (2008) and Hu and Yue (2008) argue for this processes on the basis of two observations. First, the small relaxation domain dissipates when the sample is annealed at low temperatures, consistent with the low activation energy of β-relaxation. Second, a second relaxation domain seems to be absent in strong glass-formers subjected to hyperquenching, and the α-domain is symmetrically distributed. The α- and β-relaxations in strong glasses are difficult to resolve in time or temperature space, as they are generally thought to exhibit very similar frequency response domains.

Limu o Pele from the pyroclastic units often display highly stretched vesicles indicating higher differential strain rates, in contrast to angular fragments with more rounded vesicle shapes. Yet the small relaxation domain is generally more pronounced in c_p curves derived from angular fragments. This observation is inconsistent with the model of mechanically induced energy release. On the other hand, fragilities of the pyroclastic glasses are fairly similar (note the nearly parallel curves in Fig. 4), yet the small relaxation domains vary in their extent and are rather small for the samples exhibiting the fastest cooling rates. Based on the "relaxation map" presented by Dingwell (1990) for sodium silicate melts, the expected temperature differences for the α- and β-relaxations are more than twice those observed here.

We hypothesize that in general the excess enthalpy released is entirely accounted for by extensive downward α-relaxation, and the asymmetry of the distribution is caused by the non-Arrhenian temperature dependence of the relaxation time in fragile systems. Due to a paucity of experimental data, a satisfying accounting for this observed

phenomenon is challenging. We speculate that some of the complexity seen in the c_p curves may be attributed to a combination of further effects including annealing.

5. Discussion

The extremely large range of apparent cooling rates seen in submarine basaltic glasses, from about $10^{1.8}$ to 10^6 K s^{-1} as seen on Axial Seamount to less than 0.003 K s^{-1} on Seamount Six (Wilding et al., 1996), indicates a rich complexity in the cooling histories of submarine glasses. However, a rough division in terms of the emplacement mode can be made. Limu o Pele shards generally have quench rates at the upper end of the range, angular fragments are mostly intermediate, and glassy lava flow rims yield rates at the lower end. This is broadly reflected in the stored excess energies (Fig. 5). The lowest apparent cooling rates seen in samples from Seamount Six and HSDP glass samples contrast with the cooling rates of both pyroclastic units and sheet lava flows, reflecting different emplacement modes and thermal histories. Pyroclastic samples from HSDP were erupted at shallow water depths (< 10 m) and fragments are though to have been ejected above the sea surface and quenched in air to explain their slow cooling (Nichols et al. 2009). Very slow cooling of both the HSDP pillow lava crusts emplaced in several hundred meters of water, as well as some lava flow glasses on Seamount Six, were attributed in both studies to reheating and annealing processes. Nichols et al. (2009) suggest subsequent flow units or even latent heat of crystallization from the pillow interior as potential heat sources.

Evaluation of the cooling rates of the samples from Axial Seamount in light of theoretical considerations can be done by employing a simple model of linear conductive

heat flow in a half-space, based on the error function (Carslaw and Jaeger, 1959; see Appendix B, Eq. (5)). This model describes the evolution of temperature as a function of time and distance to the melt-water interface, which is kept at constant temperature (Fig. 7). To evaluate the fastest possible cooling, we used an interfacial temperature of ambient seawater (275 K) and an eruption temperature of 1475 K. No allowance for steam envelopes was made. The numerical solutions address heat loss through the one plane face of the idealized cuboid or platy fragment geometries.

In such a scenario, isotherms initially advance very rapidly through the melt. At a depth of 60 μm and 160 μm (the range of thickness of limu o Pele), cooling rates at a limiting fictive temperature of 1035 K are about 10^5 K s^{-1} and 10^4 K s^{-1}. Cooling rates at a depth of 0.5 mm, corresponding to the size of angular fragments, are about 10^3 K s^{-1}. Maximum cooling rates decrease with depth, resulting in a "stratification" of limiting fictive temperatures parallel to the cooling surface. The simplified numerical solution models the cooling rate at a certain distance from the interface, whereas the DSC analysis gives the mean limiting temperature over the full distance from the interface. The maximum cooling rates suggested by the numerical solution (Fig. 7) are about an order of magnitude lower than those derived from the DSC measurements. In nature, heat loss will occur over a larger surface area than accounted for by the numerical half-space simulations. If fragmentation precedes cooling or occurs coincidently, heat loss can be achieved over almost the entire surface of the clast and will increase drastically due to fracturing. More importantly, this comparison also indicates that in submarine environments, cooling rates can approach the theoretical limit of heat loss rates in terms of intrinsic thermal diffusivity in the absence of convection. Such extraordinarily rapid

cooling processes will influence the eruption dynamics, fragmentation, and evolution of eruptive plumes as well as syn- and post-eruptive degassing.

5.1 Pyroclastic eruptions

Two features are striking regarding the quench rates of the pyroclastic units. Limu o Pele shards have a strong tendency towards higher quench rates compared to the angular fragments, and the pyroclastic units show a wide range. Due to similar initial thermal energies of the angular fragments and limu o Pele shards, the general difference in quench rates is most likely accounted for by their different surface/mass ratios. For a given heat flux per unit area, the thin platy limu o Pele fragments with their higher surface/mass ratio will achieve faster quench rates than the angular fragments.

The wide spectrum of cooling rates, especially seen in limu o Pele samples from different units (Fig 4), ranging over more than two orders of magnitude, is somewhat surprising. Despite their comparable mean grain mass, size and surface area, the average rate of heat loss differed significantly for the limu o Pele samples from the various stratigraphic units. The total thermal energy ΔQ each limu o Pele fragment has lost as it cooled is about 0.2 Joule up to the glass transition, and 0.8 Joule when ambient seawater temperature is reached (approximated by the mean fragment mass, heat capacity and temperature difference). This energy was lost over comparable surface areas, but at a different heat flux per unit area. Although the total thermal energy that is lost per pyroclastic fragment is small, the rate of heat transfer per mass is generally high for all pyroclastic glasses (Table 2) and most likely completed close to the vent-water interface. Conditions within that region will thus determine the specific quench rate. At higher mass discharge rates, mixing with seawater directly above the vent will be less effective and

the overall cooling rate lower. At the same time, a higher mass discharge during Strombolian eruptions releases larger amounts of CO_2 bubbles (Helo et al. 2011), and the ambient surrounding fluid will adopt characteristics of a two-phase flow with a stronger insulating effect until CO_2 is dissolved into the seawater. Variations of the quench rate observed among limu o Pele from separate deposits may therefore be related to differences in mass discharge rate, reflecting vent diameter and exit velocity conditions.

Fragmentation

Viscosity at the glass transition of silicic glasses from subaerial lava flows is usually > 10^{12} Pa s, whereas for glassy crusts from basaltic pāhoehoe lava, 10^{10} to 10^{11} Pa s appear to be common (Gottsmann and Dingwell, 2002; Gottsmann et al., 2004). By contrast, melts of our studied pyroclastic glasses have entered the glassy state at viscosities as low as $10^{5.3}$ Pa s. Compared to subaerial glasses, the pyroclastic glasses were quenched as a low-viscosity liquid, with accordingly short relaxation times, immediately prior to their transition to a brittle glass. The complex morphologies and highly stretched vesicles present in many limu o Pele fragments (Fig. 2F) result from deformation and shearing within this low-viscosity regime. Yet the edges of limu o Pele shards and surfaces of angular fragments indicate brittle rupture and fragmentation, with resulting surfaces resembling those produced by hydromagmatic processes.

On the other hand, it is evident from the occurrence of fluidal forms such as curled Pele's hair and stretched ribbons that fragmentation also occurs before cooling commences. Hence, there appears to be a short time window for most of the fragmentation and cooling to occur, indicating that both processes may be coupled in time (less than 10^{-5} to $10^{-3.5}$ s) and possibly dynamically, as well. Fragmentation due to stress

wave and film collapse as envisioned by Wohletz (1983) is unlikely to occur since the necessary film boiling is restricted to pressures less than 1 MPa (Zimanowski and Büttner, 2003). Similarly, cooling-contraction granulation (Head and Wilson, 2003; Kokelaar, 1986) can be ruled out. In that model, the outer rapidly quenched and rigid layer of the ejected clasts is exposed to stress, while the interior of the clast slowly cools and contracts. Compression-induced cracking and granulation is the result. Fragmentation in this case occurs after the melt has quenched, hence in the glassy state rather than close to the glass transition. The differences in cooling rates between sheet lava crusts and angular fragments further support the idea that angular fragments are not simply produced by the disintegration of lava flow crusts.

As a simple but potentially effective alternative mechanism, we suggest that fragmentation is assisted by water expansion-induced stresses. As clasts are ejected and their outermost skin quenched, small fractures develop and deepen as the inner part of the clast continues to deform by viscous flow and the glass rind thickens. Water entrapped in the growing fractures will be heated and expand, potentially achieving metastable film boiling conditions to generate extensional stress perpendicular to the surface. In this manner the initially ductile fragmentation process (strombolian type bubble bursts) producing larger clasts is assisted by simultaneous quenching and stress-induced brittle fragmentation in the vicinity of the glass transition, or even within the glass transition if strain rates approach $10^{3.5}$ to 10^{5} s^{-1}. This coupling of processes is one of the key consequences of such extreme quench rates. Upon the onset of cooling, shear deformation, such as the expansion of melt films or bubbles, must overcome a viscosity that is rapidly increasing. The melt viscosity changes from about 10 Pa s at the time of

eruption to about $10^{5.3}$ to $10^{7.3}$ Pa s when the glassy state is reached within 0.0004 to 0.1 s, respectively. This inhibits significant deformation or expansion of the melt films with the onset of cooling.

Eruption plumes

The discrepancy in cooling timescales between the pyroclastic glasses and glassy lava flow crusts reflects differences in the rate of heat transfer Φ per mass Φ/m ($\Phi = \Delta Q/\Delta t$), an important parameter that can influence the dynamics of eruption plumes. The impact on the plume will depend on the size of the pyroclastic event, which is unconstrained for Axial Seamount. This conceptual discussion applies to significantly energetic eruptions as defined by Head and Wilson (2003). Given the high quench rates, the small total thermal energy loss per fragment is achieved over short timescales, resulting in very high rates of heat transfer. For Axial Seamount the rate delivered by the coarser grained fragments sections is on the order of 7×10^{6} to 1.4×10^{9} W m^{-2}, significantly exceeding those for sheet lava flows. For a small lava flow body of 0.5 m × 5 m × 20 m, heat transfer rates are on the order of 3×10^{3} W m^{-2} (Table 2, Appendix B). For a cooling rate of 10^{4} K s^{-1} and assuming a linear heat loss rate from magmatic to low temperatures, the coincident fragmentation of one m^3 of magma would be sufficient to produce a large 30 GW eruption plume. Although this estimate is rather crude, it indicates the capability of such eruption events. The total heat loss during the eruption cannot be assessed as the size of the historical eruptions forming these deposits is unconstrained. Nevertheless, certain constraints can be made on the dynamics of eruption plumes of these pyroclastic eruptions. In deep submarine environments, eruptions are characterized by reduced bubble rise velocities and ejecta momentum due to suppressed gas expansion.

Given the very short cooling times, ejected fragments mix with the water immediately above the vent. This small volume of water is then rapidly heated at a rate of ~ 10^5 to 10^4 K s^{-1} and expands at a rate depending on the ratio between the mass of the melt and the seawater. For comparison, average heat transfer rates in eruptions plumes from the NW Rota-1 were inferred to be > 200 K s^{-1} within the first 2 m above the vent (Deardorff et al., 2011). This lower heat transport in these plumes might reflect the larger median grain size of clasts. The basal part of the eruption column, which is purely momentum-driven (Sparks, 1986), is characterized by expansion of the rapidly heated seawater above the vent, and rapid loss of the initially small momentum of the ejecta due to turbulent mixing above the vent and the high density of the overlying water column. Consequently, the basal part of the eruption column will be restricted in height.

Above the basal part, a sudden onset of buoyancy-drive convective flow promoted by the rapid heat loss can be expected, causing the plume to rise until neutral buoyancy is reached by continuous seawater entrainment. The sudden development of a buoyant plume is anticipated to promote an efficient separation of clasts. Larger ejecta will deposit close to the vent, as they are decelerated within the basal region. Smaller fragments, especially thin platy limu o Pele fragments, will be lifted by the heated buoyant seawater and entrained into the rising plume. If the buoyant plume reaches depths of deep-water currents, it will be deflected, and long-range dispersal of the smaller fragments can occur. The anticipated characteristics of eruption plumes developing during the course of submarine strombolian bubble bursts differ from Head and Wilson's (2003) model for which uplift by thermally buoyant seawater is not explicitly taken into account, and absolute plume heights are limited.

Our conceptual model is in good agreement with the widespread distribution of deposits on the flanks of Axial Seamount, the Northern Escanaba Trough (Clague et al., 2009) and at Gakkel Ridge (Sohn et al., 2008), as well as the dispersal model by Barreyre et al. (2011). But it is contrary to the spatial size distribution anticipated by Head and Wilson's (2003) model. Their model assumes the loss of initial momentum to be the key factor governing deposition of larger and smaller fragments. In their model, larger clasts will fall out beyond the finer grained deposits, due to their greater inertia. Given the very rapid cooling rates reported here, the likelihood of welding of pyroclastic ash deposits is strongly reduced, as the heat loss experienced prior to deposition is too great. Agglutinated deposits may only form in the presence of larger blocks or bombs that have maintained a hot interior.

5.2 Lava flow rheology

Reduced cooling rates of basaltic lava flow crusts, as seen in samples *D70-1SLR-1* and *D70-2SLR*, have also been described for various submarine basaltic glasses from Seamount Six (Wilding et al., 2000), HSPD pillow crusts (Nichols et al., 2009), and subaerial pāhoehoe lava flow crusts (Gottsmann et al. 2004). Wilding et al (2000) and Nichols et al (2009) invoke reheating and high temperature annealing as one of the possible processes causing slow apparent cooling rates. Heat may be supplied by crystallization of the pillow interior or by subsequent, overriding flows. Gottsmann et al. (2004) suggested insulation by a vesiculated crust as a mechanism to induce isothermal annealing, which may affect flow emplacement and assist inflation.

Submarine lava flow morphologies can be interpreted generally within the conceptual model of Griffiths and Fink (1992a, b) and Gregg and Fink (1995). Lava flow

inflation is seen as the result of slowly moving lobate or tube-fed flows that cease to advance but are continuously supplied with new lava and inflate (Appelgate and Embley, 1992; Gregg and Chadwick, 1996). The relation between emplacement and cooling history has been studied extensively in subaerial lava flow fields of intermediate to silicic composition (Gottsmann and Dingwell, 2001; Stevenson et al., 2001; Wilding et al., 1996). If complex time-temperature histories within the glass transition interval, caused by reheating and annealing during flow emplacement, are indeed the reason for slow apparent cooling of submarine lava flow crusts, ductile deformation can be expected to influence flow emplacement. In analogy to subaerial lava flow inflation (Hon et al., 1994; Gottsmann et al. 2004), annealing may consequently facilitate submarine flow inflation or the development of ropy textures and lava whorls in channelized flows. This model involves primary quenching of the outer surface, thermal annealing/relaxation within the glass transition interval through heat supplied from the flow interior, and ductile deformation of the flow crust. After initial lobate flow emplacement and rapid quenching of the outer crust, the interior is essentially sustained at a constant temperature close to that at the point of eruption, as hot lava continuously passes through tubes or channelled flows. Such a heat source could partially reheat the crust, eventually maintaining an isothermal hold at a dwell temperature (T_1, T_2 or T_3 in Fig. 8). Complete relaxation is achieved after the relaxation time interval Δt, and ductile deformation of the crust can be sustained as long as deformation timescales are slower than the relaxation timescale. In the case of inflated flows, ductile deformation at late stages may become less important. As the flow crust thickens and cools, deformation rates can exceed relaxation time scales. Prominent cracks as observed along the crest of large inflated tumuli (Paduan et al. 2009)

can result. Paths similar to $\Delta t_{1,2} - T_{1,2}$ would result in thermal histories as seen in *D70-1SLR-1* and *D70-2SLR*. For path $\Delta t_3 - T_3$ apparent cooling rates fall in the range of those from Seamount Six (Wilding et al., 2000). Such complex temperature-time histories may also affect the formation of and transitions between various flow morphologies (Gregg and Fink, 1995; 1992a, b) by reducing the effective solidification timescale and promoting the transition from lineated to ropy sheet flows. Viscosities at the glass transition of the subaerial flows investigated by Gottsmann et al. (2004) are high (~10^{11} Pa s), compared to viscosities as low as $10^{8.3}$ Pa s displayed by the lava flow crusts on Axial Seamount. Consequently, isothermal annealing in submarine environments is possible over a wider range of temperatures and viscosities than observed in subaerial environments.

6. Conclusions

Basaltic pyroclastic glasses and glassy sheet lava flow crusts from Axial Seamount were analysed by calorimetry, and rates of cooling across the glass transition were determined. All samples were characterised by hyperquenched configurational stages revealed by a strong exothermic energy signal in the DSC curves. In general, limu o Pele fragments have the fastest cooling rates from $10^{6.3}$ to $10^{4.3}$ K s^{-1}, angular fragments have intermediate rates between $10^{5.6}$ and $10^{3.9}$ K s^{-1}, whereas sheet lava flow crusts were cooled the slowest at rates between 10^{3} to $10^{1.8}$ K s^{-1}. Details in the heat capacity curves of the pyroclastic glasses indicate a complex relaxation behaviour showing two distinct domains. The calorimetric record shows that extremely rapid rates of heat loss are feasible during submarine eruptions taking place at depths of 1400 m. It further

demonstrates the range of cooling rates possible among pyroclastic deposits derived from different pyroclastic eruptions from one volcanic system. We suggest that pyroclastic glasses and pyroclastic eruptions are characterised by interrelationships between eruption dynamics and rate of heat dissipation of the ejecta. While cooling rates in the central part of the eruption column will be reduced during large eruption events, lower turbulence during small, low-energetic bubble burst eruptions could give rise to buoyant plumes promoting dispersal of small particles with high surface/mass ratios such as limu o Pele.

On the basis of the wide range of cooling rates of glassy lava flow crusts determined from this study and previous investigations (Wilding et al., 2000), annealing appears to be a common process. This mechanism could facilitate the development of various lava flow morphologies and structures such as inflated lava flows, allowing for ductile deformation of the quenched flow crust.

Appendix A – cooling rate determination

The approach taken in this study to determine cooling rates is based on the calculation of the limiting fictive temperature after Yue et al. (2002). The more common Tool-Narayanaswamy method (Narayanaswamy, 1971; Tool, 1946; Wilding et al., 1995) is not applicable in the case of hyperquenched glasses, exhibiting a strong exothermic enthalpy release observed during the first heating treatment. Yue et al.'s (2002) method has been applied successfully in two previous studies on natural hyperquenched glasses (Nichols et al., 2009; Potuzak et al., 2008), agreeing well with the Tool-Narayanaswamy method for samples where both methods could be applied. The natural limiting fictive

temperature T_f' is related to the cooling rate via a non-Arrhenian relationship, calculated after the viscosity model of Giordano et al. (2008; "GRD-model"). The key concepts of the energy balancing method are briefly outlined here (Fig. 3A; for a complete discussion see Yue et al. (2002)). The strong downward inflection in the curve seen during the first heating scan c_{p1st} is related to the enthalpy stored in the glass as it was naturally quenched.

To obtain T_f', the total excess enthalpy ΔH_{tot} relative to the glassy state c_{pg} during the first heating treatment is balanced with the enthalpy necessary to "push" the supercooled liquid back to the temperature at which it started to deviate from its equilibrium configuration:

$$\Delta H_{tot} = \int_{Tex}^{Tg*} (c_{pg} - c_{p1st}) \mathrm{d}T \,, \tag{2}$$

$$\int_{Tex}^{Tg*} (c_{pg} - c_{p1st}) \mathrm{d}T = \int_{Tg*}^{Tf'} (c_{p1st} - c_{pg}) \mathrm{d}T \tag{3}$$

where T_{ex} is the temperature where the enthalpy release starts, and T_g* the temperature at which the c_{p1} curve crosses the c_{pg} curve, hereafter termed the crossover temperature. The heat capacity of the glassy state c_{pg} is fitted to the c_p curve below the glass transition (Fig. 3A) using the Maier-Kelley approximation:

$$c_{pg} = \mathrm{a} + \mathrm{b} \times T + \mathrm{c} / T^2 \,, \tag{4}$$

The left-hand side of Eq. (3) is represented by the area A in Fig. 3A, and the right-hand side by area B. T_f' is then determined such that areas A and B match. The limiting fictive temperature T_f' for the additional family of curves, for which the cooling/heating

rates were experimentally controlled, are derived by the method described in Moynihan et al. (1976). For these curves T_f' and the associated cooling rates are known.

T_f' is related to its natural cooling rate by the non-Arrhenian relationship between temperature and viscosity or cooling rate (Fig. 4). This relationship is calculated after Giordano, et al. (2008) for each sample chemistry. Shear viscosity η_s at T_g is translated into cooling rate q by:

$$\log_{10} \eta_s \text{ (at } T_g) = K - \log_{10} | q |, \quad (5)$$

where K is the shift factor (Gottsmann et al., 2002; Stevenson et al., 1995). The limiting fictive temperature T_f' as defined by Moynihan et al. (1976) is similar to the onset temperature of the glass transition interval (T_g^{onset}), for which an empirical shift factor of 11.3 has been determined (Scherer, 1984). The position of the curves in $q - 1/T_f'$ space is adjusted using the pairs of known cooling rate/limiting fictive temperatures (Fig. 4).

Appendix B – additional equations

Conductive heat flow in two half-spaces with a constant temperature at the interface was modelled after Carslaw and Jaeger (1959):

$$T(x,t) = \Delta T \, erf\left(\frac{x}{2\sqrt{\kappa t}}\right) + Ti \quad (6)$$

where x is the distance [m] to the melt-water interface (i.e., the thickness of a limu o Pele or angular fragment), t is the time [s], and κ the thermal diffusivity. The initial temperature difference ΔT = 1200 K, and an ambient seawater temperature of 275 K is

taken as the constant interfacial temperature T_i.

The heat flux per unit area $\Phi/A = \Delta Q \times \Delta t^{-1} \times A^{-1}$ [W m^{-2}] of the hyaloclastic glasses at the time of the glass transition is approximated after $\Phi/A = c_p \times D \times \rho \times q$, where A is the area [m^2], c_p the specific heat capacity [J kg^{-1} K^{-1}], D the particle diameter [m], ρ the density [kg m^{-3}] and q the cooling rate [K s^{-1}]. Simplified particle morphologies (cuboids and thin plates) and unidirectional heat transfer are used. The heat transfer rate per mass Φ/m [W kg^{-1}] of the hyaloclastic glasses is approximated by $\Phi/m = c_p \times q$.

The rate of heat uptake of the surrounding seawater is calculated after $h = \Phi/m$ x c_{pw}^{-1}, and its expansion rate as $e = \Phi/m$ x c_{pw}^{-1} x α x (m/m_w), where m_w, c_{pw} and α denote the mass [kg], specific heat capacity [J kg^{-1} K^{-1}] and thermal expansion coefficient [K^{-1}] for 3.2 wt% NaCl seawater under ambient conditions. For the sheet lava flows, Φ/m is approximated with the heat flux ϕ_{total} (convective plus radiative flux) using Eqn. 7a, b, and substituting $\Delta Q = \phi_{\text{total}}$ x *area* x Δt, giving $\Phi/m = \phi_{\text{total}}$ x *area* x m^{-1} (volume dimension of the lava flow used: 0.5 m x 5 m x 20 m).

The buoyancy-driven convective flux ϕ_{conv} in the absence of film boiling and the radiative flux ϕ_{rad} are numerically given by (Griffiths and Fink, 1992a):

$$\phi_{\text{conv}}(T) = \rho_w c_{pw} \gamma \left(g \alpha \frac{\kappa_w^2}{\nu_w}\right)^{\frac{1}{3}} (T - T_w)^{\frac{4}{3}} \quad (7a)$$

$$\phi_{\text{rad}}(T) = \varepsilon \sigma (T^4 - T_w^4) \quad (7b)$$

where ρ_w, κ_w, ν_w, and T_w denote density, heat capacity, thermal diffusivity, and kinematic viscosity of the ambient seawater, γ is a constant, g is the gravitational

acceleration, σ is the Stefan-Boltzmann constant, and ε emissivity from the lava flow surface. See Table 3 for parameter values.

References

Appelgate, B., Embley, R.W., 1992. Submarine tumuli and inflated tube-fed lava flows on Axial Volcano, Juan-De-Fuca Ridge. Bull. Volcanol. 54, 447-458.

Archer, D.G., 1993. Thermodynamic properties of synthetic sapphire (α-Al_2O_3), standard reference material 720 and the effect of temperature-scale differences on thermodynamic properties. Journal of Physical and Chemical Reference Data 22, 1441-1453.

Barreyre, T., Soule, S.A., Sohn, R.A., 2011. Dispersal of volcaniclasts during deep-sea eruptions: Settling velocities and entrainment in buoyant seawater plumes. J. Volcanol. Geotherm. Res. 205, 84-93, doi:10.1016/j.jvolgeores.2011.05.006.

Bischoff, J.L., Rosenbauer, R.J., 1985. An empirical equation of state for hydrothermal seawater (3.2% NaCl). Amer. J. Sci. 285, 725-763.

Carslaw, H.S., Jaeger, J.C., 1959. Conduction of heat in solids. Oxford University Press, Oxford.

Chadwick, W.W., Jr., 2003. Quantitative constraints on the growth of submarine lava pillars from a monitoring instrument that was caught in a lava flow. J. Geophys. Res. 108, 2534. doi:10.1029/2003jb002422.

Clague, D.A., 2009. Accumulation rates of volcaniclastic deposits on Loihi Seamount, Hawaii. Bull. Volcanol. 71, 705-710. doi:10.1007/s00445-009-0281-y.

Clague, D.A., Batiza, R., Head, J.W.I., Davis, A.S., 2003a. Pyroclastic and Hydroclastic Deposits on Loihi Seamount, Hawaii, in: White, J.D.L., Smellie, J.L., Clague, D.A. (Eds.), Explosive Subaqueous Volcanism. American Geophysical Union, Washington, D.C., pp. 73-95.

Clague, D.A., Davis, A.S., Dixon, J.E., 2003b. Submarine Eruptions on the Gorda Mid-Ocean Ridge, in: White, J.D.L., Smellie, J.L., Clague, D.A. (Eds.), Explosive Subaqueous Volcanism. American Geophysical Union, Washington, DC, pp. 111-125.

Clague, D.A., Paduan, J.B., Davis, A.S., 2009. Widespread strombolian eruptions of mid-ocean ridge basalt. J. Volcanol. Geotherm. Res. 180, 171-188.

doi:10.1016/j.jvolgeores.2008.08.007.

Davis, A.S., Clague, D.A., 2003. Hyaloclastite from Miocene Seamounts Offshore Central California: Compositions, Eruptions Styles, and Depositional Processes, in: White, J.D.L., Smellie, J.L., Clague, D.A. (Eds.), Explosive Subaqueous Volcanism. American Geophysical Union, Washington, DC, pp. 129-141.

Deardorff, N.D., Cashman, K.V., Chadwick Jr, W.W., 2011. Observations of eruptive plume dynamics and pyroclastic deposits from submarine explosive eruptions at NW Rota-1, Mariana arc. J. Volcanol. Geotherm. Res. 202, 47-59, doi:10.1016/j.jvolgeores.2011.01.003.

Dingwell, D.B., 1990. Effects of structural relaxation on cationic tracer diffusion in silicate melts. Chem. Geol. 82, 209-216.

Dingwell, D.B., 1995. Relaxation in silicate melts; some applications, in: Stebbins, J.F., McMillan, P.F., Dingwell, D.B. (Eds.), Reviews in mineralogy. Mineralogical Society of America, Washington, D.C, pp. 21-66.

Dingwell, D.B., Webb, S.L., 1989. Structural Relaxation in Silicate Melts and Non-Newtonian Melt Rheology in Geologic Processes. Phys. Chem. Miner. 16, 508-516. doi:10.1007/BF00197020.

Embley, R.W., Murphy, K.M., Fox, C.G., 1990. High-resolution studies of the summit of Axial Volcano. J. Geophys. Res. 95, 12785-12812.

Fox, C.G., Chadwick, W.W., Embley, R.W., 2001. Direct observation of a submarine volcanic eruption from a sea-floor instrument caught in a lava flow. Nature 412, 727-729.

Giordano, D., Russell, J.K., Dingwell, D.B., 2008. Viscosity of magmatic liquids: A model. Earth Planet. Sci. Lett. 271, 123-134. doi:10.1016/j.epsl.2008.03.038.

Gottsmann, J., Dingwell, D.B., 2001. The cooling of frontal flow ramps: a calorimetric study on the Rocche Rosse rhyolite flow, Lipari, Aeolian Islands, Italy. Terra Nova 13, 157-164.

Gottsmann, J., Dingwell, D.B., 2002. The thermal history of a spatter-fed lava flow: the 8-ka pantellerite flow of Mayor Island, New Zealand. Bull. Volcanol. 64, 410-422. doi:10.1007/s00445-002-0220-7.

Gottsmann, J., Harris, A.J.L., Dingwell, D.B., 2004. Thermal history of Hawaiian

pahoehoe lava crusts at the glass transition: implications for flow rheology and emplacement. Earth Planet. Sci. Lett. 228, 343-353. doi:10.1016/j.epsl.2004.09.038.

Gregg, T.K.P., Chadwick, W.W., 1996. Submarine lava-flow inflation: A model for the formation of lava pillars. Geology 24, 981-984.

Gregg, T.K.P., Fink, J.H., 1995. Quantification of submarine lava-flow morphology through analog experiments. Geology 23, 73-76.

Griffiths, R.W., Fink, J.H., 1992a. The morphology of lava flows in planetary environments: Prediction from analog experiments. J. Geophys. Res. 97, 19739-19748.

Griffiths, R.W., Fink, J.H., 1992b. Solidification and Morphology of Submarine Lavas - a Dependence on Extrusion Rate. J. Geophys. Res. 97, 19729-19737.

Hammond, S.R., 1990. Relationships between lava types, seafloor morphology, and the occurrence of hydrothermal venting in the ASHES Vent Field of Axial Volcano J. Geophys. Res. 95, 12875-12893.

Head, J.W., Wilson, L., 2003. Deep submarine pyroclastic eruptions: theory and predicted landforms and deposits. J. Volcanol. Geotherm. Res. 121, 155-193.

Helo, C., Clague, D.A., Stix, J., 2008. Pyroclastic eruptions from Axial caldera, Juan de Fuca Ridge, NE Pacific Ocean. IOD Conf. Ser.: Earth Environ. Sci. 3, 012005. doi:10.1088/1755-1307/3/1/012005.

Helo, C., Longpré, M.-A., Shimizu, N., Clague, D.A., Stix, J., 2011. Explosive eruptions at mid-ocean ridges driven by CO_2-rich magmas. Nature Geosciences 4, 260-263. doi:10.1038/ngeo1104.

Hon, K.E.N., Kauahikaua, J.I.M., Denlinger, R., Mackay, K., 1994. Emplacement and inflation of pahoehoe sheet flows: Observations and measurements of active lava flows on Kilauea Volcano, Hawaii. Geol. Soc. Am. Bull. 106, 351-370. doi:10.1130/0016-7606(1994)106<0351:eaiops>2.3.co;2.

Hornbøll, L., Lonnroth, N., Yue, Y.Z., 2006. Energy release in isothermally stretched silicate glass fibres. J. Amer. Ceram. Soc. 89, 70-74. doi:10.1111/j.1551-2916.2005.00736.x.

Hornbøll, L., Yue, Y.Z., 2008. Enthalpy relaxation of hyperquenched glasses and its

possible link to α- and β-relaxations. J. Non-Cryst. Solids 354, 350-354. doi:10.1016/j.jnoncrysol.2007.06.101.

Hu, L., Yue, Y.Z., 2008. Secondary relaxation behavior in a strong glass. J. Phys. Chem. B 112, 9053-9057. doi:10.1021/jp711696p.

Kokelaar, B.P., 1986. Magma-water interactions in subaqueous and emergent basaltic. Bull. Volcanol. 48, 257-289.

Lemmon, E.W., McLinden, M.O., Friend, D.G., retrieved May 2010. Thermophysical Properties of Fluid Systems, in: Linstrom, P.J., Mallard, W.G. (Eds.), NIST Chemistry WebBook, NIST Standard Reference Database. National Institute of Standards and Technology, Gaithersburg MD, 20899, http://webbook.nist.gov.

Maicher, D., White, J.D.L., 2001. The formation of deep-sea Limu o Pele. Bull. Volcanol. 63, 482-496.

Martin, B., Wondraczek, L., Deubener, J., Yue, Y.Z., 2005. Mechanically induced excess enthalpy in inorganic glasses. Appl. Phys. Lett. 86, 121917. doi:10.1063/1.1895483.

Moynihan, C.T., Easteal, A.J., Debolt, M.A., Tucker, J., 1976. Dependence of fictive temperature of glass on cooling rate. J. Amer. Ceram. Soc. 59, 12-16.

Muncill, G.E., Lasaga, A.C., 1988. Crystal-growth kinetics of plagioclase in igneous systems: Isothermal H_2O-saturated experiments and extension of a growth model to complex silicate melts. Amer. Mineral. 73, 982-992.

Narayanaswamy, O.S., 1971. Model of structural relaxation in glass. J. Amer. Ceram. Soc. 54, 491-498.

Navon, O., Chekhmir, A., Lyakhovsky, V., 1998. Bubble growth in highly viscous melts: theory, experiments, and autoexplosivity of dome lavas. Earth Planet. Sci. Lett. 160, 763-776. doi:10.1016/S0012-821X(98)00126-5.

Nichols, A.R.L., Potuzak, M., Dingwell, D.B., 2009. Cooling rates of basaltic hyaloclastites and pillow lava glasses from the HSDP2 drill core. Geochim. Cosmochim. Acta 73, 1052-1066.

Nooner, S.L., Chadwick, W.W., Jr., 2009. Volcanic inflation measured in the caldera of Axial Seamount: Implications for magma supply and future eruptions. Geochem. Geophys. Geosyst. 10, Q02002. doi:10.1029/2008gc002315.

Paduan, J., Clague, D.A., Caress, D.W., Thomas, H., Thompson, D., Conlin, D., 2009. High-Resolution AUV Mapping Reveals Structural Details of Submarine Inflated Lava Flows. Eos Trans. AGU 90, V51D-1732.

Papale, P., 1999. Strain-induced magma fragmentation in explosive eruptions. Nature 397, 425-428. doi:10.1038/17109.

Potuzak, M., Nichols, A.R.L., Dingwell, D.B., Clague, D.A., 2008. Hyperquenched volcanic glass from Loihi Seamount, Hawaii. Earth Planet. Sci. Lett. 270, 54-62.

Rowland, S.K., MacKay, M.E., Garbeil, H., Mouginis-Mark, P.J., 1999. Topographic analyses of Kilauea Volcano, Hawai'i, from interferometric airborne radar. Bull. Volcanol. 61, 1-14.

Rymer, H., Cassidy, J., Locke, C.A., Sigmundsson, F., 1998. Post-eruptive gravity changes from 1990 to 1996 at Krafla volcano, Iceland. J. Volcanol. Geotherm. Res. 87, 141-149.

Scherer, G.W., 1984. Use of the Adam-Gibbs Equation in the Analysis of Structural Relaxation. J. Amer. Ceram. Soc. 67, 504-511.

Schipper, C.I., White, J.D.L., 2010. No depth limit to hydrovolcanic limu o Pele: analysis of limu from Lo'ihi Seamount, Hawai'i. Bull. Volcanol. 72, 149-164. doi:10.1007/s00445-009-0315-5.

Sohn, R.A., et al., 2008. Explosive volcanism on the ultraslow-spreading Gakkel ridge, Arctic Ocean. Nature 453, 1236-1238. doi:10.1038/nature07075.

Sparks, R.S.J., 1986. The dimensions and dynamics of volcanic eruption columns. Bull. Volcanol. 48, 3-15.

Spera, F.J., 2000. Physical properties of magmas, in: Sigurdsson, H., Houghton, B., McNutt, S., Rymer, H., Stix, J. (Eds.), Encyclopedia of Volcanoes. Academic Press, San Diego, pp. 171–190.

Stevenson, R.J., Dingwell, D.B., Bagdassarov, N.S., Manley, C.R., 2001. Measurement and implication of "effective" viscosity for rhyolite flow emplacement. Bull. Volcanol. 63, 227-237.

Tool, A.Q., 1946. Relation between inelastic deformability and thermal expansion of glass in its annealing range. J. Amer. Ceram. Soc. 29, 240-253.

West, M., Menke, W., Tolstoy, M., Webb, S., Sohn, R., 2001. Magma storage beneath

Axial volcano on the Juan de Fuca mid-ocean ridge. Nature 413, 833-836.

Wilding, M., Dingwell, D., Batiza, R., Wilson, L., 2000. Cooling rates of hyaloclastites: applications of relaxation geospeedometry to undersea volcanic deposits. Bull. Volcanol. 61, 527-536.

Wilding, M., Webb, S., Dingwell, D.B., Ablay, G., Marti, J., 1996. Cooling variation in natural volcanic glasses from Tenerife, Canry Islands. Contrib. Mineral. Petrol. 125, 151-160.

Wilding, M.C., Webb, S.L., Dingwell, D.B., 1995. Evaluation of a relaxation geospeedometer for volcanic glasses. Chem. Geol. 125, 137-148.

Wilson, D.S., 1993. Confidence intervals for motion and deformation of the Juan de Fuca Plate. J. Geophys. Res. 98, 16053-16071.

Wohletz, K.H., 1983. Mechanisms of Hydrovolcanic Pyroclast Formation - Grain-Size, Scanning Electron-Microscopy, and Experimental Studies. J. Volcanol. Geotherm. Res. 17, 31-63.

Yue, Y.Z., Christiansen, J.D., Jensen, S.L., 2002. Determination of the fictive temperature for a hyperquenched glass. Chem. Phys. Lett. 357, 20-24.

Zimanowski, B., Büttner, R., 2003. Phreatomagmatic explosions in subaqueous volcanism, in: White, J.D.L., Smellie, J.L., Clague, D.A. (Eds.), Explosive Subaqueous Volcanism. American Geophysical Union, Washington, DC, pp. 51-60.

Zonenshain, L.P., Kuzmin, M.I., Bogdanov, Y.A., Lisitsin, A.P., Podrazhansky, A.M., 1989. Geology of Axial Seamount, Juan de Fuca Spreading Center, Northeastern Pacific, in: Sinton, J.M. (Ed.), Evolution of Mid-ocean Ridges. American Geophysical Union, Washington, D.C., pp. 53-64.

Acknowledgments

The authors thank the Captain and crew of the R/V Western Flyer and the pilots of the ROV Tiburon and Doc Ricketts for their support during the MBARI 2006 Vance and 2009 Pacific Northwest

expeditions. C.H. was supported by a R.H. Tomlinson Fellowship, a J.W. McConnell Memorial Fellowship, and a GEOTOP scholarship. J.S. was supported by grants from the Natural Sciences and Engineering Research Council of Canada, and D.A.C. by support to MBARI from the David and Lucile Packard Foundation. D.B.D acknowledges the support of a research professorship of the Bundesexzellenzinitiative (LMUexcellent) and the ERC Advanced Grant “EVOKES”.

Table

Table 1. Chemical composition of volcaniclastic and sheet lava glasses from Axial Seamount.

Sample (rock)	T1009-VC 1 20.8-23, (Hy)		T1009-VC 9 3.0, (Hy)		T1010-VC 11 28.0, (Hy)		T1010-VC 15 12.6, (Hy)		T1010-VC 16 18.5, (Hy)	
SiO_2	48.90	(0.39)	49.83	(0.29)	48.74	(0.29)	48.20	(0.19)	49.50	(0.50)
TiO_2	1.36	(0.13)	1.10	(0.18)	1.44	(0.06)	1.29	(0.06)	1.43	(0.04)
Al_2O_3	14.59	(0.47)	16.08	(0.75)	14.61	(0.33)	15.60	(0.14)	14.65	(0.27)
FeO^t	10.57	(0.48)	9.54	(0.72)	10.54	(0.33)	9.67	(0.11)	10.57	(0.10)
MnO	0.20	(0.04)	0.17	(0.02)	0.18	(0.02)	0.18	(0.02)	0.19	(0.02)
MgO	7.82	(0.44)	8.88	(0.72)	7.60	(0.38)	8.44	(0.15)	7.58	(0.13)
CaO	12.35	(0.12)	12.63	(0.11)	12.49	(0.18)	12.44	(0.12)	12.41	(0.08)
Na_2O	2.59	(0.14)	2.36	(0.16)	2.63	(0.06)	2.54	(0.08)	2.65	(0.04)
K_2O	0.139	(0.03)	0.088	(0.03)	0.143	(0.01)	0.121	(0.01)	0.146	(0.01)
P_2O_5	0.126	(0.02)	0.088	(0.02)	0.125	(0.01)	0.109	(0.01)	0.127	(0.01)
Cl	0.020	(0.01)	0.012	(0.01)	0.021	(0.01)	0.012	(0.01)	0.020	(0.01)
S	0.126	(0.01)	0.110	(0.01)	0.130	(0.01)	0.118	(0.00)	0.127	(0.01)
H_2O	0.308	(0.09)	n.a.		0.320	(0.05)	0.295	(0.10)	0.421	(0.06)
F	0.017	(0.00)	n.a.		0.018	(0.00)	0.017	(0.00)	0.018	(0.00)
Total	99.13	(2.37)	100.89	(3.02)	98.98	(1.75)	99.03	(0.99)	99.82	(1.26)
$H_2O_{corr.}$	0.236				0.258		0.237		0.258	

Sample (rock)	D70-1SLR-1,(Sl) prior DSC		D70-1SLR-1,(Sl) after DSC		D70-2SLR, (Sl) prior DSC		D70-2SLR, (Sl) after DSC		D70-3SLR, (Sl)	
SiO_2	49.30	(0.11)	49.53	(0.12)	49.64	(0.14)	49.93	(0.10)	49.48	(0.16)
TiO_2	1.36	(0.04)	1.35	(0.05)	1.49	(0.03)	1.49	(0.04)	1.35	(0.04)
Al_2O_3	15.55	(0.09)	15.56	(0.09)	14.83	(0.07)	14.88	(0.08)	15.58	(0.09)
FeO^t	9.94	(0.14)	9.92	(0.12)	10.82	(0.15)	11.01	(0.12)	9.95	(0.12)
MnO	0.18	(0.02)	0.17	(0.03)	0.19	(0.03)	0.19	(0.03)	0.18	(0.03)
MgO	8.31	(0.06)	8.30	(0.06)	7.67	(0.06)	7.68	(0.06)	8.35	(0.06)
CaO	12.48	(0.09)	12.58	(0.07)	12.45	(0.05)	12.57	(0.05)	12.50	(0.05)
Na_2O	2.57	(0.04)	2.50	(0.05)	2.73	0.03)	2.70	(0.05)	2.54	(0.04)
K_2O	0.173	(0.01)	0.174	(0.01)	0.140	(0.01)	0.141	(0.01)	0.170	(0.01)
P_2O_5	0.133	(0.01)	0.135	(0.02)	0.128	(0.01)	0.125	(0.01)	0.132	(0.01)
Cl	0.008	(0.00)	0.009	(0.00)	0.137	(0.01)	0.139	(0.01)	0.124	(0.01)
S	0.124	(0.01)	0.125	(0.01)	0.015	(0.00)	0.015	(0.00)	0.008	(0.00)
H_2O	n.a.		n.a.		n.a.		n.a.		n.a.	
F	n.a.		n.a.		n.a.		n.a.		n.a.	
Total	100.12	(0.61)	100.35	(0.16)	100.24	(0.60)	100.87	(0.25)	100.37	(0.64)

Hy: hyaloclastites, sl: sheet lava crust. All values in wt %, FeO^t total iron as FeO, and n.a. not analyzed. Standard deviations of 1σ are given in parentheses. Major elements were averaged for 10-15 limu o Pele and angular fragments (with 3 analyses per grain), and 12 spots for sheet lavas. Volatiles were averaged for 5-8 fragments per sample. $H_2O_{corr.}$: Water content corrected for post-eruptive hydration, based on H_2O/F (Helo et al. 2011).

Table 2. Calorimetry-derived parameters for hyaloclastic glasses and sheet lava glasses from Axial Seamount.

Sample	Rock type	T_f' [K]	ΔH_{tot} [J kg^{-1} K^{-1}]	$\log_{10} q$ [K s^{-1}]	T_f' *ctr.* [K]	Φ/m [W kg^{-1}]
T1009-VC1 20.8-23	Hy, limu	1033	38.3×10^3	4.7	887 [a]	7.5×10^7
	Hy, limu (2 mm)	995	27.2×10^3	3.7		8×10^6
	Hy, angular (1 mm)	993	36.4×10^3	3.7		7×10^6
T1009-VC9 3.0	Hy, limu	1070	39.7×10^3	6.0	874	1.4×10^9
	Hy, angular	1028	36.9×10^3	5.1		1.6×10^8
T1010-VC11 28.0	Hy, limu	1006	29.8×10^3	4.3	878	2.7×10^7
	Hy, angular	999	22.9×10^3	4.1		1.8×10^7
T1010-VC15 12.6	Hy, limu	1076	37.6×10^3	5.8	886	8.8×10^8
	Hy, angular	998	23.1×10^3	3.9		1.1×10^7
T1010-VC16 18.5	Hy, limu	1022	42.2×10^3	4.6	861 [a]	5×10^7
	Hy, angular	988	33.5×10^3	4.4	861 [a]	3.5×10^7
D70-R1	Sheet lava crust	967	15.4×10^3	2.1	905	3×10^3 [b]
D70-R2	Sheet lava crust	954	11.0×10^3	1.8	900	3×10^3 [b]
D70-R3	Sheet lava crust	998	21.5×10^3	3.0	909	3×10^3 [b]

Hy: hyaloclastites. Grain size of limu o Pele and angular fragments is~ 1 mm and ~ 0.5 mm, respectively, unless otherwise noted. For sheet lavas, the outermost 1.0-1.3 mm were analyzed. T_f', T_g^{peak}, and T_{eq} denote natural limiting fictive temperature, temperature of the calorimetric peak in the glass transition interval, and temperature at which the enthalpy of the supercooled liquid is reached, respectively. ΔH_{tot} is total exothermic enthalpy release during the initial heating, and q is natural cooling rate. T_f' *ctr.* is limiting fictive temperature of controlled heating/cooling of 20/20 K min^{-1}, except [a] 25/25K min^{-1}. Φ/m is heat transfer rate per mass at the glass transition ($\Phi/m = c_p \times q$),
[b] approximated with a heat flux of $10^{6.5}$ W m^{-2} (Griffiths and Fink, 1992a) for a lava flow body of 0.5×5×20 m (see Appendix B).

Table 3. Parameters used for numerical cooling and heat flow solutions of basaltic lava in contact with seawater at 1400 m water depth.

Parameter	Value	Description	Reference
Basalt			
K, W m^{-1} K^{-1}	1.5	Thermal conductivity	Spera (2000)
κ, m^2 s^{-1}	3.9×10^{-7}	Thermal diffusivity	Calculated
ρ, kg m^{-3}	2.7×10^3	Density	
c_p, J kg^{-1} K^{-1}	1.4×10^3	Specific heat capacity	This study
Seawater			
K_w, W m^{-1} K^{-1}	0.64 (a)	Thermal conductivity	Lemmon et al. (retrieved May 2010)
κ_w, m^2 s^{-1}	1.6×10^{-7}	Thermal diffusivity	Calculated
ρ_w, kg m^{-3}	0.889×10^3 (a)	Density	Lemmon et al. (retrieved May 2010)
c_{pw}, J kg^{-1} K^{-1}	4.55×10^3 (a)	Specific heat capacity	Lemmon et al. (retrieved May 2010)
η_w, Pa s	3.1×10^{-4} (a)	Dynamic viscosity	Lemmon et al. (retrieved May 2010)
ν_w, m^2 s^{-1}	3.3×10^{-7}	Kinematic viscosity	Calculated
α_w, K^{-1}	2.2×10^{-3}	Thermal expansion	Bischoff and Rosenbauer (1985)
γ	0.1	Constant	Hubert and Sparks (1988)
ε	0.9	Emissivity	Griffiths and Fink (1992a)
σ, W m^{-2} K^{-4}	5.67×10^8	Stefan-Boltzmann constant	

All values for 14 MPa confining water pressure, if applicable. Subscript "*w*" denotes property for seawater.
(a) Temperature dependent; average values over the range from 273 K to the maximum liquid phase temperature were used.

Figure legends

Figure 1 **A)** Schematic overview map depicting the tectonic setting of the Juan de Fuca ridge and adjacent oceanic plates. **B)** Bathymetric map showing the summit caldera and flanks of Axial Seamount and the location of dive sections T1009, T1010, and D70. The map is at a 20-m resolution.

Figure 2 Two types of pyroclastic ash fragments from Axial Seamount investigated in this study. **A-C)** Scanning electron images of angular fragments. **D, E)** Scanning electron images of limu o Pele fragments, mostly described as thin melt films or bubble walls, often strongly folded, or bent. **F)** Photomicrograph of a limu o Pele shard displaying strongly stretched vesicles, indicating quenching of the melt while subjected to high strain rates. A detailed description and comparison of basaltic ash fragments from Axial Seamount and other Pacific sites is given in Clague et al. (2009).

Figure 3 **A)** Determination of the limiting fictive temperature of hyperquenched glasses based on Yue et al.'s (2002) method relating excess enthalpy ΔH_{tot} (area A, left-hand side of Eq. 5) and excess internal energy ΔE_{tot} (area B, right-hand side of Eq. 5). ΔH_{tot} is the excess enthalpy released during the initial heating scan c_{p1st} up to T_g* relative to a Maier-Kelly fit representing the glassy state extrapolated to higher temperatures. T_f' is defined as the upper temperature limit for area B to equal area A. T_{ex} is the start of the exothermic enthalpy release, T_g^{onset} and T_g^{peak} are characteristic temperatures in the calorimetric glass transition interval. **B)** DSC curves of the initial and subsequent thermal treatments with controlled cooling/heating for representative samples of limu o Pele shards, angular fragments and glassy sheet lava crust, depicting the hysteresis of heat capacity observed during heating of the samples.

Figure 4 Cooling rate and relaxation time versus inverse of limiting fictive temperature T_f' for the Axial Seamount pyroclastic glasses and sheet lava crusts. The lines demonstrate the non-Arrhenian temperature dependence of viscosity and are modelled after Giordano et al. (2008) and adjusted using T_f' derived by the controlled cooling/heating cycles (after Moynihan et al., 1976). The natural cooling rate can then be determined from the natural T_f' calculated after Yue et al. (2002).

Figure 5 Excess enthalpies ΔH_{tot} stored in glassy limu o Pele, angular fragments, and sheet lava crusts from Axial Seamount compared to rapidly quenched submarine basaltic glasses from Loihi, Hawaii (Potuzak et al., 2008), Hawaiian drill core HSDP2 (Nichols et al., 2009), and synthetic fibre-quenched glasses (Yue et al., 2002).

Figure 6 Normalized excess enthalpies expressed as derivatives of temperature as a function of temperature, revealing an asymmetric distribution of enthalpy release. Two distinct peaks characterise most of the curves derived from A) angular shards and B) limu o Pele fragments. The main relaxation peak occurs at high temperatures (right arrow), with a subordinate peak or "shoulder" at lower temperatures (left arrow). The latter could represent a second, superimposed relaxation domain. It appears to be slightly more pronounced for the energy distribution curves of the angular fragments and absent in the glasses from the sheet lava flows.

Figure 7 Simple conductive cooling model. A) Temperature-time profile for various distances from the cooling surface. A distance of 60 to 160 μm corresponds to the thickness of the analyzed limu o Pele shards, 0.5 mm to the thickness of the angular fragments, and 1 mm for the lava crust. B) Quench rates versus distance. The maxima in the curves depict the cooling rates reached at a specified distance (e.g., corresponding to limu o Pele thickness) when the glass transition is crossed at the natural limiting

temperature T_f'. For simplicity a mean T_f' of 1035 K for the pyroclastic glasses and 975 K for the sheet lavas was used. The model computes temperature-time relations at a particular distance from the interface, while the DSC analyses provide the mean thermal history over the same distance.

Figure 8 Arrhenian plot of cooling rate and relaxation rate at the glass transition illustrating a possible annealing mechanism in sheet lava flow crusts. Time-temperature relation (grey curve) is calculated after the GRD-model (Giordano et al., 2008), and Eqs (1) and (5) and separates the supercooled liquid and the glassy field. A lava flow crust quenched at ~ 10^3 K s^{-1}, e.g., *D70-3SLR*, enters the glassy field at ~1000 K (primary cooling). Three different paths schematically describe the structural relaxation during possible isothermal annealing. Samples subjected to paths T_1–Δt_1 and T_2–Δt_2 record the same cooling rate of about $10^{1.8}$ K s^{-1} (as for *D70-3SLR*), but differ in the temperature and time required to re-enter the supercooled liquid field and structurally relax, erasing any evidence of the primary cooling event. As long as the heat supply from the interior of the flow is sufficient, the crust can deform close to the glass transition at rates of < 0.02 s^{-1}. Annealing at temperatures of 100 K below the primary T_g can still allow viscous deformation to occur at timescales of 10 s (path T_3–Δt_3). In this hypothetical case, recorded cooling rates will be less than those of the sheet lavas studied and close to those of Wilding et al., (2000).

Figures

Figure 1

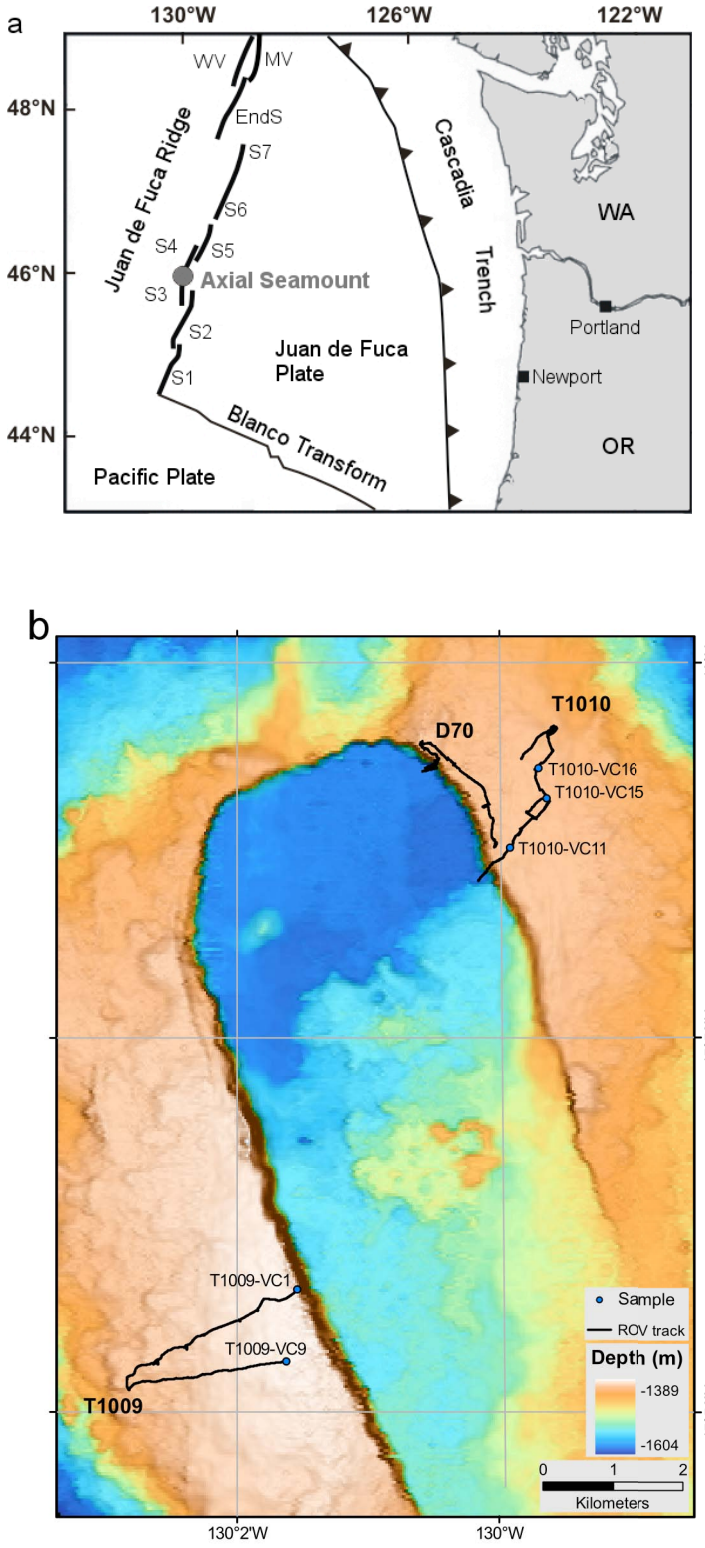

Figure 2

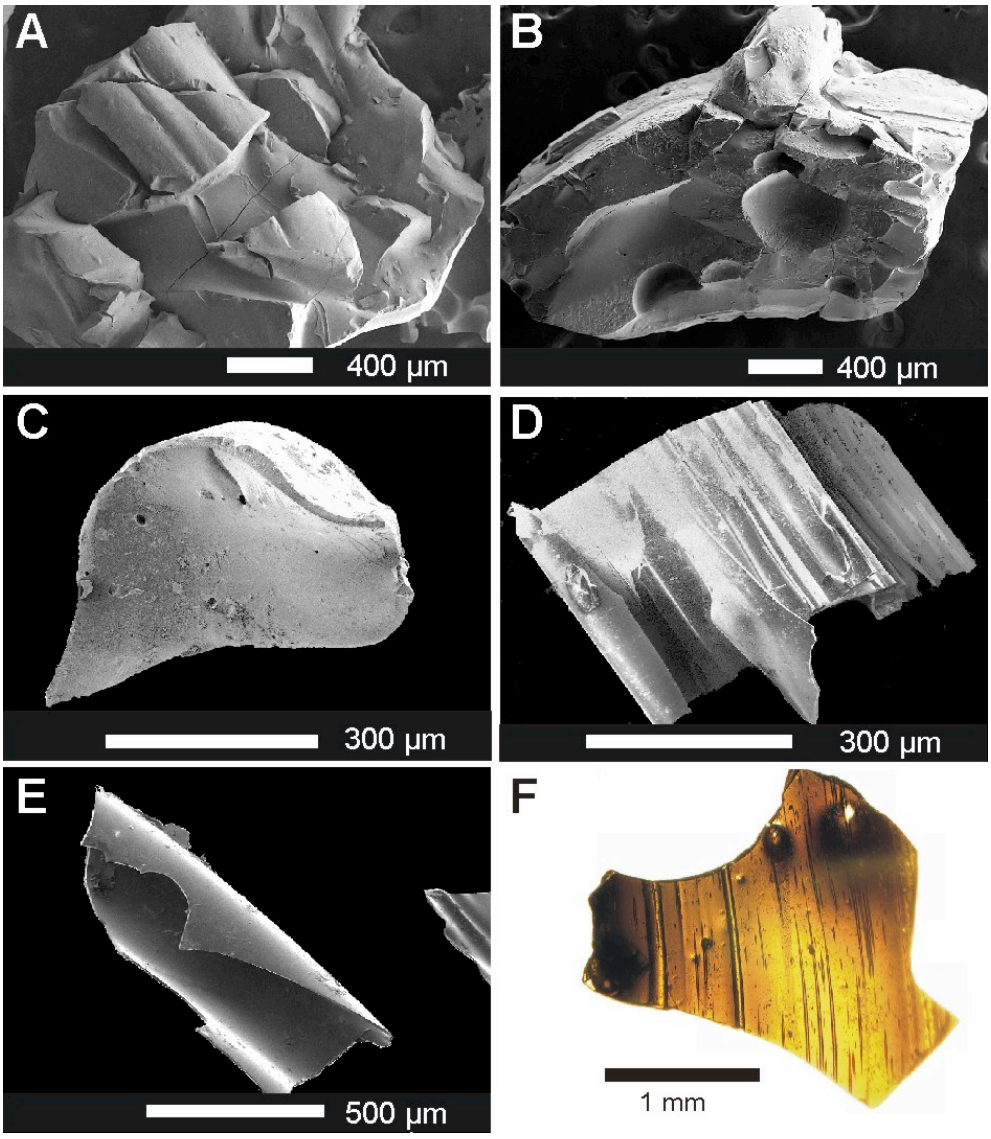

Figure 3

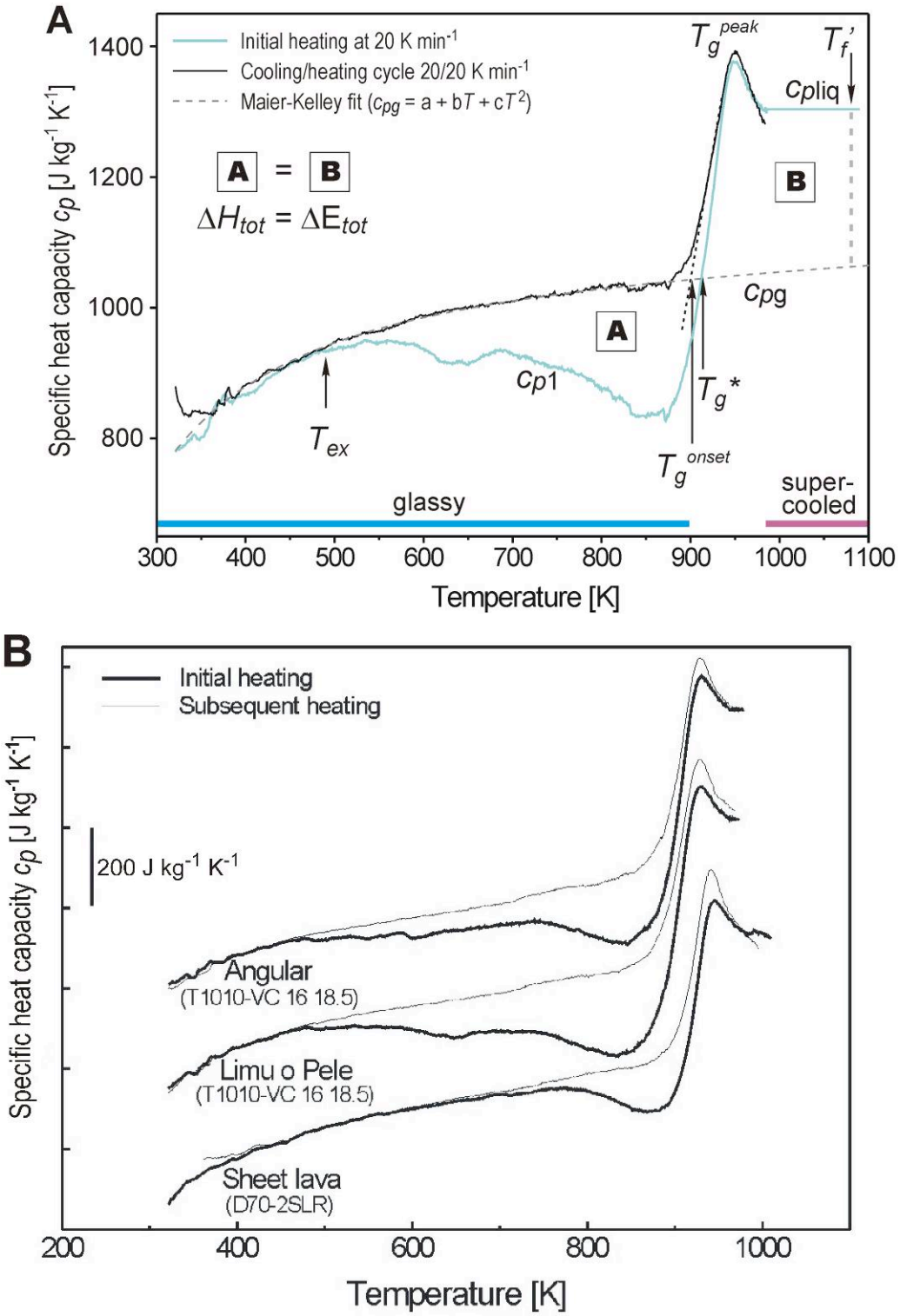
A
Initial heating at 20 K min-1
Cooling/heating cycle 20/20 K min-1
Maier-Kelley fit (cpg = a + bT + cT2)
A = B
ΔHtot = ΔEtot
Tg peak
Tf'
Cpliq
B
Cpg
A
Cp1
Tg*
Tex
Tg onset
glassy
super-cooled
Specific heat capacity cp [J kg-1 K-1]
Temperature [K]
B
Initial heating
Subsequent heating
200 J kg-1 K-1
Angular
(T1010-VC 16 18.5)
Limu o Pele
(T1010-VC 16 18.5)
Sheet lava
(D70-2SLR)
Specific heat capacity cp [J kg-1 K-1]
Temperature [K]

Figure 4

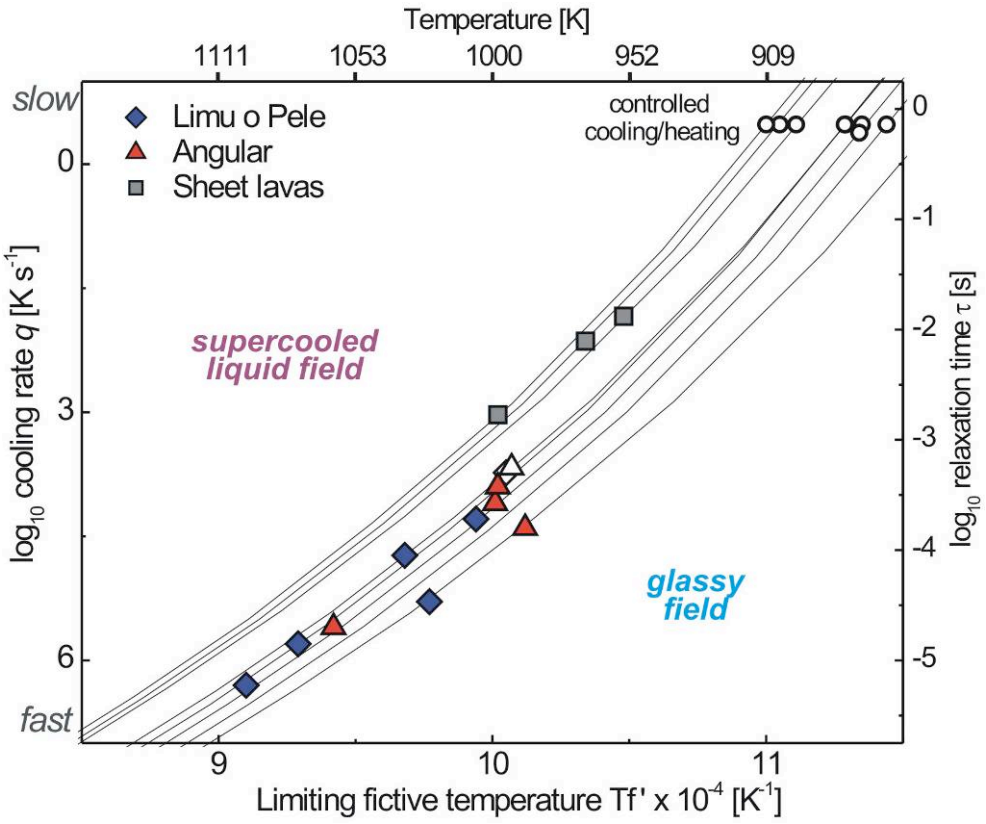
Temperature [K]
1111
1053
1000
952
909
slow
fast
Limu o Pele
Angular
Sheet lavas
controlled
cooling/heating
supercooled
liquid field
glassy
field
log10 cooling rate q [K s-1]
log10 relaxation time τ [s]
0
3
6
-1
-2
-3
-4
-5
9
10
11
Limiting fictive temperature Tf' x 10-4 [K-1]

Figure 5

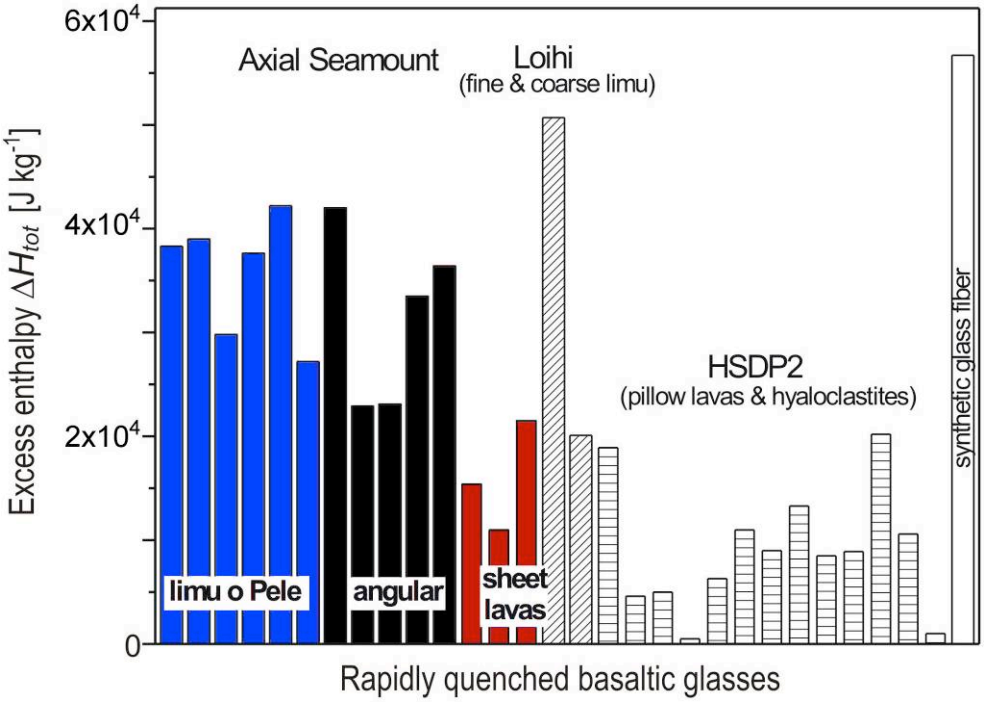
6x10^4
4x10^4
2x10^4
0
Excess enthalpy ΔH_tot [J kg^-1]
Axial Seamount
Loihi
(fine & coarse limu)
HSDP2
(pillow lavas & hyaloclastites)
synthetic glass fiber
limu o Pele
angular
sheet
lavas
Rapidly quenched basaltic glasses

Figure 6

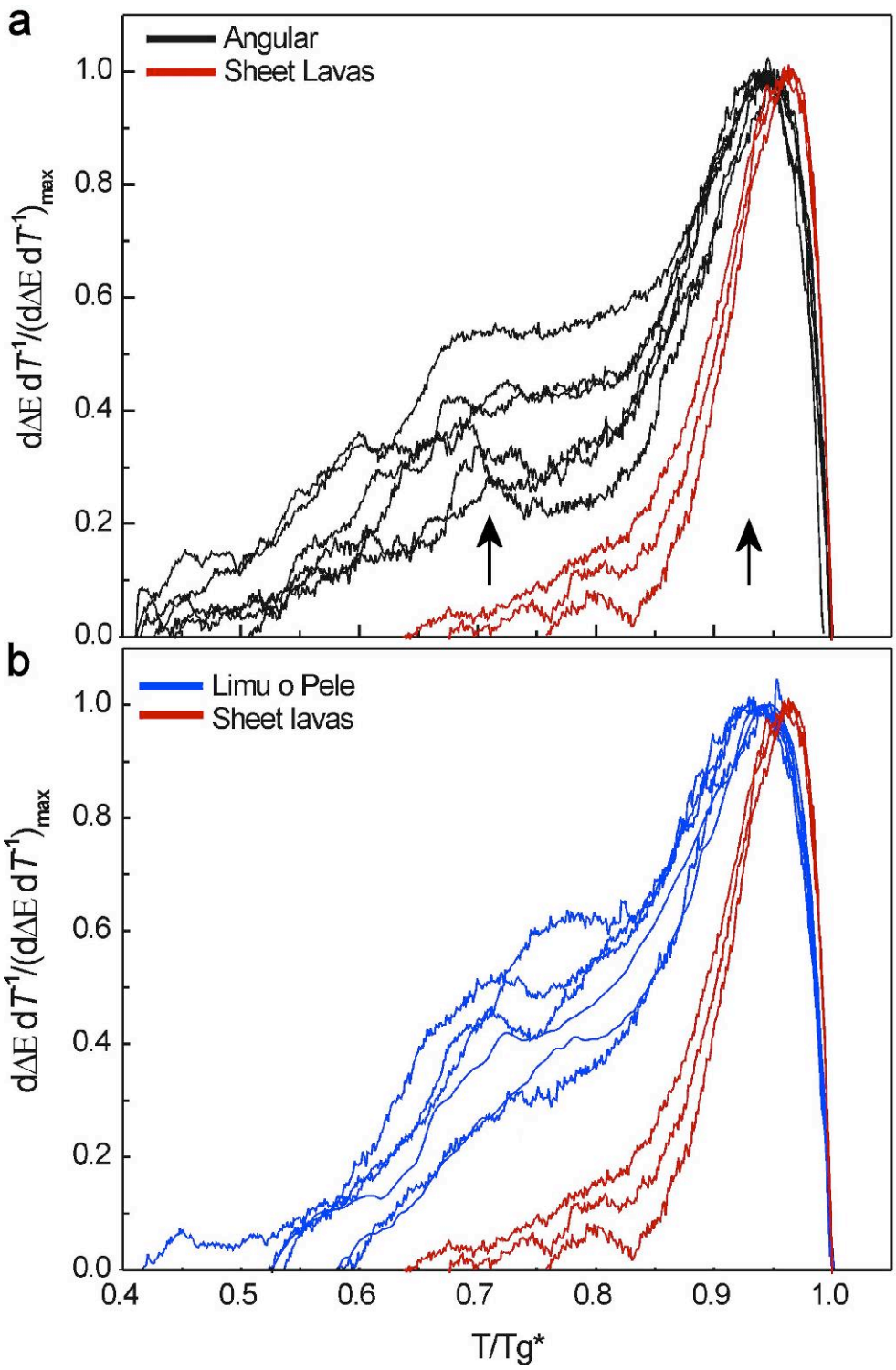
a
Angular
Sheet Lavas
b
Limu o Pele
Sheet lavas
dΔE dT⁻¹/(dΔE dT⁻¹)max
T/Tg*
0.0
0.2
0.4
0.6
0.8
1.0
0.4
0.5
0.6
0.7
0.8
0.9
1.0

Figure 7

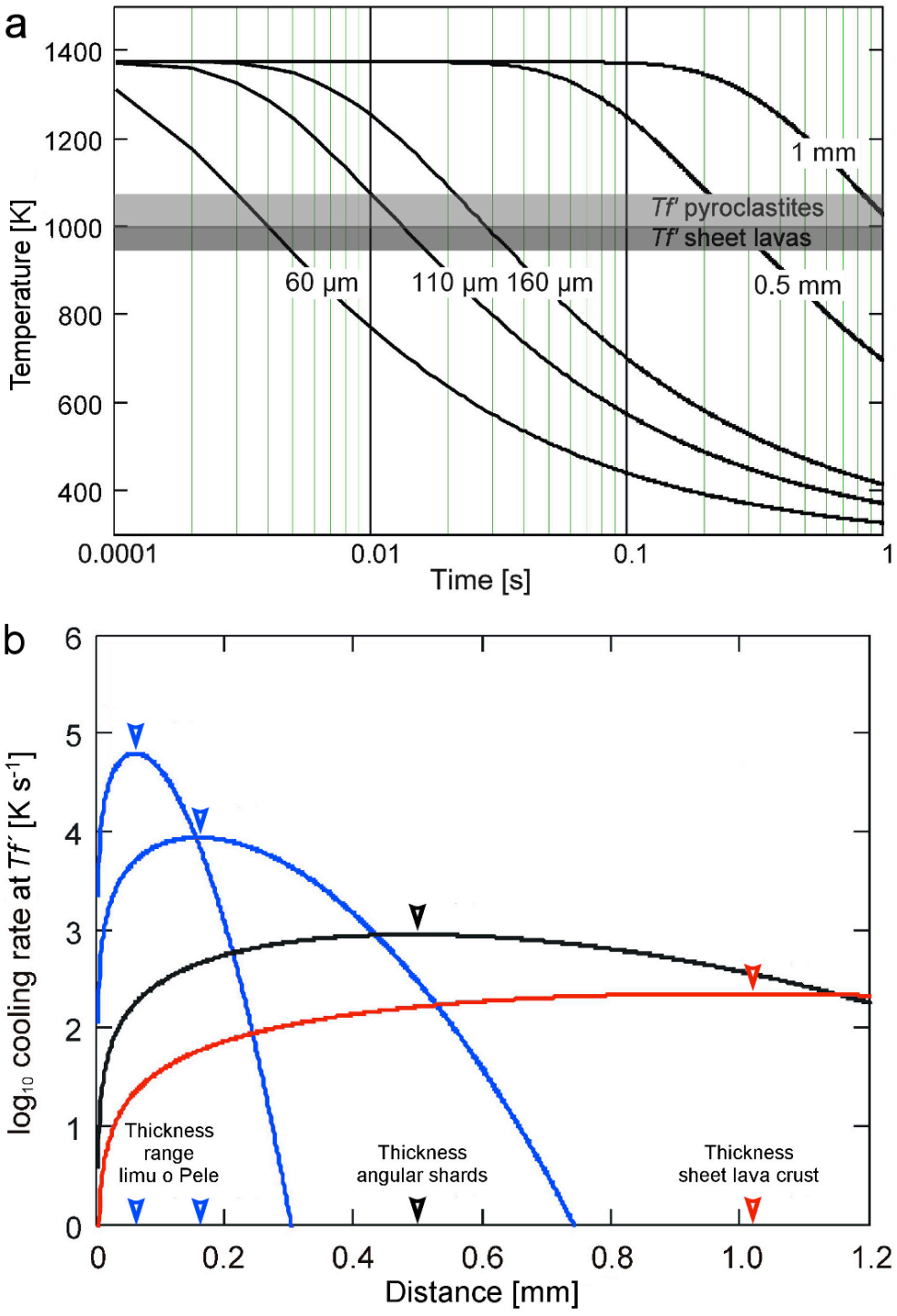
a
1400
1200
1000
800
600
400
Temperature [K]
0.0001
0.01
0.1
1
Time [s]
1 mm
Tf' pyroclastites
Tf' sheet lavas
60 µm
110 µm 160 µm
0.5 mm
b
6
5
4
3
2
1
0
log10 cooling rate at Tf' [K s-1]
0
0.2
0.4
0.6
0.8
1.0
1.2
Distance [mm]
Thickness range limu o Pele
Thickness angular shards
Thickness sheet lava crust

Figure 8

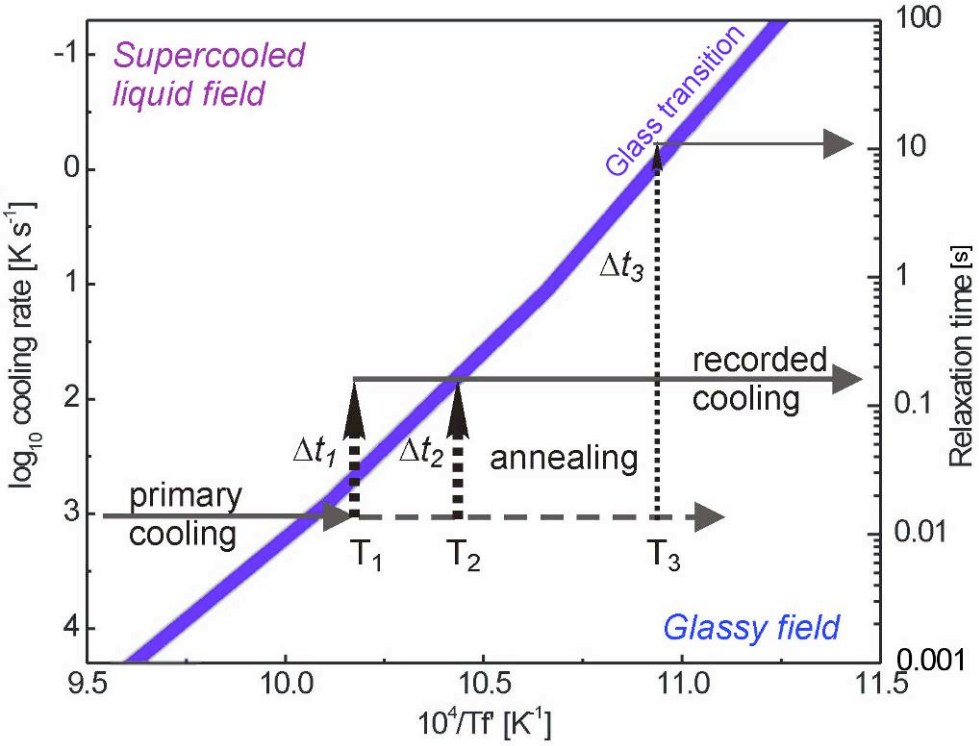
Supercooled
liquid field
Glass transition
Glassy field
recorded
cooling
primary
cooling
annealing
Δt1
Δt2
Δt3
T1
T2
T3
log10 cooling rate [K s-1]
Relaxation time [s]
10^4/Tf [K-1]
-1
0
1
2
3
4
100
10
1
0.1
0.01
0.001
9.5
10.0
10.5
11.0
11.5

Bridge between Chapter 3 and Chapter 4:

The study of pyroclastic eruptions at mid-ocean ridges has been constrained by volcaniclastic deposits from Axial Seamount, complemented by a series of analogue experiments. These experiments were designed to simulate eruptions of vesiculating magma under degrees of decompression appropriate for submarine conditions. The overall aim was to identify and explore factors that can facilitate explosive eruptions in high-pressure environments where strong volatile exsolution is inhibited. Two parameters were chosen as extrinsic variables, (1) the pre-eruptive bubble content and (2) rapid variations of conduit diameter.

Chapter 4. Eruptions in deep sea environments – insights from analogue modelling using gum rosin-acetone mixtures

Christoph Helo,[1] Irving Mungúia,[2] Jeremy C. Phillips,[3] John Stix[1]

[1]*Department of Earth & Planetary Sciences, McGill University, 3450 University Street, Montréal, Québec H3A 2A7, Canada*

[2]*Centre of Exchange and Research in Volcanology, University of Colima, Bernal Díaz del Castillo #340, Colima, Mexico*

[3]*Departmentof Earth Sciences, University of Bristol, Queen's Road, Bristol BS8 1RJ, United Kingdom*

Manuscript IV – to be published.

Abstract

We conducted analogue experiments using gum-rosin acetone (GRA) mixtures to investigate the eruption behaviour of rapidly decompressed magmas undergoing volatile exsolution during ascent in the conduit in deep-sea environments. Our main intention was to evaluate the role of initial, pre-eruptive bubbles and sudden changes in conduit diameter on the accent and fragmentation behaviour of volatile oversaturated magma. GRA mixtures of two different viscosities were rapidly decompressed to various final pressures covering degrees of oversaturation (= ratio of exsolution to final pressure) of 1.6 to 80. The reduction of the tube cross-section with an area ratio of 7.5:1 was used to simulate constrictions within a vertical cylindrical conduit, whereas a cross-section increase of 1:15 was used to simulate the eruption into a laterally unconfined space. We find that runs with pre-eruptive bubbles deviate in their initial expansion behaviour from runs without initial bubbles, especially if the degree of decompression is low. Under these conditions flows expand with increasing acceleration and according power law coefficients >1, the fragmentation threshold can be shifted. At higher degrees of decompression, the expansion behaviour becomes very similar. Recorded acoustic pressure oscillations are limited to the 10 to 200 Hz region and cannot be resolved as a single monopole source, but may rather relate to the superposition of various dynamic pressure changes spatially distributed throughout the system. Acoustic emissions are strongly reduced in runs with pre-eruptive bubbles, which is interpreted as a damping effect caused by the initial bubbles. We further find constrictions to efficiently promote gas segregation during ascent. Expanding GRA flows encountering the reduced cross-section tube part are briefly choked and then eject a very low-density gas-rich

fragmenting mixture into upper tube. This process is repeated several times, and associated with the emission of very strong acoustic pressure oscillations. In contrast, strong fragmentation is more hampered if GRA flows expand into a wide tube section, due to the loss of shear strain along the tube walls. Instead GRA flows vesiculate to large domal structures. The geometry of these structures is controlled principally by the viscosity of the flow. High viscosity flows produce very tall, steep domes, whereas low-viscosity domes would collapse and spread laterally as a more degassed lava flow. For eruptions in submarine environment our experiments show that threshold depths or degrees of decompression for explosive activity cannot strictly be defined. Instead, pyroclastic eruptions can be expected to occur over a wide range of depths including the deep-sea. Especially at high ambient pressures, the presence of initial bubbles and changes in the conduit geometry can facilitate pyroclastic eruptions.

1. Introduction

Pressure and temperature are two extrinsic key properties for many Earth system processes. For physical evolution of magmas, from melt generation at mantle or crustal levels until extrusion onto the surface or seafloor, both play a fundamental role. In terms of the nature and style of volcanic and eruptive activity, pressure is the fundamental extrinsic factor. Confining pressures on the Earth's surface, including the seafloor, can vary by almost three orders of magnitude between subaerial regions and deep sea settings. Parameters such as the solubility of water in the melt or gas volume expansion, which depend on pressure, show considerable variations for eruptions from different settings. These parameters are most affected during eruptions in submarine environments, i.e.,

under high confining pressure. Effusive lava extrusion is the most common style of submarine volcanic activity, producing a range of lava flow morphologies (Perfit and Chadwick, 1998). Within the past several decades, a growing body of compelling evidence has come to light indicating the occurrence of at least a minor component of pyroclastic, hence explosive, magmatic activity at substantial water depths. Pyroclastic deep sea deposits have been recovered from various settings and localities such as, Loihi Seamount, Hawaii, various seamounts offshore of California, back-arc basin systems and along different mid-ocean ridge systems, e.g., Gorda Ridge, Juan de Fuca Ridge and Gakkel Ridge (4000 m water depth) (Gill et al., 1990; Clague et al., 2003a; Clague et al., 2003b; Davis and Clague, 2003; Eissen et al., 2003; Davis and Clague, 2006; Sohn et al., 2008; Schipper et al., 2010).

Likewise, eruption of silicic magma in deep sea settings can occur both effusively or explosively. Formation of lava domes and block lava flows and associated deposits have been described at several volcanoes in the Kermadec arc region in depths of 900–1800 m below sea level (bsl.), SW Pacific, from the Shimane Peninsula at 200– 1000 m bsl., SW Japan, or Yali island, eastern Greece (Kano et al., 1991; Allen and McPhie, 2000; Wright et al., 2003). Submarine pumice deposits with clasts ranging from lapilli to blocks several meters in diameter, are known from several volcanic systems in the Izu-Bonin arc, SW Japan, the Shimane Peninsula, Japan, or Healy caldera, Kermadec arc. In several cases they are thought to originate from highly energetic caldera forming events, possibly as deep as 1400 m water depth (Kano, 1996; Fiske et al., 2001; Wright et al., 2003; Stern et al. 2008). Allen et al. (2010) studied pumice deposits from the Sumisu volcanic complex, Izu-Bonin arc, inferring a change in eruption style at a water depth of

about 500 m. They envisioned pyroclastic eruptions to operate at depths shallower than 500 m producing rough-textured pumice clasts and lapilli fallout, while non-explosive dome breakup seemed the major fragmentation mechanism at depths below 500 m, producing giant pumice blocks.

Thus, over a wide range of hydrostatic pressures, a considerable range of volcanic eruption styles seems to exist. The present information and deposits suggest that a threshold depth, below which pyroclastic activity is hampered, may not be expected *a priori*. The general effect of high hydrostatic pressure on eruption behaviour is not well understood. We therefore designed a series of decompression experiments simulating the eruption of two-phase flows into a high-pressure environment, i.e., eruptions undergoing reduced degrees of decompression compared to subaerial eruptions. In particular, we examined the effect of two factors over a wide range of final pressures that might promote or reduce magmatic fragmentation at increased exit pressures typical for deep sea environments: (1) pre-eruptive bubbles, and (2) changes in the conduit diameter. The observations and underlying processes are discussed in the light of current models of bubble growth rates and acoustic emissions of ascending gas bubbles. We then develop conceptual eruption models for basaltic and silicic eruptions in submarine environments, considering the effects of rapid cooling of the lava not explicitly accounted for in our analogue experiments.

2. Comparison of the analogue with natural systems

We used mixtures of gum rosin and acetone, herein termed GRA, as an analogue for magma-volatile (water) systems. Gum rosin is a natural pine resin (colophony), which

can be mixed with acetone (C_3H_6O) in any ratio. Decompression of a water bearing magma below its saturation pressure results in exsolution of water vapour, growth of bubbles and subsequent expansion of the flow within the conduit by vesiculation. Likewise, rapid decompression of a GRA mixture below its exsolution pressure triggers the nucleation and growth of acetone bubbles, foaming and expanding the flow within the experimental glass tube. In detail the two systems differ slightly in that the saturation pressures in magmatic systems depend on the dissolved volatile contents, while the exsolution pressure of acetone appears independent of its concentration, although Phillips et al (1995) have suggested a pressure dependence for low acetone concentrations. As a consequence of a constant exsolution pressure, which was found to be about 25 kPa in our experiments, there is no need to adjust laboratory pressure conditions to different acetone concentrations for the GRA mixtures used. The same final (exit) pressure can be used to achieve the same ratio of final pressure to exsolution pressure, which is independent of the acetone content, allowing us to simply vary viscosity (see below).

2.1 Volatile concentration and expansion

GRA mixtures have been found as a suitable magma-volatile analogue as certain key properties are similar and scalable to natural systems (Phillips et al., 1995; Lane et al., 2001; Phillips and Woods, 2001). Following Lane et al. (2001), we compare volatile concentration in mole per cubic meter (mol m^{-3}) which allows us to scale the volume expansion of the two-phase flow. GRA and magmatic flows with similar amounts of dissolved volatile concentrations (in mol m^{-3}) will thus undergo similar degrees of expansion during decompression. We used GRA mixtures with 20 and 30 wt. % acetone equal to about 3490 and 5100 mol m^{-3}, corresponding to a range of water concentrations

in silicate melts of about 2.5 to 4 wt. %. For simplicity, we refer to volatile concentration within the text in wt. % notation.

Bubble growth within a decompressed volatile-bearing liquid occurs by diffusion of volatiles into the bubble from the surrounding liquid boundary layer and by expansion of the bubble volume due to pressure decrease. Using the Stokes-Einstein equation (Dowty, 1980) $D = kT/(3\pi\eta r)$, we can approximate diffusivities of acetone in GRA mixtures of 20 to 30 wt. % acetone at ~ 10^{-11} to 10^{-10} m^2 s^{-1} (D, diffusivity; k, Boltzmann's constant; T, temperature of 293 K; η, viscosity and r, molecular radius of 0.31 nm). This compares to diffusivities of water of ~ 10^{-11} to 10^{-10} m^2 s^{-1} and ~ 10^{-13} to 10^{-10} of CO_2 under magmatic conditions (Watson, 1994; and references within). The degree of expansion of the exsolving bubbles is represented by the ratio of the free gas volume at the exit pressure to the free gas volume at the exsolution level (Figure 1). Approximating expansion of the flow this way neglects the instant volume change for initial bubble growth at the saturation pressure. Initial bubble sizes are fairly small, and the error is in the same sense for both systems. Under our laboratory conditions we produce gas volume ratios of 1.6 to 80. In comparison, magmatic systems may exhibit expansion with ratios significantly higher than 1000, depending on the volatile content. The main extrinsic control on the ratio is the exit pressure at the vent. Volcanic flows exiting the vent at atmospheric pressure will undergo strong gas volume changes during ascent in the conduit from the exsolution level to the vent, while expansion will be suppressed considerably if eruptions take place under deep-sea conditions with high ambient pressures (Table 1). For a magma saturated with H_2O or CO_2 at 100 MPa, the ratio of exit to initial (at the saturation pressure) gas volume will be 1000 at sea-level, but only 10 to

2.5 at water depths between 1000 m and 4000 m, assuming ideal gas behaviour. (Figure 1). Our experiments thus scale well to volcanic eruptions taking place under greater pressure or very low saturation pressures.

2.2 Viscosity and non-Newtonian behaviour

Silicate liquids exhibit a non-linear dependence of viscosity on water concentration, especially if strongly polymerized. This is considerably accentuated at low water contents. In Figure 2 we compare viscosities of rhyolite-water and tholeiitic basalt-water systems with those of GRA mixtures. Data for rhyolite-water are parameterized after Hess and Dingwell (1996), and for basalt-water after Giordano et al. (2008). As for hydrated magmas, the viscosity of GRA mixtures varies strongly in a non-linear fashion with the acetone concentration. GRA viscosity data for 20, 15, 12 and 0 wt. % GRA are taken from Phillips et al. (1995), and are fit by an equation of the form $\log_{10}$ viscosity = A + B/([acetone concentration] + C). The shear viscosity η_s is related to shear relaxation time τ_s and the shear modulus at infinite frequency G_∞ by the Maxwell equation $\tau_s = \eta_s \times G_\infty^{-1}$. In the case of silicate liquids, the shear modulus G_∞ is identical to the bulk modulus K_∞, with an average value of 10±0.5 GPa (Dingwell and Webb, 1989). Using a speed of sound of 2000 m s^{-1} for gum rosin-organic solvent mixtures (Lane et al., 2001) we can approximate a bulk modulus $K_\infty \sim 4$ GPa using $K_\infty = c^2 \times \rho$, where c is the speed of sound and ρ is density (~ 1020 kg m^{-3}). Assuming a shear modulus on the order of the bulk modulus, shear relaxation times of the GRA mixtures with 30 wt. % to 0 wt. % acetone range from 10^{-11} to 10^3 s, encompassing the range typical for magmatic systems (10^{-5} to $10^{2.6}$ s for rhyolites and 10^{-9} to 10^{-8} s for basalts). The assumption of $G_\infty \cong K_\infty$ requires

shear waves (at high frequencies) to show roughly comparable velocities as compressional sound waves. Silicate melts experience the onsets of non-Newtonian behaviour, leading to brittle fragmentation, at shear strain rates between two to three orders of magnitude below the calculated critical strain rate $1/\tau_s$ (Dingwell and Webb, 1989). During volcanic eruptions, brittle fragmentation is common in high-silica systems, whereas brittle failure of basaltic magma under typical natural conditions appears feasible only if the crystal content is high enough to substantially increase viscosity (Papale, 1999). For GRA mixtures, the exact point of the onset of the non-Newtonian regime has not been determined, but both natural magmas and GRA mixtures can undergo the transition from a regime dominated by viscous forces to a regime dominated by brittle - response, either before (silicate melts) or close to the relaxation strain rate $1/\tau_s$.

2.3 Flow dynamics

Dynamic similarities of experimental and natural two phase flows can be evaluated in terms of three parameters. The first is the dimensionless Reynolds number *Re,* a measure of inertial to viscous forces and is defined as $Re = \upsilon \rho r / \eta$, where υ is velocity, ρ density, r radius of the conduit/tube and η viscosity of the fluid. For small Reynolds numbers < 2000 the flow is generally considered to be laminar. During early stages of experimental and magmatic flows, expansion will take place under such laminar conditions if velocities are less than 6 to 60 m s^{-1} for the GRA mixture (ρ = 1000 kg m^{-3}, r = 0.025 m , $\eta = 10^{-1.5}$ to $10^{-0.2}$ Pa s), 8 m s^{-1} for a basalt (ρ = 2600 kg m^{-3}, r = 1 m, η = 10 Pa s), and 10^4 m s^{-1} for a rhyolite (ρ = 2200 kg m^{-3}, r = 50 m, $\eta = 10^6$ Pa s). When gas volume fraction increases, acceleration and viscosity will increase, while bulk density

decreases, in both the laboratory and natural flows. All systems can therefore experience similar changes in the flow regime, from a slow laminar flow to a fast turbulent dispersed flow. Time and length dimensions of the flow and conduit system can be scaled using the shear strain rate ($d\upsilon_z/dx$) parallel to the tube/conduit wall, where $d\upsilon_z$ is the vertical velocity of the non-dispersed flow, and dx the distance from the centre to $0.05 \times r$ from the tube/conduit wall. For GRA mixtures with velocities of 0.05 to 0.5 m s^{-1} strain rates are 2–20 s^{-1} and for natural magmas 5 to 0.02 s^{-1} (using $\upsilon_z = 5 - 1$ m s^{-1}, and r = 1 – 50 m).

Another key parameter is the Capillary number *Ca*, relating viscous forces to the surface tension, which reflects the ability of a sheared bubble in a two-phase flow to rebound. The Capillary number is expressed as $Ca = (d\upsilon_z/dx)\, r\, \eta / \sigma$, where σ is the surface tension and η the viscosity. As the flow is sheared, bubbles will act as rigid spheres when *Ca* is small (< 1), but will deform when *Ca* is large (> 1). In contrast to spherical bubbles, strongly deformed bubbles weakly affect viscosity (Manga et al., 1998) and are less likely to coalesce. The occurrence of tube pumices in rhyolitic systems (e.g., Marti et al., 1999) as well as strongly elongated vesicles in basaltic submarine glass fragments (Helo et al., 2008; Helo et al., unpublished) are manifestations of large Capillary numbers during natural volcanic eruptions. Scanning electron analyses of laboratory fragments produced by fragmentation of GRA reveal strongly elongated and tubular vesicles, similar to those in natural fragments (Phillips et al., 1995). Therefore, bubbles in the laboratory and the natural systems will have a comparable effect on the rheological behaviour of the expanding flow.

3. Experimental method

In order to simulate decompression and subsequent expansion of volatile bearing magmas, we used the following experimental set-up. A system of QVF® borosilicate glass tubes of about 75 cm length was mounted beneath a decompression tank and separated by a metal sliding gate, allowing rapid decompression of the tube section (Figure 3). The internal diameter of the tube system is 38 mm, and the decompression tank occupies a volume of 0.3 m^3. GRA mixtures were prepared by mixing solid gum rosin with 20 wt. % and 30 wt. % acetone and leaving the mixture overnight in a closed glass flask on a stirring plate to assure complete dissolution. The mixtures remained cloudy, indicating the presence of insoluble microparticles. Experiments were performed by filling the bottom of the tube with 30 cm^3 GRA mixtures. The decompression tank was evacuated to the desired pressure, and rapid decompression of the GRA mixture was then triggered, by pneumatically opening the sliding gate. This has been shown to initiate strong volatile exsolution and corresponding expansion of the flow. Vesiculation is initiated close to the interface and then proceeds downwards (Phillips et al., 1995). We used final pressures of 12.5 to 0.5 kPa within the tank, to simulate eruptions with various ratios of exsolution to final pressure p_{exs}/p_{final} (decompression ratio, Table 1).

We investigated two main variables: first, the presence of pre-eruptive volatile bubbles within the magma and second, change in conduit diameter. A vertical cylindrical conduit in the natural system is assumes. In our experiments, bubbles were introduced by rapidly decompressing the GRA mixture in a first step to the exsolution pressure of acetone, which was found to be 25 kPa. This first step resulted in the production of small bubbles (in some cases one bigger bubble was additionally found to escape from the top

of the GRA mixture, but no significant expansion was observed during this step. The gate was then closed again, and the decompression tank further evacuated to the final pressure. For each final pressure, both initially bubbly and non-bubbly runs were conducted. The effect of diameter changes was investigated by narrowing or widening the diameter from 38 mm in the lower tube part to 14 mm or 147 mm. Expanding flows experienced a change of the cross sectional area expressed as the ratio A_{ratio} (standard area : reduced/widened area) of 7.5:1 and 1:15, respectively.

The experiments were recorded using a Redlake MotionScope® high-speed camera at either 250 or 500 frames per second (fps), as well as a regular-speed camera (25 fps). Pressure variations within the expanding two phase flow were monitored by pressure transducers installed in the basal plate and in the upper tube section (bottom and upper transducers; Figure 3). The frequency response of the transducers is between 10 Hz and 100 kHz, and pressure oscillations were logged at a sampling frequency of 10 kHz. Blank runs were evaluated for background noise and artefacts. The data were corrected for the decompression step and band-pass filtered using Mirocal Origin® 6.0.

4. Results

Some fundamental aspect in the behaviour of decompressed GRA mixtures are described by Phillips et al. (1995) and Stix and Phillips (in preparation). At extremely slow decompression rates it was observed that the style of bubble growth and coalescence depend on the achieved decompression Δp. Initially, at low decompression, bubbles grow and collapse close to the surface, feeding both upward and downward growth of a foam layer as decompression proceeds. As decompression rates are increased, GRA mixtures

experience strong foaming at virtually all stages of decompression, and expanding GRA flows will fragment, if decompressed below a certain threshold. Fragmentation thresholds are sensitive both to the viscosity/acetone content and the timescale of decompression.

In the following sections, we will use the notation "GRA20–12.5–wB", when referring to specific runs and their conditions; here the notation refers to the decompression of a GRA mixture with 20 wt. % acetone to a final pressure of 12.5 kPa with pre-eruptive bubbles ("wB). The notation "noB" identifies runs without initial bubble content.

4.1 Simple conduit

The primary goal of these experiments was to investigate the influence of pre-eruptive bubbles on the flow expansion rate, acceleration, and fragmentation thresholds of GRA mixtures expanding in a simple conduit of constant diameter. Consistent with previous studies, rapid decompression of the GRA mixtures of 30 wt. % and 20 wt. % acetone induced rapid expansion and foaming of the GRA mixtures within the tube. With increasing decompression ratio, a head region composed of larger bubbles can be distinguished from a denser flow body of smaller bubbles (GRA20–2.5–noB, Figure 9a). This distinction is affected by both pre-eruptive bubbles and low viscosity. The distribution of bubbles generally appears more homogeneous over the entire flow if pre-eruptive bubbles are present prior to final decompression, while large bubbles at the flow front of a low-viscosity GRA mixture of 30 wt. % acetone would usually burst (e.g., GRA20–2.5–wB, GRA30–10–noB) and escape as free gas.

The expansion of the flow is monitored as $\Delta h/h_0$, where h_0 is the initial height of

the GRA mixture and Δh the difference of the expanded height relative to h_0 (Fig. 3). The expansion $\Delta h/h_0$ over time is directly proportional to velocity of the flow front. The expansion–time curves (Figure 4 and 5) can be evaluated via power law relations, $f(x) = a\ x^b$, with the exponent $b = 1$ indicating constant expansion (constant velocity of the flow front; slopes are parallel to the dashed lines in Figures 4 and 5), $b \sim 2$ indicating constant acceleration, or $b > 2$ indicating increasing acceleration. In general, higher decompression ratios (lower final pressure) and lower viscosity result in faster expansion rates. For final pressures between 10 and 2.5 kPa we observe two distinctive regimes in the expansion rate curves of mixtures of 30 wt. % acetone (Figure 4). First, during initial stages, the flow expansion rates are constant (parallel slopes, with power law exponent b~1). Second, during later stages flows develop accelerating expansion rates, with exponents $b \geq 2$. By contrast, the regime of constant expansion rate is absent in flows with pre-eruptive bubbles. Under these conditions, expansion rates are characterized by power law exponents $b \geq 2$, at all stages. This effect of a greater expansion rate at a given time becomes less pronounced as the decompression ratio is increased (Figure 4b), to be reversed at final pressures of 0.2 kPa. Here, flows with and without pre-eruptive bubbles show almost parallel expansion trends, which are characteristic for the late stages of flow.

Mixtures of 20 wt. % acetone (Figure 5) with higher viscosity behave similarly to the low viscosity mixtures, although with some differences that most likely are related to the higher viscosity. The onset of fragmentation occurs at higher decompression ratios with final pressures < 5 kPa. Under non-fragmenting conditions ($p_{exs}/p_{final} = 2–5$) flows exhibit two expansion regimes. Constant initial expansion rates ($b \sim 1$) are followed by a long period of slowly decreasing expansion rates approaching zero (Figure 5a), before the

foam finally collapses. Mixtures undergoing the same range of decompression with pre-eruptive bubbles initially expand faster over a given time with power law exponents b of 1–1.5, but then fall back or collapse to the degree of expansion of their standard counterparts. Flow development during very late stages are thus identical for runs with and without pre-eruptive bubbles. At higher decompression ratios ($p_{exs}/p_{final} = 10$) the effect of faster initial expansion is almost absent, and again appears reversed at even higher lower final pressures.

Figure 6 depicts recorded pressure fluctuations within the liquid body during the first 1.5 s after decompression of GRA mixtures with 30 wt. % for various final pressures with decompression ratios between 2.5 and ~ 80. The data are corrected for the pressure drop due to decompression and subsequent relaxation signal of the transducer. Oscillatory signals occur dominantly within the 10 to 100 Hz regions and are of durations of generally less than 0.6 s, which compares to expansion timescales of low decompression runs but significantly higher than those for high decompression runs. The signal almost immediately after decompression is characterized by a significant pressure rise and a few high-amplitude pressure peaks (Δp = 2 to 1 kPa, peak-to peak) most prominent within the 10 to 50 Hz band. The amplitude of these peaks appears to be correlated with the extent of decompression. By contrast, higher frequency bands of 20 to 75 Hz and 50 to 100 Hz exhibit continuous oscillations for several tens of seconds at amplitudes around 0.6 Hz and 0.5-0.2 Hz, respectively.

The general appearance of the recorded pressure fluctuations, i.e., the active frequency bands and the waning intensity with time, is common to all runs decompressed from atmospheric pressure to various final pressures. Pressure oscillations/peaks at the

base of the reservoir within the 10-100 Hz region are characteristic both of rapidly expanding, strongly fragmenting flows (e.g., final pressures of 0.2 kPa) and slowly expanding, mostly bubbling flows (e.g., final pressures of 10 kPa). Only the amplitudes and time intervals of oscillations vary with the experimental conditions. More viscous flows (20 wt. % acetone) show somewhat reduced amplitudes. A significant contribution from resonant frequencies is unlikely as they depend on the acoustic velocity and height of the liquid, which are both highly variable under the experimental conditions, and the individual runs. In general, higher amplitudes/ excess acoustic pressures, especially within the low frequency band of to 10-50 Hz, are observed when decompression is high. As the acoustic excess pressure is dependent on the mass flow rate (Vergniolle and Brandeis, 1996), the low frequency signature may reflect a higher volatile exsolution rate at stronger oversaturation. The time taken to exhaust or dampen the acoustic source is comparable between runs of different decompression, typically < 0.4 s. The notable reduction of pressure variations observed in initially bubbly flows may be caused by the dampening effect of initial bubbles distributed throughout the liquid body (see discussion below).

A measure of acoustic energy emitted from the bubbles within the two phase flows is the sound energy density E_s, describing the sound field at a given point (here the source) in terms of energy per volume. It can be expressed as $E_s = p_{ac}^2 \times (\rho \times c^2)^{-1}$, where p_{ac} is the acoustic pressure, ρ the density and c the sound of speed. To compare average energy densities recorded over a time interval Δt we use the time-integrated form $\int_0^t Es(t)$.

As can be seen from Figure 6d, the highest energy density values are recorded at the

beginning and cease within 0.6 s to background. Decompression of the flows starts at time zero, and energy densities are given for any point in time after the decompression interval. The decompression interval was masked with synthetic data to avoid strong artefacts during band-pass filtering. The energetically most active frequencies are found in the region between 10 to 20 Hz, from which both the highest energy peaks and highest energy densities integrated over the 0.6 s interval are recorded for a given degree of decompression. For instance, the 10 to 50 Hz band reaches integrated energy densities of 1.6×10^{-5} μJ m^{-3}s at a decompression of p_{exs}/p_{final} of 83, compared to only 3×10^{-6} μJ m^{-3} s recorded from the 20 to 75 Hz band for the same decompression (Fig. 6d, right abscissa). Within the same low frequency band, the integrated energy densities correlate positively with the extent of decompression, whereas a clear correlation is either absent or weak at frequency bands above 20 Hz. Recorded energy densities of the decompressed GRA mixtures are also affected by viscosity and/or volatile content of the GRA mixtures. GRA mixtures with 20 wt. % acetone exhibit an overall tendency towards lower energy emissions from the recorded frequency bands. The extent of this effect appears to be a non-linear function of various parameters, as it is sensitive to the degree of decompression and the frequency range. Again, at frequencies between 10 and 20 Hz the behaviour is the clearest. Within this frequency band, energy emission over time is observed to be two to six times lower during decompression of GRA mixtures with 20 wt. % acetone compared to mixtures with 30 wt. % acetone.

The above behaviour contrasts strongly with decompressed GRA mixtures with pre-eruptive bubbles. In these cases, energy densities recorded over the same time interval are strongly reduced within all frequencies between 10 and 100 Hz. The energy recorded

over the 0.6 s interval from the 10 to 50 Hz band is lowered by eight to two times compared to runs without initial bubbles. Even within the low frequencies, no clear correlation among the recorded energies and the decompression is observed, which may indicate some variability in the pre-eruptive bubble content between the different runs.

4.2 Changing diameter conditions

Reducing conduit diameter

In this set of experiments the cross-sectional area was significantly reduced with an area ratio A_{ratio} of 7.5 : 1, introducing a significant obstruction to the expanding GRA mixtures. However, the expansion rate of the flow front was not reduced compared to the simple conduit when entering the constriction. When expanding into the narrow tube section, the head of low viscous flows (30 wt. % acetone) experiences increased acceleration, in particular if decompression ratio is low (p_{exs}/p_{final} of 2.5) and the expansion-time profile shows a clear kink (Figure 7a). Likewise, a high viscosity flow (20 wt. % acetone) experiencing a low decompression ratio (p_{exs}/p_{final} of 2) deviates significantly from simple conduit behaviour, changing from a roughly constant expansion rate to accelerating rates within the constriction. When decompression ratios are increased to 10 or ~80, acceleration of the flow front within the constriction becomes comparable to simple conditions, with relatively constant and similar rates (Figure 7b). The velocity of a fluid within a tube varies with the square of the tube radius for constant driving forces and viscosity (e.g., Nicholls, 1990). To achieve similar or higher expansion rates, the viscosity of the flow front must be reduced significantly. This agrees well with visual details of the expanding GRA mixtures, revealing strong separation of a volatile rich flow front within

the narrow tube (Fig. 9b). The head of the flow is continuously fragmenting and dispersed, reducing density, viscosity and friction along the tube wall, and promoting high expansion rates.

Flows subjected to reducing conduit conditions reveal strong initial excess acoustic pressures, with pressure fluctuations of the first peak of several kPa even at lower decompressions and the acoustic source remaining active for about 4 to 6 times longer compared to the standard cases. In GRA mixtures of 30 wt. % acetone reveal initial peak-to-peak amplitudes of 10 to 7 kPa within the 10-50 Hz band are recorded at p_{exs}/p_{final} between ~80 and 2.5. Flows exposed to reducing conduit conditions are therefore characterized by higher sound energy densities. At high decompressions and low viscosity, peak energy densities E_s within the low frequency band are increased by an order of magnitude, as is the emitted energy density over the 0.6 s time interval (Figure 8). Flows of higher viscosity exhibit an analogous behaviour, although the total energy density emitted over time increases in a more stepwise fashion and over a slightly longer timescales.

Increasing conduit diameter

A further subset of experiments was carried out, in which expanding flows experience an increase change in cross section with an area ration A_{ratio} of 1: 15. This represents the expansion of the flow within a laterally unconfined space, at least for the earlier stages (Fig. 10). Only in a few cases did the tube walls of the wide section impinge on late-stage development of the flows. Flows undergoing low degrees of decompression did not expand into the wide section and simply continued to degas by bubbling. In the case of flows experiencing high degrees of decompression, the most obvious result is the

drastic change in fragmentation behaviour. The likelihood or at least the violence of fragmentation was reduced, especially in the case of more viscous runs. GRA mixtures with 30 wt. % acetone exhibit strong bubble bursts at a fragmentation level just below the opening when subjected to strong decompression. More viscous mixtures underwent no fragmentation, even at a final pressure of 0.3 kPa. The shift in eruptive style is most likely the effect of the wide conduit preventing flows from accelerating to rates sufficient for fragmentation to occur.

Instead, at final pressures of 2.5 kPa and 0.3 kPa (p_{exs}/p_{final} =10 and 80), viscous GRA mixtures start to form highly vesiculated dome structures (Figure 10), and the final size and general extrusion behaviour depends on the extent of decompression. At p_{exs}/p_{final} of 10 a gas-rich bulge grew initially, then gravitationally collapsed spreading laterally (Figure 10a, left and middle panel) as bubbles degassed and vesicularity decreased. Further lateral spreading was promoted by newly rising material injected into the side parts (Figure 10a, right panel). At higher decompression (p_{exs}/p_{final} = 80) no gravitational collapse was visible, and the vesicular bulge remained stable. Internal support of such a structure is possibly provided by a higher bubble density and higher viscosity of the interstitial liquid and bubble films due to strong volatile exsolution, causing a strong liquid network. Continuous growth from below takes place in both a horizontal and lateral sense, producing domal or stretched "cauliflower" structures (Figure 10d). Runs with pre-eruptive gas bubbles decompressed to 2.5 kPa and 0.3 kPa bubbles produced structures systematically larger in size, but with analogous behaviour.

The extreme degrees of expansion achieved indicate the capacity of liquid-volatile systems to strongly vesiculated and collapse even in the absence of strong shear strain and

at decompression ratios typical for intermediate water depths.

5. Discussion of the observed features

5.1 Flow expansion

Both expansion and acoustic pressure fluctuations are, in principle, induced by the same process, namely exsolution of acetone and growth of bubbles as GRA mixtures are decompressed. The expansion rate of the flow is coupled to the growth rate of the bubbles, which is mainly controlled by volatile diffusion and volume. In the simplest case, diffusion-induced bubble growth can be continuous and the rate R_g constant, depending on the activation energy of the transport across the bubble-liquid interface, $R_g \propto \exp[-\Delta G/(RT)]$, if kinetics rather than diffusivity is rate controlling (Dowty, 1980). If diffusivity is low, it becomes rate limiting, and the parabolic growth law (Scriven, 1959) with a rate $R_g(t) \propto \sqrt{D/t}$ has been used (e.g., Sparks, 1978). Blower et al. (2001b) demonstrated that constant bubble growth rates can also result from coupling of viscous and diffusive effects, if both are dependent on volatile concentration. In our experiments, initially bubble-free GRA mixtures undergoing low to moderate decompression initially expand at constant rates (power law exponent $b \sim 1$) at both high and low viscosities (Figures 4a and 5a). This can be interpreted as a regime of generally constant net gas volume growth at a low number of initial nucleation events. The constant growth in free gas volume does not necessarily reflect a constant growth rate of individual bubbles, but rather the net effect of bubble growth and changes in nucleation rate over time. Since high and low viscosity mixtures initially expand in a similar fashion, viscosity

appears to assert no significant influence on the early expansion behaviour affecting only the degree of expansion. The strong increase in expansion rates (with power law exponents $b > 1$) of volatile rich flows can be interpreted as a regime of strongly increasing nucleation events. Numerical and experimental studies suggest nucleation to proceed continually (Navon et al., 1998; Simakin et al., 1999; Blower et al., 2001a, 2002). In these numerical models applying e.g., the Voronoi cell method, new bubbles nucleate within the given liquid volume at greatest distance to already existing bubbles, where volatile depletion is least. The total amount of nucleation events may increase in a fractal pattern/cascading mechanism (Lyakhovsky et al., 1996; Blower et al., 2002). The higher volatile content, lower viscosity and higher diffusivity of the 30 wt. % acetone GRA mixtures should promote nucleation events. The transition from flow behaviour with exponents of $b \sim 1$ to $b > 1$ reflects the point of significant increase in bubble number (cascading nucleation), hence a drastic increase in the total gas-liquid interface, allowing for a high diffusive net mass transfer of volatiles into the bubbles and consequently increasing expansion rates. By contrast, the volatile supersaturation of mixtures with 20 wt. % acetone may be significantly reduced by the early nucleation and growth events. Lower supersaturation and lower diffusivity consequently reduces the driving force for nucleation and the number of nucleation events and/or the number of new nuclei per event remain low. The abrupt change in expansions rates with power law exponents b decreasing from ~ 1 to <1 from observed in runs with 20 wt. % acetone mixtures and decompressed to 12.5 kPa and 5 kPa at $t = 0.2$ s and 0.007 s, respectively, might indicate a very strong reduction of new nuclei and a regime of parabolic growth at a rate $R_{g(t)} \propto \sqrt{D/t}$. Visual observations, as well as the expansion profile of run GRA20–

12.5–nB (Figure 5c) reveal the upward coalescence of bubbles and their escape at the flow front (open degassing) and thus a partial decoupling of the movement of single bubbles from the entire flow, in agreement with a lower bubble number density.

When the decompression ratio is high, e.g., p_{exs}/p_{final} ~80, GRA two-phase flow expansion is strongly accelerating with power law exponents $b > 1$ (Figures 4b and 5b). We interpret this as strong cascading nucleation being induced at very early stages, due to high driving force (strong rapid decompression). The first generation of bubbles will grow very rapidly due to the strong driving force, promptly depleting the immediate, surrounding liquid in volatiles and provoking nucleation at new sites. Such a scenario will result in increasing expansion rates.

This view offers a way to interpret our results derived from runs with pre-eruptive bubbles. As can be seen in Figures 4 and 5, and described above, bubbly runs expand at higher rates, at least during later stages, with power law exponents b commonly >1. This is the direct consequence of a higher initial nucleus/bubble number. As long as the pre-eruptive bubble content is significant with respect to the first generation of bubbles nucleating during the final decompression, these pre-eruptive bubbles will have a notable impact on initial flow behaviour. As a result of this significantly increased net free gas-liquid interface, the net exsolution rate and thus expansion rate will increase more rapidly. Conversely, this effect will diminish as decompression, and therefore the driving force for nucleation, increases and the number of first-generation bubbles nucleating after the final decompression becomes larger. With a transition towards a rapidly cascading nucleation mechanism and likely a larger number of initial nuclei, the role of pre-eruptive bubbles will progressively become less important at high decompressions so that initially bubbly

and non-bubbly runs behave similarly (e.g., compare GRA run with 20 wt. % acetone decompressed to 2.5 kPa; Fig. 5b). The apparent switch in the bubble effect at very high decompression, if meaningful, is more challenging to explain. It might indicate "competition" between bubble nucleation and growth of existing bubbles at very high decompressions. Pre-existing bubbles may initially grow more rapidly, not requiring any nucleation step. This will be of particular advantage at decompressions to very low pressures which require larger stable nuclei (Bottinga and Javoy, 1990). The preferential diffusive growth of existing bubbles, combined with static bubble growth due to the pressure change could introduce a trade-off. Accumulating the free volatile phase in larger bubbles reduces the growth rate of the net free gas-liquid interface, hence the net exsolution and expansion rate. Mourtada-Bonnefoi and Mader (2004) have suggested, similar to our results, an expansion-enhancing effect induced by pre-eruptive air bubbles. In their experiments diffusive growth was likely to be further promoted by the low partial pressure of acetone within the air bubbles.

5.2 Acoustic pressures

Emission of acoustic signals and pressure fluctuations are typical features of two-phase fluid motions within conduit systems (e.g., Lane and Gilbert, 2008). The ascent of a gas slug expanding as it rises and bursts at the liquid surface is capable of inducing dynamic pressure changes within the liquid. Constrictions within the conduit or inclined conduit systems assert a significant effect on the acoustic or seismic signal of a rising gas slug (Ohminato et al., 1998; Ripepe et al., 2001; James et al., 2004; James et al., 2006). Oscillating pressure fluctuations have been interpreted considering various mechanisms of bubble vibration/deformation and surface waves (Lu et al., 1989; Vergniolle and

Brandeis, 1994; Vergniolle et al., 1996).

A spherical bubble of radius r within an infinite liquid of the density ρ may constitute oscillating changes in shape at constant volume, constrained by the surface tension σ. The oscillation frequency is given by (Lu et al., 1989):

$f_s(r) = 1/(2\pi)\sqrt{\sigma/(\rho r^3)}$. When approximating the surface tension of GRA using that of acetone (0.024 N m^{-1}), frequencies of ≥ 10 Hz result in bubble radii r of ≤ 2 mm.

Volume oscillation is caused by overpressurized bubbles expanding and contracting around the equilibrium radius, providing a frequency of (Lu et al., 1989):

$f_v(r) = 1/(2\pi r)\sqrt{p_g/\rho}$. For internal bubble gas pressures p_g of 10 to 0.2 kPa and frequencies ≥ 10 Hz, radii of ≤ 5 cm and ≤ 7 mm are required. Here, the frequency is dependent on the final pressure, varying for a constant bubble radius by a factor of ~6 between the high and low decompression end members.

In a semi-infinite liquid, gravity acts to balance the distortion of the interface by floating bubbles, resulting in oscillating gravity waves. For an interface, confined laterally within a container, the active frequencies can be calculated using: $f_g(r) = 1/(2\pi)\sqrt{gk}$ (Patterson, 1983; Vergniolle et al., 1996), where g is the gravitational acceleration and k is the angular wavenumber derived from the tube dimensions and a set of experimentally determined numbers for the different modes. For our experiments the first three modes yield frequencies less than 5 Hz.

None of these three mechanisms appears to be able to account for the observed record of acoustic emissions within the 10 to 200 Hz region. Their frequencies are either too low (gravity waves), the maximum bubble radius needed to match the frequency

region too small (shape oscillations), or they show an appreciable pressure dependence, which is not observed, and a bubble radius larger than the tube radius at high final pressures (volume oscillation). Also, continuous bubble growth and bubble deformation due to shearing will likely interfere with the shape and volume oscillations.

Vergniolle et al. (1996) have envisioned another process to induce oscillatory behaviour, namely lateral film flow around the bubbles inducing dynamic pressure changes at the tip of the bubble and kinematic waves within the liquid. For a lateral liquid film of the density σ and viscosity η exceeding the asymptotic thickness, the frequency becomes $f_k = 0.81n/(2\pi)\sqrt[3]{\rho g^2/\eta}$. For our experiments using 30 wt. % acetone mixtures, this yields 13 Hz for the first mode (n=1), 26 Hz and 39 Hz for the second and third mode (n=2, 3), and for 20 wt. % 7 Hz, 14 Hz, and 21 Hz. This shows significantly better agreement with our observed frequency record. However, this model requires laminar liquid flow around the bubbles, as in Vergniolle et al.'s (1996) model of a single rising slug. This may be slightly different from our experimental conditions, in which the motion of the liquid is strongly coupled to the expansion of the gas bubbles. Yet if bubbles undergo pure shear during expansion, this will induce laminar motion of the fluid relative to the bubble, which might trigger dynamic pressure fluctuations in a similar fashion.

James et al. (2004) describe a pressure decrease within the liquid below a single gas slug expanding during ascent, linked to dynamic pressure losses within the liquid film around the slug. Likewise, a dynamic pressure increase results from bubbles bursting and draining of the liquid film. If a similar mechanism can operate on multiple bubbles ascending and bursting in close time intervals, this might introduce a quasi-oscillatory

behaviour whose frequency depends on the interval between the bursts.

From Figure 6 it can be seen that acoustic pressure amplitudes, especially of the initial peaks, relate to the degree of decompression and are highest in low viscosity mixtures, signifying bubble overpressure within the bubbles. This is interpreted in terms of the interplay between diffusivity and volatile concentration-dependent viscosity. As low viscosity allows for rapid diffusion of acetone into the bubble, the surrounding liquid film is rapidly depleted, introducing a strong viscosity gradient across the liquid film. The effective viscosity of the liquid shell restricting bubble growth is very close to that at the gas-liquid interface (Lensky et al., 2001). A delayed elastic response (due to the increased viscous relaxation time) of the liquid shell to the expansion pulse of the bubble can be expected, causing a sudden pressure rise within the bubble. The acoustic record suggests that overpressures are maintained for short time scales only. Assuming a viscosity-dependent diffusivity, the gas flux into the bubble will cease, and the strong volatile concentration gradient across the liquid shell may start to re-equilibrate. One could speculate that an oscillating system with detectable pressure fluctuations might arise from such alternating depletions and equilibrations, with some dependence of the frequency on viscosity.

In our experiments, the acoustic signal recorded in runs with pre-eruptive bubbles is reduced, presumably indicating stronger damping effects. Although vesiculation during rapid decompression of GRA is known to be initiated close to the interface and then proceeds downwards (Phillips et al., 1995), in our experiments with pre-eruptive bubble nucleation and growth also occurred during the time interval between the first and second decompression step. Here, nucleation probably occurred throughout the liquid and at the

containment walls. During the second decompression to final pressures, downwards directed vesiculation can then proceed more rapidly, damping pressure fluctuations propagating through the vesiculated lower part of the liquid. Unfortunately the cloudy nature of the GRA mixtures prevents direct observation of bubble growth within the liquid.

The high overpressures and pulsatory acoustic signal recorded from GRA flows experiencing a constriction (Figure 8) is the direct consequence of repeated rapid gas segregation events. Flow expansion appears hampered as soon as the flow front reaches the reduced diameter. The volume increase due to volatile exsolution and static expansion within the lower part cannot be balanced by volume flux through the narrow tube, leading to overpressurization and foam collapse. The overpressure is released by the separation of a very volatile-rich, low-density flow expanding very rapidly through the tube. The acoustic and visual record suggests that this is repeated several times. This is different from a foam collapse scenario (Jaupart and Vergniolle, 1989), as in our case the flow actively expands by diffusion-driven bubble growth and experiences a sudden drop in static pressure.

Thus, two-phase flow systems undergoing strong dynamic decompression and continuous nucleation and diffusive bubble growth appear to be characterized by a more complex acoustic pressure and probably seismic record than systems dominated by single ascending gas slugs. In particular, pressure oscillations are difficult to relate to a single monopole source; instead they may be caused by the superposition of various dynamic pressure changes which are spatially distributed within the system. The generally rapid damping of the pressure signal is more likely a consequence of the experimental setup,

with vesiculation growing rapidly downwards. Once the foam has reached the base of the system, pressure fluctuations will be effectively attenuated.

5.3 Fragmentation process

Under the experimental conditions, fragmentation can be observed to occur in a range of styles, from simple bubble bursting at the flow front of low-viscosity mixtures which are mildly decompressed (30 wt. % acetone, 10 kPa final pressure, no pre-eruptive bubbles), through the tearing apart of the flow head under higher viscosity and intermediate p_{exs}/p_{final} (e.g., 20 wt. % acetone, 2.5 kPa final pressure), to very strong dispersal of the entire flow of low-viscosity mixtures undergoing strong decompression (e.g., 30 wt. % acetone, 0.3 kPa final pressure). In our experiments, the onset of fragmentation most likely occurs within the ductile regime for the following reasons. The overall expansion rates (Figure 4 an 5) are significantly below the critical strain rate defined by the Maxwell criteria, and ductile behaviour can be assumed at any point during the flow. No direct relation is observed between the onset of the fragmentation process and the expansion rate. Instead, fragmentation appears initiated at a certain degree of expansion $\Delta h/h_0$ of 7 to 8 (corresponding to an average vesicularity of 85 % to 88 %) for low viscosity flows $\Delta h/h_0$, and between 1.7 and 3 (corresponding to a vesicularity of 60% to 75 %) for viscous flows (Figure 4 and 5). On the other hand, experiments under increasing diameter conditions have demonstrated that extreme degrees of expansion are possible without fragmentation when shear stresses along the conduit are removed or reduced (Figure 10d). Therefore, vesicularity is a prerequisite but not a sufficient condition for fragmentation to occur. This indicates that even within the ductile regime, shear stress or shear strain rate, viscosity, and vesicularity are important factors governing

the fragmentation process of two-phase flows, and that the fragmentation threshold is the product of these partially interdependent parameters. A comparison between 20 and 30 wt. % GRA runs under increasing conduit diameter conditions clearly demonstrates that a strong reduction of the shear strain rate can be the dominant effect in determining whether fragmentation does or does not occur

From Figure 4 and 5 it can be seen that fragmenting flows undergo increasing expansion rates, but no general change in the acceleration behaviour before or after the onset of fragmentation is observed. This could indicate that only minor amounts of elastic strain energy or overpressure is released as the flow breaks apart. The effect of pre-eruptive bubbles is best demonstrated with GRA mixtures of 30 wt. % decompressed to 10 kPa. While the flow is close to its fragmentation threshold under standard conditions with almost no fragmentation and only a mild bubble burst, fairly violent flow disruption and fragmentation occur when decompressing an initially bubbly flow. This presumably reflects the increase in acceleration behaviour of the flow, which is thus an indirect consequence of the pre-eruptive bubble content. Likewise, initially bubbly flows usually fragment more efficiently generating a higher free net surface, as can be seen in the shift to smaller grain sizes (Figure 11). A higher kinetic energy and possibly a greater bubble number density may be responsible for the shift in fragment size.

5.4 Degassing and permeability

Three independent factors were observed to influence the efficiency and rate of degassing, i.e., the exsolution of acetone: (1) strong decompression/fragmentation, (2) low viscosity, and (3) the presence of pre-eruptive bubbles. Degassing and volatile escape mechanisms in non-fragmenting flows were visually examined during the later stages of

GRA mixtures of 20 wt. % acetone decompressed to higher final pressures, e.g., 12.5 and 5 kPa (Figures 5a and 5c). During late stages the flows expand at decelerating rates indicating declining bubble nucleation and growth rates, reaching a near steady-state level of almost constant expansion at which bubble growth rates equal rates of permeable volatile loss at the flow front. At this stage, bubbles within the flow expand and slowly move upwards. Within the middle to upper part temporary permeability is achieved by bubbles coalescing in an upward fashion creating long gas pockets. These short-lived pathways provide an efficient mechanism to release volatiles via mild bubble bursts without the need to displace the liquid surrounding individual rising bubbles. This supports Polacci et al.'s (2008) interpretation of channel-like textures in scoria clasts as a record of passive permeable gas flow. Coalescence and subsequent volatile escape in our experiments is favoured close to the tube wall where shear rates are highest. In nature, this will promote gas loss trough a fractured conduit wall.

At a low decompression ratio (p_{exs}/p_{final} =2; 12.5 kPa final pressure), the near steady-state regime is characterized by strong oscillations of the net expansion caused by continuous bubble bursts released along these short-lived pathways. Using the amplitude of about ± 0.3 × tube radius and the frequency of the bursts of 5 Hz, we estimate the volume of a single released gas pocket to ~ 2 cm^3 (assuming a half-sphere geometry) and a rate of degassing at about 10 cm^3 s^{-1}. At higher decompression ratios (p_{exs}/p_{final} = 5; 5 kPa final pressure) degassing mechanisms are similar for net expansions $\Delta h/h_0 < 3$, but strong oscillations are replaced by small steps, apparently similar to stick-slip movements. These are caused by the coincidence of superimposed bubble bursts and expansive flow growth from below. The collapse of the uppermost flow head due to gas

loss is balanced by volume expansion within the middle section of the flow. This mechanism contrasts with the sudden slips of the magma column along the conduit wall in nature caused by reduction of the flow resistance, defined as stick-slip (Denlinger and Hoblitt, 1999). As the foam reaches higher degrees of expansion ($\Delta h/h_0 \sim 4$), it becomes static with limited bubble movement. Thus, there appears to be a certain degree of decompression between 2 and 5 at which the bubble growth rate exceeds the rate of bubble coalescence and permeable escape such that the flow can expand sufficiently fast to reach a temporarily stable foam height.

6. Implications for submarine eruptions

The experiments cover degrees of decompressions that can be achieved in water depths from 50 m to several kilometres for typical magmatic saturation pressures between 40 to 350 MPa as suggested by volatile concentration in melt inclusions from various tectonic settings (Métrich and Wallace, 2008). Our observations illustrate the importance of a pre-eruptive bubble inventory at high confining pressures, as well as the influence of sudden changes in conduit diameter on ascent rates, extrusion behaviour and volatile segregation of magmas erupted in submarine environments.

6.1 Eruption behaviour at various water depths

Low energy eruptions

Eruptions taking place in very deep marine settings will be characterized by slow volatile exsolution during ascent due to low decompression ratios, and will rise slowly at approximately constant rates, as exemplified by experiments GRA20–12.5(05)–noB or

GRA30–10–noB (Figures 4a and 5a). The kinetic energy of such flows will remain low and constant. Given equal degrees of decompression, the conduit length should assert little influence on the eruption behaviour, as the kinetic energy of the flow is time invariant. The flows will rise until their kinetic energy is balanced by their potential energy. Average liquid velocities are close to zero, while gas bubbles segregate and rise through the liquid column (Figure 5c). This corresponds to the situation described by Parfitt and Wilson (1995) as a pure Strombolian regime, but may differ in some details. Under the high hydrostatic pressures of submarine environments, large bubble sizes are suppressed, hence slugs of several meters in diameter, as observed in subaerial environments, are unlikely, and the kinetic energy of the arriving bubbles is lower. At the same time the vent will be blocked by a rigid crust due to rapid cooling of the lava surface within the conduit, as observed at NW Rota volcano (Chadwick et al., 2008). Ascending gas bubbles will accumulate beneath this lid, and pressure increases as the foam layer thickens. In more viscous magmas where relative bubble movement is retarded, upward coalescence (see 5.1) may play an important role providing transient pathways for gas segregation. Once pressures exceed the tensile strength of the lid, it fails and rapid coalescence and expansion of the foam will culminate in pyroclast forming bubble bursts. Pyroclastic deposits from mid-ocean ridges usually consist of thin glass shards (limu o Pele), which, in many cases, strongly deformed and folded, including bended ribbons, Pele's, hair, as well as low vesiculated blocky clast (Clague et al., 2003b; Helo et al., 2008). Such fragments would be expected from the ejection of small bubbly magma blobs undergoing partial foam collapse.

The formation of submarine lava balloons can likewise be understood in terms of

low degrees of decompression or slow ascent rates. Such structures, of 0.4 to 3 meters in diameter, have been described in the Azores originating from vents at 300 to 1000 m water depth (Gaspar et al., 2003). If the outer lava surface is divided into several smaller plates continuously breaking apart as is the case for submarine lava lakes, smaller gas pockets may slowly squeeze through the opening cracks, pushing a few cm thick layer of lava ahead and finally detaching as a lava balloon. Formation of lava balloons might thus be a rare intermediate example in the spectrum of effusive to pyroclastic activity in deep marine environments.

The eruption behaviour is generally dictated by the magma ascent rate (Parfitt and Wilson, 1995; Parfitt, 2004) and indirectly influenced by the presence of free pre-eruptive gas bubbles (Fig 4a, 5a). As our experiments demonstrate the influence of these bubbles to be greatest at low degrees of decompression, we expect this influence to be more significant at greater water depths. High hydrostatic pressures will favour pyroclastic eruptions arising from bubble bursts over fire fountaining induced by magma fragmentation within the conduit (Hawaiian style), since exsolution rates and expansivity will be low. Yet transitions from mild bubble bursting to strong magma dispersal within the conduit, as exemplified by our experiments GRA30–10–noB and –wB (Figure 4a), should be promoted by variations in the pre-eruptive bubble inventory.

High energy eruptions

Eruptions taking place at intermediate water depths, with appreciable volatile saturation pressures, experience higher decompression ratios, although still significantly lower than eruptions at atmospheric pressures. At water depths between 100 m and 1 km, for example, the decompression ratio is still 10 to 100 time less. Under these conditions,

ascent within the conduit can take place under accelerating rates (Figures 4b and 5b), and the kinetic energy of the flow increases continuously. This increase may be pre-requisite for efficient magma disruption to occur. Pyroclastic eruptions of relatively volatile rich magmas at intermediate depth ranges hence will be more likely to result from magma fragmentation within the conduit, similar to Hawaiian fire fountains. For these systems, the role of pre-eruptive gas bubbles, although their effect is greatly reduced, will contribute to a greater height of the lava fountain due the higher rise speed, and consequently more extensive clast dispersal.

In settings characterized by very volatile rich magmas (e.g., arc systems) eruptions will display Hawaiian style activity at shallower to intermediate depths, with a shift to regimes dominated by Strombolian activity with increasing water depth. Yet many magma reservoir systems are thought to accumulate gas bubbles beneath the reservoir roof (Jaupart and Vergniolle, 1989; Vergniolle, 1996), and decompression of this bubbly layer will promote the transition to Hawaiian style activity even at greater water depths.

Gas segregation at conduit constrictions

In natural systems, conduits typically undergo variations in width. From classical treatment of the rising magma as a Poiseuille flow, a positive correlation between diameter and flow velocity is anticipated (Nicholls, 1990), i.e., decrease of the ascent rate upon a restriction. However, our experiments indicate that narrow conduit sections allow efficient gas segregation to occur (Figure 9), rapidly releasing a very bubble rich flow into the upper part behind the constriction. We suggest that when a decompressed rising magma encounters a restriction, it initially is decelerated and choked. In result, pressure rises as gas bubbles rapidly accumulated behind the constriction (cf. Ohminato et al.,

1998) and partially coalesce. This process is associated with a strong and sudden pressure jump, with overpressurized gas-rich material being fed into the narrow section as the flow becomes unchoked. This low density flow can now continue to ascend and expand at accelerating rates (Figure 7), while a more dense flow depleted in free gas drains back. As fresh material from below rises, the process is repeated. We envision this process as an effective mechanism to produce vesiculated, rapidly rising flows which are separated from dense flows that pond or slowly rise and erupt effusively. The degree of segregation will depend on the ratio between the upper and lower conduit diameter, and the resulting flow heads may range from extremely gas-rich, almost instantaneously fragmenting and dispersing flows, to material with a mildly increased vesicularity. Similar mechanisms may operate in conduits experiencing sudden and strong changes in orientation, or sills feeding vertical dykes. In any case, this process causes enrichment of the upper parts of the rising magma in a free gas phase, and as such constitutes an effective mechanism to promote pyroclastic eruptions in submarine environments.

This gas segregation process is, in extreme cases, rather violent and associated with sudden pressure peaks and pressure fluctuations (Figure 8). These oscillations could constitute a potent source for seismic activity, producing repetitive signals of rather low to intermediate frequencies that should resolve as a point source. Lane et al. (2001) inferred that 10–30 Hz oscillations derived from fluid flow experiments using gum rosin mixtures would roughly correspond to 1.5–2 Hz tremors recorded on Stromboli. Adopting an equivalent translation scale for our pressure data, the dominant frequencies active in natural systems during constriction-induced gas segregation should range between one and ten Hertz. Subsequent ascent of the gas rich flow through the conduit can give rise to

continuous high frequency oscillations (Lane et al., 2001). Ohminato et al. (1998) interpreted sawtooth displacement waveforms at Kilauea Volcano as related to pressure changes within a sub-horizontal crack constricted at its outlet. Under choked conditions, gas pressures slowly inflate the horizontal crack. Once pressure is rapidly released as the system becomes unchoked and discharges through the outlet, the horizontal crack is deflating again. Magmatic two-phase flows undergoing decompression and volatile exsolution during ascent in a vertical conduit may in many cases undergo a rapid pressure increase when reaching a constricted section. Gas bubbles can accumulate faster as they actively rise through the liquid and at the same time they continue to grow by volatile diffusion. Even if bubbles + liquid stagnate at the constriction, diffusive growth will continue as ascending magmas can be strongly supersaturated (Paonita and Martelli, 2006). We envision such a mechanism as able to produce sharp pressure peaks analogous to Figure 8. Exact waveforms will depend on many variables, including vesicularity, speed of the rising flow and geometry of the constriction. Strong fracturing of the wall rock facilitating passive gas loss through the conduit wall should be a consequence of such rapid pressure fluctuations.

6.2 Silicic lava extrusion

A key parameter in silicic volcanism which is affected by increased pressure in submarine environments is the solubility of water in the melt. For ambient pressures at water depths of about one kilometre, equilibrium concentrations are ~1.5 wt. % H_2O, compared to only 0.1 wt. % at atmospheric levels, calculated from Henry's law (e.g., Sparks, 1978) $c_s = K_s\sqrt{p}$ where c_s is solubility in wt. % , and K_s the solubility constant

(4–4.5×10^{-6} $Pa^{-0.5}$; Dingwell, 1998). The higher water concentration results in a drastic decrease of magma viscosities by several orders of magnitude, to about $10^{6.2}$ Pa s (Hess and Dingwell, 1996). Accordingly, viscous relaxation time scales τ_s are short, on the order of $10^{-3.8}$ s, and the critical strain rate $1/\tau_s$ for brittle failure is less likely to be achieved. Extensive bubbles overpressures are also not expected to build up (Barclay et al., 1995). A change from a viscosity-governed regime to a regime more strongly influenced by inertia forces will occur. This shift in rheology will influence the extrusion behaviour of silicic lava and lava domes in submarine environments, which we have evaluated from our experimental runs under opening conduit conditions. The tendency to fragment violently is reduced, as the upward directed velocity component decreases and the flow expands unconfined in all directions once it passed the vent. The behaviour is intermediate between a subaerial lava dome and a lava flow. Depending on its kinetic energy, the foam structure will grow to a certain height and then gravitationally collapse, thereby degassing and becoming denser whilst spreading sideways (Figures 8a, left and middle panel). As new ascending magma then intrudes into the existing flattened and denser dome, it is deflected sideways, and the entire dome structure starts to spread and grow laterally in all directions (Figures 8a, right panel). We propose that this lateral spreading is a plausible mechanism to produce very large pumice clasts during deep-submarine eruptions. Pumiceous carapaces and large pumice blocks, commonly in the form of prismatic columns, have been described from various locations, e.g., Healy caldera (1150–1800 m bsl), southern Kermadec arc, and within the Sumisu volcanic complex (>1200 m bsl), Izu-Bonin arc (Wright et al., 2003; Allen et al., 2010) and have been suggested to be formed by quenching of the outer dome carapace. We suggest that

the lateral/radial spreading imposes a stress roughly perpendicular to the outer surface which is simultaneously being cooled by seawater and becoming more rigid. Small cooling fractures on the outer surface would passively propagate into the lava flow due to the spreading-induced stress field, allowing water to percolate deeper into the flow. These cracks could also serve as degassing pathways. Volume collapse of the magmatic gas due to cooling and coeval steam expansion of the seawater likely aid in disintegrating the outer carapace, breaking apart into single blocks and columns. The lateral spreading movement can also account for the observation of highly elongate vesicles parallel to the outer pumice surface (Allen et al., 2010), occasionally termed "woody" texture (Kato, 1987). This foliation/lineation parallel to the flow of the spreading flanks is in consistent with our model. As can be seen from Figure 10b, the size and height of the dome will be fairly sensitive to parameters such as the vesicularity of the head region and possibly the ascent rate. At even lower ascent rates permeable gas loss by upward coalescence will be greater (see above), and pure block lava flows may develop, as inferred by Kano et al. (1991) for the Ushikiri Formation, SW Japan.

If volatile exsolution within the head of the flow is more efficient, e.g., eruptions at shallower depths, the extruding head will be more vesiculated and more viscous. In this case it can avoid gravitational collapse and may rise and expand to significant heights (Figures 8c, d) and produce large pumice clasts. Dry densities of 230–700 kg m^{-3} are reported for pumice clasts derived from eruptions at water depths > 1000 m (Fiske et al., 2001; Wright et al., 2003), considerably lower then seawater (1027 kg m^{-3}). Not only will such densities stabilize the growing structure by buoyancy, the tendency to float will import vertical tensile stress within the pumiceous dome. We envision this tensile stress

to work in concert with rapid quenching of the outer surface causing disaggregation of the tall pumiceous dome structure. Deep cooling cracks cause deflection and concentration of tensile stress, whilst water ingested through these cracks will locally increase the density inducing heterogeneities and instabilities. These processes may culminate in a fairly sudden disintegration of the entire structure into large pumice blocks, to some degree resembling the triggered collapse of a brick tower. Gigantic pumice clasts of up to 10 meters in size described from different locations (Kano, 2003; Allen et al., 2010) may form from such eruptions.

Extrusion of silicic magma under deep sea conditions is significantly less likely to result in fragmentation triggered by rapid decompression of an extensively overpressurized rigid dome/cryptodome, due to the low magma viscosities (see above). Instead, it will rather form a pumiceous but low-viscosity dome structure undergoing lateral spreading or growing to even larger low-density pumice domes. The transition between the two types appears to be very sensitive to the ascent rate or degree of decompression. Pyroclastic eruptions in significant water depths can be expected to resemble Strombolian or Hawaiian style eruptions, expelling vesiculated low-viscosity magma blobs, as described for the Archaean Abitibi greenstone belt (Mueller and White, 1992).

7. Conclusions

The expansion behaviour of rapidly decompressed volatile-bearing liquids is dependent on various factors including volatile content/degree of decompression, presence of initial bubbles and conduit geometry. Expansion rates can vary from simply

accelerating to increasingly accelerating depending on the combination of those factors and the flow stage. Initial bubbles affect the flow expansion rate and fragmentation behaviour most significantly at high final pressures. Conduit constrictions were demonstrated to very efficiently and repeatedly choke the expanding flow and separate a strongly dispersing GRA mixture. In all cases, if achieved, fragmentation of the GRA was interpreted to occur in the ductile regime, covering a range of styles from bubble bursts to very strong and violent disrupting of the flow. Gas segregation and loss in non-fragmenting flows was characterized by upwardly directed bubble coalescence, temporarily increasing the permeability.

In the light of our experiments herein, there is little rationale in defining concrete threshold depths or degrees of decompression for transitions between styles of volcanic activity in submarine environments. Especially at great water depths where gas volume expansion is hampered, transitions between eruptions styles will be sensitive to intrinsic and extrinsic parameters such as the existence of magmatic foams and the conduit geometry, but also the rate of decompression (Stix and Phillips, in preparation). Particularly in mid-ocean ridge (MOR) settings, where the ambient pressure is high and the overall volatile content is lower compared to arc or intra-plate settings, variations in conduit geometry or the presence of magmatic foams will significantly increase the likelihood of explosive eruptions to occur.

References

Allen, S.R., McPhie, J., 2000. Water-settling and resedimentation of submarine rhyolitic pumice at Yali, eastern Aegean, Greece. J. Volcanol. Geotherm. Res. 95, 285-307.

Allen, S.R., Fiske, R.S., Tamura, Y., 2010. Effects of water depth on pumice formation in submarine domes at Sumisu, Izu-Bonin arc, western Pacific. Geology 38, 391-394.

Barclay, J., Riley, D.S., Sparks, R.S.J., 1995. Analytical models for bubble growth during decompression of high viscosity magmas. Bull. Volcanol. 57, 422-431.

Blower, J.D., Keating, J.P., Mader, H.M., Phillips, J.C., 2001a. Inferring volcanic degassing processes from vesicle size distributions. Geophys. Res. Lett. 28, 347-350.

Blower, J.D., Mader, H.M., Wilson, S.D.R., 2001b. Coupling of viscous and diffusive controls on bubble growth during explosive volcanic eruptions. Earth Planet. Sci. Lett. 193, 47-56.

Blower, J.D., Keating, J.P., Mader, H.M., Phillips, J.C., 2002. The evolution of bubble size distributions in volcanic eruptions. J. Volcanol. Geotherm. Res. 120, 1-23.

Bottinga, Y., Javoy, M., 1990. Midocean ridge basalt degassing - bubble nucleation. J. Geophys. Res. 95, 5125-5131.

Chadwick, W.W., Jr., Cashman, K.V., Embley, R.W., Matsumoto, H., Dziak, R.P., de Ronde, C.E.J., Lau, T.K., Deardorff, N.D., Merle, S.G., 2008. Direct video and hydrophone observations of submarine explosive eruptions at NW Rota-1 volcano, Mariana arc. J. Geophys. Res. 113, B08S10. doi:10.1029/2007jb005215.

Clague, D.A., Batiza, R., Head, J.W.I., Davis, A.S., 2003a. Pyroclastic and Hydroclastic Deposits on Loihi Seamount, Hawaii, in: White, J.D.L., Smellie, J.L., Clague, D.A.

(Eds.), Explosive Subaqueous Volcanism, Geophysical Monograph 140. AGU, Washington, DC, pp. 73-95.

Clague, D.A., Davis, A.S., Dixon, J.E., 2003b. Submarine Eruptions on the Gorda Mid-Ocean Ridge, in: White, J.D.L., Smellie, J.L., Clague, D.A. (Eds.), Explosive Subaqueous Volcanism, Geophysical Monograph 140. AGU, Washington, DC, pp. 111-125.

Davis, A.S., Clague, D.A., 2003. Hyaloclastite from Miocene Seamounts Offshore Central California: Compositions, Eruptions Styles, and Depositional Processes, in: White, J.D.L., Smellie, J.L., Clague, D.A. (Eds.), Explosive Subaqueous Volcanism, Geophysical Monograph 140. AGU, Washington, DC, pp. 129-141.

Davis, A.S., Clague, D.A., 2006. Volcaniclastic deposits from the North Arch volcanic field, Hawaii: explosive fragmentation of alkalic lava at abyssal depths. Bull. Volcanol. 68, 294-307.

Denlinger, R.P., Hoblitt, R.P., 1999. Cyclic eruptive behavior of silicic volcanoes. Geology 27, 459-462.

Dingwell, D.B., 1998. Recent experimental progress in the physical description of silicic magma relevant to explosive volcanism., in: Gilbert, J.S., Sparks, R.S.J. (Eds.), The physics of explosive eruptions. 145. Geol Soc Lond Spec Publ, pp. 9-26.

Dingwell, D.B., Webb, S.L., 1989. Structural Relaxation in Silicate Melts and Non-Newtonian Melt Rheology in Geologic Processes. Phys. Chem. Miner. 16, 508-516.

Dowty, E., 1980. Crystal growth and nucleation theory and the numerical simulation of igneous crystallization, in: Hargraves, R.B. (Ed.), Physics of magmatic processes. Princeton University Press, Princeton, pp. 419-485.

Eissen, J.-P., Fouquet, Y., Hardy, D., Ondres, H., 2003. Recent MORB vocaniclastic explosive deposits formed between 500 and 1750 m.b.s.l. on the axis of the Mid-Atlantic Ridge, South Azores, Explosive Subaqueous Volcanism, Geophysical Monograph 140. AGU, Washington, DC, pp. 143-166.

Fiske, R.S., Naka, J., Iizasa, K., Yuasa, M., Klaus, A., 2001. Submarine silicic caldera at the front of the Izu-Bonin arc, Japan: Voluminous seafloor eruptions of rhyolite pumice. Geol. Soc. Am. Bull. 113, 813-824.

Gaspar, J.L., Queiroz, G., Pacheco, J.M., Ferreira, T., Wallenstein, N., Coutinho, R., 2003. Basaltic Lava Balloons Produced During the 1998-2001 Serreta Submarine Ridge Eruption (Azores), in: White, J.D.L., Smellie, J.L., Clague, D.A. (Eds.), Explosive Subaqueous Volcanism, Geophysical Monograph 140. AGU, Washington, DC, pp. 205-229.

Gill, J., Torssander, P., Lapierre, H., Taylor, R., Kaiho, K., Koyama, M., Kusakabe, M., Aitchison, J., Cisowski, S., Dadey, K., Fujioka, K., Klaus, A., Lovell, M., Marsaglia, K., Pezard, P., Taylor, B., Tazaki, K., 1990. Explosive Deep-Water Basalt in the Sumisu Backarc Rift. Science 248, 1214-1217.

Giordano, D., Russell, J.K., Dingwell, D.B., 2008. Viscosity of magmatic liquids: A model. Earth Planet. Sci. Lett. 271, 123-134.

Helo, C., Clague, D.A., Stix, J., 2008. Pyroclastic eruptions from Axial caldera, Juan de Fuca Ridge, NE Pacific Ocean. IOD Conf. Ser.: Earth Environ. Sci. 3, 012005.

Hess, K.-U., Dingwell, D.B., 1996. Viscosities of hydrous leucogranitic melts: A non-Arrhenian model. Amer. Mineral. 81, 1297.1300.

James, M.R., Lane, S.J., Chouet, B., Gilbert, J.S., 2004. Pressure changes associated with the ascent and bursting of gas slugs in liquid-filled vertical and inclined conduits. J. Volcanol. Geotherm. Res. 129, 61-82.

James, M.R., Lane, S.J., Chouet, B.A., 2006. Gas slug ascent through changes in conduit diameter: Laboratory insights into a volcano-seismic source process in low-viscosity magmas. J. Geophys. Res. 111, B05201.

Jaupart, C., Vergniolle, S., 1989. The generation and collapse of a foam layer at the roof of a basaltic magma chamber. J. Fluid. Mech. 203, 347-380.

Kano, K., Takeuchi, K., Yamamoto, T., Hoshizumi, H., 1991. Subaqueous rhyolite block lavas in the Miocene Ushikiri Formation, Shimane Peninsula, SW Japan. J. Volcanol. Geotherm. Res. 46, 241-253.

Kano, K., 1996. A Miocene coarse volcaniclastic mass-flow deposit in the Shimane Peninsula, SW Japan: product of a deep submarine eruption? Bull. Volcanol. 58, 131-143.

Kano, K., 2003. Subaqueous Pumice Eruptions and Their Products: A Review, in: White, J.D.L., Smellie, J.L., Clague, D.A. (Eds.), Explosive Subaqueous Volcanism, Geophysical Monograph 140. AGU, Washington, DC, pp. 213-230.

Kato, Y., 1987. Woody pumice generated with submarine eruption. Journal - Geological Society of Japan 93, 11-20.

Lane, S.J., Chouet, B.A., Phillips, J.C., Dawson, P., Ryan, G.A., Hurst, E., 2001. Experimental observations of pressure oscillations and flow regimes in an analogue volcanic system. J. Geophys. Res. 106, 6461-6476.

Lane, S.J., Gilbert, J.S., 2008. Fluid motions in volcanic conduit: a source of seismic and acoustic signals, Special Publications. Geological Society, London, p. 244.

Lensky, N.G., Lyakhovsky, V., Navon, O., 2001. Radial variations of melt viscosity around growing bubbles and gas overpressure in vesiculating magmas. Earth Planet. Sci. Lett. 186, 1-6.

Lu, N.Q., Oguz, H.N., Prosperetti, A., 1989. The oscillations of a small floating bubble. Physics of Fluids a-Fluid Dynamics 1, 252-260.

Lyakhovsky, V., Hurwitz, S., Navon, O., 1996. Bubble growth in rhyolitic melts: experimental and numerical investigation. Bull. Volcanol. 58, 19-32.

Manga, M., Castro, J., Cashman, K.V., Loewenberg, M., 1998. Rheology of bubble-bearing magmas. J. Volcanol. Geotherm. Res. 87, 15-28.

Marti, J., Soriano, C., Dingwell, D.B., 1999. Tube pumices as strain markers of the ductile-brittle transition during magma fragmentation. Nature 402, 650-653.

Métrich, N., Wallace, P.J., 2008. Volatile abundances in basaltic magmas and their degassing paths tracked by melt Inclusions, in: Putrika, K.D., Tepley III, F.J. (Eds.), Minerals, inclusions and volcanic processes, Reviews in Mineralogy and Geochemistry 69. The mineralogical Society of America, Chantilly, Virginia, pp. 363-402.

Mourtada-Bonnefoi, C.C., Mader, H.M., 2004. Experimental observations of the effect of crystals and pre-existing bubbles on the dynamics and fragmentation of vesiculating flows. J. Volcanol. Geotherm. Res. 129, 83-97.

Mueller, W., White, J.D.L., 1992. Felsic fire-fountaining beneath Archean seas: pyroclastic deposits of the 2730 Ma Hunter Mine Group, Quebec, Canada. J. Volcanol. Geotherm. Res. 54, 117-134.

Navon, O., Chekhmir, A., Lyakhovsky, V., 1998. Bubble growth in highly viscous melts: theory, experiments, and autoexplosivity of dome lavas. Earth Planet. Sci. Lett. 160, 763-776.

Nicholls, J., 1990. The Mathematics of fluid flow and a simple application to problems of magma transport, in: Nicholls, J., Russell, J.K. (Eds.), Modern methods of igneous petrology; understanding magmatic processes, Reviews in Mineralogy 24. Mineralogical Society of America, Washington, D.C., pp. 109-123.

Ohminato, T., Chouet, B.A., Dawson, P., Kedar, S., 1998. Waveform inversion of very long period impulsive signals associated with magmatic injection beneath Kilauea Volcano, Hawaii. J. Geophys. Res. 103, 23839-23862.

Paonita, A., Martelli, M., 2006. Magma dynamics at mid-ocean ridges by noble gas kinetic fractionation: Assessment of magmatic ascent rates. Earth Planet. Sci. Lett. 241, 138-158.

Papale, P., 1999. Strain-induced magma fragmentation in explosive eruptions. Nature 397, 425-428.

Parfitt, E.A., Wilson, L., 1995. Explosive Volcanic-Eruptions .9. The Transition between Hawaiian-Style Lava Fountaining and Strombolian Explosive Activity. Geophysical Journal International 121, 226-232.

Parfitt, E.A., 2004. A discussion of the mechanisms of explosive basaltic eruptions. J. Volcanol. Geotherm. Res. 134, 77-107.

Perfit, M., Chadwick, W.W., 1998. Magmatism at Mid-Ocean Ridges: Constraints from Volcanological and Geochemical Investigations, in: Buck, R.W., Delaney, P.T., Karson, J.A., Lagabrielle, Y. (Eds.), Faulting and magmatism at mid-ocean ridges, Geophysical Monograph 106. AGU, Washington, D.C., pp. 59-116.

Phillips, J.C., Lane, S.J., Lejeune, A.-M., Hilton, M., 1995. Gum rosin-acetone system as an analogue to the degassing behaviour of hydrated magmas. Bull. Volcanol. V57, 263-268.

Phillips, J.C., Woods, A.W., 2001. Bubble plumes generated during recharge of basaltic magma reservoirs. Earth Planet. Sci. Lett. 186, 297-309.

Polacci, M., Baker, D., Bai, L., Mancini, L., 2008. Large vesicles record pathways of degassing at basaltic volcanoes. Bull. Volcanol. 70, 1023-1029.

Ripepe, M., Ciliberto, S., Della Schiava, M., 2001. Time constraints for modeling source dynamics of volcanic explosions at Stromboli. J. Geophys. Res. 106, 8713-8727.

Schipper, C.I., White, J.D.L., Houghton, B.F., Shimizu, N., Stewart, R.B., 2010. Explosive submarine eruptions driven by volatile-coupled degassing at Lo`ihi Seamount, Hawai`i. Earth Planet. Sci. Lett. 295, 497-510.

Scriven, L.E., 1959. On the dynamics of phase growth. Chemical Engineering Science 10, 1-13.

Simakin, A.G., Armienti, P., Epel'baum, M.B., 1999. Coupled degassing and crystallization: experimental study at continuous pressure drop, with application to volcanic bombs. Bull. Volcanol. 61, 275-287.

Sohn, R.A., Willis, C., Humphris, S., Shank, T.M., Singh, H., Edmonds, H.N., Kunz, C., Hedman, U., Helmke, E., Jakuba, M., Liljebladh, B., Linder, J., Murphy, C., Nakamura, K.-i., Sato, T., Schlindwein, V., Stranne, C., Tausenfreund, M., Upchurch, L., Winsor, P., Jakobsson, M., Soule, A., 2008. Explosive volcanism on the ultraslow-spreading Gakkel ridge, Arctic Ocean. Nature 453, 1236-1238.

Sparks, R.S.J., 1978. Dynamics of Bubble Formation and Growth in Magmas - Review and Analysis. J. Volcanol. Geotherm. Res. 3, 1-37.

Stern, R.J., Tamura, Y., Embley, R.W., Ishizuka, O., Merle, S.G., Basu, N.K., Kawabata, H., Bloomer, S.H., 2008. Evolution of West Rota Volcano, an extinct submarine volcano in the southern Mariana Arc: Evidence from sea floor morphology, remotely operated vehicle observations and 40Ar–39Ar geochronological studies. Island Arc 17, 70-89. doi:10.1111/j.1440-1738.2007.00600.x.

Stix, J., Phillips, J.C., in preparation. Analogue experiments of magma fragmentation and degassing: effects of pressure, volatile content , and decompression rate.

Vergniolle, S., Brandeis, G., 1994. Origin of the sound generated by Strombolian explosions. Geophys. Res. Lett. 21, 1959-1962.

Vergniolle, S., 1996. Bubble size distribution in magma chambers and dynamics of basaltic eruptions. Earth Planet. Sci. Lett. 140, 269-279.

Vergniolle, S., Brandeis, G., 1996. Strombolian explosions 1. A large bubble breaking at the surface of a lava column as a source of sound. J. Geophys. Res. 101, 20433-20447.

Vergniolle, S., Brandeis, G., Mareschal, J.C., 1996. Strombolian explosions 2. Eruption dynamics determined from acoustic measurements. J. Geophys. Res. 101, 20449-20466.

Watson, E.B., 1994. Diffusion in volatile-bearing magmas, in: Carroll, M.R., Holloway, J.R. (Eds.), Volatiles in magmas, Reviews in Mineralogy 30. Mineralogical Society of America, Washington, DC, p. 517.

Wright, I.C., Gamble, J.A., Shane, P.A.R., 2003. Submarine silicic volcanism of the Healy caldera, southern Kermadec arc (SW Pacific): I - volcanology and eruption mechanisms. Bull. Volcanol. 65, 15-29.

Acknowledgements

The department for Earth Sciences, University of Bristol is thanked for hosting C.H., I.M., and J.S. and provision of the laboratory facilities. J.S. was supported by grants from the Natural Sciences and Engineering Research Council of Canada. I.M. was supported by the eHaz program. C.H. was supported by R.H. Tomlinson, GEOTOP, and J. W. McConnell Memorial Fellowships at McGill University.

Table

Table 1. Ratios of exsolution to exit pressure for the experimental and magmatic systems.

Exsolution pressure		25 kPa[a]	50 MPa (2.2; 0.02)[b]	150 MPa (4.0; 0.07)	300 MPa (6.1; 0.15)	650 MPa (10.5; 0.4)
		$p_{exsolution}/p_{final}$ [c]				
Exit pressure (magmatic)	0.1 MPa		500	1500	3000	6500
	5.0 MPa		10	30	60	130
	20 MPa		3	8	15	33
	40 MPa		1	4	8	16
Exit pressure (experiment)	0.2 kPa	125				
	2.5 kPa	10				
	5 kPa	5				
	10 kPa	2.5				
	12.5 kPa	2				

[a] Gum rosin-acetone mixture.

[b] Volatile saturation concentrations in wt. % for either H_2O or CO_2 in a basalt.

[c] $p_{exsolution}/p_{final} = V_{final}/V_{exsolution}$

Figure legends

Figure 1 Expansion of the exsolving gas phase as a function of the exit (final) pressure for experimental and magmatic pressure ranges. Expansion is expressed as the ratio of final free gas volume to the free gas volume at the exsolution pressure. The exit pressure is normalized to the exsolution pressure, and gases were assumed to behave ideally. Magmatic saturation pressures greater than 100 MPa result in greater gas expansion for a given exit pressure.

Figure 2 Viscosity versus volatile concentration for gum rosin-acetone mixture and magmatic systems. Data for gum rosin-acetone are taken from Phillips et al. (1995) and are fit by the equation $\log_{10}$ *viscosity* = -3.716 + 15490 / (*acetone* [mol/m^3] + 941.5). Mixtures with 30, 20, 15, 12, and 0 wt. % acetone are shown. Viscosities of the hydrous rhyolite at 800 °C and tholeiitic basalt at 1200 °C were calculated after Hess and Dingwell (1996) and Giordano et al. (2008), respectively. A constant density of 2200 kg m^{-3} for the rhyolite and 2600 kg m^{-3} for the basalt was used for the conversion of wt. % to mol m^{-3}.

Figure 3 General experimental setup. Gum-rosin acetone mixtures in a borosilicate glass tube system are rapidly decompressed from an initial pressure (either 100 kPa or 25 kPa) to final pressures between 15 kPa and 0.5 kPa. h_0: initial height, h: expanded height after decompression. For one series of experiments the tube diameter was either expanded from 28 mm 147 mm or reduced to 14 mm about one cm above h_0. Reducing and increasing conduit conditions are indicated to the right and left, respectively.

Figure 4 Expansion versus time of GRA mixtures with 30 wt. % acetone rapidly decompressed to final pressures between 10 and 0.2 kPa (ratios of exsolution to exit pressure are given in parenthesis). Open symbols denote runs with initial bubbles. All

flows underwent fragmentation; the black arrows indicate the point of fragmentation. Continuous dashed lines represent constant elongational strain rates; the short lines at the top of the diagrams indicate slopes of constant acceleration. **a**, Decompression with lower exsolution to final pressure ratio. 10 kPa is likely the fragmentation threshold for runs without initial bubbles, as this experiment only produced mild bubble burst at the head. **b**, Higher exsolution to final pressure ratio.

Figure 5 Expansion versus time of GRA mixtures with 20 wt. % acetone, instantaneously decompressed to various final pressures. Open symbols denote runs with initial bubbles. **a**, Non-fragmenting flows at higher final pressures, **b**, Fragmenting flows at lower final pressures. The black arrows designate the point of fragmentation. **c**, Enlarged inlay of (**a**) depicting an oscillating flow front during late stages for small decompressions.

Figure 6 Pressure data from bottom pressure transducer under simple conduit conditions with GRA mixtures of 30 wt. % acetone. Data are corrected for the decompression event and band-pass filtered. Additionally, the decompression interval was fed with artificial data. Zero time is taken as the onset of pressure step recorded in the raw data. **a**–**c**, Comparison of pressure fluctuations in GRA mixtures with and without pre-eruptive bubbles for various decompression rations, p_{exs}/p_{final} (various final pressures, p_{final}). **d**, Sound energy densities ($E_s = p_{ac}^2 \times (\rho \times c^2)^{-1}$, see text) for the same experiments emitted from the frequency band 10–50 Hz.

Figure 7 Expansion-time evolution of 30 and 20 wt. % GRA mixtures experiencing reducing diameter conditions. The point of the internal diameter reduction from 38 mm to 14 mm is indicated. Normal flow profiles are shown for comparison. Other symbols as in Figure 4.

Figure 8 Pressure data from bottom pressure transducer under reducing conduit conditions with GRA mixtures of 20 and 30 wt. % acetone. **a–c**, Pressure fluctuations for various decompression ratios p_{exs}/p_{final} (various final pressures, p_{final}). **d**, Sound energy densities. See Figure 6 for further explanations of analysis. Note, wider time windows shown than in Figure 6.

Figure 9 High-speed camera still images of GRA flows with 20 wt. % acetone during rapid decompression under different conduit diameter conditions. Final pressure is 2.5 kPa (p_{exs}/p_{final} = 10). Recording rate is 250 fps. **a**, Constant internal diameter of 38 mm. The rising flow head is composed of clearly defined cm sized bubbles, and fragmentation does not occur before 72 ms. **b**, Conduit is reduced from 38 to 14 mm. The flow head rapidly advances as a strongly dispersed flow, fragmenting at early stages.

Figure 10 High-speed camera still images of GRA flows with 20 wt. % acetone during rapid decompression under increasing diameter conditions. Flow conditions and elapsed times are shown. **a**, **b**, Decompression to 2.5 kPa (p_{exs}/p_{final} = 10) of GRA mixtures without and with initial bubbles, respectively. **c**, **d**, Decompression to 0.3 kPa (p_{exs}/p_{final} = 83) of GRA mixtures without and with initial bubbles, respectively. The final images in each row represent the final degree of expansion, except **d**, where foam expanded further upwards then shown. Flow margins are outlined in some images for better visibility. Note, that in **c**, **d** the head of the flow does not touch the sidewall of the tube.

Figure 11 Cumulative frequency curve of fragment size produced during rapid decompression of GRA mixtures with 30 wt. % acetone to 2.5 kPa (p_{exs}/p_{final} = 10). Size is calculated as the area on a binary-colour image occupied by the fragment.

Figures

Figure 1

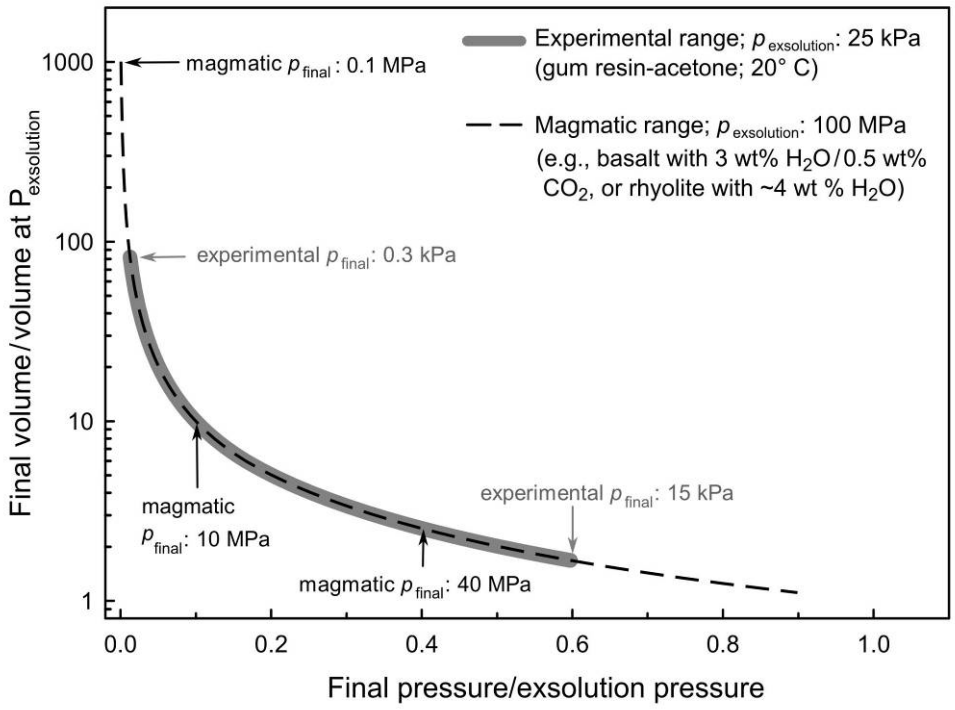

Figure 2

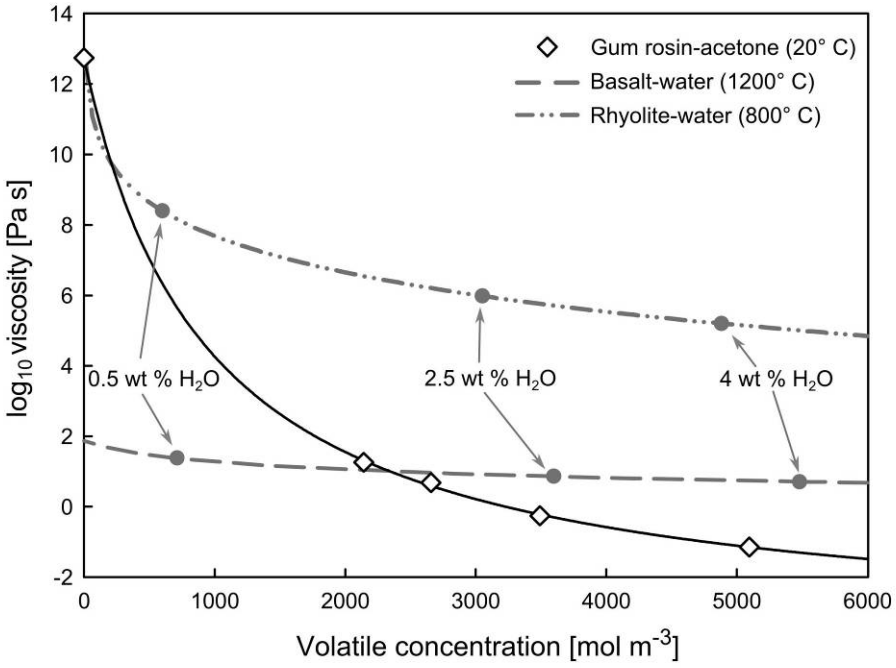
Gum rosin-acetone (20° C)
Basalt-water (1200° C)
Rhyolite-water (800° C)
0.5 wt % H2O
2.5 wt % H2O
4 wt % H2O
log10 viscosity [Pa s]
Volatile concentration [mol m-3]
14
12
10
8
6
4
2
0
-2
0
1000
2000
3000
4000
5000
6000

Figure 3

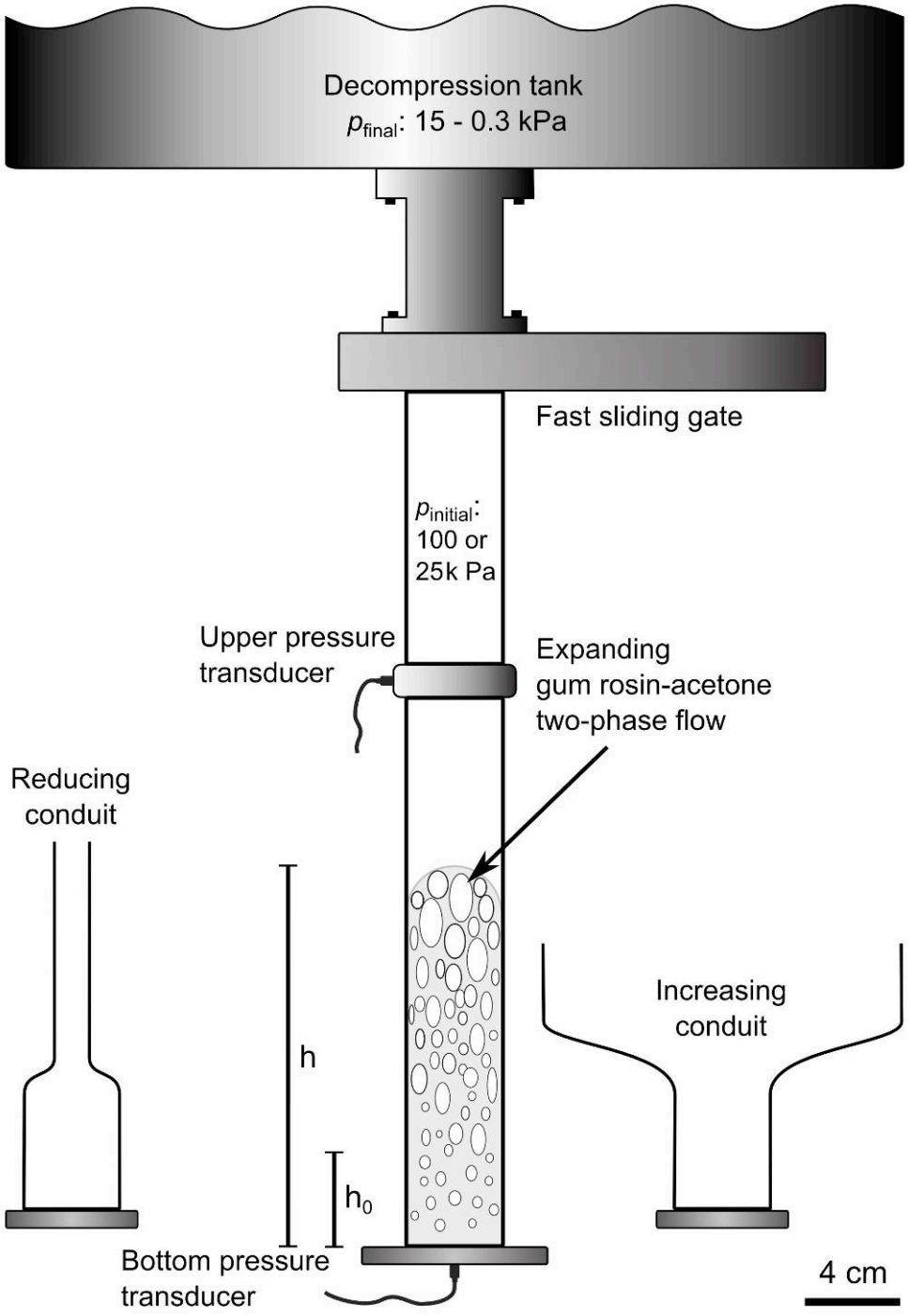
Decompression tank
p_{final}: 15 - 0.3 kPa
Fast sliding gate
$p_{initial}$:
100 or
25k Pa
Upper pressure
transducer
Expanding
gum rosin-acetone
two-phase flow
Reducing
conduit
h
h_0
Increasing
conduit
Bottom pressure
transducer
4 cm

Figure 4

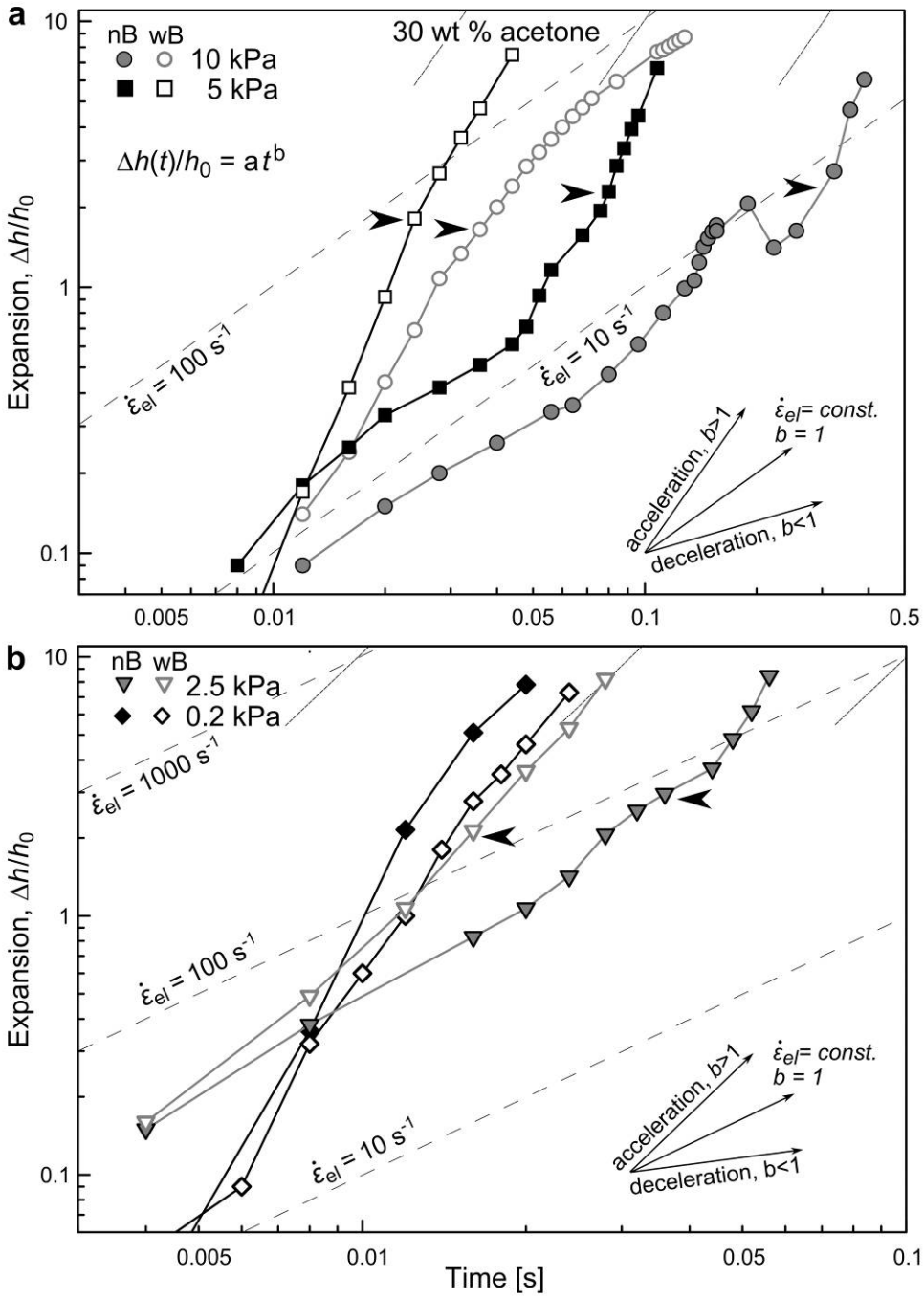
a
nB wB
10 kPa
5 kPa
30 wt % acetone
$\Delta h(t)/h_0 = a t^b$
Expansion, $\Delta h/h_0$
$\dot{\varepsilon}_{el} = 100\ s^{-1}$
$\dot{\varepsilon}_{el} = 10\ s^{-1}$
acceleration, b>1
$\dot{\varepsilon}_{el}$= const.
b = 1
deceleration, b<1
b
nB wB
2.5 kPa
0.2 kPa
$\dot{\varepsilon}_{el} = 1000\ s^{-1}$
$\dot{\varepsilon}_{el} = 100\ s^{-1}$
$\dot{\varepsilon}_{el} = 10\ s^{-1}$
Time [s]

Figure 5

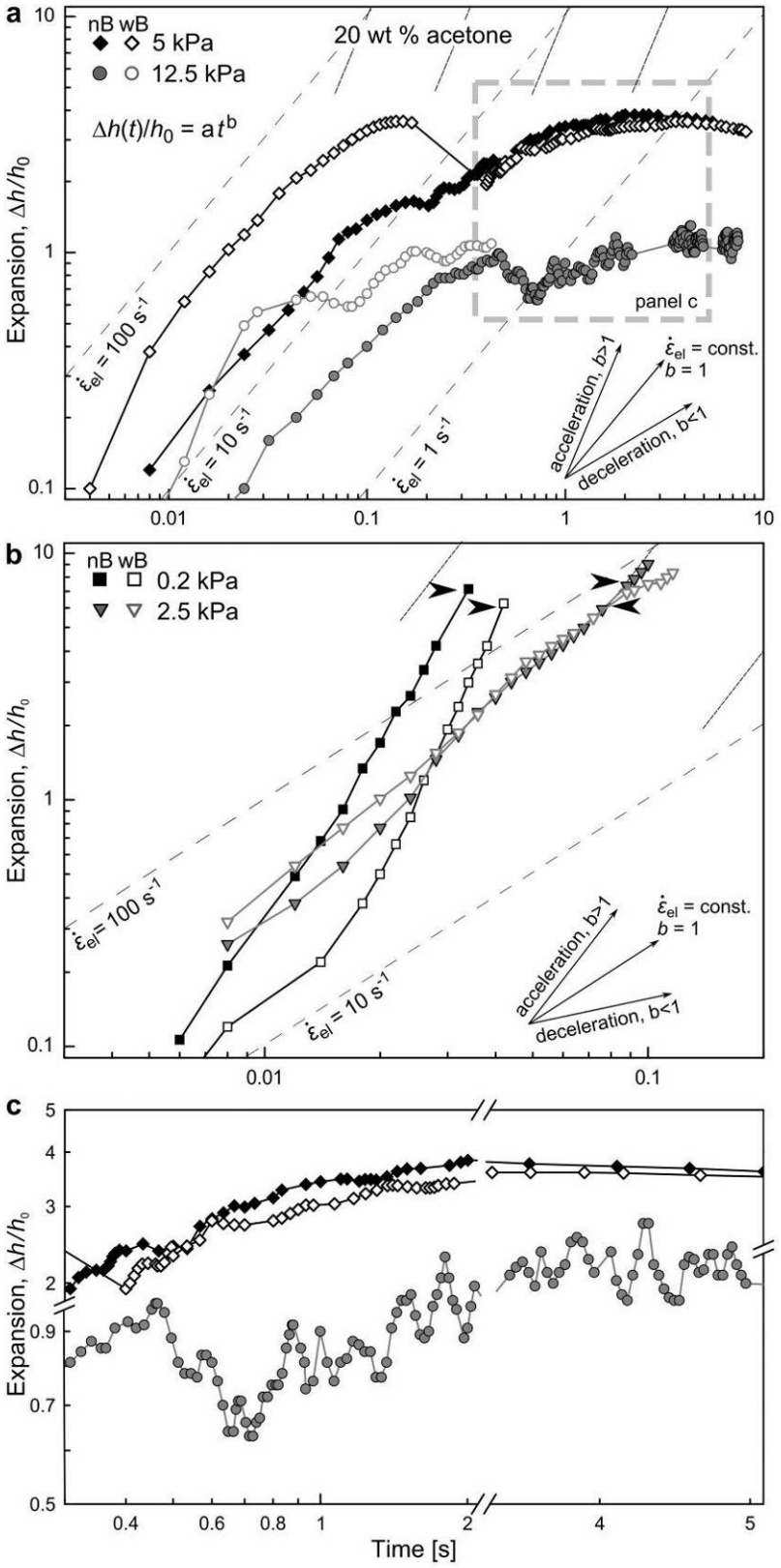
a
nB wB
5 kPa
12.5 kPa
20 wt % acetone
$\Delta h(t)/h_0 = a t^b$
Expansion, $\Delta h/h_0$
$\dot{\varepsilon}_{el}$ = 100 s^{-1}
$\dot{\varepsilon}_{el}$ = 10 s^{-1}
$\dot{\varepsilon}_{el}$ = 1 s^{-1}
panel c
acceleration, b>1
$\dot{\varepsilon}_{el}$ = const.
b = 1
deceleration, b<1
b
nB wB
0.2 kPa
2.5 kPa
Expansion, $\Delta h/h_0$
$\dot{\varepsilon}_{el}$= 100 s^{-1}
$\dot{\varepsilon}_{el}$ = 10 s^{-1}
acceleration, b>1
$\dot{\varepsilon}_{el}$ = const.
b = 1
deceleration, b<1
c
Expansion, $\Delta h/h_0$
Time [s]

Figure 6

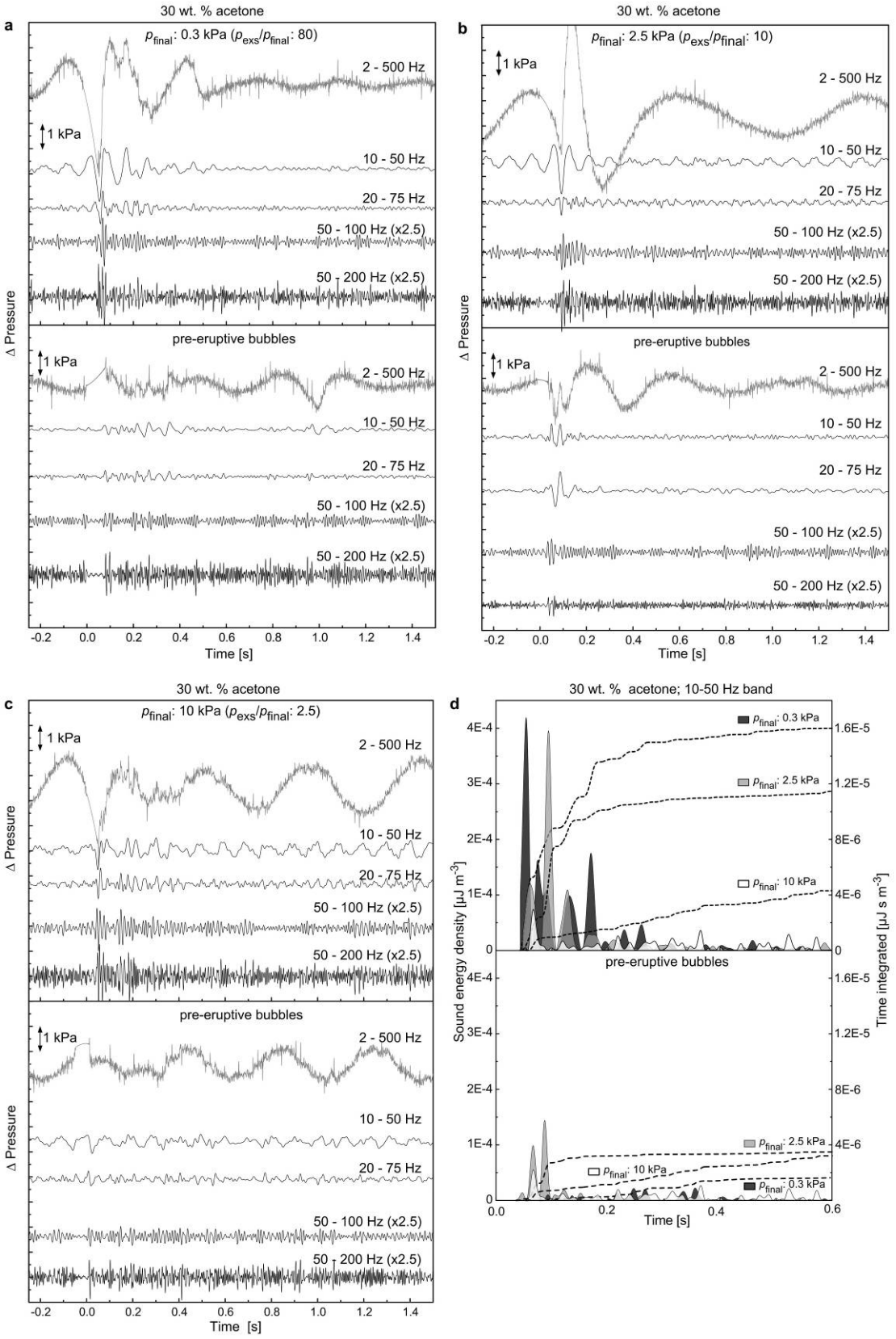
a
30 wt. % acetone
p_{final}: 0.3 kPa (p_{exs}/p_{final}: 80)
2 - 500 Hz
1 kPa
10 - 50 Hz
20 - 75 Hz
50 - 100 Hz (x2.5)
50 - 200 Hz (x2.5)
pre-eruptive bubbles
Δ Pressure
Time [s]
b
30 wt. % acetone
p_{final}: 2.5 kPa (p_{exs}/p_{final}: 10)
c
30 wt. % acetone
p_{final}: 10 kPa (p_{exs}/p_{final}: 2.5)
d
30 wt. % acetone; 10-50 Hz band
Sound energy density [µJ m^{-3}]
Time integrated [µJ s m^{-3}]

Figure 7

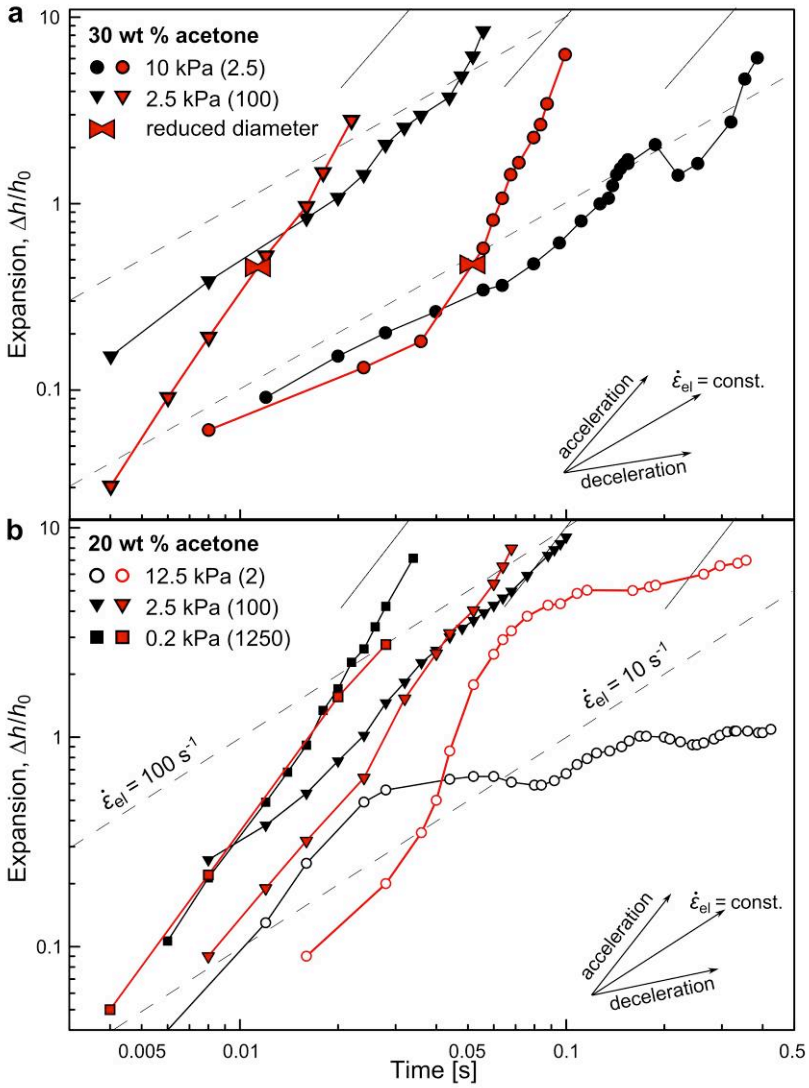
a
30 wt % acetone
10 kPa (2.5)
2.5 kPa (100)
reduced diameter
Expansion, $\Delta h/h_0$
10
1
0.1
acceleration
$\dot{\varepsilon}_{el}$ = const.
deceleration
b
20 wt % acetone
12.5 kPa (2)
2.5 kPa (100)
0.2 kPa (1250)
$\dot{\varepsilon}_{el}$ = 100 s^{-1}
$\dot{\varepsilon}_{el}$ = 10 s^{-1}
acceleration
$\dot{\varepsilon}_{el}$ = const.
deceleration
0.005
0.01
0.05
0.1
0.5
Time [s]

Figure 8

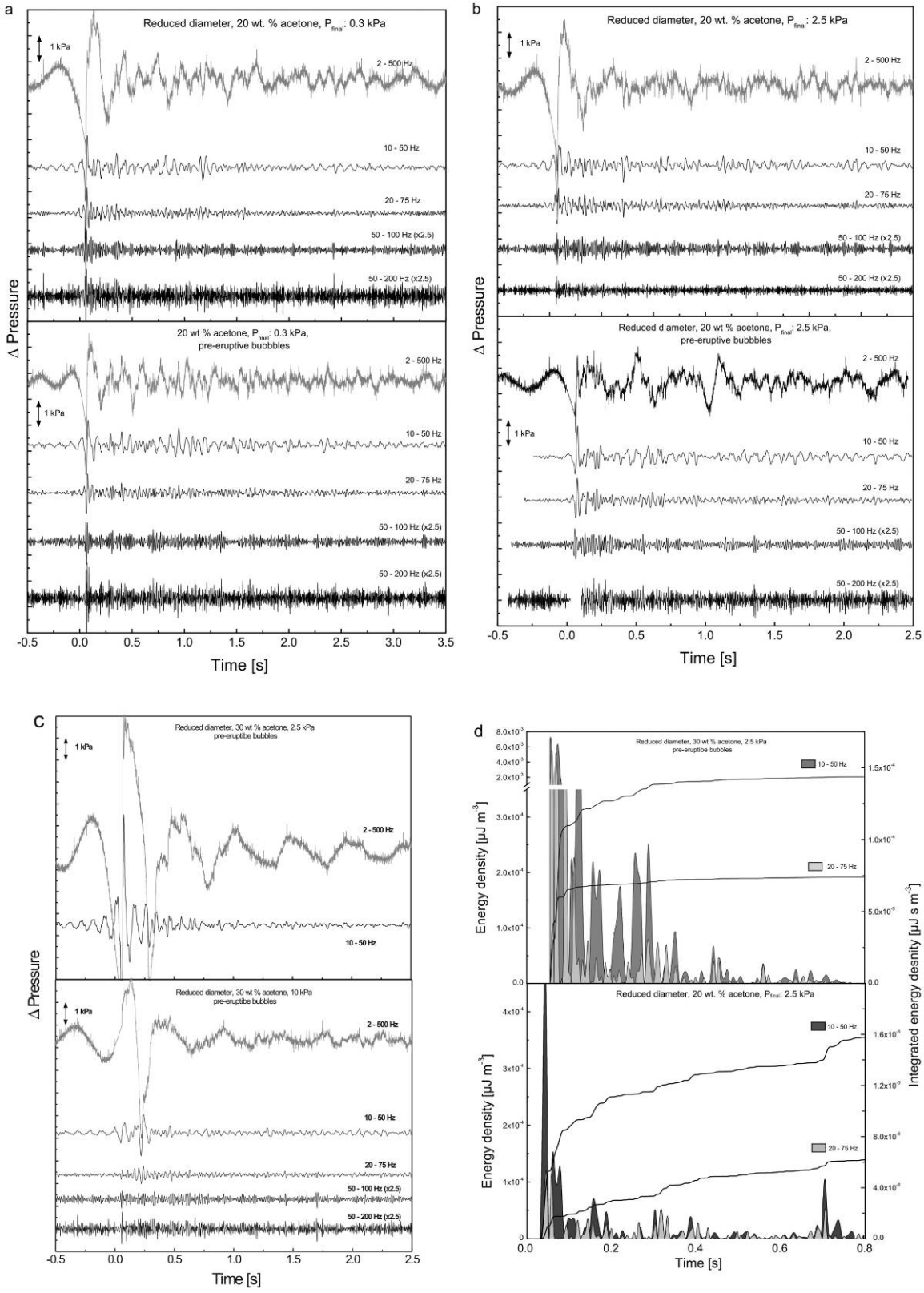
a
Reduced diameter, 20 wt. % acetone, P final: 0.3 kPa
1 kPa
2 - 500 Hz
10 - 50 Hz
20 - 75 Hz
50 - 100 Hz (x2.5)
50 - 200 Hz (x2.5)
20 wt % acetone, P final: 0.3 kPa,
pre-eruptive bubbles
Δ Pressure
Time [s]
b
Reduced diameter, 20 wt. % acetone, P final: 2.5 kPa
Reduced diameter, 20 wt % acetone, P final: 2.5 kPa,
pre-eruptive bubbles
c
Reduced diameter, 30 wt % acetone, 2.5 kPa
pre-eruptibe bubbles
Reduced diameter, 30 wt % acetone, 10 kPa
pre-eruptibe bubbles
d
Energy density [μJ m-3]
Integrated energy desnity [μJ s m-3]

Figure 9

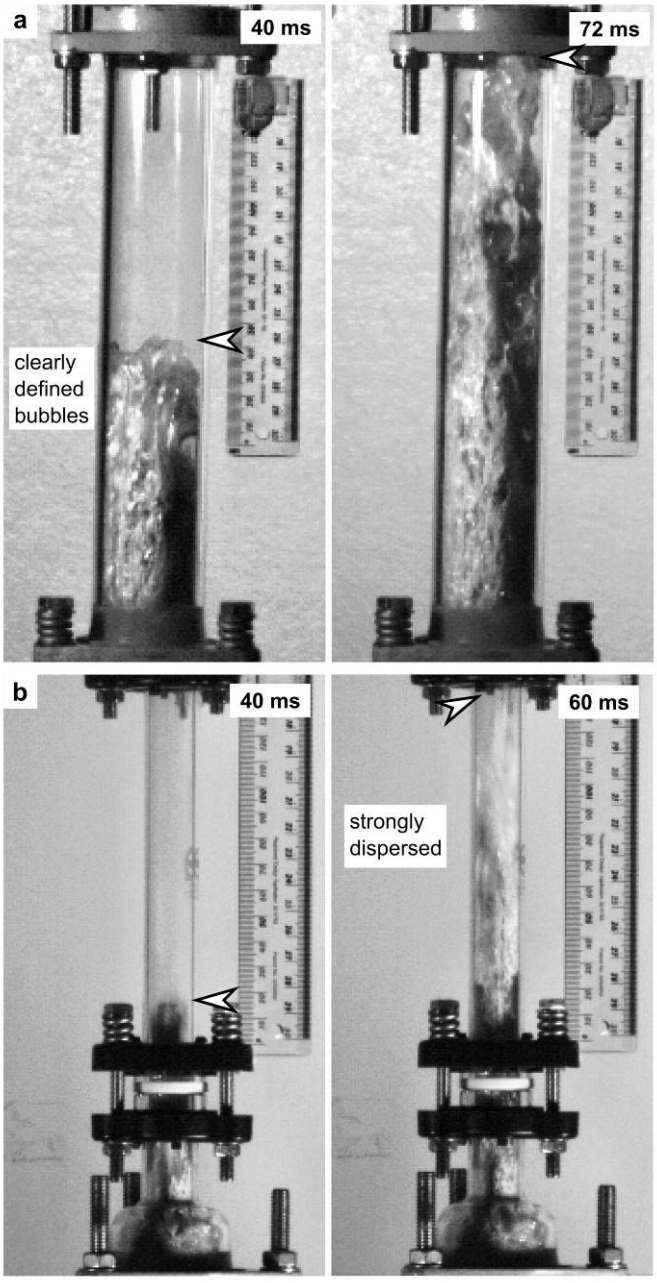
a
40 ms
72 ms
clearly
defined
bubbles
b
40 ms
60 ms
strongly
dispersed

Figure 10

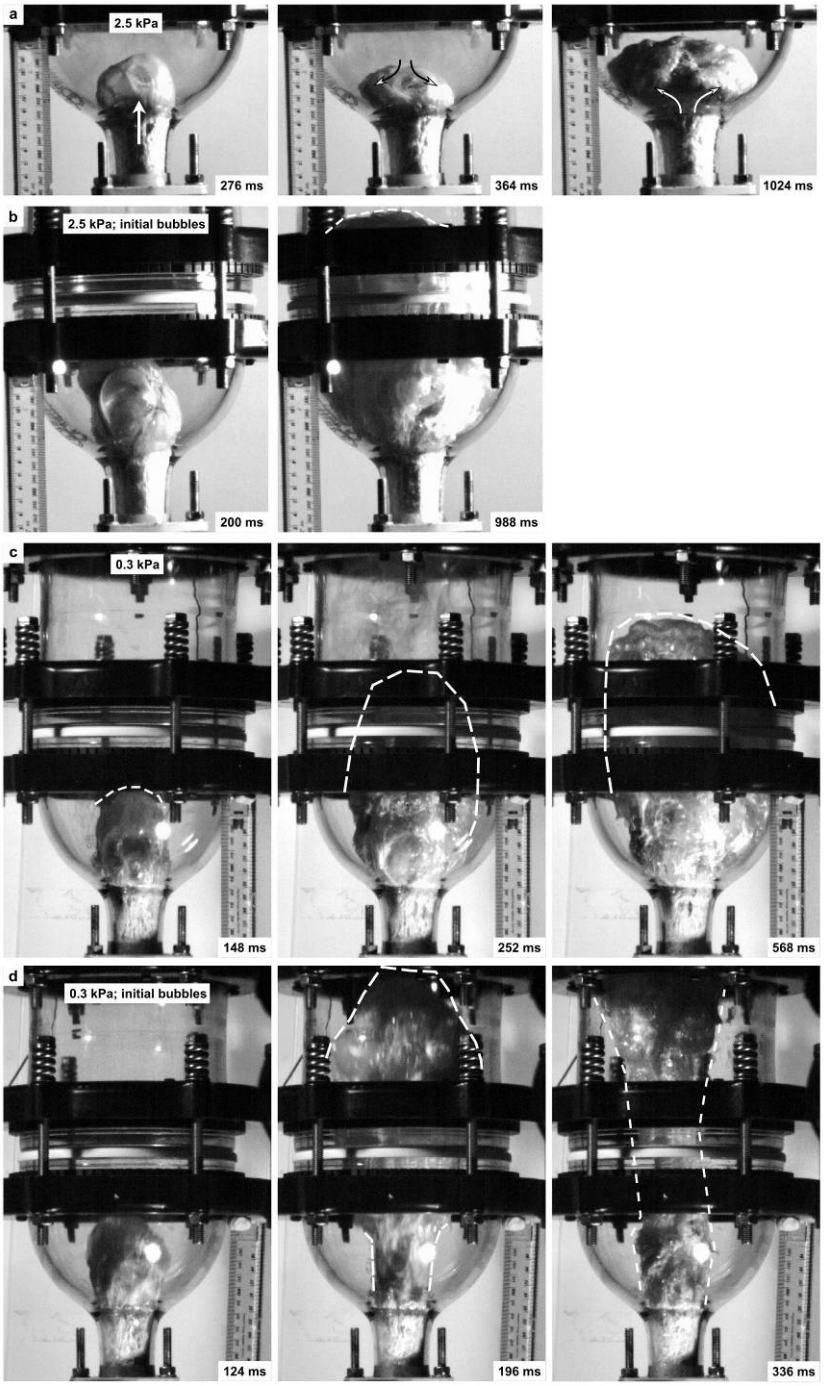
a
2.5 kPa
276 ms
364 ms
1024 ms
b
2.5 kPa; initial bubbles
200 ms
988 ms
c
0.3 kPa
148 ms
252 ms
568 ms
d
0.3 kPa; initial bubbles
124 ms
196 ms
336 ms

Figure 11

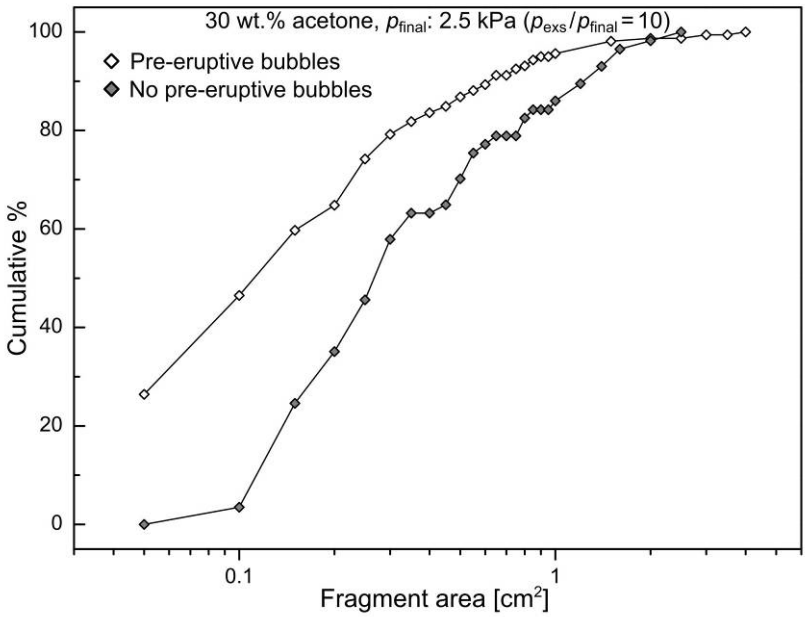
30 wt.% acetone, p_{final}: 2.5 kPa (p_{exs}/p_{final} = 10)
Pre-eruptive bubbles
No pre-eruptive bubbles
Cumulative %
100
80
60
40
20
0
0.1
1
Fragment area [cm^2]

General conclusions and future work

The following conclusions regarding pyroclastic eruptions on mid-ocean ridges can be drawn from my detailed analysis of volcaniclastic sequences on Axial Seamount, Juan de Fuca Ridge, and my analogue modeling experiments:

(1) Deposits of unconsolidated volcaniclastic material sampled from Axial Seamount resemble those found along other mid-ocean ridges and seamount sites. The volcaniclastic component is mainly comprised of angular, dense fragments and limu o Pele. On Axial Seamount these deposits appear unique in (a) their thickness, of up to two meters, (b) their composition of almost pure volcaniclastic particles and a very small mud and clay component, and (c) the variety of glass fragments including strongly deformed limu o Pele, pumiceous fragments, and Pele's hair.

(2) A pyroclastic origin is the favoured model for formation of such volcaniclastic deposits on mid-ocean ridges. Disintegration of a sheared, vesiculated magma is in best agreement with the types of fragments produced during the eruption. Submarine eruptions are, in principle, governed by the same general processes as subaerial eruptions, and a similar range of equivalent eruption styles can be expected. However, various extrinsic parameters, most notably confining pressure and rate of heat transfer, influence eruptions in deep-sea and subaerial environments differently, affecting the style of eruption and magma fragmentation.

(3) The recognition of CO_2-rich magmas at mid-ocean ridge systems provides the magmatic motor to drive explosive eruptions, linking subsurface magma reservoir conditions and surface volcaniclastic deposits. A high carbon content of the mantle results in ascent of CO_2-supersaturated magmas and strong volatile exsolution in the shallower

magmatic plumbing system. For a given CO_2 budget, the bubble rise model of Head and Wilson (2003), the foam collapse model of Jaupart and Vergniolle (1989), or a combination of both can lead to Strombolian-type bubble burst activity. Volatile exsolution during ascent of vesiculated magma from the shallow reservoir to the seafloor is limited, and vesiculation is increased primarily by volume expansion of existing bubbles. The interstitial liquid remains relatively dense in the course of the eruption. Correspondingly, limu o Pele, representing the vesicularity, and angular dense fragments are the dominant fragment types produced.

(4) Cooling rates of volcaniclastic fragments are extremely high, exhibiting hyperquenched states, and exceed those of sheet lava flow crusts. Differences in heat transfer rates between the different particle types can be attributed to the surface/volume ratio, whereas the notable range of cooling rates between different horizons is interpreted in terms of the size of the eruptive event. Fastest quenching is proposed to result from small individual eruptions where erupted magma plus free CO_2 gas are efficiently mixed with cold seawater. Final fragmentation and rapid quenching upon contact with seawater are coupled within a very short time window, and fragmentation occurs within the ductile and onset of the brittle regime as the glass transition is crossed. We suggest that rapid expansion of seawater steam in superficial cracks of the fragments introduces large stresses within the clasts, facilitating fragmentation and resulting in small grain sizes.

(5) Individual pyroclastic eruptions on Axial Seamount produced thin horizons of volcaniclastic glass fragments; the widespread thick deposits are the result of continuous accumulation from many eruptions. Volcaniclastic deposits along mid-ocean ridges therefore provide fairly simple access to prolonged time windows of volcanic activity,

allowing rapid sampling of numerous eruptions. This offers an efficient way to unveil the magmatic histories of mid-ocean ridge systems.

(6) On Axial Seamount, pyroclastic activity is most common during syn-caldera collapse and/or post-collapse history. The deposits are interpreted to represent the evolution of the magmatic reservoir after a major disruption, caused by a period of strong magma withdrawal which significantly evacuated the reservoir, potentially associated with a major caldera collapse event or events. The geochemical signature of the fragments can be understood in terms of a magma reservoir re-evolving towards a steady-state. This affirms the presence of a robust long-term magmatic reservoir capable of significant magma mixing over timescales similar to or shorter than the magma residence time.

(7) The mantle source feeding Axial Seamount is heterogeneous with end-member compositions similar to the average depleted MORB mantle (DMM) and a DMM with elevated concentrations of highly incompatible elements. The mean composition of the source tapped by the melting column shows a highly incompatible LILE budget elevated to about twice that of the average DMM. Melts appear to be efficiently pooled and mixed. Occasionally LREE depleted magmas reflecting higher degrees of melting are extracted and erupted.

(8) Dissolved CO_2 concentrations in plagioclase-hosted melt-inclusions are as high as 9160 ppm, demonstrating a very high CO_2 mantle flux along the Axial Seamount MORB segment. The carbon enrichment of the mantle source significantly exceeds that predicted by previous models. Entrapment of high-CO_2 melt inclusions in plagioclase indicates that large degrees of oversaturation are possible during magma ascent from the mantle into the shallow magma reservoir.

Future work:

Future work may focus on three broad issues: (1) the detailed history of full volcaniclastic sections on Axial Seamount, (2) CO_2 fluxes along mid-ocean ridge systems derived from melt inclusions, and (3) an in-depth study of the calorimetric signal of hyperquenched glasses.

A detailed geochemical and geochronological analysis of selected complete volcaniclastic sequences will be necessary to constrain their relationship to pre- and post-collapse lava flows, in order to decipher the evolution of the magmatic system and volcanic edifice. One of the key questions to be answered is the timing of the collapse event or events, the number of individual collapse events involved, and the association of strong pyroclastic activity with syn- and post-collapse time periods.

The global mantle CO_2 flux along mid-ocean ridges, and even more so the inter- and intra-ridge variability, remains a poorly constrained variable. A systematic analysis of dissolved CO_2 concentrations in melt inclusions from various mid-ocean ridge sites is required to arrive at a more robust value. Careful comparison of the degree of CO_2-supersaturation in magma from slow, medium, and fast-spreading centres could provide improved insight into the dynamics of magma ascent and the evolution of the CO_2 volatile phase from the mantle to the magma reservoir.

Calorimetric analysis of natural hyperquenched glasses is currently still hampered by the limited knowledge base regarding hyperquenched states and potential post-quenching relaxation mechanisms, and also by analytical instrumentation which is neither capable of analysing individual grains nor able to perform measurements under pressures comparable to those of the submarine environment. An improved experimental dataset

and better understanding of processes are required for a more complete interpretation of differential scanning calorimetry spectra of hyperquenched glasses, particularly the nature of the bimodal distribution of relaxation peaks observed in many of the volcaniclastic samples. With expanded knowledge and improved analytical facilities, a detailed study of grain-to-grain cooling rate variations, covering samples from a wide range of water depths, will provide a more comprehensive understanding of the interplay between fragmentation and cooling during pyroclastic eruptions in submarine environments.

Contributions of authors

Manuscript I: C.H. performed all analyses and analysed the data. D.A.C was responsible for the organisation of the cruise and sample collection, and J.S. supervised the work in general. The manuscript was written primarily by C.H., with contributions from D.A.C. and J.S.

Manuscript II: C.H. performed volatile analysis and major element analysis of the melt inclusions and host glasses, and analysed the data. M.-A.L performed the trace element analysis of the melt inclusions, N.S. supervised the volatile and trace element analysis, D.A.C was responsible for the organisation of the cruise and sample collection, and J.S. supervised the work. The manuscript was written primarily by C.H., with contributions from M.-A.L., N.S., D.A.C., and J.S.

Manuscript III: C.H. performed all analyses and analysed the data. D.B.D. provided the lab facilities at the University of Munich, and D.A.C was responsible for the organisation of the cruise and sample collection, and J.S. supervised the work. The manuscript was written primarily by C.H., with contributions from D.A.C., D.B.D., and J.S.

Manuscript IV: C.H. performed the experiments and analysed the data. I.M. assisted in the lab. J.P. provided the lab facilities at the University of Bristol and supervised the experimental work, and J.S. supervised the work in general. The manuscript was written primarily by C.H., with contributions from J.S.